Tailored Colloidal Quasicrystals

Inaugural-Dissertation

zur Erlangung des Doktorgrades
der Mathematisch-Naturwissenschaftlichen Fakultät
der Heinrich-Heine-Universität Düsseldorf

vorgelegt von

Matthias Sandbrink

aus Ankum

Düsseldorf, Dezember 2014

aus dem Institut für Theoretische Physik II: Weiche Materie
der Heinrich-Heine-Universität Düsseldorf

Gedruckt mit der Genehmigung der
Mathematisch-Naturwissenschaftlichen Fakultät der
Heinrich-Heine-Universität Düsseldorf

Referent: Dr. Michael Schmiedeberg
Korreferent: Prof. Dr. Hartmut Löwen

Tag der mündlichen Prüfung: 24. Februar 2015

Abstract

In 1982 the discovery of quasicrystals caused a revolution in crystallography and augmented the concept of ordered matter. On this account, Dan Shechtman was awarded the Nobel Prize in Chemistry 2011. Although quasicrystals are not comprised of a periodically repeating unit cell, they exhibit long-range order that can be detected in diffraction experiments. Several decisive differences to periodic crystals arise from the fact that quasicrystals are aperiodic. The rotational symmetry is not restricted to two-, three-, four-, or sixfold. Another important difference is the existence of so-called phasons, which denote additional hydrodynamic modes. Analogue to phonons, they do not cost free energy in the limit of long wave lengths. Phasons are a topic of current research and of many discussions. They are essential for the description of the elastic properties of quasicrystals and their topological defects. Yet, their eventual contribution to the stabilization of quasicrystals is disputed.

Most of the quasicrystals known today are complex metallic alloys consisting of several elements. In the recent past, several mesoscopic quasicrystals have been discovered, for instance in micelles or polymeric networks. In particular, the photonic properties of quasicrystalline structures with such length scales have caught interest. In this work, the point is to find out by means of computer simulations how colloidal quasicrystals can be constructed by design under controlled conditions.

Colloids are particles with a diameter in the range of microns that are dispersed in a solvent. Usually, the particles carry an electrostatic charge in order to stabilize the suspension. In statistical physics colloidal suspensions are a well-known model system to investigate atomic processes. On the one hand, the interaction between the particles can be tuned precisely, and on the other hand motion and position of the particles are directly observable by means of video-microscopy. In addition, the behavior of the suspension can be influenced by applying external fields. In this work, we use three different methods to stabilize quasicrystalline order in colloidal suspensions. As an advantage, the perspective on colloids may grant access to properties involving quasicrystals that remains often denied in atomic systems.

At first, we consider a two-dimensional suspension that is exposed to an interference pattern of several laser beams. In a laser field, forces directed towards the spots of high laser intensity act on the colloids. Therefore, quasicrystalline order can externally be enforced on the colloidal suspension representing a versatile model system. As particular advantage of such an optical quasicrystal, phasonic excitations can be implemented by tuning the individual phases of the laser beams. A phasonic drift causes complex rearrangements

between the minima and maxima of the intensity field, leading again to complex trajectories for the colloids. For various rotational symmetries, we determine characteristic areas in phononic and phasonic space into which all colloids can be mapped. On the basis of the characteristic areas, similar to an effective unit cell, the trajectories can be predicted. Furthermore, we investigate the influence of the particle diameter in this system as a model for molecular deposition on atomic quasicrystalline surfaces. The ratio between the length scale of the potential and the particle diameter yields self-similar patterns in the colloidal structure, whose rotational symmetry remains predetermined by the laser field. However, each pattern belongs to a different local isomorphism class.

Aside from enforcing by external fields, quasicrystalline order may also be stabilized by modifying the interaction between the particles. In this respect, we show that a concentration of smaller polymer coils added to the suspension is sufficient to alter the phase behavior in such a way that colloids self-assemble into a state with dodecagonal symmetry. Since several experimental implementations on the colloid-polymer mixture are documented in the literature, our result may provide assistance in growing colloidal quasicrystals in a controlled manner by processes of self-assembly.

In order to grow quasicrystalline structures comprised of colloids in three dimensions, we simulate the epitaxy of particles on substrates whose design is borrowed from quasicrystalline tilings. Under gravitation the colloids sediment onto the substrate and arrange according to the predefined order such that quasicrystalline layers emerge upon continued deposition. A specifically tuned particle-particle interaction is not required in this template-guided approach. We investigate the growth process for different substrate symmetries and address the question which tiling is most suitable. Moreover, we explore how defects in the substrate may influence the grown structure. We differentiate between local flips in the tiling, as a result of thermally excited phasonic fluctuations, and global defects like dislocations. In the considered symmetries, dislocations are characterized by a four-dimensional Burgers vector. During the epitaxial process they lead to defect lines in the three-dimensional structure, whose course can directly be analyzed in our model. We elucidate how the elastic strain accompanying a dislocation as well as the position of the dislocation seed within the substrate affect the course of the defect lines. Moreover, we explore the topological behavior of the defect lines. Thereby, we discover significant difference compared to periodic crystals.

In principle, all colloidal quasicrystalline structures that we tailor in simulations can be achieved in experiments. After all, the colloid-polymer mixture as well as the template-guided approach have already been successfully implemented in experiments in order to obtain periodic structures.

Zusammenfassung

Im Jahr 1982 leitete die Entdeckung der Quasikristalle eine Revolution in der Kristallographie ein und erweiterte die bisherige Sichtweise, wie sich Materie anordnen kann. Dafür wurde Dan Shechtman mit dem Nobelpreis für Chemie 2011 ausgezeichnet. Obwohl Quasikristalle nicht aus einer sich periodisch wiederholenden Einheitszelle bestehen, weisen sie eine langreichweitige Ordnung auf, die sich in einem Beugungsexperiment nachweisen lässt. Aus der Tatsache, dass Quasikristalle aperiodisch sind, ergeben sich mehrere wesentliche Unterschiede zu periodischen Kristallen. Zum einen bleibt die Rotationssymmetrie nicht auf zwei-, drei-, vier-, oder sechsfach beschränkt. Ein weiterer wichtiger Unterschied die Existenz sogenannter Phasonen. Dabei handelt es sich um zusätzliche hydrodynamische Moden, die wie Phononen im Grenzfall langer Wellenlängen keine Erhöhung der freien Energie erfordern. Phasonen sind Gegenstand der aktuellen Forschung und vieler Diskussionen. Sie sind unerlässlich bei der Beschreibung elastischer Eigenschaften von Quasikristallen oder ihrer topologischen Defekte. Inwiefern Phasonen eventuell sogar zur Stabilisierung von Quasikristallen beitragen ist umstritten.

Die meisten bekannten Quasikristalle sind komplexe metallische Legierungen, die aus mehreren Elementen bestehen. In jüngerer Vergangenheit wurden jedoch auch einige mesoskopische Quasikristalle entdeckt, z.B. in Mizellen oder Polymernetzwerken. Auf einer solchen Längenskala wecken insbesondere die photonischen Eigenschaften quasikristalliner Strukturen vermehrt Interesse. In dieser Arbeit geht es darum mit Hilfe von Computersimulationen herauszufinden, wie kolloidale Quasikristalle unter kontrollierten Bedingungen hergestellt werden können.

Kolloide sind Teilchen mit einem Durchmesser im Mikrometer Bereich, die in einer Flüssigkeit gelöst sind. Um die Lösung zu stabilisieren sind die Teilchen häufig elektrostatisch aufgeladen. In der statistischen Physik sind kolloidale Suspensionen ein beliebtes Modellsystem zur Erforschung atomarer Prozesse. Zum einen lässt sich die Wechselwirkung zwischen den Teilchen sehr genau einstellen und zum anderen können ihre Bewegung und Position direkt über Video-Mikroskopie beobachtet werden. Zusätzlich kann über externe Felder auf das Verhalten der Suspension Einfluss genommen werden. In dieser Arbeit werden drei Methoden verwendet, um quasikristalline Ordnung in einer kolloidalen Suspension zu stabilisieren. Der Blick auf Kolloide bietet den Vorteil, Fragestellungen im Zusammenhang mit Quasikristallen nachgehen zu können, die in atomaren Systemen bisher nur indirekt zugänglich sind.

Zunächst betrachten wir eine zweidimensionale Suspension, die einem Interferenzmuster aus mehreren Laserstrahlen ausgesetzt ist. Im Laserfeld wirken Kräfte auf die Kolloide,

die zu den Stellen mit hoher Laserintensität gerichtet sind. Aus diesem Grund lassen sich durch Interferenzmuster quasikristalline Anordnungen von außen vorgeben. Dieser optische Quasikristall verkörpert ein vielseitiges Modellsystem. Als besonderer Vorteil lassen sich phasonische Anregungen direkt über die Phasen der Laser einstellen. Ein phasonischer Drift verursacht komplexe Neuordnungen zwischen den Minima und Maxima des Intensitätsfeldes, was wiederum komplexe Trajektorien für die Kolloide ergibt. Wir bestimmen für verschiedene Rotationssymmetrien charakteristische Bereiche in der phononischen und phasonischen Verschiebung, in die alle Kolloide abgebildet werden können. Anhand dieser charakteristischen Bereiche lassen sich gleichsam einer effektiven Einheitszelle die Trajektorien vorhersagen. Zusätzlich untersuchen wir in diesem System den Einfluss des Teilchendurchmessers auf die induzierte Anordnung als Modell für molekulare Deposition auf atomaren quasikristallinen Oberflächen. Das Verhältnis zwischen der Längenskala des Potentials und des Teilchendurchmessers führt zu selbstähnlichen Mustern in der kolloidalen Struktur, deren Rotationssymmetrie weiterhin vom Laserfeld bestimmt wird. Jedes Muster fällt jedoch in eine andere lokale Isomorphismus-Klasse.

Anstatt die quasikristalline Ordnung über externe Felder vorzugeben, kann diese auch stabilisiert werden, indem die Wechselwirkung zwischen den Teilchen modifiziert wird. Wir zeigen in diesem Zusammenhang, dass eine Konzentration von kleineren Polymeren, die der Suspension hinzugefügt wird, ausreicht, um das Phasenverhalten dahingehend zu ändern, dass die Kolloide sich in eine dodekagonale Symmetrie selbst anordnen. In der Literatur sind bereits einige Experimente zu dieser Kolloid-Polymer Mischung dokumentiert. Daher können unsere Simulationsergebnisse dazu beitragen, kolloidale Quasikristalle kontrolliert selbsorganisiert wachsen zu lassen.

Um quasikristalline Strukturen aus Kolloiden in drei Dimensionen zu erhalten, wird die Epitaxie von Teilchen auf Substraten simuliert, deren Ordnung quasikristallinen Parkettierungen entliehen ist. Durch die Gravitation sedimentieren die Teilchen auf das Substrat und folgen der vorgegebenen Ordnung, sodass sich unter weiterer Deposition quasikristalline Schichten herausbilden. Eine speziell abgestimmte Teilchen-Teilchen-Wechselwirkung ist dazu nicht erforderlich. Wir untersuchen verschiedene Substratsymmetrien und gehen der Frage nach, welche Parkettierung am geeignetsten ist. Desweiteren erforschen wir, welchen Einfluss Defekte im Substrat auf den Wachstumsprozess haben. Dabei unterscheiden wir zwischen lokalen Flips in der Parkettierung, wie sie durch thermisch angeregte phasonische Fluktuationen entstehen können, und Dislokationen als globale Defekte, die für die betrachteten Symmetrien durch einen vierdimensionalen Burgers-Vektor gekennzeichnet sind. Die Dislokationen führen im Zuge der Epitaxie zu Defektlinien in der dreidimensionalen Struktur, deren Verlauf in unserem Modell direkt analysiert werden kann. Wir beleuchten die Auswirkungen von elastischen Spannungen sowie die Position des Dislokationskeims im Substrat auf den Verlauf der Defektlinien und erforschen ihr topologisches Verhalten. Dabei stellen wir wesentliche Unterschiede zum Verhalten in periodischen Kristallen fest.

Grundsätzlich sollten sich alle quasikristallinen Strukturen aus Kolloiden, wie wir sie hier in Simulationen erzeugen, auch im Experiment realisieren lassen. Denn sowohl die Kolloid-Polymer Mischung als auch die Epitaxie auf Substraten ist bereits erfolgreich zur

Herstellung periodischer Strukturen umgesetzt worden.

Contents

> There is no such thing as quasicrystals, only quasiscientists.
>
> *(Linus Pauling* 1901-1994*)*

CHAPTER 1

Introduction

The topic of colloidal quasicrystals is introduced in four steps. In the first part, we recount the historical background surrounding the discovery of quasicrystals. In the second, the subsequent development of the diverse research fields from the discovery until today is briefly explained with special focus on those aspects directly connected to this work. In the third subsection, we shortly present as a foundation for the following chapters how aperiodic order looks like from a mathematical point of view. In the final subsection, the general field of colloidal physics is introduced before the colloidal approach on the subject of quasicrystals is explained.

1.1. A historic tale

The persistent need for technological innovations within our economy goes hand in hand with a quest for new advanced materials. In this environment, the material scientist D. Shechtman conducted his research. In the 1980s he was on a sabbatical at John Hopkins University where he worked in a joint project with the National Bureau of Standards on rapidly solidified aluminum transition metal alloys. Although much effort was and is still put into this research today certain fundamental laws were widely accepted and unquestioned.

At least the structure of crystalline materials was limited to the fourteen Bravais lattices displayed in Fig. 1.1 and already formulated in the 19th. century [1]. The Bravais lattices represent cells that repeat periodically in space to form the macroscopic bulk material. The lattice points may be occupied by atoms or clusters of several atoms of different species allowing for rather complex alloys. Many properties of the bulk can be deduced from the cell and the periodicity. In those times a crystal was defined as a periodic arrangement of these cells. Periodically ordered and crystalline were treated as synonyms. As a consequence of periodicity the rotational symmetry is restricted to a few cases. In the following we prove this for two dimensions by contradiction.

Consider a discrete periodic lattice whose points are generated by applying two elemental translations. Each translation consisting of linear combinations of these elemental ones maps the lattice back onto itself. In a physical system, the lattice sites may be occupied

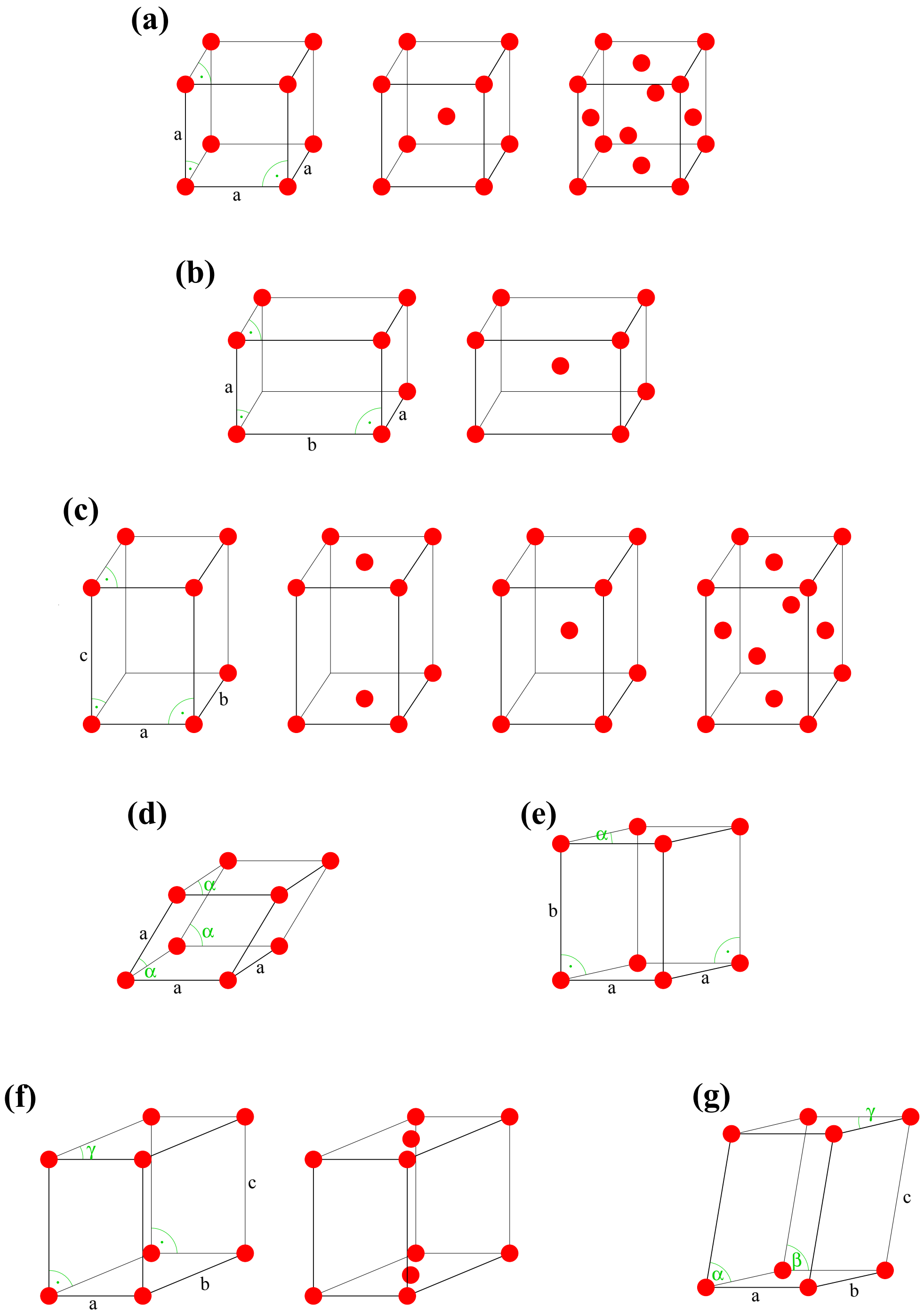

Figure 1.1.: The fourteen Bravais lattices in three-dimensional space described in terms of unit cells. Cubic (a), tetragonal (b), orthorhombic (c), trigonal (d), hexagonal (e), monoclinic (f), and triclinic (g).

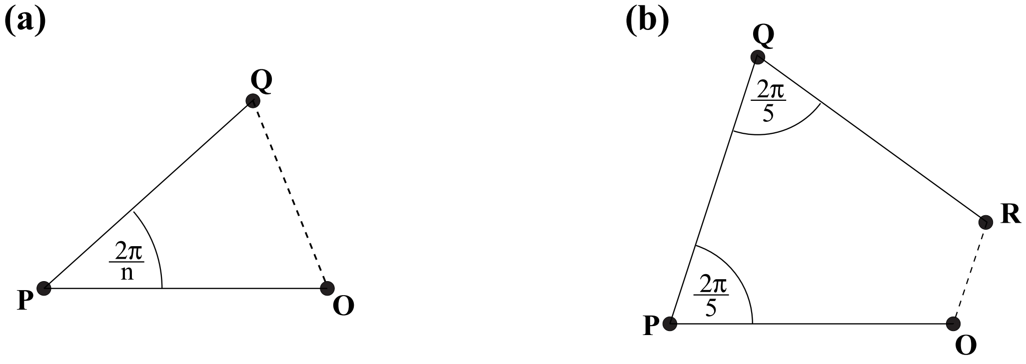

Figure 1.2.: Illustration of the crystallographic restriction theorem in two dimensions. The proof is constructed as contradiction of the initial assumption of a periodic lattice with global symmetry centers $\mathbf{O}$, $\mathbf{P}$, $\mathbf{Q}$, and $\mathbf{R}$. See the text below for a detailed explanation.

by atoms or complex clusters of atoms. As a next step, we investigate which rotations are compatible with the translations and hence with periodicity. Let the site $\mathbf{O}$ be a global symmetry center for n-fold rotation such that a rotation around $\mathbf{O}$ by an angle of $2\pi/n$ leaves the lattice invariant. Due to translational symmetry there exist also other global symmetry centers. Our assumption states that a site $\mathbf{P}$ is the closest global symmetry center to $\mathbf{O}$. Now we rotate $\mathbf{O}$ around $\mathbf{P}$ by an angle $2\pi/n$ to obtain a lattice point $\mathbf{Q}$ (see Fig. 1.2 (a)). By construction, $\mathbf{Q}$ must also be a global symmetry center. However, for rotations with $n \geq 7$ the distance $\overline{\mathbf{QO}}$ is smaller than the distance $\overline{\mathbf{PO}}$ such that $\mathbf{Q}$ is closer to $\mathbf{O}$. This contradicts our initial assumption. For $n = 5$ a point $\mathbf{R}$ violating the initial assumption is obtained after another consecutive rotation around $\mathbf{Q}$ as illustrated in Fig. 1.2 (b). Therefore, translational order in two dimensions is restricted to two-, three-, four-, and sixfold rotational symmetry. This restriction theorem holds in three dimensions as well.

Yet in 1982, when performing a routine analysis on an AlMn alloy by electron diffraction, Shechtman observed a diffraction pattern with sharp peaks violating the above theorem. He noted his own initial disbelief by marking the angle exhibiting the fivefold symmetry with three question marks. Most of his colleagues dismissed his findings immediately as twinning when he revealed his results to them. Twinning is the occurrence of several crystalline domains in a symmetric manner and can give rise to complex diffraction patterns with arbitrary symmetry. Nevertheless, Shechtman had the firm conviction from his experiments to exclude twinning as a possible explanation. As he remained stubborn about the topic, the head of his research group recommended Shechtman to read the textbooks again probably referring to the simple examples from above.

Still he managed to get support from Ilan Blech and John Cahn. Blech, unaware of the mathematics of aperiodic tilings, showed by a computer simulation that a structure defined by angles and distances could reproduce the observed diffraction pattern of Shechtman's experiment. Hence, the idea of a state of matter with long-range order yet without periodicity became the necessary paradigm shift which Shechtman *et al.* communicated in 1984 via two publications [2, 3]. These had a controversial impact and caused the start of a fierce scientific battle within the crystallographic community.

While those in favor of Shechtman's conclusion were assured by the works of other groups reporting soon similar findings, namely structures with octagonal [4] and dodecagonal [5] diffraction patterns, the leader of the opposition was the Nobel Prize laureate Linus Pauling. He explained the tenfold diffraction pattern from Shechtman's data as a result of a complex cubic twin [6]. For years until Pauling's death, the dispute about the existence of quasicrystals was continued in various journals [7–10]. The term quasicrystal itself was coined by publications from Levine and Steinhardt who connected Shechtman's diffraction pattern to the Penrose tiling [11, 12]. In 1992, the International Union of Crystallography changed its definition of a crystal omitting the necessity of periodicity and reducing it to the ability to produce clear-cut diffraction patterns in experiment such that quasicrystals were included [13]. Therefore, the term crystal refers to a state of matter with long-range order. This order can either be periodic or aperiodic. In case of the latter, the term quasicrystal is customary in literature [14]. Finally in 2011, Shechtman was awarded with the Nobel Prize of Chemistry for the discovery of quasicrystals.

Although the applications in technology have been limited up to this date, the resulting paradigm shift in science about ordered matter has influenced research in numerous other fields as will become clear in the following section.

1.2. Quasicrystals today

Although the discovery of an icosahedral AlMn alloy with decagonal diffraction pattern proved that matter could organize into a quasicrystalline state, the initial samples were of pure quality, as they were of limited size and thermodynamically unstable. Upon heating, they changed into a periodic state. Moreover, since they were obtained under non-equilibrium conditions like rapid melt quenching, ion beam mixing or sputtering, the samples contained many defects and thus were unqualified for further investigations of the properties of the quasicrystalline state. However, sample quality increased significantly, when the first stable quasicrystals were reported in the AlCuLi and GaMgZn system [15, 16]. Soon further compositions were known to yield stable quasicrystals [17–19]. One of the best ordered quasicrystalline materials available today is $Al_{72}Ni_{20}Co_8$ with decagonal symmetry. In a diffraction experiment, such a sample exhibits diffraction peaks whose sharpness compares to those of silicon and almost reaches the instrumentation limit [20].

The improved sample quality allowed systematic studies of the various material properties of quasicrystals which proved to be unique. For instance, the electronic properties have been investigated intensively (see [21] for a review) revealing the unconventional conductance properties [22–24]. Although the compounds of a quasicrystal may be good metals, the electronic conductivity may still be below the minimum metallic value [25]. Moreover, their resistivity in the low temperature regime may exceed the values for disordered metals and metallic glasses by four magnitudes leading to an insulator-like behavior [26, 27]. Quasicrystals exhibit a special pseudo-gap within their electronic band structure [28–31]. Tiling models have been applied to link experimental observations to the aperiodic structure [32–36].

Magnetism of quasicrystals covers a wide range of properties. The observed behaviors range from diamagnetism [37], Curie- and Pauli-like paramagnetism [38, 39] to ferromagnetism [40]. While paramagnetic quasicrystals exhibit large effective magnetic moments, the magnetization of ferromagnetic quasicrystals seems to be weak due to the aperiodic environment [41]. In addition, long-range antiferromagnetism has been observed as well [42]. Again, aperiodic tiling based calculations and symmetry considerations confirm the experimental results [43–45].

In addition, the research regarding the mechanical properties of quasicrystals also revealed interesting behaviors like pressure induced phase transitions [46], an increased fracture strength through doping [47] or a special crack propagation mechanism, as the material opens up along a phason wall [48]. In general, quasicrystals are often very brittle at low temperatures, while they become deformable at higher temperatures [49, 50]. As in a periodic crystal, the macroscopic plastic behavior of quasicrystals is governed by defects like disclinations and dislocations. The topological charge, the Burgers vector of a dislocation, can be determined by experimental techniques like convergent beam electron diffraction or a mode analysis from real space images obtained for instance by transmission electron or scanning tunneling microscopy [51–55]. While the dislocation in a crystal is exactly described by a Burgers vector with d components, where d denotes the number of dimensions, the Burgers vector in a quasicrystal has additional phasonic components. Aside from phonons which culminate in lateral displacements of the lattice sites, there are additional modes called phasons in a quasicrystal. These new modes manifest themselves in complex correlated rearrangements of the lattice tiles and are fundamental for the elastic properties and the melting behavior as well as the description of defects after all. Some scientists conjecture that they might even be of significance regarding the stability of quasicrystals as was shown in a special model system [56]. Therefore, phasons will be introduced in more detail in the separate section 2.2.

The increase in sample quality has enabled the preparation of clean quasicrystalline surfaces and thus established an active field in surface science. Though, in order to determine the structure, the conventional observation techniques have to be adopted to aperiodicity like for example periodic approximants for dynamical low energy electron diffraction [57–59]. Several unique phenomena in relation to quasicrystalline surfaces have been reported (see [60] for a review). Quasicrystals offer the potential as low friction coatings by decreasing the sliding wear significantly [61, 62]. Due to the observation of a large frictional anisotropy between the sliding along periodic and aperiodic directions, quasicrystalline order is associated with lower friction than conventional periodic order [63–65]. This has been further confirmed on a nanotribology level by the sliding of a colloidal suspension above a quasicrystalline surface constructed by interfering laser beams [66–68].

Together with their high hardness and oxidation resistance the tribological properties of quasicrystals in various environments have been harnessed in coatings for machine parts, cutting blades, and non-stick frying pans [69]. Since in this scope of applications lubricants like hydrocarbons or other gases are widely used, research effort is devoted to investigate the behavior of different gases on quasicrystalline substrates. In this respect, ethylene can form a protective passivating layer on decagonal Al–Ni–Co quasicrystal surfaces [70]. On the other hand, benzene and pentacene on i–Al–Pd–Mn do not form an ordered molecular overlayer [71, 72]. In general, rare gas like Xe or Ar serve as a model to predict parameters for more complex hydrocarbon substances [73–78].
The properties of quasicrystalline surfaces have been further explored by the deposition of various metals like for instance gold [79], silver [80], iron [81], copper [82–84], tin [85] or semimetals like silicon [86] leading to solid films (see also [87, 88] for overviews). Often only some aspects of the complex quasicrystalline substrates are transmitted to the films during the growth process such that the obtained new metal thin films exhibit unusual and unprecedented structures. Therefore, quasicrystal surfaces represent potential templates to design new materials [89]. An interesting feature of epitaxy on quasicrystalline surfaces is polymorphic growth in various systems [82, 90]. Copper forms an uniaxially aperiodic ordered film on the fivefold surface of Al–Pd–Mn [84]. A surprising discovery has been the stabilization of islands with particular heights by quantum well states as dominant energetic contribution [91, 92]. In addition, it has been demonstrated that quasicrystals may serve as interfacial interlayers epitaxial linking two incommensurate materials [93]. As the quasicrystalline substrates consist of several elements the emergence of quasicrystalline films by single element deposition is unlikely. Yet, the growth of artificial single element quasicrystalline monolayers has been reported [94, 95]. Supplementing the experimental results, there are also grand-canonical and molecular dynamic simulations for various adatoms reporting a decrease in quasicrystalline order after a few layers [96–101].

Aside from these artificial quasicrystalline samples produced in a laboratory, evidence for a naturally formed quasicrystal has been provided in a mineral sample of an Al–Cu–Fe alloy from the collection of the Museo di Storia Naturale of the Università degli Studi di Firenze [102]. *Icosahedrite* were approved by the International Mineralogical Association as a new mineral [103]. They are extraterrestrial in origin, possibly delivered to the Earth by an asteroid that dates back 4.5 billion years [104].

Although originally a subject of solid state physics or crystallography, for the last decade, perhaps pushed by exciting experimental discoveries, there has been an increasing interest in soft matter quasicrystals (see [105, 106] for reviews). In contrast to atomic systems, the dominating symmetry reported seems to be dodecagonal. Since the formation of quasicrystalline ordering has been reported for a supermolecular dendritic liquid [107], a network of ABC-star polymers [108], and an aqueous solution of micelles [109, 110], its universal nature has been extended to the mesoscale. Prior to these experimental reports, theoretical calculations by density functional theory predicted a stable quasicrystalline phase for a colloid-polymer mixture [111]. There, short-range attraction compensates the loss in packing efficiency. Moreover, energy calculations for various purely repulsive pair-potentials indicated conditions for quasicrystalline ordering as well [112–114]. As one necessary condition for the self-assembly of such interacting particles into a quasicrystalline state has been assumed the presence of two incommensurate length scales in the system [115, 116]. For pairwise interacting particles, this condition has been elaborated theoretically by precise fine tuning of the length scale ratio of the interaction potential which may even be purely repulsive [117, 118]. Further evidence has been provided recently in a systematic simulation study in two dimensions of hard spheres with soft shoulder potential revealing numerous quasicrystalline states depending on the shoulder width [119]. Even a state with 24-fold rotational symmetry is observed. Yet, up to now an experimental setup in which the particle-particle interaction can be controlled to the required degree to assemble soft quasicrystals by design has not been reported. Regarding experimental feasibility, one possible drawback may be that the interaction potentials often discussed are too artificial. In chapter 7, we will discuss suitable parameters for the self-assembly of colloidal quasicrystals via the depletion potential in a colloid-polymer mixture which can be controlled in experiments [120–122]. As an alternative approach to the tuning of the interaction potential for quasicrystalline self-assembly, a formation governed by surface entities or shape polydispersity has been demonstrated extensively in simulations [123, 124]. Besides, it was shown by free energy calculations that a system of patchy-particles exhibits an entropically stabilized quasicrystalline phase [125]. Molecular dynamic simulations revealed for particles interacting via a double-well potential decagonal and dodecagonal quasicrystalline states [126]. In addition quasicrystalline order has been stabilized in a binary dipolar system [127], in self-assembled cluster crystals [128] and in a dynamical phase field crystal model [129].

Instead of achieving intrinsic self-assembly by particle-particle relations, quasicrystalline ordering can be enforced by an external potential. Especially, a suspension of charged-stabilized colloidal particles subjected to a quasicrystalline laser field can form a two-dimensional quasicrystalline ordered monolayer in all kinds of symmetries [130, 131]. Depending on the density of the suspension as well as the laser intensity a rich phase behaviour is observed [132–136]. In this respect, the emergence of an Archimedean tiling phase as a compromise between the competing aperiodic order of the substrate and the preferred periodic arrangement of the colloids is most notable [132]. Furthermore, the minimal laser intensity necessary to enforce the quasicrystalline order against the periodic preference of the colloids depends on the desired rotational symmetry [137]. Moreover, since the phases of the individual laser beams can be tuned as well, this colloidal setup provides a useful model to investigate phasonic excitations and their influence on the colloids regarding structure [138] as well as dynamics [139]. We extend this research in chapter 4, when we explore colloidal trajectories caused by a phasonic drift for the octagonal, dodecagonal and tetradecagonal field. In addition, we analyze the potential for colloids with finite diameter. Upon driving the suspended monolayer over the aperiodic substrates, directional locking was observed [140]. Furthermore, in agreement with the Frenkel-Kontorava model, which describes a sliding monolayer of interacting particles on a periodic substrate, the presence of Kinks and Anti-Kinks could be detected for periodic as well as aperiodic substrates [66, 68]. This offered further insight into the tribological properties of quasicrystalline surfaces on the micro level. In addition, different particle geometries of the suspension like needles or rods were considered and the resulting phase behavior was explored [141, 142].

In this work, we also make the step from the two-dimensional quasicrystalline monolayer of colloidal particles, to a three-dimensional quasicrystal. In chapter 5, we introduce a new model based on colloidal epitaxy to grow colloidal structures on well-defined quasiperiodic substrates. As we will show, in contrast to self-assembled intrinsic quasicrystals, no fine-tuning is required to obtain structures with quasicrystalline order, instead a simple short-range repulsive interaction is sufficient.
On periodic substrates the method of colloidal epitaxy is well established for colloids with various interaction ranges and under gravity [143–147]. Therefore, we are confident that our results can in principle be realized in experiments.
In chapter 6, we will demonstrate the control over defects in the grown colloidal structure as another major advantage of this template-guided approach. Dislocations with well-defined Burgers vectors can be incorporated in the quasicrystalline substrates and through the epitaxial process these seeds evolve into defect lines. As a result, we obtain three-dimensional quasicrystalline structures with specially designed defects. These might be of additional relevance for possible photonic applications [148]: The concept of aperiodic structures has stimulated research in photonics in his own way (see for [149] a review). A major goal is to construct components analogue to conventional electronic semiconductor devices but based on channeling photons instead of electrons. In this context, the potential of quasicrystals has been identified for applications [148]. As a desired property, quasicrystals, independent from their respective symmetry, seem to possess a special photonic band structure which can exhibit a complete band gap [150–155]. In addition, due to their wider variety of symmetry centers compared to crystals, quasicrystals may allow the creation of defect modes with different geometries [156]. As further possible applications, a color fan for frequency conversion [157] and slabs with multiple cavity modes [158] have been demonstrated.

Apart from the research fields presented above, the formation of quasicrystals has been reported in various other systems. The most recent examples for the emergence of quasicrystals are the surprising formation of hydrogen bonded ferrocenecarboxylic acids [159], an interface-driven formation of ultrathin quasicrystals from perovskite oxide [160], and the self-assembly of nanoparticles into binary aperiodic superlattices [161, 162]. A model to realize a two-dimensional quasiperiodic cold-atom quasicrystal has already been proposed [163]. Besides, it was shown that a spin-orbit coupled Bose gas can exhibit several quasicrystalline ground states [164]. Eventually, this amount of manifold examples does emphasize the universal nature of quasiperiodic order. While icosahedral order is aperiodic in all three dimensions of space, octagonal, decagonal, and dodecagonal quasicrystals consists of periodic stacks of two-dimensional quasicrystalline planes. The latter group is of special interest for this work. In the next section, it is presented how a plane can be tiled with aperiodic order and how this order might finally look like.

1.3. Aperiodic tilings

For a long time in mathematics, an aperiodic tiling of the plane was deemed to be impossible until 1966, when Berger presented a tiling that consisted of 20426 elementary tiles [165]. His explicit example lacks translational order yet nevertheless it exhibits long-range order. In the following years his proof was further elaborated until an aperiodic tiling consisting of merely six elementary tiles was achieved [166].

Astonishingly, it seems that medieval Islamic architects were capable of decorating their sacral buildings with nonperiodic, quasicrystalline mosaics. Patterns, found in the Darb-i Imam shrine in Isfahan, Iran, and dated back to 1453 A.D. are regarded as the first aperiodic tiling [167]. However, the claim about the principal status and the aperiodicity itself is contested by implying that patterns found in the Gunbad-i Kabud tomb tower in Maragha, Iran, and already dating back to 1197 A.D. represent the actual methodical breakthrough in achieving aperiodic tilings [168, 169]. In any case, it seems that the knowledge about aperiodic geometry had to be rediscovered.

Today, an abundance of aperiodic tilings with long-range order is known [170, 171]. The most famous one is probably the Penrose tiling [172]. It has fivefold rotational but no translational symmetry. With the discovery of quasicrystals it gained further prominence when Levine and Steinhardt compared the diffraction pattern calculated from the Penrose tiling to Shechtman's experimental observation [11]. Despite the development of direct imaging techniques like electron microscopy, this approach remains quite powerful, as for many tilings the analytical diffraction pattern can be calculated [173]. In this section, we will give a brief introduction to aperiodic tilings with a special emphasis on the Penrose-Rhomb, the Ammann-Beenker, and the Square-Triangle tiling, since these are the tilings we will encounter regularly in the scope of this work.

1.3.1. Local matching and inflation rules

While the original Penrose tiling still consisted of six elementary tiles, a whole family was subsequently established until solely two geometric shapes, a fat and a skinny rhomb, were sufficient to tile the plane in an aperiodic manner [174–176]. In order to achieve aperiodic order, these tiles cannot be arranged arbitrarily. Instead, so-called matching rules have to be obeyed between adjacent tiles. In case of the Penrose-Rhomb tiling, one possible implementation is illustrated in Fig. 1.3. Adjacent edges are well arranged when the blue and red lines are smoothly sustained across neighboring tiles to form closed loops. As a fascinating aspect, the edges of the two rhombs can be arbitrarily distorted against each other. As long as they fit smoothly together and the matching rules are implemented, the resulting pattern will remain aperiodic, even for chickens [175].

An alternative method to construct aperiodic tilings is the so-called inflation approach, which utilizes the self-similarity of a tiling. In each step the current pattern is scaled by an irrational number. For the Penrose tiling, the scaling factor is precisely the golden mean,

$\tau = (1+\sqrt{5})/2$, a magic number with great relevance for beauty and aesthetics [177]. The scaled tiles are replaced by sets of elementary tiles depending on the original type. These inflation steps can be conducted iteratively and in agreement with the matching rules to produce a perfect quasicrystalline tiling (see Fig. 1.3).

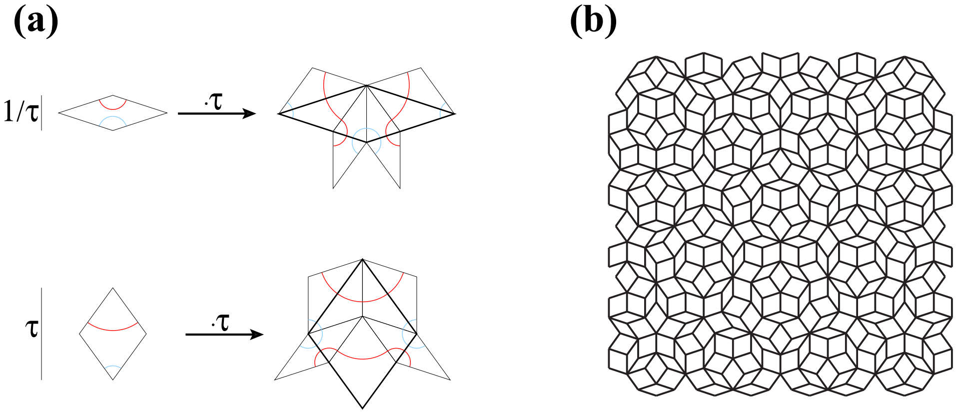

Figure 1.3.: Pentagonal Penrose-Rhomb tiling by matching and inflation rules. (a) The basic tiles, a fat and a skinny rhomb, are scaled by the golden mean $\tau = (1+\sqrt{5})/2$. Afterwards, the scaled objects (thick line) are composed from a conglomeration of the original tiles. According to the matching rules the tiles have to be arranged such that the blue and red lines are sustained smoothly throughout the tiling. (b) A patch of the tiling after several inflation steps.

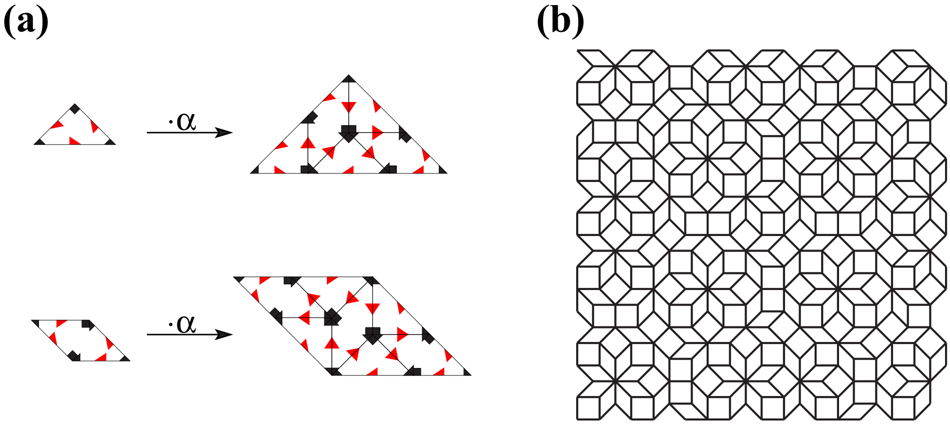

Figure 1.4.: Octagonal Ammann-Beenker tiling by matching and inflation rules. (a) The basic tiles, a right triangle and a rhomb, are scaled by the silver mean $\alpha = 1+\sqrt{2}$. Subsequently, the scaled objects are segmented into a conglomeration of the original tiles. In order to obey the matching rules, adjacent edges form red arrows, while adjacent vertices form black ones. Hence, the right triangles form pairwise a square. (b) A patch of the tiling after several inflation steps.

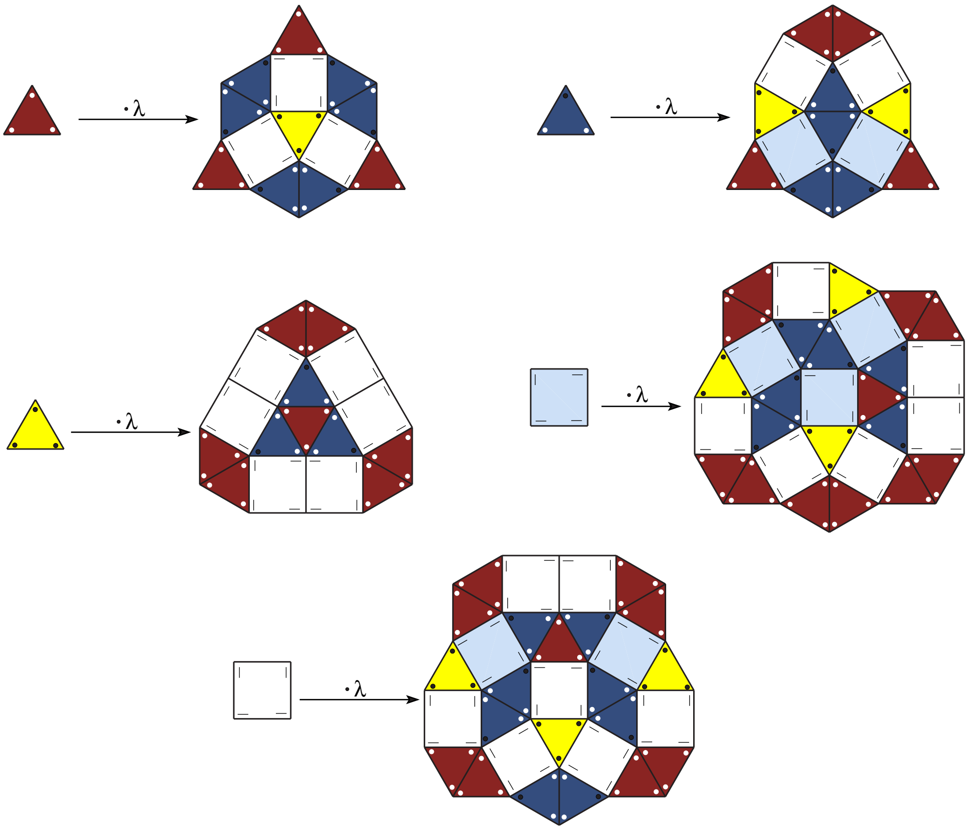

Figure 1.5.: Dodecagonal Square-Triangle tiling by matching and inflation rules. (a) The basic tiles, three regular triangles and two squares, are scaled by the factor $\lambda = 2+\sqrt{3}$. Subsequently, the scaled objects are segmented into a conglomeration of the original tiles. A patch of the tiling is displayed in Fig. 1.10.

Another tiling with matching and inflation rules of similar simplicity to the Penrose ones is the octagonal Ammann-Beenker tiling [178]. It is composed of squares, or rather right triangles, and rhombs as elementary tiles. The scaling factor is given by $\alpha = 1 + \sqrt{2}$, sometimes referred to as the silver mean. The inflation step and matching rules are illustrated in Fig. 1.4. The Ammann-Beenker tiling has been linked to octagonal quasicrystals [4, 179] and will feature in the context of this work about suitable substrate symmetries for colloidal epitaxy.

A tiling whose inflation rules are more complicated than the previous examples is the dodecagonal Square-Triangle tiling. Its inflation rules are displayed in Fig. 1.5. As the name suggests, it is composed of two squares and three regular triangles. The scaling factor amounts to $\lambda = 2 + \sqrt{3}$ which is rather big. This can lead to problems when finding suitable box sizes for computational methods. We address this issue in section 3.2.2. So far, dodecagonal symmetry seems to be the most reported symmetry for mesoscopic quasicrystals [108, 119]. Therefore, it will also feature in the section about intrinsic quasicrystal formation in the colloid-polymer mixture. The tiling has been studied extensively as a model for entropically stabilized growth of quasicrystals [180–182]. In general, such inflation rules can be formulated for tilings of n-fold rotational symmetry, though these become more complicated with higher order [183].

1.3.2. Dual grid method

In a different construction method bands of parallel lines are drawn in each symmetry direction to form a grid. For pentagonal symmetry this yields a pentagrid, for octagonal a tetragrid. The grid is called regular if no more than two lines intersect in one point, otherwise it is called singular. The different types of intersection points are then transformed to the respective types of elementary tiles to produce the dual lattice. In order to construct for instance the Ammann-Beenker tiling we require a regular tetragrid [184]. Details of the construction are given in Fig. 1.6.

In similar fashion, the Penrose tiling is obtained from a regular pentagrid [185, 186]. In addition, this method also allows to incorporate strain or defects in the tiling, as a distortion in the grid is transferred to the resulting lattice [187].

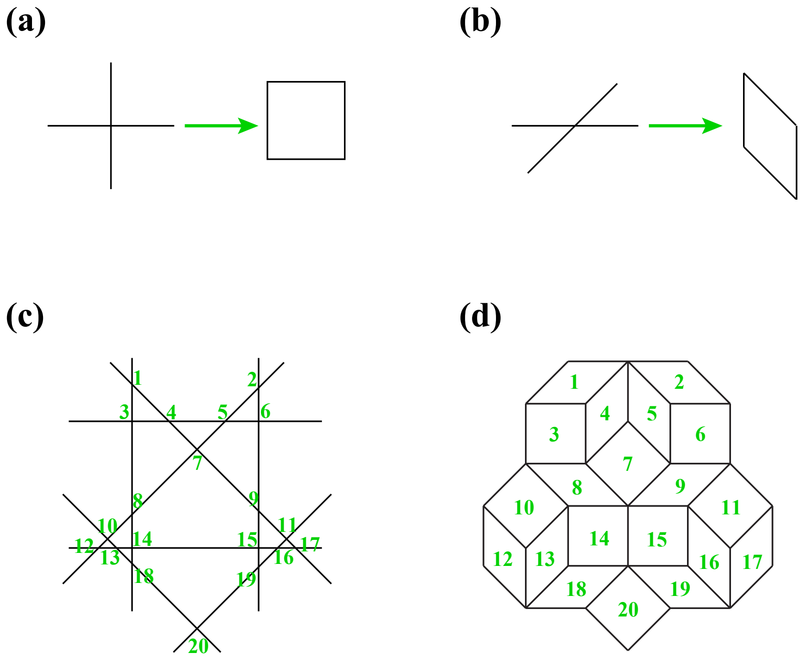

Figure 1.6.: Construction of the octagonal Ammann-Beenker tiling by the dual grid method. (a-b) Replacement rules for the vertices of the tetragrid into the elementary tiles, a square and a rhomb. (c) An excerpt of the regular tetragrid with numbered vertices. (d) The resulting patch of the octagonal tiling composed of squares and rhombs when the rules from (a) and (b) are applied to the vertices of (c).

1.3.3. Projection method

Another method to construct aperiodic tilings is the projection from a periodic lattice of higher dimension. It is a powerful concept in crystallography, as many properties, like for instance phasons, can be explored in the higher-dimensional nature of quasicrystals. We start our demonstration on the basis of the silver mean chain (Fig. 1.7 (a)) .

Consider a two-dimensional rectangular lattice with lattice points $(x^{||}, x^{\perp})$, where $x^{||}$ comprises the physical dimension and $x^{\perp}$ the mathematical one respectively. The lattice points are generated by integer combinations of the basis vectors $\boldsymbol{a}_1 = (1, 1)$ and $\boldsymbol{a}_2 = (-\sqrt{2}, \sqrt{2})$. Along the axis of abscissa, two parallel lines at $x^{\perp} = -1/\sqrt{2}$ and $x^{\perp} = 1/\sqrt{2}$ define a strip, the so-called acceptance window. All points of the lattice which are inside the window are projected on the abscissa. As the original two-dimensional lattice is tilted by an irrational angle against the abscissa, the projected points form an one-dimensional lattice without translational, yet nevertheless with long-range order. Thus, this chain of small S and large segments L whose ratio is the number of the silver mean α is aperiodic. It also follows the iterative replacement rules: $L \rightarrow LSL$ and $S \rightarrow L$ and successive iterations yield:

$$
\begin{aligned}
&L\\
&LSL\\
&LSLLLSL\\
&LSLLLSLLSLLSLLLSL\\
&LSLLLSLLSLLSLLLSLLSLLLSLLSLLLSLLSLLSLLLSL\\
&\dots
\end{aligned}
$$

Note that a slightly different tilting angle between the lattice and the abscissa would result in a chain consisting of repeating units. Now, we want to investigate what happens if we displace the original lattice. For a displacement along the physical direction, e.g. along the $x^{||}$-direction, the projected chain is also lateral displaced as illustrated in Fig. 1.7 (b). In a physical system this would correspond to a phononic excitation in the long wave length limit. In Fig. 1.7 (c) a displacement in the direction of $x^{\perp}$ is applied to the whole lattice. The principle nature of the projected sequence remains unchanged, although some segments L and S have switched position within the chain. In a physical system such flips correspond to a so-called phasonic excitation in the long wave length limit. Such an additional degree of freedom in quasicrystals is a consequence of their higher-dimensional nature. Obviously, there exist combinations of displacements in $x^{||}$ and $x^{\perp}$ direction which leave the chain completely unaffected. These are the basis vectors $\boldsymbol{a}_1$ and $\boldsymbol{a}_2$. They will become important in the context of Burgers vectors of dislocations in quasicrystals. In Fig. 1.7 (d) flips have been inserted in the chain by a spatial distortion of the acceptance window as an illustration for phasonic strain.

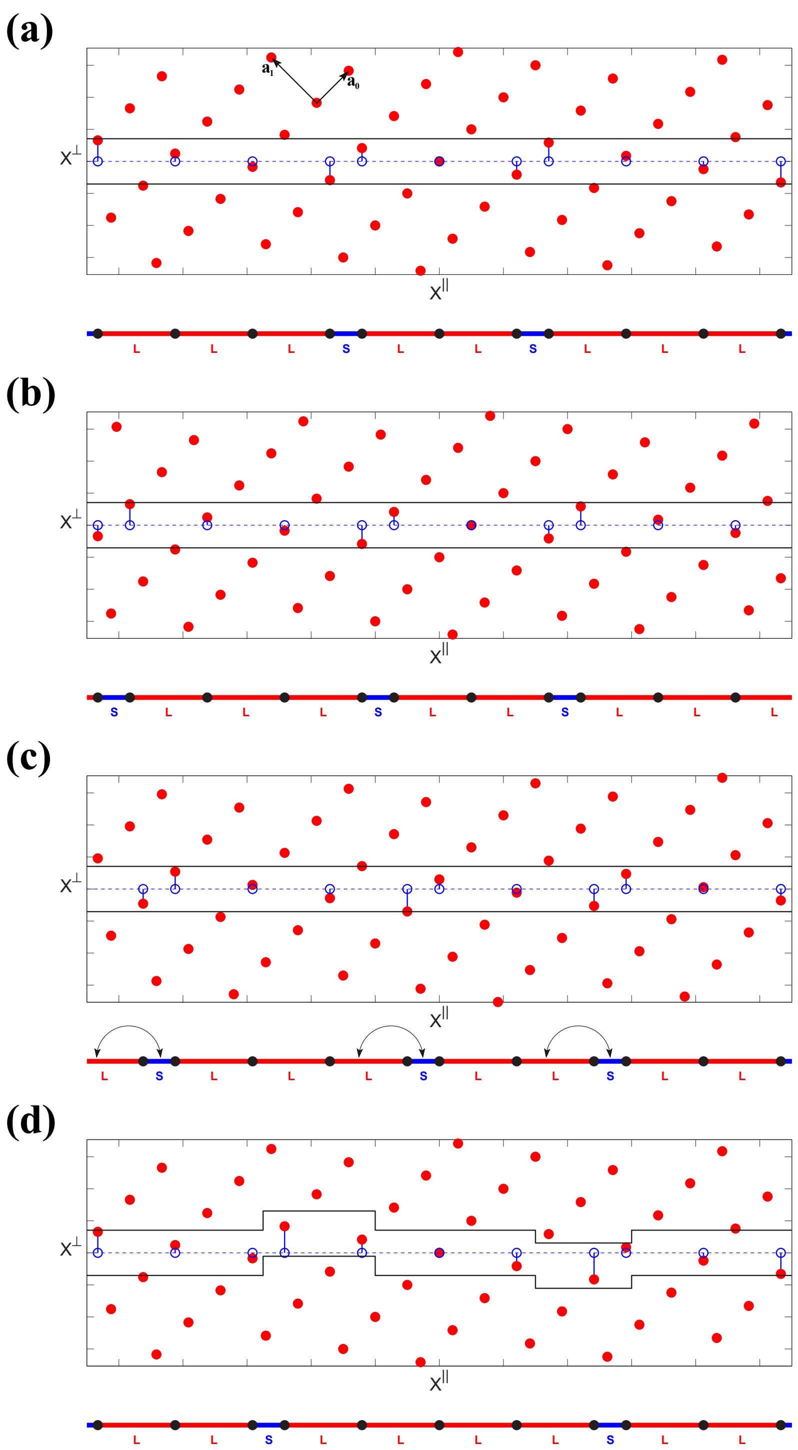

Figure 1.7.: Construction of the one-dimensional silver mean chain by projection from a two-dimensional rectangular lattice (a) without displacements, (b) with a displacement along $x^{||}$, (c) with a displacement along $x^{\perp}$, and (d) with a distorted window. Detailed explanation is given in the text.

The projection approach to gain the silver mean chain can be generalized to higher dimensions. We now consider four-dimensional basis vectors $\boldsymbol{a}_i$ with two components for both the parallel physical space, $\boldsymbol{a}_i^{||}$, and for orthogonal space, $\boldsymbol{a}_i^{\perp}$. In each space, they are arranged to cover the incommensurate directions on an eightfold star as illustrated in Fig. 1.8. While linear combinations of the basis vectors generate the whole lattice of points $(\boldsymbol{x}^{||}, \boldsymbol{x}^{\perp})$, only those points whose components $\boldsymbol{x}^{\perp}$ are located within an octagon with unit edge length are relevant for projection. In Fig. 1.9 (a) it is displayed how these projected points form a patch of the octagonal Ammann-Beenker tiling. If this patch was infinitely large, the unit octagon in orthogonal space would be populated with uniform density. In fact, the projection process is also beneficial in the reverse direction. Granted that we observe a tiling like structure in our physical system, we can obtain the $\boldsymbol{x}^{\perp}$ counterparts to the physical coordinates by employing the basis vectors $\boldsymbol{a}_i$ when traversing the different vertices of the tiling. In Fig. 1.9 (b) this has been exploited to identify the flips in the tiling, since the flipped vertices have coordinates in orthogonal space that reside outside the unit octagon.

Other symmetries can also be generated by this approach like for example the Penrose tiling [185, 186]. With adjusted basis vectors the dodecagonal Square-Triangle tiling can be constructed as depicted in Fig. 1.10. However different from the previous octagonal case, the acceptance window possesses a fractal boundary [188, 189].

Finally, a further generalization to gain long-range aperiodic arrangements in three dimensions is possible. For instance, the Penrose tiling has been elevated from a planar tiling to fill space aperiodically in three directions to describe icosahedral quasicrystals [190–193].

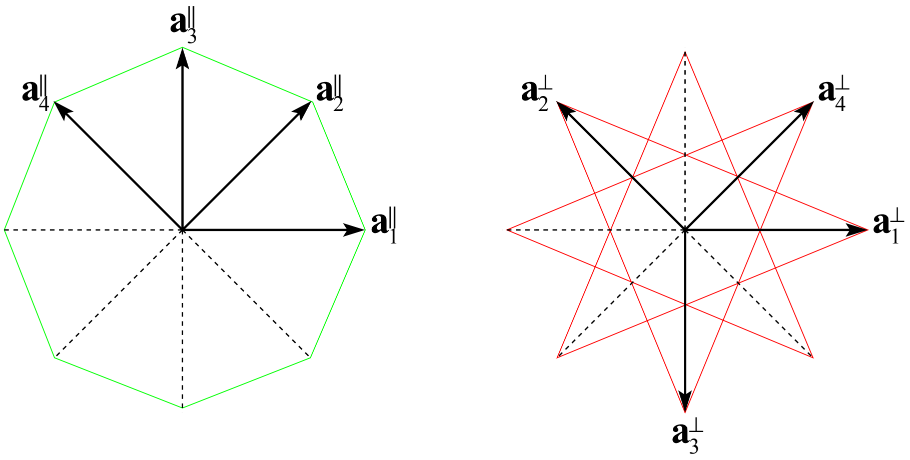

Figure 1.8.: The basis vectors $(\boldsymbol{a}_i^{||}, \boldsymbol{a}_i^{\perp})$ of the four-dimensional lattice $(\boldsymbol{x}^{||}, \boldsymbol{x}^{\perp})$.

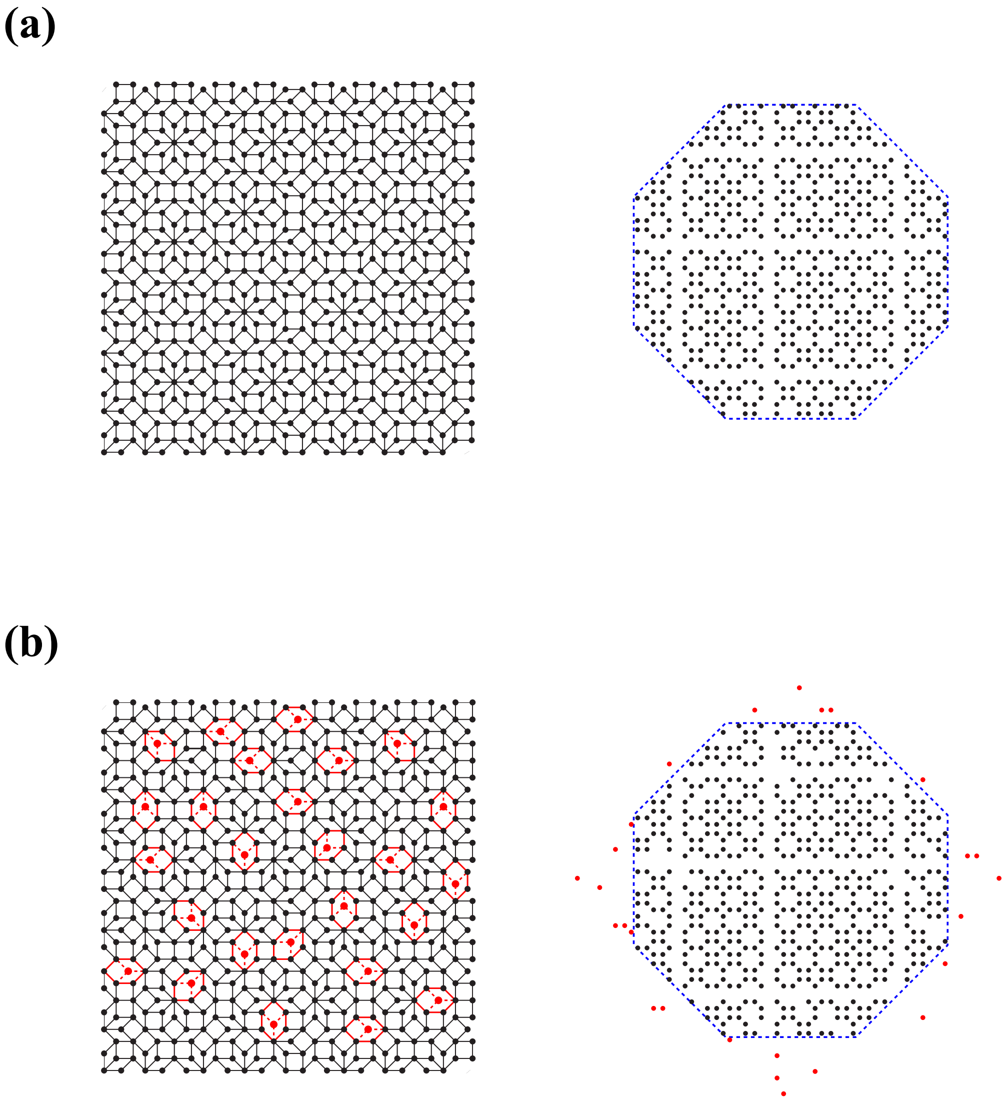

Figure 1.9.: Construction of the octagonal Ammann-Beenker tiling by projection. (a) The four-dimensional lattice $(\boldsymbol{x}^{||}, \boldsymbol{x}^{\perp})$ is given by integer linear combinations of the basis vectors $(\boldsymbol{a}_i^{||}, \boldsymbol{a}_i^{\perp})$. From those pairs the $\boldsymbol{x}^{||}$ whose $\boldsymbol{x}^{\perp}$ reside inside an octagon with unit edge length (dashed blue line) yield the coordinates of the tiling. (b) Tile flips, marked in red, are inserted by hand in the tiling . As we translate from the real space coordinates to orthogonal space by the basis vectors, the flipped vertices now correspond to the red points which are located outside of the octagon.

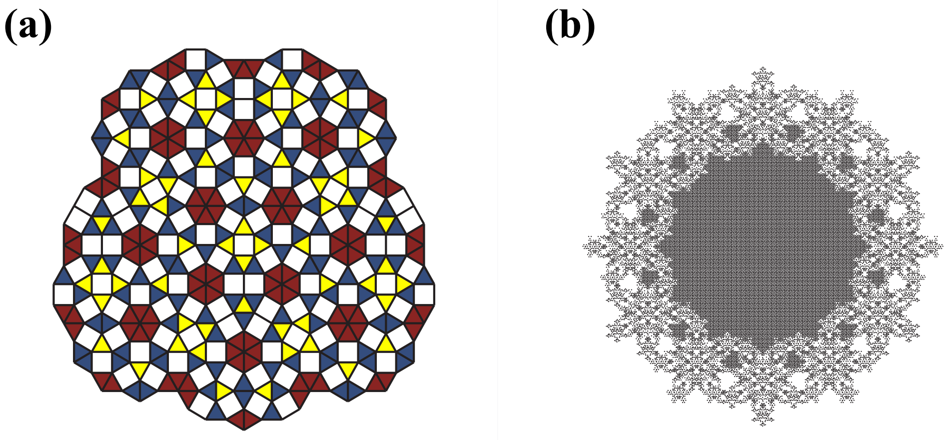

Figure 1.10.: The dodecagonal Square-Triangle tiling. (a) A patch of the physical coordinates $\mathbf{x}^{||}$ comprising the tiling. (b) In orthogonal space the points $\mathbf{x}^{\perp}$ selected for projection form an object with fractal boundaries. The image was calculated from a finite tiling patch consisting of $N = 40561$ vertices.

1.4. Colloidal physics

Literally, the word colloid is a composition of the Greek words for glue and appearance. Colloids are micron-sized particles of 0.01 to $10\,\mu\mathrm{m}$ diameter dispersed in a continuous solution. A homogeneous colloidal suspension has to be stabilized. Otherwise the attractive Van der Waals interaction between close particles leads to the aggregation of clusters as close particles stick to each other. Therefore, the colloids have to be kept at a large distance such that Van der Waals forces are effectively disabled. This can be achieved by adding electrical charges of identical sign to the particles such that they repel each other via Coulomb forces. Screening effects originating from counter ions in the solvent that accumulate around a colloidal particle can contribute to a decrease in the range of the interactions. The complete pair potential was derived by Derjaguin, Landau, Verwey and Overbeck [194, 195] and is given by

$$V_{\mathrm{DLVO}}(r) = \frac{(Z^{*}e)^{2}}{\pi\epsilon_{0}\epsilon_{r}\left(2+\kappa\sigma\right)^{2}} \frac{\exp[-\kappa(r-\sigma)]}{r}\,, \tag{1.1}$$

where r denotes the distance between two colloids, σ the diameter and Z^{*} its effective charge. ϵ_r is the dielectric constant of the solvent and κ the inverse Debye screening length. In our case, an additional excluded volume contribution is assumed such that the colloids are not allowed to overlap as hard spheres. Depending on the parameter values in Eq. (1.1) either contribution may dominate the interaction. While the interaction of the colloidal particles in chapters 5 and 6 is dominated by the hard-core like behavior, both contributions are decisive in chapter 7.

Colloidal suspensions serve as a model system in statistical physics to study fundamental principles [196]. They are frequently applied to investigate crystallization processes [197–200], the properties of binary mixtures [201, 202], and glassy dynamics [203, 204]. In addition, lane formation [205–208] or other collective behaviors as for instance in shear flows [209–211] are studied as well. Furthermore, in the past years, a great attention has also been devoted to the physics of so-called active systems (for a review see [212]). These systems involve various kinds of colloidal particles that possess an internal propulsion mechanism which drives the system out of equilibrium [213–222]. In this work, we allude the topic of colloidal physics in three different ways to investigate the formation and properties of mesoscopic quasicrystals.

Of particular relevance for the first part of this work is the fact that colloidal suspensions can be manipulated by light fields due to the optical tweezer effect [223, 224]. Since in a light field the force acting on the colloid is directed towards the highest light intensity, colloidal particles can be forced to form complex structures [225]. The manipulation can be exerted in detail such that even quantities like for example the osmotic pressure can be measured [226]. As external potentials periodic light fields [227–229] but also aperiodic ones have been deployed [131–133]. Concerning the latter, we consider the experimental setup of Mikhael *et al.* who exposed a two-dimensional charged-stabilized colloidal suspension to a quasicrystalline intensity field by interfering symmetrically arranged laser beams [132, 134, 135]. In chapter 4, we study new aspects in this system. A finite colloidal diameter is assumed which influences the general ordering. Besides, Kromer *et al.* developed a method to predict colloidal trajectories when a phasonic drift is applied by tuning the laser phases [138]. We generalize this approach to other rotational symmetries of the interference pattern and prove its universality for quasicrystals with higher rank.

Yet, as a new system, we apply the method of colloidal epitaxy to grow three-dimensional colloidal quasicrystals from aperiodic tilings in chapter 5. The experimental feasibility has been extensively demonstrated for colloidal suspension with various interaction lengths that sediment under gravity on periodic substrates [143–147]. Moreover, in the subsequent chapter 6, we incorporate dislocation lines into these grown quasicrystalline structures. Again, comparable studies have only been conducted for periodic colloidal crystals so far [230, 231]. We present some specific quasicrystalline properties.

In chapter 7, we consider a mixture of hard, charged colloids and smaller polymer coils. In addition to the repulsive Coulomb interaction between the colloidal particles the polymers provide a short-range attraction to the pair potential that can promote the formation of a quasicrystal. Therefore, this mixture is related to other colloidal systems in which a two length scale pair potential is tuned to stabilize a self-assembled quasicrystal [111, 117, 119].

Aside from these research chapters, we refer to chapter 2 for a theoretical background. There, phasons are introduced in more detail as additional hydrodynamic modes. Besides, we review the concept of *local isomorphism* classes for quasicrystals and elucidate the description of topological defects like dislocations in quasicrystals. Technical aspects regarding our research like the simulation procedure or the construction of approximants are explained in chapter 3.

> If it can be used again, it is not wisdom but theory.
>
> *(James Richardson* 1950*)*

CHAPTER 2

Theoretical Background

In the preceding chapter the colorful research field of quasicrystal physics has been introduced. In addition, a mathematical description of aperiodic tilings was presented. Here, we review refined theoretical concepts of quasicrystal physics in order to establish a foundation for the subsequent chapters. In the first part, the geometric concept of local isomorphism to characterize two-dimensional quasicrystals is introduced [232, 233]. Within this framework phasons arise as a symmetry operation and are introduced as additional hydrodynamic modes in the second part in section 2.2. Subsequently, we recount the injection of topological defects, i.e. dislocations in quasicrystals [234].

2.1. Local isomorphism class

Periodic crystals consist of a unit cell and are invariant under translations [235, 236], i.e. by a translational operation two crystals with identical unit cells can be mapped onto each other. In contrast, aperiodic crystals, represented for instance by the mathematical tilings from section 1.3, are not invariant under translations. Yet, on the basis of a finite region two tilings may still be indistinguishable, since any finite region in one tiling may exist somewhere in the other [237]. This is illustrated in Fig. 2.1 for two superimposed identical octagonal Ammann-Beenker tilings, where the red colored tiling is displaced by an increasing offset relative to the other. Note that the further the red tiling is translated the more the area of coincidence increases. Therefore, the two tiling patches are called to be locally isomorphic. This concept to characterize quasicrystals has been elaborated by Socolar *et al.* in [232, 233] and states:

> Two tilings are locally isomorphic if and only if given any point $\mathbf{P}$ in either tiling and any finite distance l, there exists a pure translation of the other tiling that causes the two to coincide everywhere in a circle of diameter l about $\mathbf{P}$.

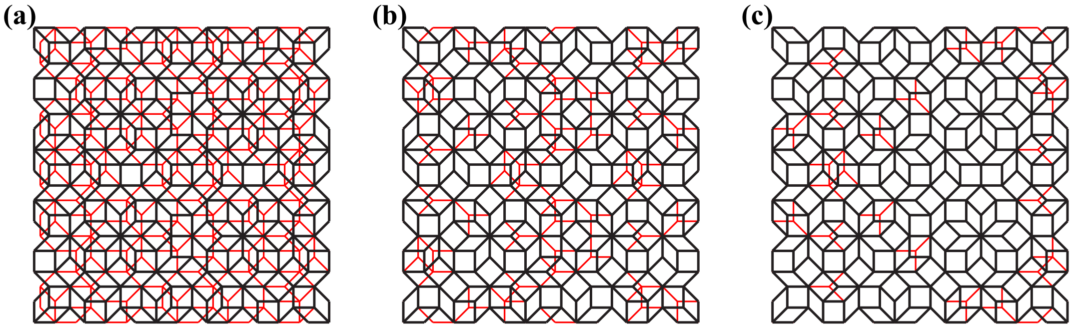

Figure 2.1.: Two superimposed identical octagonal Ammann-Beenker tilings, a red and a black colored one. From (a) to (c) the red tiling is translated lateral in x-direction with increasing step size. Despite the aperiodicity of the patterns, there are certain areas where the elementary tiles perfectly coincide. The further the red tiling is translated the bigger becomes the area of coincidence. This fulfills the definition of local isomorphism. However, a complete coincidence of infinite structures cannot be achieved by nonzero translation alone. In order to remove all missmatches correlated groups of tiles and vertices have to be rearranged. This corresponds to a deployment of the phasonic degree of freedom in quasicrystals.

A physical consequence is that infinite tilings from the same local isomorphism (LI) class cannot be distinguished by any finite measurement [233]. Moreover, they possess identical auto correlation functions and, in particular, identical diffraction properties including intensities. Therefore, quasicrystals within one LI class remain indistinguishable such that all physical properties share the same behavior [237].

Thus, of interest might be both excitations that conserve the local isomorphism class and those that break it. Regarding the former, translations, i.e. long wave length phonons comprise one group of elementary excitations that reside within a given LI class. The other group is also visible in Fig. 2.1. No symmetry operation consisting of pure nonzero translations will result in a complete and infinite coincidence of the superimposed tilings. There will remain correlated mismatches of red tiles that have to be rearranged, namely flipped, in order to yield the original tiling. These necessary rearrangements can be achieved by the phasonic degree of freedom. Similar to phonons, phasons represent hydrodynamic modes as they do not cost free energy in the limit of long wave lengths. Besides, in this limit, the occurring tile flips will conserve the local matching rules of the aperiodic tilings. Note that this is not the case for local flips, i.e. phasonic flips with finite wavelength violate the matching rules and thus lead to a different LI class. In general, excitations that change the LI class are associated with an increase of the free energy [232]. We investigate this further by considering a continuum description of two-dimensional quasicrystals in section 2.2.1.

2.2. Phasons

Analogue to phonons, phasons are low energy excitations that influence the elastic properties of quasicrystals, for instance the propagation of cracks [48]. Phasons correspond to complex rearrangements of the elementary tiles defining the quasicrystalline structure. In the limit of long wave length, phasons induce correlated tile flips that leave the free energy unchanged and conserve the LI class [232, 238]. Aside from this limit, uncorrelated phasons of finite wave length may occur due to thermal fluctuations [239]. Furthermore, in some systems, namely random tiling models, phasonic flips might contribute significantly to the stability of the quasicrystalline state because they increase the entropy of the system [56, 181, 240, 241]. On the other hand, concerning the preparation of metallic quasicrystals, uncorrelated phason flips induced by thermal fluctuations are the source of frozen-in disorder after lowering the temperature. This form of disorder is frequently detected from broadening Bragg peaks and additional diffusive scattering [187, 242, 243]. After all, local phasonic excitations break the LI class and violate the matching rules of the tiling. Besides, individual phasonic flips have been observed via high resolution transmission electron microscopy (hrTEM) [244] or in photonic quasicrystals [245]. Still today, phasons are at the center of active research and scientific debate [243, 246]. As a recent example, the claim that a quantum mechanical system of a boson gas with Rashba spinorbit coupling exhibits more phason modes in the quasicrystalline state than the classical counterparts has caused controversy [164, 247]. The claim has been refuted by two different approaches. We have refuted this claim by geometric considerations [C], while an alternative approach considering a general free energy yielded the same conclusion [248]. In the following, phasons are introduced in a general continuum description.

2.2.1. Hydrodynamic modes

In order to identify the hydrodynamic modes in quasicrystals we follow the approach derived by Socolar *et al.* [233]. Assuming the periodic or aperiodic crystal is given in the continuum description by a density field $\rho(\mathbf{r})$, then the Fourier series of that density is

$$\rho(\mathbf{r}) = \sum_{j=0}^{N-1} \rho_j \exp[-i\mathbf{G}_j \cdot \mathbf{r}] \,. \tag{2.1}$$

The reciprocal lattice vectors $\mathbf{G}_j = G(\cos[2\pi j/N], \sin[2\pi j/N])$ with $G = 2\pi/a_V$ are arranged in a symmetric, starlike manner and define the desired rotational symmetry. A small set of reciprocal vectors is sufficient to denote an ordered state. The complex components of the series are $\rho_j = |\rho_j| \exp[i\varphi_j]$.

In the next step, a general expansion of the phenomenological free energy $\mathcal{F}$ in terms of

$\rho(\mathbf{r})$ is considered:

$$\mathcal{F} = \int dA \sum_{k=1}^{\infty} B_k \rho(\mathbf{r})^k \,. \tag{2.2}$$

The details of the actual physical system are comprised in the coefficients B_k. Inserting $\rho(\mathbf{r})$ in Eq. (2.2) yields for the free energy

$$\mathcal{F} = \int dA \sum_{k=1}^{\infty} B_k \sum_{j_1,\ldots,j_k} \prod_{l=1}^{k} \rho_{j_l} \exp\left[-i \sum_{l=1}^{k} \mathbf{G}_{j_l} \cdot \mathbf{r}\right] \,. \tag{2.3}$$

After conducting the integration over the whole plane one obtains

$$\mathcal{F} = A \sum_{k=1}^{\infty} B_k \sum_{j_1,\ldots,j_k} \delta\left[\sum_{l=1}^{k} G_{j_l}\right] \prod_{l=1}^{k} \rho_{j_l} \,, \tag{2.4}$$

where A denotes the area of the system. The Kronecker symbol $\delta[x]$ is 1 if x equals zero and 0 otherwise. Therefore, only specific combinations of $\mathbf{G}_j$ contribute to the free energy. Inserting the Fourier components ρ_j results finally in

$$\mathcal{F} = A \sum_{k=1}^{\infty} B_k \sum_{j_1,\ldots,j_k} \delta\left[\sum_{l=1}^{k} G_{j_l}\right] \prod_{l=1}^{k} |\rho_{j_l}| \exp\left[i \sum_{l=1}^{k} \varphi_{j_l}\right] \,. \tag{2.5}$$

Note that the free energy $\mathcal{F}$ solely depends on the sum of the phases $\sum_{l=1}^{k} \varphi_{j_l}$. As a consequence, true hydrodynamic modes must be comprised of collective changes in the phases φ_j that leave the sum unaffected.

Although N reciprocal vectors have been initially considered in the series of Eq. (2.1), only $D < N$ are required, where D is termed the rank of the crystal. If D equals the dimension d, the crystal is periodic, while in the case of $D > d$ the crystal is aperiodic, i.e. a quasicrystal. A way to determine the minimal set D is to count the number of incommensurate length scales n_R in each lattice direction given by $\mathbf{G}_j$. Then, the minimal set of reciprocal vectors consists of $D = n_R d$ vectors. Alternatively, the rank can be calculated by Euler's totient function [189]. It is given by

$$\Phi(n) = \{a \in \mathbb{N} |\, 1 \leq a \leq n \wedge \gcd(a, n) = 1\} \,, \tag{2.6}$$

where $\gcd(a, n)$ denotes the greatest common divisor between a and n. $\Phi(n)$ returns the amount of integers smaller or equal to N that are coprime to N. Thus $N - \Phi(N)$ reciprocal vectors can be expressed by $\mathbf{G}_j = \sum_{k=0}^{\Phi(N)-1} a_{jk} \mathbf{G}_k$. Then $\rho(\mathbf{r})$ is rewritten and it can be shown that the sum of $\Phi(N)$ independent phases has to be constant in order to preserve the local isomorphism class [C].

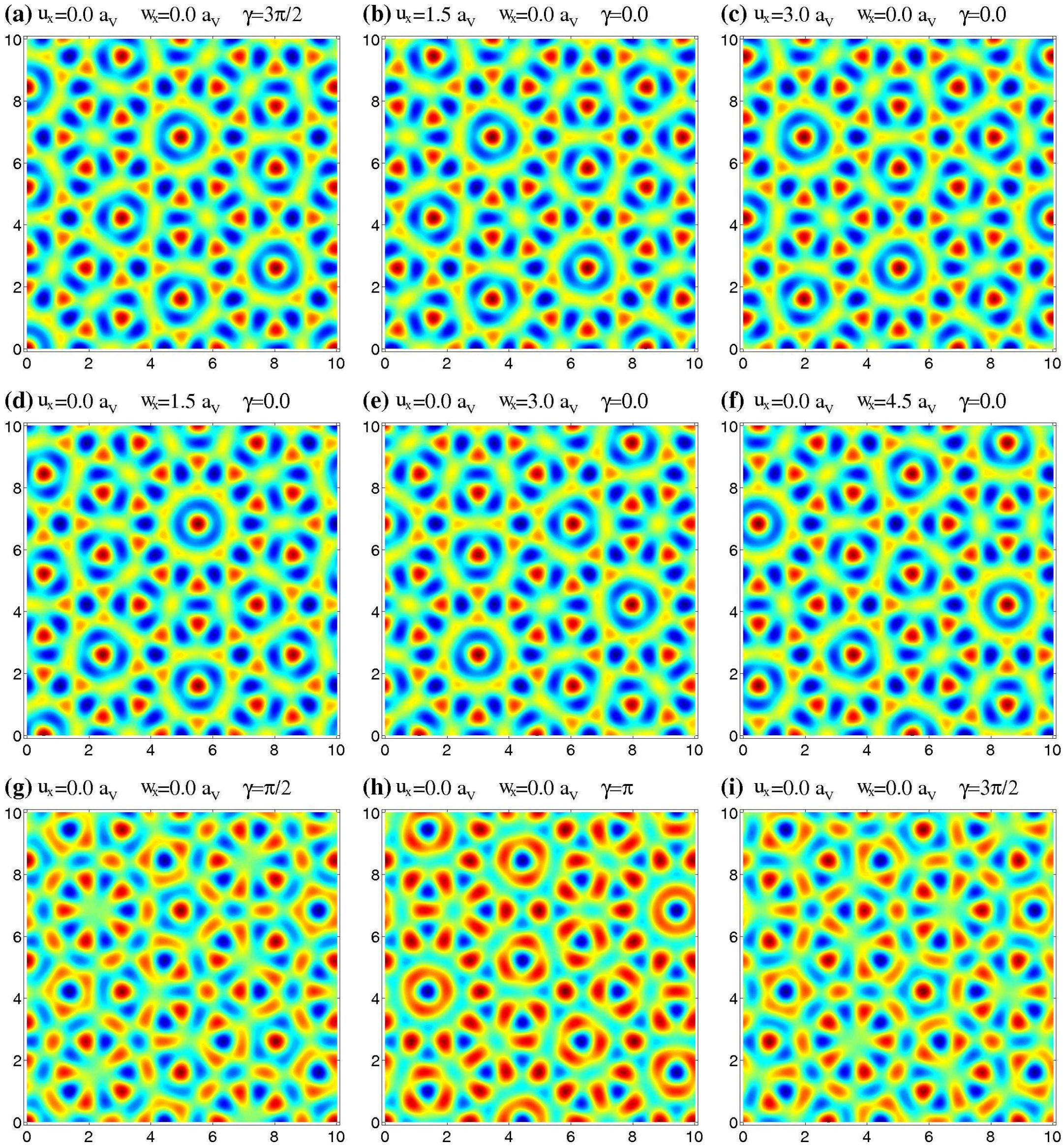

Figure 2.2.: Examples for different excitations on the basis of a decagonal quasicrystal. The quasicrystalline pattern is generated by the real space of the Fourier series in Eq. (2.1) with $N = 5$. The phases are parameterized according to Eq. (2.7). (a-c) A long wave length phononic displacement corresponds to a translation of the whole pattern. (d-f) A long wave length phasonic displacement induces complex rearrangements of minima and maxima and causes some local symmetry centers to disappear and others to appear. (g-i) Changing the global phase γ leads to a broadening of the minima and maxima. Note that in contrast to the previous excitations the local isomorphism class is broken as finite patches from (g-i) are not found in (a-f).

Regarding the expansion of the free energy in Eq. (2.5), N symmetrically arranged reciprocal lattice vectors $\mathbf{G}_j$ are used such that there are N phases φ_j. Since hydrodynamic modes conserve the LI class as well as the free energy the sum $\sum_{l=1}^{k} \varphi_{j_l}$ also has to remain constant. Therefore, this amounts to D independent hydrodynamic modes in a quasicrystal of rank D, where d are attributed to phononic and $D - d$ to phasonic excitations. Concerning the symmetries mainly investigated in the scope of this work, namely octagonal, decagonal, and dodecagonal rotational symmetry the rank equals four. For $D = 4$ the parameterization of the phases is usually according to [233, 238] given by

$$\varphi_j = \mathbf{G}_j \cdot \mathbf{u} + \mathbf{G}_{m\,j \bmod N} \cdot \mathbf{w} + \gamma/N\,, \tag{2.7}$$

where $\mathbf{u} = (u_x, u_y)$ denotes the phononic and $\mathbf{w} = (w_x, w_y)$ the phasonic displacement. Note that the global phase γ is not a hydrodynamic mode as it affects the sum of the phases. In Fig. 2.2 examples for a decagonal density pattern with different values of the phononic and phasonic displacements as well as the global phase are displayed. An increase in $\mathbf{u}$ culminates in a lateral translation of the whole pattern along $\mathbf{u}$. Therefore, $\mathbf{u}$ describes a phonon in the limit of long wave length. On the other hand, a change of $\mathbf{w}$ induces complex rearrangements between minima and maxima of the density field. These hydrodynamic modes are termed phasons. An increase in γ leads to changes in the height and width of the maxima and minima respectively. This breaks the definition of local isomorphism class as for instance a finite patch in (h) is not found anywhere in (a-f). Besides, such an excitation is expected to demand a significant increase in the free energy. Only long wave length phonons and phasons conserve the LI class.

2.3. Topological defects

Both in periodic and in aperiodic crystals, the topology of a dislocation is defined by a Burgers vector. In a periodic system of d dimensions, the Burgers vector of an edge dislocation has d components and can directly be obtained in real space by considering a closed loop around a dislocation core (see Fig. 2.3 (b)). If one follows a similar path with exactly the same number of steps in each direction in the corresponding defect-free crystal, the difference from the end point to the starting constitutes the Burgers vector (see Fig. 2.3 (a)). As an alternative method, the Burgers vector can be obtained by integrating over all displacements along a closed loop around the dislocation. For a given displacement field $\mathbf{u}(\mathbf{r})$, the total displacement that is denoted in the Burgers vector is $\mathbf{\Delta u} = \oint d\mathbf{u}(\mathbf{r})$. In a periodic crystal and in the case of full edge dislocations only, $\mathbf{\Delta u}$ has to be a sum of integer multiples of the lattice basis vectors, such that the density field $\rho(\mathbf{r})$ of the defect-free crystal is not changed by a displacement along $\mathbf{\Delta u}$, i.e.,

$$\rho(\mathbf{r}) = \rho(\mathbf{r} + \mathbf{\Delta u})\,. \tag{2.8}$$

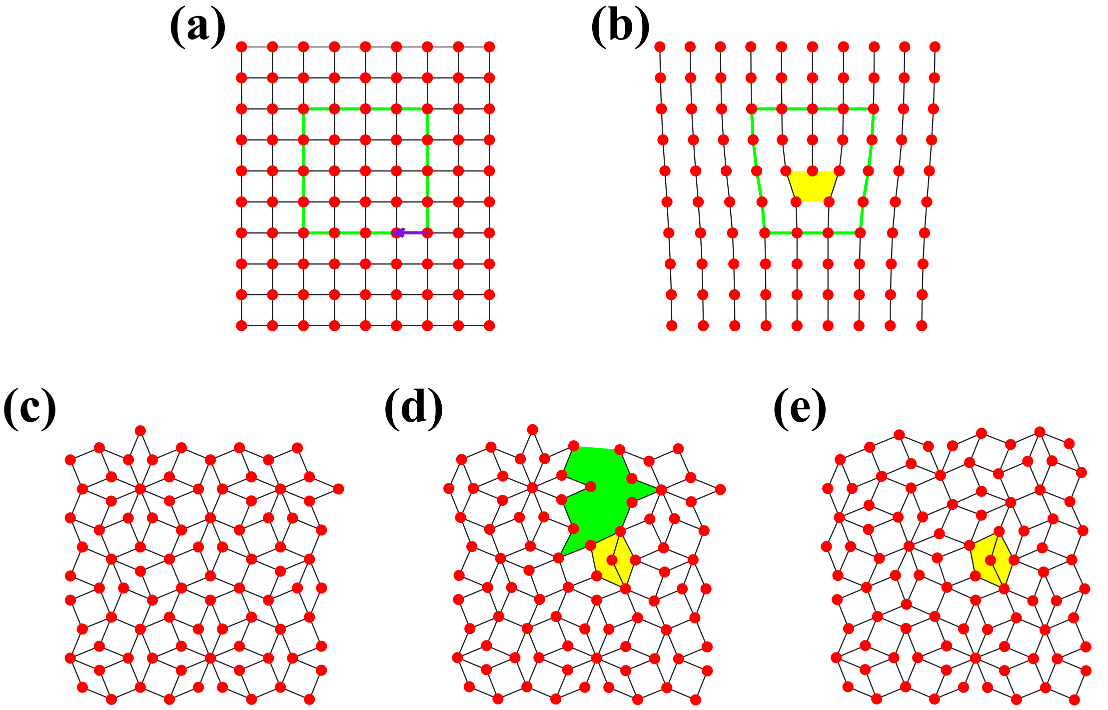

Figure 2.3.: Schematic illustration for dislocations in crystals quasicrystals in two dimensions (cf. [D]). (a) Square lattice without any defect. (b) Upon injecting or removing half of a line of nodes a single dislocation (surrounded by a yellow shading) is created in the square lattice. By considering a closed loop (green line) around the dislocation and a corresponding path in the defect-free lattice, the Burgers vector is given by the difference from the end to the starting point in the perfect crystal [cf. green path and magenta vector in (a)]. (c) A defect-free patch of an octagonal quasicrystal. (d) After omitting half a row of nodes, it is not possible to connect the neighboring rows in a straightforward way due to the aperiodicity of a quasicrystal. As a consequence, there remains a gap (green) in a quasicrystal with a partial dislocation (marked yellow) that contains only the phononic contribution of the Burgers vector. The gap cannot be filled with the elementary tiles of the tiling. (e) Quasicrystal with a dislocation (marked yellow) whose Burgers vector contains a phononic and a phasonic part. The additional phasonic contribution manifests into rearrangements of the tiles adjacent to the cut line such that the previously empty gap area can be covered with elementary tiles.

In quasicrystals, a dislocation with a displacement field $\mathbf{u}(\mathbf{r})$ but no other perturbations must be associated with a gap in the structure (see Fig. 2.3 (d)) because due to the aperiodicity there is no nonzero phononic displacement vector $\boldsymbol{\Delta}\mathbf{u} = \oint d\mathbf{u}(\mathbf{r})$ that fulfills the condition of Eq. (2.8). However, in order to close the gap, one can employ the additional degrees of freedom of quasicrystals, namely a phasonic displacement field $\mathbf{w}(\mathbf{r})$. While in a quasicrystal there are no pure phononic displacements $\boldsymbol{\Delta}\mathbf{u}$ or pure phasonic displacements $\boldsymbol{\Delta}\mathbf{w}$ that leave the density $\rho(\mathbf{r})$ unchanged, there exist combinations of phononic and phasonic displacements, $\mathbf{\Delta u}$ and $\mathbf{\Delta w}$, that do not alter the density [138, A, B], i.e.,

$$\rho_{\mathbf{w}=\mathbf{0}}(\mathbf{r}) = \rho_{\mathbf{w}=\mathbf{\Delta w}}(\mathbf{r} + \mathbf{\Delta u})\,, \tag{2.9}$$

where $\rho_{\mathbf{w}}(\mathbf{r})$ denotes the density field with a constant phasonic displacement $\mathbf{w}$. As a consequence, dislocations can be incorporated into quasicrystals by a spatial varying phononic displacement field $\mathbf{u}(\mathbf{r})$ in combination with a phasonic one $\mathbf{w}(\mathbf{r})$, such that $\mathbf{\Delta u} = \oint d\mathbf{u}(\mathbf{r})$ and $\mathbf{\Delta w} = \oint d\mathbf{w}(\mathbf{r})$ fulfill the condition in Eq. (2.9) [238, D]. An example of a dislocation in a quasicrystal is shown in Fig. 2.3. The Burgers vector $\mathbf{B}$ is composed of the phononic and the phasonic displacement, i.e., $\mathbf{B} = (\mathbf{\Delta u},\, \mathbf{\Delta w})$. In general, the Burgers vector of a dislocation in quasicrystals in d dimensions has D components, where D is the rank of the quasicrystal denoting the number of basis vectors that are required to characterize the structure. While d components can be attributed to the phononic contribution, the remaining $D - d$ components determine the phasonic contribution.

In the following, we briefly review the work by De and Pelcovits who calculated the phononic and phasonic displacement fields describing dislocations in decagonal quasicrystals [234]. A phenomenological harmonic elastic energy density is readily constructed and has the form

$$\begin{aligned} f_{\text{el}} = {} & \frac{1}{2}\lambda u_{ii}u_{ii} + \mu u_{ij}u_{ij} + \frac{1}{2}K_1 w_{ij}w_{ij} + K_2\left(w_{xx}w_{yy} - w_{xy}w_{yx}\right) \\ & + K_3\left[(u_{xx} - u_{yy})(w_{xx} + w_{yy}) + 2u_{xy}(w_{xy} - w_{yx})\right] - \tilde{\mathbf{f}}\cdot\tilde{\mathbf{u}}\,, \end{aligned} \tag{2.10}$$

where $u_{ij} = \frac{1}{2}(\partial_i u_j + \partial_j u_i)$ denotes the strain tensor and $w_{ij} = \partial_i w_j$. While the first two terms on the right hand side characterize a two-dimensional isotropic solid, the last term represents a general coupling of the D-dimensional elastic field $\tilde{\mathbf{u}} = \mathbf{u} \oplus \mathbf{w}$ to a generalized force $\tilde{\mathbf{f}}$. Specific choices for $\tilde{\mathbf{f}}$ can model dislocations.

Following the Euler-Lagrange procedure f_{el} is extremized with respect to small variables δu_x, δu_y, δw_x, and δw_y. This yields a system of equations

$$\mathcal{L}_i[\tilde{\mathbf{u}}] = -\tilde{f}_i\,, \tag{2.11}$$

where $\mathcal{L}_i$ is a linear differential operator. A convenient way to solve these inhomogeneous equations is to calculate the associated D^2-component Green's tensor:

$$\tilde{\mathbf{u}}(\mathbf{r}) = \int d\mathbf{r}'\, \bar{\mathbf{G}}(\mathbf{r} - \mathbf{r}')\, \tilde{\mathbf{f}}(\mathbf{r}')\,. \tag{2.12}$$

The elastic fields surrounding a dislocation are obtained by determining all components in $\bar{\mathbf{G}}$. Analogue to periodic solids, $\mathbf{u}(\mathbf{r})$ and $\mathbf{w}(\mathbf{r})$ can be chosen as single valued functions which undergo a fixed discontinuity as they cross the cut line. This cut line yields a singular stress which must be compensated by fictious forces into the Euler-Lagrange equations. Upon solving the modified equations and conducting the integration along the whole cut line the strain field of a dislocation located at the origin with Burgers vector

$\mathbf{B} = (\mathbf{\Delta u},\ \mathbf{\Delta w})$ is given by

$$
\begin{aligned}
u_x(\mathbf{r}) &= \frac{\Delta u_x}{2\pi}\left\{\arctan\left[\frac{y}{x}\right] + \frac{(\mu+\lambda)K_1}{(\mu+\lambda)K_1 + (\mu K_1 - K_3^2)}\frac{xy}{r^2}\right\} \\
&= \frac{\Delta u_y}{2\pi}\left\{\frac{\mu K_1 - K_3^2}{(\mu+\lambda)K_1 + (\mu K_1 - K_3^2)}\ln\left[\frac{r}{a}\right] - \frac{(\mu+\lambda)K_1}{(\mu+\lambda)K_1 + (\mu K_1 - K_3^2)}\frac{x^2}{r^2}\right\} \\
&= \frac{\Delta w_x}{2\pi}\left\{\frac{(K_3K_1)}{\mu K_1 - K_3^2}\frac{xy}{r^2} - \frac{K_3K_1^2(\mu+\lambda)}{2(\mu K_1 - K_3^2)[(\mu+\lambda)K_1 + (\mu K_1 - K_3^2)]}\frac{2xy^3}{r^4}\right\} \\
&= \frac{\Delta w_y}{2\pi}\left\{-\frac{(K_3K_1)}{(\mu+\lambda)K_1 + (\mu K_1 - K_3^2)}\frac{x^2}{r^2}\right. \\
&\quad \left. -\frac{K_3K_1^2(\mu+\lambda)}{2(\mu K_1 - K_3^2)[(\mu+\lambda)K_1 + (\mu K_1 - K_3^2)]}\frac{x^2(x^2-y^2)}{r^4}\right\}
\end{aligned}
\tag{2.13}
$$

where a denotes the dislocation core size.

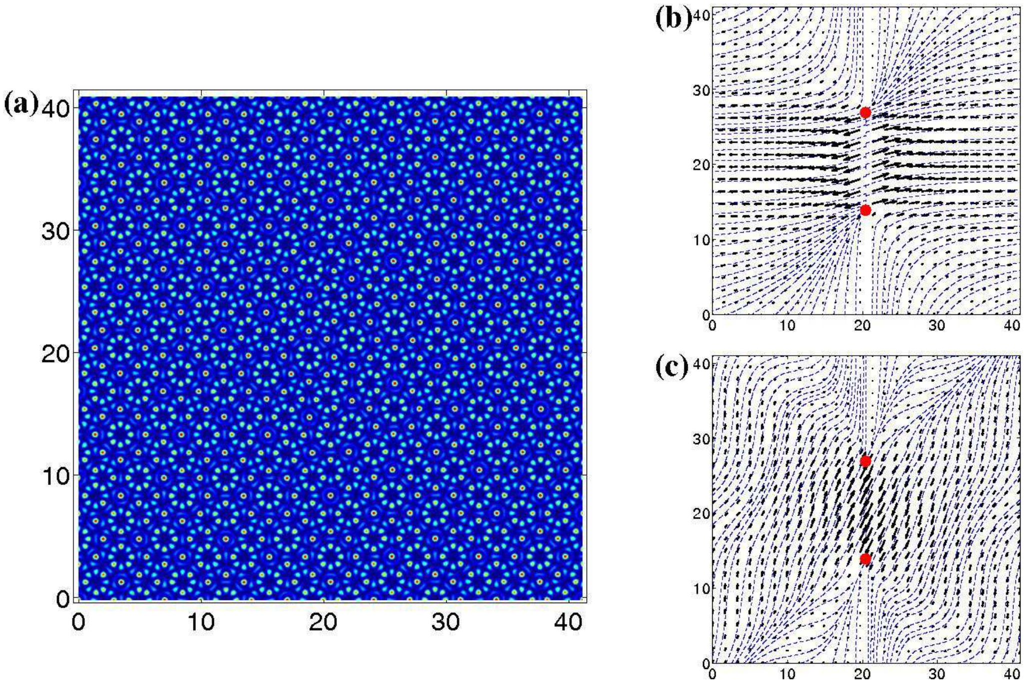

Figure 2.4.: Dislocation and associated strain fields in an octagonal interference pattern. The spatial varying fields $\mathbf{u}(\mathbf{r})$ and $\mathbf{w}(\mathbf{r})$ can be incorporated by tuning the respective phases of the laser beams. (a) The octagonal intensity field exhibits two dislocations with oppositely charged Burgers vectors such that the whole sample is neutral. From real space observation the dislocations are hard to detect. The associated phononic (b) and phasonic strain field (c) have a discontinuity at the cut line connecting the two dislocation cores marked as red spots. The values of displacement are denoted by black arrows while dashed blue lines serve as an additional guide to the eye. Far away from the dislocation pair the displacement fields are almost zero as the effective topological charge is zero.

For the other components $u_y(\mathbf{r})$, $w_x(\mathbf{r})$, and $w_y(\mathbf{r})$ we explicitly refer to [234]. An example for a quasicrystal containing a pair of dislocations as well as the corresponding phononic and phasonic strain fields is displayed in Fig. 2.4.

On the basis of these fields the single energy of a dislocation E_c as well as their pairwise interaction H_D can be calculated [234]. Furthermore, the procedure above can be applied to another type of topological defect. Analogue to dislocations, disclinations are described by spatially varying phononic and phasonic strain fields [249], which allows to determine their energies as well [250]. From this, a theory of defect-mediated two stage melting in two-dimensional quasicrystals has been developed [251]. It represents an extension of the KTHNY-theory for the melting of two-dimensional periodic solids formulated by Kosterlitz and Thouless [252], Halperin [253], Nelson [236, 254, 255] and Young [256, 257].

In chapter 6, we deploy Eq. (2.13) in order to incorporate dislocations as defects into quasicrystalline templates on which colloidal epitaxy is conducted. Therefore, three-dimensional colloidal structures with controlled and well-defined dislocation lines are produced.

> Random number generation is too important to be left to chance.
>
> *(Robert Coveyou* 1951-1996*)*

CHAPTER 3

Methods

In this chapter, we explain how we have implemented the Monte-Carlo algorithm to model the epitaxial deposition on various substrates as well as the two-dimensional suspension of a colloid-polymer mixture. In particular, the choice of suitable box sizes is elucidated when simulating quasicrystals under periodic boundary conditions. Moreover, we introduce a way to quickly identify dislocations in a two-dimensional quasicrystal.

3.1. Simulation technique

In our simulations, we use the Monte-Carlo algorithm originally developed by Metropolis *et al.* [258, 259], which has become a standard technique in the field of computational physics [260, 261]. The algorithm allows to treat the system in the canonical ensemble with the canonical partition function

$$Z = \sum_{\{i\}} \exp[-\beta E_i] \tag{3.1}$$

as the central object to calculate any further observable. The sum in Eq. (3.1) is over all configurations and $\beta = 1/k_\mathrm{B}T$ denotes the inverse of the thermal energy.

The general procedure of the algorithm is as follows: At the beginning of each Monte-Carlo step the current configuration is changed randomly into a new one. Then the energy E_new of this new configuration is calculated and compared to E_old, the energy of the previous configuration. If $E_\mathrm{new} < E_\mathrm{old}$ the new configuration is immediately accepted and serves as the initial configuration in the next step. In case of $E_\mathrm{new} > E_\mathrm{old}$, the new configuration might still be accepted but only with probability $\exp[-\beta(E_\mathrm{new} - E_\mathrm{old})]$. Otherwise, the next Monte-Carlo step will begin with the old configuration again. This choice of acceptance probabilities satisfies detailed balance, since the ratio between the transition probability $p_{i\to j}$ to get from configuration i to configuration j and the probability of the contrary transition $p_{j\to i}$ is

$$\frac{p_{i\to j}}{p_{j\to i}} = \frac{\exp[-\beta E_j]}{\exp[-\beta E_i]}\,. \tag{3.2}$$

As a consequence, for an ergodic system i.e. a system, where all possible configurations are explored, the probability to be in configuration i is proportional to $\exp[-\beta E_i]$, such that a canonical ensemble of configurations is obtained. Although a finite simulation can never explore the whole configurational space, the algorithm will still include the most important contributions in Z by gradually minimizing E. Therefore, the average of an arbitrary observable A, for instance an order parameter, simplifies to

$$\langle A \rangle = \frac{1}{Z} \sum_{\{i\}} A_i \exp[-\beta E_i] = \lim_{N \to \infty} \frac{1}{N} \sum_{n=1}^{N} A_n \, , \tag{3.3}$$

where N is the number of considered Monte-Carlo configurations. In fact, such a measurement is usually started after a considerable number of Monte-Carlo steps have already been performed such that the system is in thermal equilibrium of the canonical ensemble. In addition, several steps might separate the individual configurations to account for substantial differences in the averaging process. In the end, the quality of the implementation is determined by the speed of finding the configurations close to the ground state and the explored area of configurational space during the process. This can be influenced by the suggested trial configurations.

In our implementation, trial configurations are generated by two possible modifications of an old configuration. In a local transition, a colloid is randomly displaced in an area surrounding its original position. The size of this trial area is adapted during the simulation such that the average acceptance according to the Metropolis rule remains around 50%. If the average of accepted transitions drops to a threshold below 50% the trial area is reduced to increase the acceptance probability again. On the other hand, if the acceptance rate reaches a threshold above 50%, the trial area is increased. By this procedure it is guaranteed that a large number of configurations close to the state of lowest energy is generated. However, that minimum may just be a local minimum in the energy landscape in which the procedure is trapped unless one enables the crossing of high energy barriers. Therefore, we perform a global transition with a probability of 20%. In contrast to local transitions, the colloid is now randomly displaced in the whole sample, while the Metropolis rule still determines acceptance or rejection. In our epitaxial code, global transitions can only be attempted for colloids belonging to the top most layer in order to conserve the already grown film. Further subtle differences between the Metropolis implementation for the two-dimensional colloid-polymer mixture and the template-guided epitaxy in three-dimensional systems will be adressed in the respective sections. In both cases, we use the widespread Mersenne-Twister mt19937 [262] as pseudo-random number generator. The name is due to its period length of $2^{19937} - 1$ which is a Mersenne prime number. Its output sequences are up to 623 dimensions uniformly distributed.

3.2. Size of simulation box

In the following section, we address the issue of suitable box sizes for aperiodic structures in simulations. While periodic boundary conditions are genericly applied to model bulk behavior in numerical physics, they are contradictory to the aperiodicity of quasicrystals. If implemented without special care, periodic boundary conditions may lead to a significant discontinuity in the substrate system. Here, we explain methods to minimize this discontinuity for continuous potentials like the laser interference pattern as well as discrete ones like aperiodic tilings.

3.2.1. Approximants for continuous potentials

In general, the continuous potentials or patterns are generated by a set of reciprocal lattice vectors $\mathbf{G}_j$. These are are arranged in a starlike, symmetric manner: $\mathbf{G}_j = G(\cos[2\pi j/N], \sin[2\pi j/N])$ and $G = 2\pi/a_V$. Instead of distorting these patterns near the boundaries, we choose width L_x and height L_y of the simulation box appropriately such that the discontinuities experienced by particles crossing these boundaries are negligible small. Since quasicrystals possess length scales whose ratio is an irrational number like for example the golden mean τ, these box dimensions are limited to certain integer multiples of a length scale. Usually, these integers are part of a fractional approximation of the involved irrational number.

For the decagonal potential, $N = 5$ or $N = 10$, the length scales in x-direction are $2\pi/G_{0,x} = a_V$, $2\pi/G_{1,x} = 2\tau a_V$, and $-2\pi/G_{2,x} = 2\tau{-}1 a_V$, while for the y-direction $2\pi/G_{1,y} = \tau^{-1} a_V/\sin[\pi/5]$ and $2\pi/G_{2,y} = a_V/\sin[\pi/5]$ are determined. The golden mean can be approximated by successive elements of the Fibonacci sequence, since

$$\lim_{n\to\infty} \frac{f_{n+1}}{f_n} = \tau \,, \tag{3.4}$$

with

$$f_n = \begin{cases} f_{n-1} + f_{n-2} & \text{if } n > 2 \\ 1 & \text{otherwise} \end{cases} \tag{3.5}$$

is valid. Therefore, appropriate box sizes for the decagonal potential are $L_x = 2f_n a_V$ and $L_y = 2f_m a_V$.

The octagonal pattern is generated by $N = 8$ reciprocal vectors. Since it is invariant under rotations by $\pi/2$, the appropriate box is a square. Thus, it is sufficient to discuss the x-direction whose length scales are given by $2\pi/G_{0,x} = a_V$ and $2\pi/G_{1,x} = \sqrt{2}a_V$. Similar to the previous case, we can approximate the irrational number $\sqrt{2}$ by

$$\lim_{n\to\infty} \frac{P_{n+1} + P_n}{P_n} = \sqrt{2} \tag{3.6}$$

where P_n are elements of the Pell sequence defined by

$$P_n = \begin{cases} 0 & \text{if } n = 0 \\ 1 & \text{if } n = 1 \\ 2P_{n-1} + P_{n-2} & \text{otherwise} \end{cases} . \tag{3.7}$$

Consequently, a suitable box size is given by $L = ma_V$, while m is constructed according to Eq. (3.6). For instance, the sequence of appropriate integers is $\{1,\ 3,\ 7,\ 17,\ 41,\ 99, \ldots\}$ and the quality of the approximation is illustrated in Fig. 3.1 (a,b).

In case of the dodecagonal pattern which is constructed by $N = 12$ vectors the approximated box is also a square with edge length $L = 2ma_V$. The length scales are determined to $2\pi/G_{0,x} = a_V$, $2\pi/G_{1,x} = 2a_V/\sqrt{3}$, and $2\pi/G_{2,x} = 2a_V$. In order to obtain appropriate integer values for m, we use a continuous fraction approximation which is

$$\sqrt{3} = [1; 1, 2, 1, 2, 1, 2, 1, 2, 1, 2, \ldots] \tag{3.8}$$

$$= 1 + \cfrac{1}{1 + \cfrac{1}{2 + \cfrac{1}{1 + \cfrac{1}{2 + \cfrac{1}{1 + \cfrac{1}{2 + \cfrac{1}{1 + \cdots}}}}}}} . \tag{3.9}$$

In this way, suitable values are $\{1,\ 2,\ 4,\ 7,\ 15,\ 26,\ 56,\ 97, \ldots\}$ as can be observed in Fig. 3.1 (c,d). Here, we demonstrated how suitable box sizes can be obtained for octagonal, decagonal, and dodecagonal rotational symmetry, i.e. symmetries of rank $D = 4$. Note that this approach is less applicable to rotational symmetries of higher rank, for instance tetradecagonal symmetry with rank $D = 6$, where two incommensurate ratios have to be approximated simultaneously.

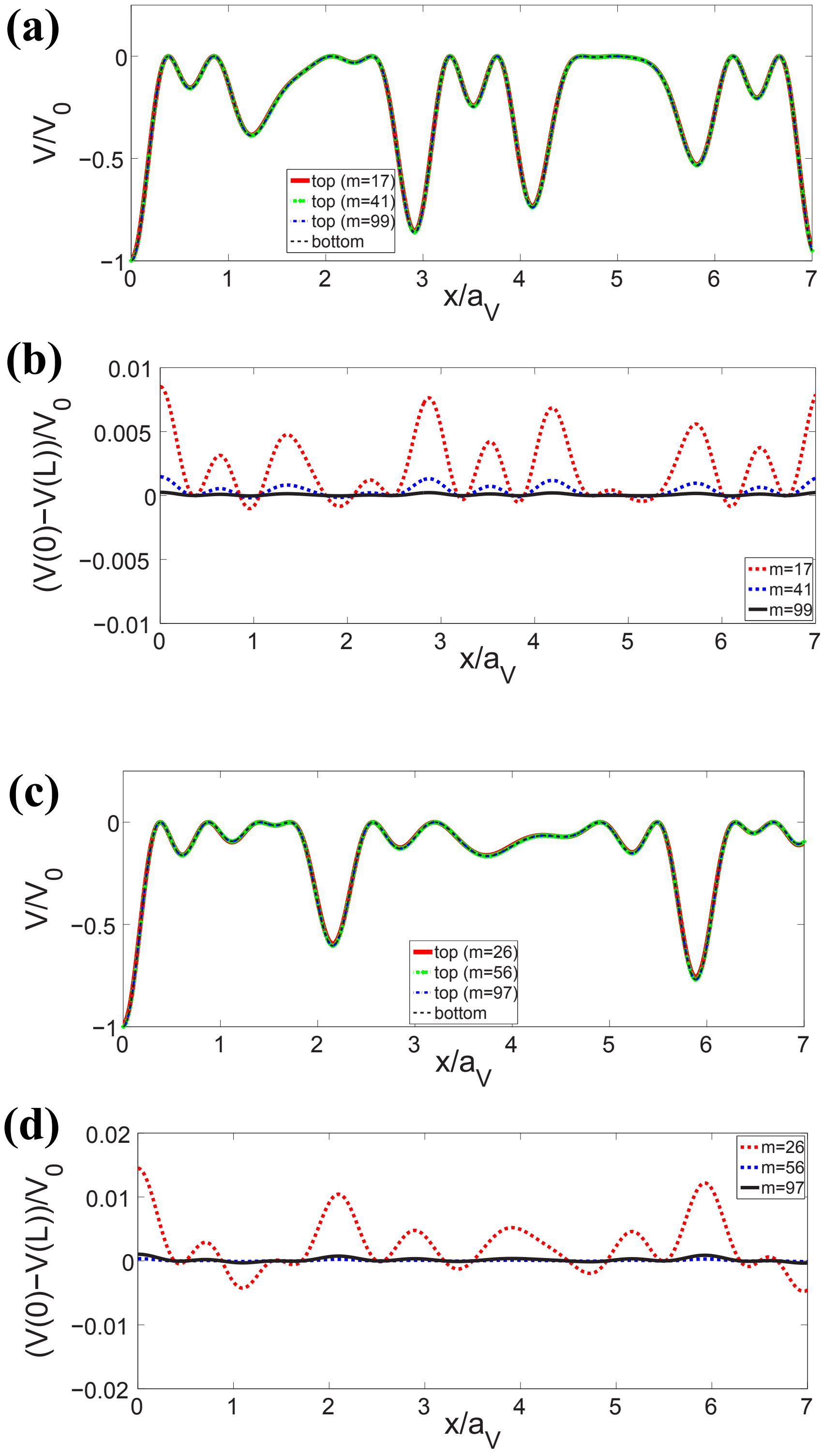

Figure 3.1.: Boundaries in laser potentials. (a) Different values of the octagonal laser potential at the top of the box $V(y = m \cdot a_0)$ are compared to the values $V(y = 0)$ at the bottom. (b) The difference from (a) are displayed. (c) Analogue to (a) for the dodecagonal laser potential as the top of the box $V(y = m \cdot a_0)$ is compared to $V(y = 0)$ at the bottom. In (d) the difference from (c) are shown.

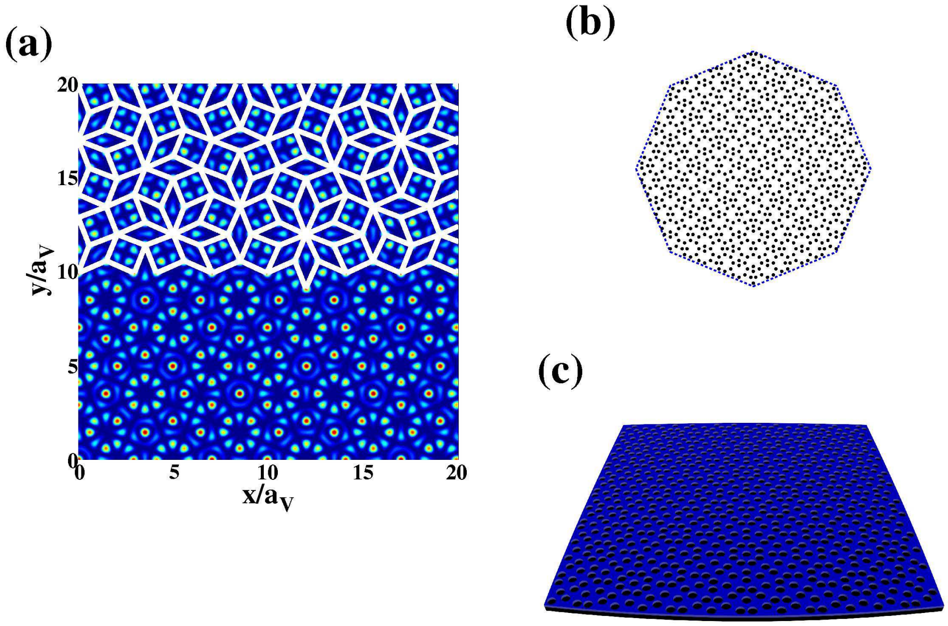

Figure 3.2.: Substrate construction from an intensity field of eight interfering laser beams. (a) The most pronounced maxima of the intensity field seem to be ordered according to an Ammann-Beenker like tiling. (b) When transferring the coordinates of the vertices $\mathbf{x}^{||}$ from (a) to orthogonal space $\mathbf{x}^{\perp}$, all vertices are located inside an octagon with unit edge length. Thus, the long-range octagonal order like the tiling is confirmed for the intensity field. (c) The continuous field is discretized by arranging holes in the plane according to the tiling. Therefore, small intensity differences between maxima on the boundary become almost irrelevant.

These laser patterns serve as substrates in our model for colloidal epitaxy with induced defects. In section 2.3, we already explained how to integrate the strain fields surrounding dislocations into continuous laser intensity fields. As substrate, these fields are discretized by arranging circular slots in an otherwise planar surface according to the position of their most pronounced maxima. Through this process a tilinglike structure is obtained. For instance, discretizing the intensity field of eight interfering laser beams leads to an Ammann-Beenker like tiling, as illustrated for a patch in Fig. 3.2. In orthogonal space the development of the Ammann-Beenker tiling is further confirmed as all points $\mathbf{x}_{\perp}$ are located inside an octagon with unit edge length. The final substrate is displayed in Fig. 3.2 (c).

3.2.2. Approximants for aperiodic tilings

In contrast to the continuous fields in the previous section, an appropriate choice of box dimensions is not sufficient in order to construct rational approximants to the aperiodic tilings presented in section 1.3. Therefore, we outline in this section how so-called phasonic approximants can be derived for the aperiodic tilings used in this work. Instead of distorting the coordinates of the tiling close to the boundary, the tiles are rearranged such that the tiling is sustained smoothly across the periodic boundaries, while at the same time the shape of the elementary tiles is conserved. Usually, this requires slight modifications to the inflation rules, the dual grid or the projection angle. In the following, we will briefly explain for each tiling used in the scope of this work how we generate useful approximants.

We implemented the inflation rules from section 1.3.1 into a program to construct the tilings (see Appendix A) and cut out a patch by a rectangular box. However, if periodically repeated, these boxes might fail to yield a sustained tiling consisting of the original tiles, as shown in Fig. 3.3 (a) on the basis of the Penrose tiling. Close to the top and bottom boundaries the elementary tiles, a fat and a skinny rhomb, would be distorted. In order to overcome this set back, small conglomerations of the tiles can be arranged in a different manner, by employing small phasonic flips. In this way, the cut out box becomes a periodic cell as the sequence of tiles along the top and bottom boundary is now identical such that the cell in Fig. 3.3 (b) may serve as a reasonable rational approximant. Aside this manual approach, similar approximants of the Penrose tiling can be obtained by the dual grid method [263] or the projection approach [264, 265]. In both cases the golden mean τ in the slope of the pentagrid or the angle in the projection matrix is replaced by fractions involving Fibonacci numbers.

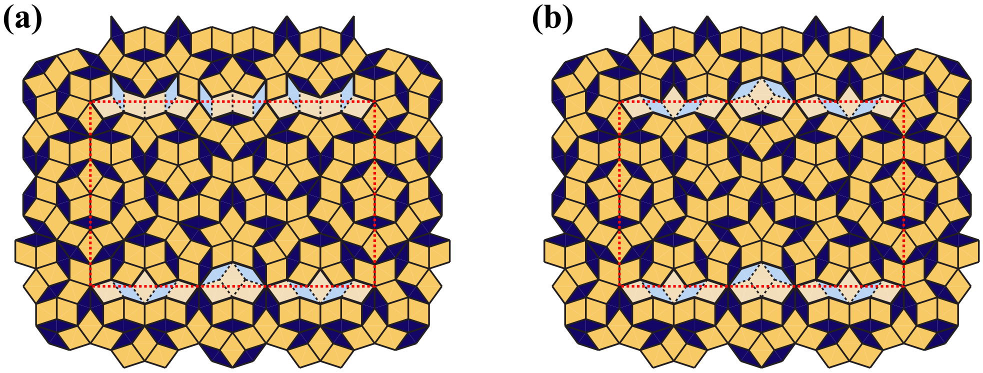

Figure 3.3.: (a) A patch of the Penrose-Rhomb tiling generated by inflation rules. A cut by the rectangular area (red dashed line) does not comprise a periodically sustained cell as the sequence of tilings along the top border differs from the one at the bottom border. (b) The same tiling as in (a), but with a few phasonic flips in the vicinity of the top boundary. Now the sequences of tiles along the top and bottom boundary are identical and sustained through periodic repetition.

Due to its matching and inflation rules the Ammann-Beenker tiling can be produced

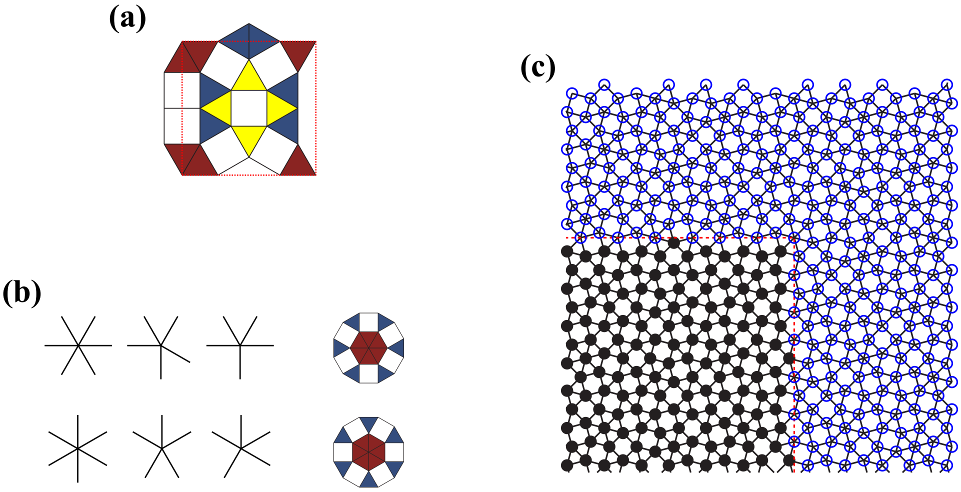

Figure 3.4.: Illustration of the extended Schlottmann rule for the Square-Triangle tiling. (a) As starting configuration a periodic cell is chosen. (b) In each iteration step the six types of vertices are replaced by two types of dodecagons. In this way, the initial periodicity is conserved. (c) Extract of an initial configuration in a two-dimensional Monte-Carlo simulation. Black dots denote simulated colloidal particles while blue dots represent mirror particles through periodic boundary conditions. The tiling of squares and triangles is smoothly sustained across the periodic boundary (dashed red line).

iteratively in a square domain if two right triangles compose the initial arrangement. This domain already sustains the tiling across periodic boundary conditions. Nevertheless, manually located tile flips might still be applied to generate box dimensions in between the ones obtained by inflation, as these scale with $\alpha = 1 + \sqrt{2}$.

In case of the Square-Triangle tiling, there exist modified inflation rules in order to generate rational approximants [180, 266, 267]. Starting from an initial periodic arrangement of triangles or squares the vertices are replaced iteratively by dodecagons consisting of six triangles in the center surrounded by a ring of alternating squares and triangles. The orientation of these dodecagons depends on the two types of vertices. This procedure is known as the extended Schlottmann rule and is illustrated in Fig. 3.4. As a disadvantage the difference in size between subsequent generations of tilings becomes quickly quite huge, since the scaling factor in each iteration step remains $\lambda = 2 + \sqrt{3}$. In order to overcome this and to produce approximants whose generations exhibit a smaller difference in growth, so-called half-step rules have been developed for the Square-Triangle tiling [267]. A vertex replacement according to the Schlottmann rule and an inflation scaling with $\sqrt{\lambda}$ are alternately applied to produce approximants with smaller size deviations in the generations.

3.3. Mode analysis

Usually, it is hard to recognize or even characterize dislocations in quasicrystals by just looking on snapshots. Instead of conducting a tiling based analysis as for example in [268], we follow a different method which was deployed in [55] and is illustrated for an octagonal quasicrystal in Fig. 3.5. We assume a two-dimensional quasicrystalline density $\rho(\mathbf{r})$ obtained, for instance, by averaging over all colloidal positions and consider isolated density modes of this density. At first, we perform a Fourier transformation of the colloidal density $\rho(\mathbf{r})$ to obtain $\tilde{\rho}(\mathbf{r})$. Then we extract an isolated density mode by performing an inverse Fourier transformation on a single pair of peaks in $\tilde{\rho}(\mathbf{r})$. This reveals the location of dislocations whose Burgers vectors possess contributions to the mode direction. In chapter 5, we will apply this analysis to our epitaxially grown colloidal structures. By collecting mode informations from every layer we are able to follow the three-dimensional course of dislocations originally induced by the substrate.

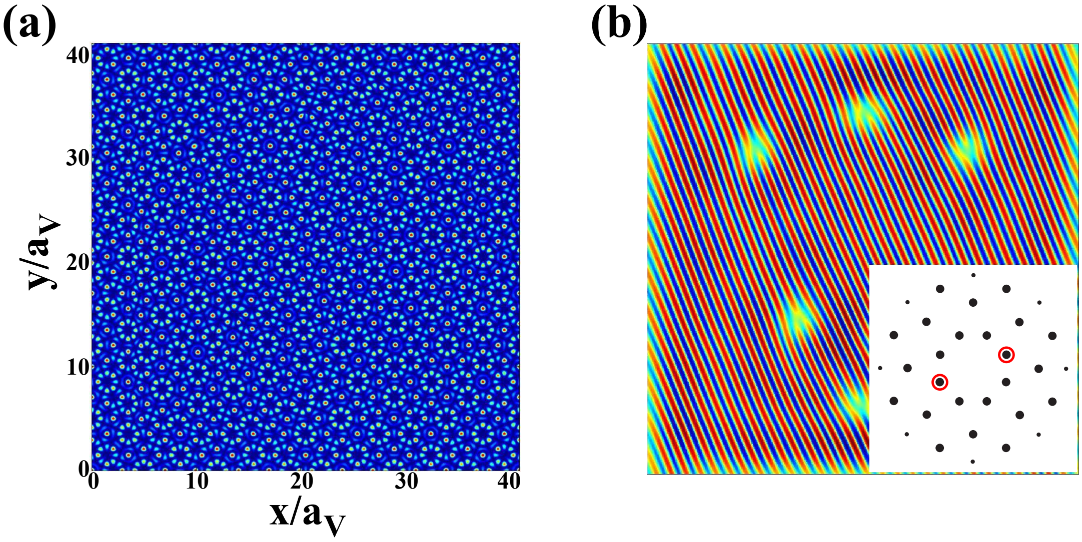

Figure 3.5.: (a) Real space pattern of an octagonal laser intensity field with dislocations. The dislocations are incorporated following the description from section 2.3. In real space, the dislocations are difficult to identify in this pattern. However, isolated density modes can be employed to localize the dislocations and to determine their Burgers vectors. (b) Pattern denoting one isolated mode of the field shown in (a). In this presentation, the dislocations can easily be identified. The pattern that shows one isolated mode is obtained by an inverse Fourier transformation of two selected peaks of the Fourier transformed density $\tilde{\rho}$ (see inset where the selected peaks are marked by red circles). Figure is adapted from [D].

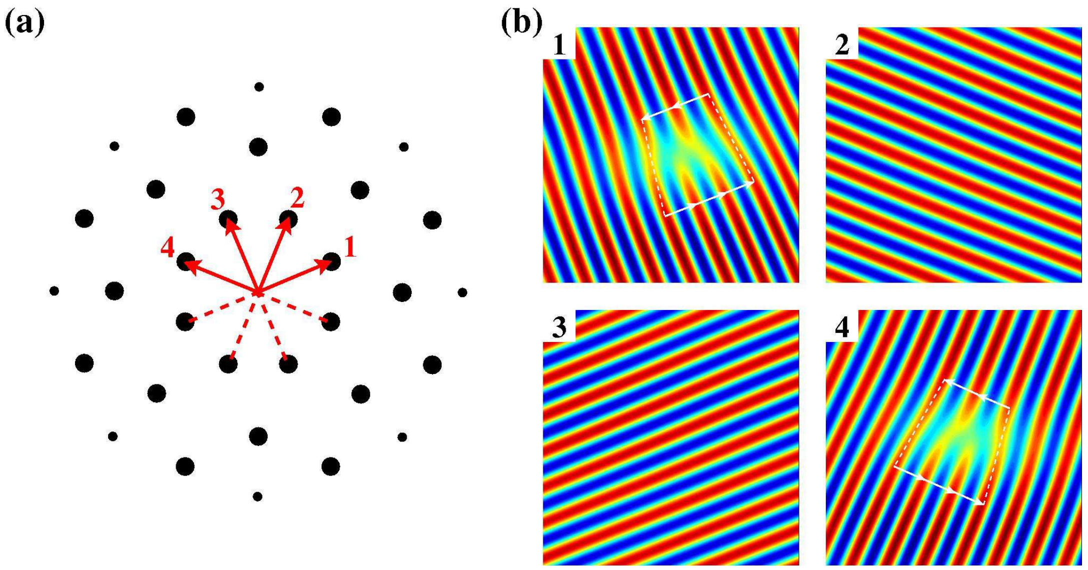

Figure 3.6.: (a) Fourier transform of the density of an octagonal intensity field. The respective mode directions are indicated by red arrows. (b) All four density modes around a dislocation. The dislocation is visible in modes 1 and 4. In order to obtain the winding number, we traverse the dislocation core counterclockwise and count the net amount of crossed stripes in mode direction. Therefore, the winding numbers for this dislocation are $\mathbf{n} = (1,\, 0,\, 0,\, -1)$.

In addition, it is possible to calculate the topological charge, the Burgers vector $(\mathbf{\Delta u},\, \mathbf{\Delta w})$, of a dislocation as well. In every mode a so-called winding number n_i is determined by counting the net displacement of stripes in a loop around the dislocation core. This leads to a vector of winding numbers $\mathbf{n}$ with D components, where D is the rank of the crystal, and subsequently to a system of D equations

$$2\pi\mathbf{n} = \begin{pmatrix}\tilde{\mathbf{G}}_0 & \tilde{\mathbf{G}}_1 & \dots & \tilde{\mathbf{G}}_D\end{pmatrix}\begin{pmatrix}\mathbf{\Delta u}\\ \mathbf{\Delta w}\end{pmatrix}. \tag{3.10}$$

In Eq. (3.10) $\tilde{\mathbf{G}}_i$ denotes the D-dimensional reciprocal vector $\tilde{\mathbf{G}}_i = \mathbf{G}_i \oplus \mathbf{G}_{ki \bmod N}$ associated with the respective peak in the Fourier image. An example to determine the winding numbers defining the Burgers vector is carried out in Fig. 3.6. The explained analysis has also been applied in nonlinear photonic quasicrystals to monitor phonon and phasonic strain relaxation in relationship with defects [245, 269]. Note that the described procedure is sensitive to the size of the filter. In particular, if $\rho(\mathbf{r})$ contains many dislocations, the associated peak in $\tilde{\rho}(\mathbf{r})$ is fuzzy. In order to detect all dislocations the filter radius has to be chosen appropriately. Therefore, we usually check whether a larger filter choice reveals differences or not.

> If you do not change direction, you may end up where you are heading.
>
> (*Siddhartha Gautama* 563 B.C. - 483 B.C.)

CHAPTER 4

Degrees of Freedom in Quasicrystalline Laser Fields for Colloids

Although quasicrystals originally emerged as a subject of metallurgy or crystallography, in the last years the study of mesoscopic quasicrystals became an active research field [105]. Compared to atomic systems, mesoscopic quasicrystals as for instance from colloidal suspensions possess the advantage of a feasible real space analysis. Therefore, certain properties like for example phasonic degrees of freedom can be observed with less effort from a mesoscopic perspective without losing fundamental insight. In this chapter, we consider a laser induced quasicrystal comprised of a monolayer of colloidal particles to explore ordering for different particle sizes. In addition, we derive trajectories for the colloidal particles when a phasonic drift is applied to the laser potential.

Colloidal particles are widely employed to study ordering, crystallization and dynamics in external potentials [196]. In a laser field, a force in the direction towards the highest light intensity acts on the colloids [223, 224]. Therefore, colloidal particles can be forced to form complex structures [225]. In particular, quasicrystalline ordering of the colloids can be obtained and studied by employing an interference pattern with quasicrystalline symmetry [131, 132]. The setup of the pioneering experiment of Mikhael *et al.* represents the central basis of this chapter and has also been enhanced to investigate tribological properties of sliding aperiodic and periodic monolayers [66, 68].

Several tunable parameters offer access to special quasicrystalline properties. While various adjustments of the polarization of the laser beams produce interference patterns of different local isomorphism (LI) class, the phases of the laser beams can be utilized to activate the phononic and phasonic modes [133]. Regarding the latter degree of freedom, Kromer *et al.* studied a monolayer of colloidal particles in a decagonal laser field when the phasonic displacement is changed [138, 139]. They presented a method to predict the trajectories of the colloids under a phasonic drift [138]. Here, we extend their approach for quasicrystals to all rotational symmetries of rank $D = 4$, i.e. octagonal and dodecagonal symmetry [A]. Moreover, we show on the basis of seven laser beams that the method can in principle be further generalized to interference patterns of rank $D = 6$ [B]. The higher rank increases the complexity to a four-dimensional phasonic space. Another degree of freedom in the suspension is given by the particle size or shape. Similar to settings of the laser polarization, different particle sizes result in orderings of different LI classes. Kählitz *et al.* considered needle- and rodlike particles subjected to a quasicrystalline interference pattern and determined the phase diagram [141, 142]. Here, we consider a two-dimensional system of hard discs in an quasicrystalline interference pattern with arbitrary rotational symmetry. We show how the ratio between the diameter of the particle and the length scale of the laser field influences the ordering. Degenerate quasicrystalline patterns of different LI class yet identical rotational symmetry to the laser field are observed. This behavior is reminiscent of molecular deposition on atomic quasicrystalline surfaces [270].

The chapter is divided into four parts. In the first one, the properties of the quasicrystalline interference pattern are briefly reviewed. Thereby, we focus on explaining the tunable parameters to access the degrees of freedom considered in the subsequent sections. In the second part, we study colloids with finite diameter subjected to a decagonal laser field and estimate a similar behavior as observed for molecular ordering on atomic surfaces. In the third part, we extend the previous work of Kromer *et al.* by analyzing trajectories occurring for colloids in octagonal, dodecagonal and tetradecagonal laser fields with a phasonic drift. Finally, we conclude in section 4.4.

4.1. Magnifold of interference patterns

In this section, we introduce the experimental setup of Mikhael *et al.* [132]. A single laser beam is split up in N beams of equal power. These are arranged in a symmetric manner and focused onto the sample cell containing the colloidal suspension. The setting is displayed for the case of five beams in Fig. 4.1 (a). In the sample plane, the beams interfere leading to intensity patterns of $2N$-fold rotational symmetry if N is odd an N-fold if N is even. Therefore, crystalline as well as quasicrystalline patterns can be produced [135, 137]. The resulting intensity pattern is given by the square of the sum over the electric fields of the beams and averaging over one period $T = 2\pi/\omega$ of the pattern that oscillates with the circular frequency ω of the light (see also [131]):

$$
\begin{aligned}
V(\mathbf{r}) &= -\int_0^T dt \left\{ \sum_{i=0}^{N-1} \mathbf{E}_i \cos[\mathbf{G}_i \cdot \mathbf{r} + \varphi_i + \omega t] \right\}^2 \\
&= -\int_0^T dt \sum_{i=0}^{N-1} \sum_{j=0}^{N-1} \mathbf{E}_i \cdot \mathbf{E}_j \{ \cos[(\mathbf{G}_i - \mathbf{G}_j) \cdot \mathbf{r} + \varphi_i - \varphi_j] \\
&\qquad\qquad + \cos[(\mathbf{G}_i + \mathbf{G}_j) \cdot \mathbf{r} + \varphi_j + \varphi_j + 2\omega t] \} \\
&\propto \sum_{i=0}^{N-1} \sum_{j=0}^{N-1} \mathbf{E}_i \cdot \mathbf{E}_j \{ \cos[(\mathbf{G}_i - \mathbf{G}_j) \cdot \mathbf{r} + \varphi_i - \varphi_j] + \mathrm{const}\,, \qquad (4.1)
\end{aligned}
$$

where φ_j denotes the phase of a laser beam, $\mathbf{r} = (x, y)$ is a position within the sample plane and $\mathbf{G}_j$ are the projected wave vectors onto that plane. The polarization vectors $\mathbf{E}_j$ have to be chosen in a symmetric way as for example illustrated in Fig. 4.1 (a), where ψ is the angle to the radial reference direction of the respective beam.

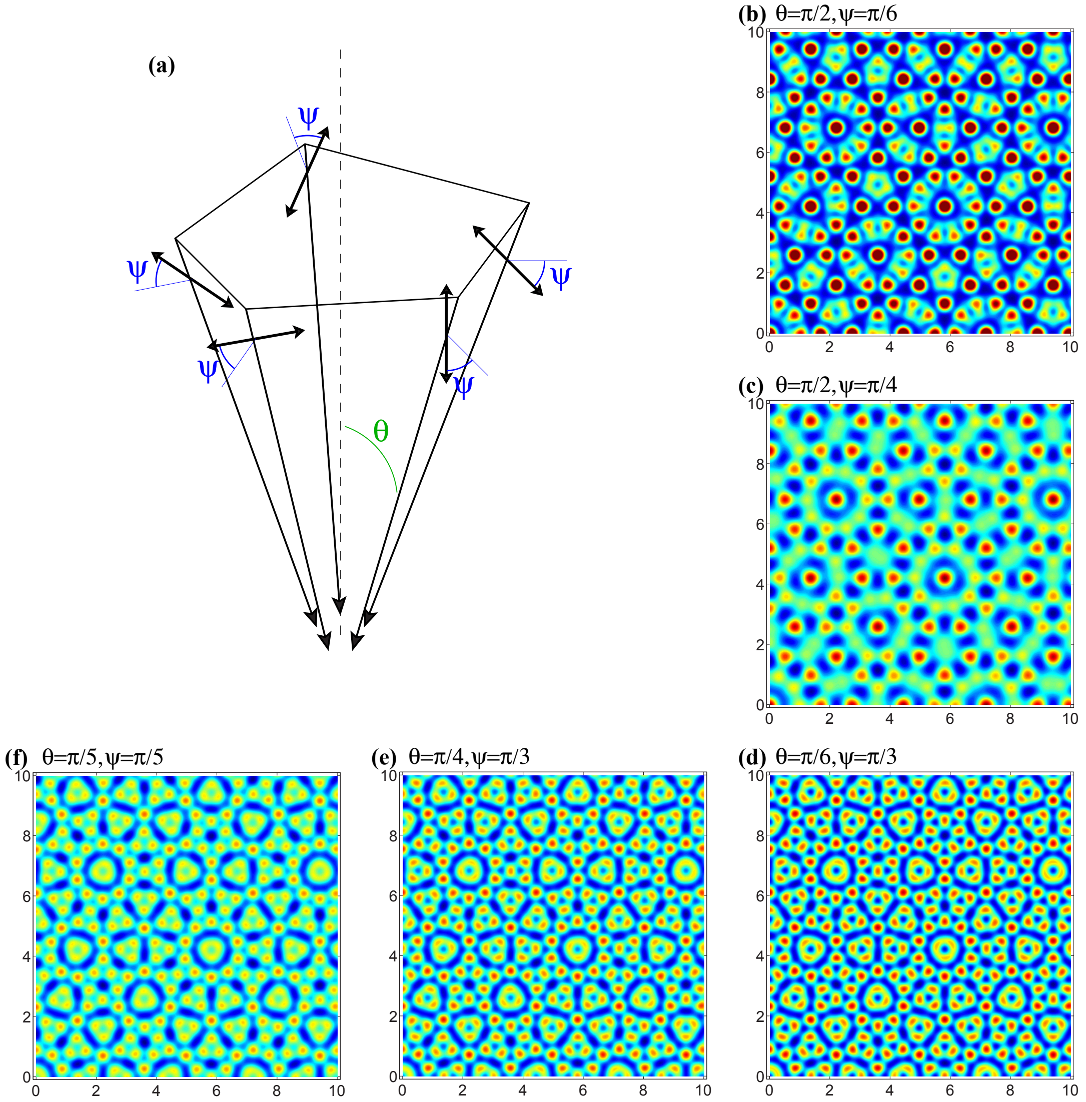

Figure 4.1.: Experimental setup for decagonal intensity fields (cf. [133]). (a) The laser beams as well as their polarization vectors are arranged in a symmetric manner to produce quasicrystalline intensity fields with perfect tenfold rotational symmetry. θ denotes the opening angle between the beams and the axis orthogonal to the sample plane, while ψ defines the polarization to the radial reference direction. (b)-(f) Examples of intensity fields for different polarizations and opening angles. Every field belongs to a different LI class. Coordinates are given in units of the length scale $a_V = 2\pi/G$. The color coding in all plots is identical to reveal subtle differences in intensities.

Together with the opening angle θ, tuning of ψ and θ allows to obtain patterns of different

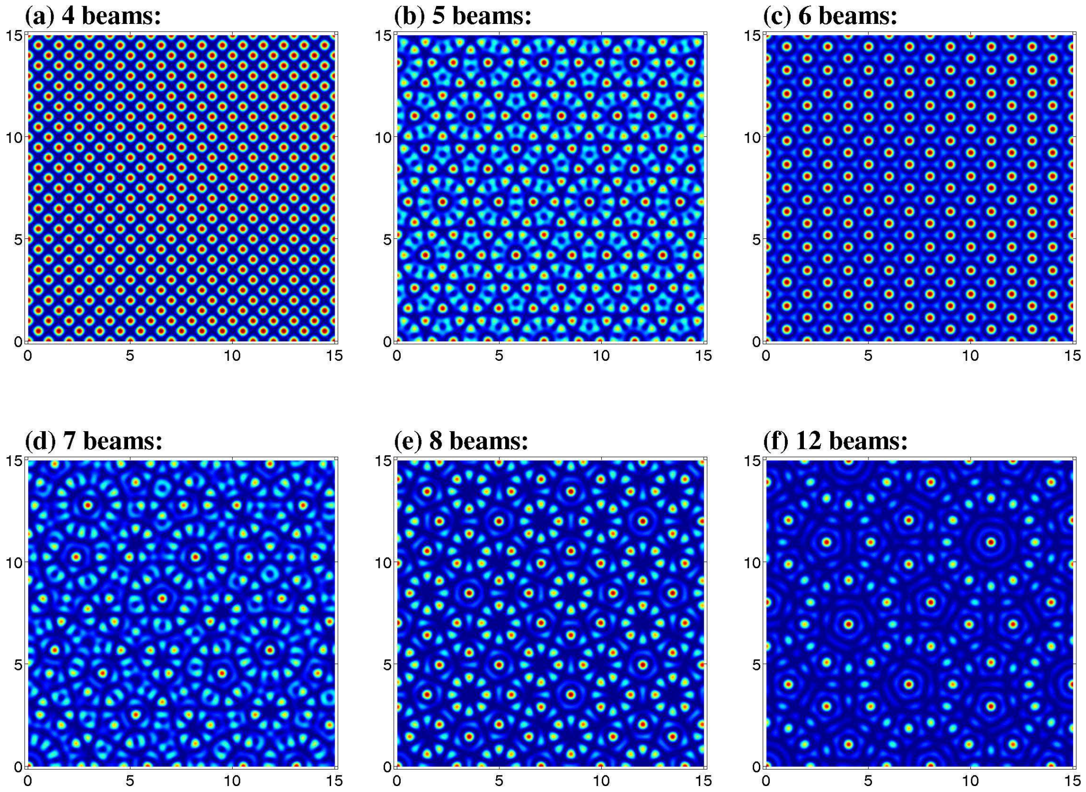
(a) 4 beams: **(b) 5 beams:** **(c) 6 beams:**

(d) 7 beams: **(e) 8 beams:** **(f) 12 beams:**

Figure 4.2.: Intensity fields of interference patterns produced by a varying number of beams (cf. [137]). Both, crystalline and quasicrystalline symmetries are possible. Coordinates are given in units of the length scale $a_V = 2\pi/G$

LI classes within one rotational symmetry defined by N. To demonstrate the possibilities, a small collection of decagonal patterns has been assembled in Fig. 4.1 (b)-(f). In section 4.2, we illustrate an alternative approach to the adjustment of the polarization in order to influence the LI class of the ordered colloidal suspension.

Yet, a configuration in which all beams possess an identical polarization is more feasible in experiment. Such a configuration has the consequence that for a finite opening angle $\theta > 0$, the intensity pattern would cease to exhibit perfect rotational symmetry. However, since θ is usually very small, we can still assume the limit $\theta \to 0$ in Eq. (4.1), which yields

$$V(\mathbf{r}) = -\frac{V_0}{N^2} \sum_{i=0}^{N-1} \sum_{j=0}^{N-1} \cos[(\mathbf{G}_i - \mathbf{G}_j) \cdot \mathbf{r} + \varphi_i - \varphi_j] \,. \tag{4.2}$$

The prefactor has been chosen such that the deepest minimum at $\mathbf{r} = (0, 0)$, at the same time a or rather the center of perfect rotational symmetry, has the value $-V_0$. Examples for different N are provided in Fig. 4.2. There, all phases φ_j have been set to zero. A different choice can induce phasonic excitations as we will address in section 4.3. In the following sections, Eq. (4.2) serves as initial point to describe the potential of colloidal particles in laser fields.

4.2. Colloids with finite diameter

Molecular deposition on quasicrystalline atomic surfaces can lead to monolayers with quasicrystalline symmetry. However, the scaling difference between the molecule and the atomic adsorption sites can give rise to a different class of symmetry structure in the adsorbed film in comparison to the surface. For example, fullerene C_{60} adsorbs at separated Fe atoms on icosahedral Al–Cu–Fe while further deposition leads to the formation of a degenerated quasicrystalline lattice [270]. In order to model the adsorption of particles with different size on a quasicrystalline substrate, we investigate the energy landscape of a spherical colloidal particle with finite diameter σ in an intensity field of N interfering laser beams. This can be described by integrating over the particle area:

$$V_\sigma(\mathbf{r}_0) = \frac{4}{\pi\sigma^2} \int\limits_0^{\sigma/2} l \, dl \int\limits_0^{2\pi} d\phi \, V(\mathbf{r}_0 + l\mathbf{e}_l(\phi)) \,. \tag{4.3}$$

Note that an integration over the particle volume will lead to similar results. For the following calculations it is convenient to rewrite the potential for pointlike particles in Eq. (4.2). As illustrated in Fig. 4.3 for the decagonal case, instead of a double sum over pairs of projected wave vectors $\mathbf{G}_j$ the potential can be expressed as a series of $k \in \lfloor N/2 \rfloor$ starlike patterns of $j \in N$ wave vectors leading to

$$V(\mathbf{r}) = -\frac{V_0}{N^2} \sum_{j=0}^{\lfloor N/2 \rfloor} A_{j,N} \sum_{k=0}^{N-1} \cos[\mathbf{\Delta G}_{jk} \cdot \mathbf{r} + \Delta\varphi_{jk}] \,, \tag{4.4}$$

where $\mathbf{\Delta G}_{jk} = \mathbf{G}_k - \mathbf{G}_{k+j}$ and $\Delta\varphi_{jk} = \varphi_k - \varphi_{k+j}$. The prefactor $A_{j,N}$ depends on the symmetry and is given by

$$A_{j,N} = \begin{cases} 1 & \text{if } j = 0 \vee j = N/2 \\ 2 & \text{otherwise} \end{cases} \,. \tag{4.5}$$

If we insert the new formula for the laser potential of pointlike particles in Eq. (4.3), we obtain

$$V_\sigma(\mathbf{r}_0) = -\frac{V_0}{N^2} \frac{4}{\pi\sigma^2} \int\limits_0^{\sigma/2} l \, dl \int\limits_0^{2\pi} d\phi \sum_{j=0}^{\lfloor N/2 \rfloor} A_{j,N} \sum_{k=0}^{N-1} \cos[\mathbf{\Delta G}_{jk} \cdot (\mathbf{r}_0 + l\mathbf{e}_l(\phi)) + \Delta\varphi_{jk}] \,. \tag{4.6}$$

We consider the cos-term and due to symmetry extract the pointlike contribution from the integration by

$$\frac{4}{\pi\sigma}\int_0^{\sigma/2} l\,dl \int_0^{2\pi} d\phi\, \cos[\mathbf{\Delta G}_{jk}\cdot(\mathbf{r}_0 + l\mathbf{e}_l(\phi)) + \Delta\varphi_{jk}] \tag{4.7}$$

$$= \frac{2}{\pi\sigma}\Bigg\{ \exp[-i(\mathbf{\Delta G}_{jk}\cdot\mathbf{r}_0 + \Delta\varphi_{jk})] \int_0^{\sigma/2} l\,dl \int_0^{2\pi} d\phi\, \exp[-il\mathbf{\Delta G}_{jk}\cdot\mathbf{e}_l(\phi)] \tag{4.8}$$

$$+ \exp[i(\mathbf{\Delta G}_{jk}\cdot\mathbf{r}_0 + \Delta\varphi_{jk})] \int_0^{\sigma/2} l\,dl \int_0^{2\pi} d\phi\, \exp[il\mathbf{\Delta G}_{jk}\cdot\mathbf{e}_l(\phi)] \Bigg\} \tag{4.9}$$

$$= \cos[\mathbf{\Delta G}_{jk}\cdot\mathbf{r}_0 + \Delta\varphi_{jk}]\; I(\mathbf{\Delta G}_{jk})\,, \tag{4.10}$$

where

$$I(\mathbf{\Delta G}_{jk}) = \frac{4}{\pi\sigma^2}\int_0^{\sigma/2} l\,dl \int_0^{2\pi} d\phi\, \exp[il\mathbf{\Delta G}_{jk}\cdot\mathbf{e}_l(\phi)] \tag{4.11}$$

remains to be calculated.

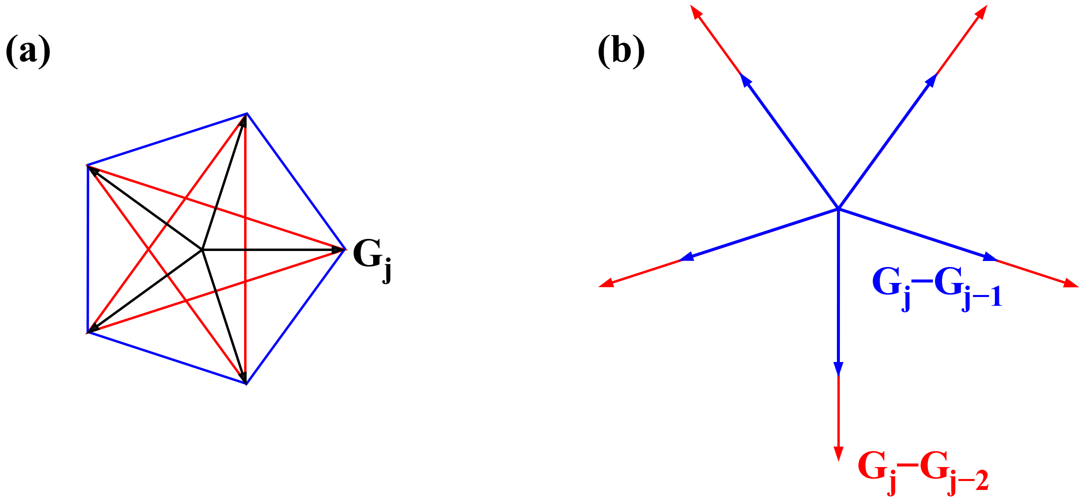

Figure 4.3.: The differences of the projected wave vectors $\mathbf{G}_j$ in the pentagonal arrangement can be expressed by two pentagonal starlike patterns. The ratio between the stars is the golden mean τ.

We can exploit the symmetric arrangement as each wave vector $\mathbf{\Delta G}_{jk}$ in the starlike pattern j has the same length ΔG_j and the integration runs from 0 to 2π. With $\mathbf{\Delta G}_{jk} \cdot \mathbf{e}_l(\phi) = \Delta G_j \cos[2\pi k/N + \alpha_j - \phi] = \Delta G_j \cos\vartheta$ Eq. (4.11) becomes

$$I(\Delta G_j) = \frac{4}{\pi\sigma^2} \int\limits_0^{\sigma/2} l\, dl \int\limits_0^{2\pi} d\vartheta\ \exp[il\Delta G_j \cos\vartheta]\,. \tag{4.12}$$

Upon substituting $\omega = \Delta G_j l$ and $\Omega = \Delta G_j \sigma/2$ as well as incorporating Bessel functions of the first kind $J_n(x)$ the integration is finally carried out to yield

$$I(\Omega) = \frac{1}{\pi\Omega^2} \int\limits_0^{\Omega} \omega\, d\omega \int\limits_0^{2\pi} d\vartheta\ \exp[i\omega\cos\vartheta] = \frac{2}{\Omega^2} \int\limits_0^{\Omega} \omega J_0(\omega) d\omega = \frac{2}{\Omega} J_1(\Omega)\,. \tag{4.13}$$

Therefore, we can express the laser potential for finite particle size as a modulation of the pointlike particle potential

$$V_\sigma(\mathbf{r_0}) = -\frac{V_0}{N^2} \sum_{j=0}^{\lfloor N/2 \rfloor} I(\Delta G_j \sigma/2)\ A_{j,N} \sum_{k=0}^{N-1} \cos[\mathbf{\Delta G}_{jk} \cdot \mathbf{r}_0 + \Delta\varphi_{jk}]\,. \tag{4.14}$$

In contrast to the pointlike case, where the potential can be written as an expansion of equally weighted starlike patterns of projected wave vectors, the respective weights for the finite diameter case are nonuniform. Especially the sign may be different which can give rise to further variations in the potential. In Fig. 4.4 we have assembled a collection of patterns for increasing diameter σ. Note that due to the decay in $I(\Omega)$ the contrast in the potentials decreases significantly with σ. We adjusted the color coding to enhance visibility again. Nevertheless, in a real system with high enough density the particle-particle interactions would become more dominant again with increasing σ, unless the laser intensity is increased accordingly to counter balance this effect. Yet, if the decay in $I(\Omega)$ can be neglected because of the overall intensity, its oscillation due to the Bessel functions will result in the repetition of to some extend similar patterns for increasing diameter. Preliminary results from Brownian dynamics simulations conducted by F. Rühle confirm these predictions.

As another aspect, we want to point out the structural similarity to the intensity fields with different polarizations from Fig. 4.1. For instance, the case $\sigma = 0.64\, a_V$ resembles a polarization defined by $\theta = \pi/2$ and $\psi = \pi/4$, while the case $\sigma = 0.74\, a_V$ almost corresponds to a polarization with $\theta = \pi/5$ and $\psi = \pi/5$. This further illustrates the versatility of quasicrystalline structures that can be induced in one colloidal suspension by interfering laser beams.

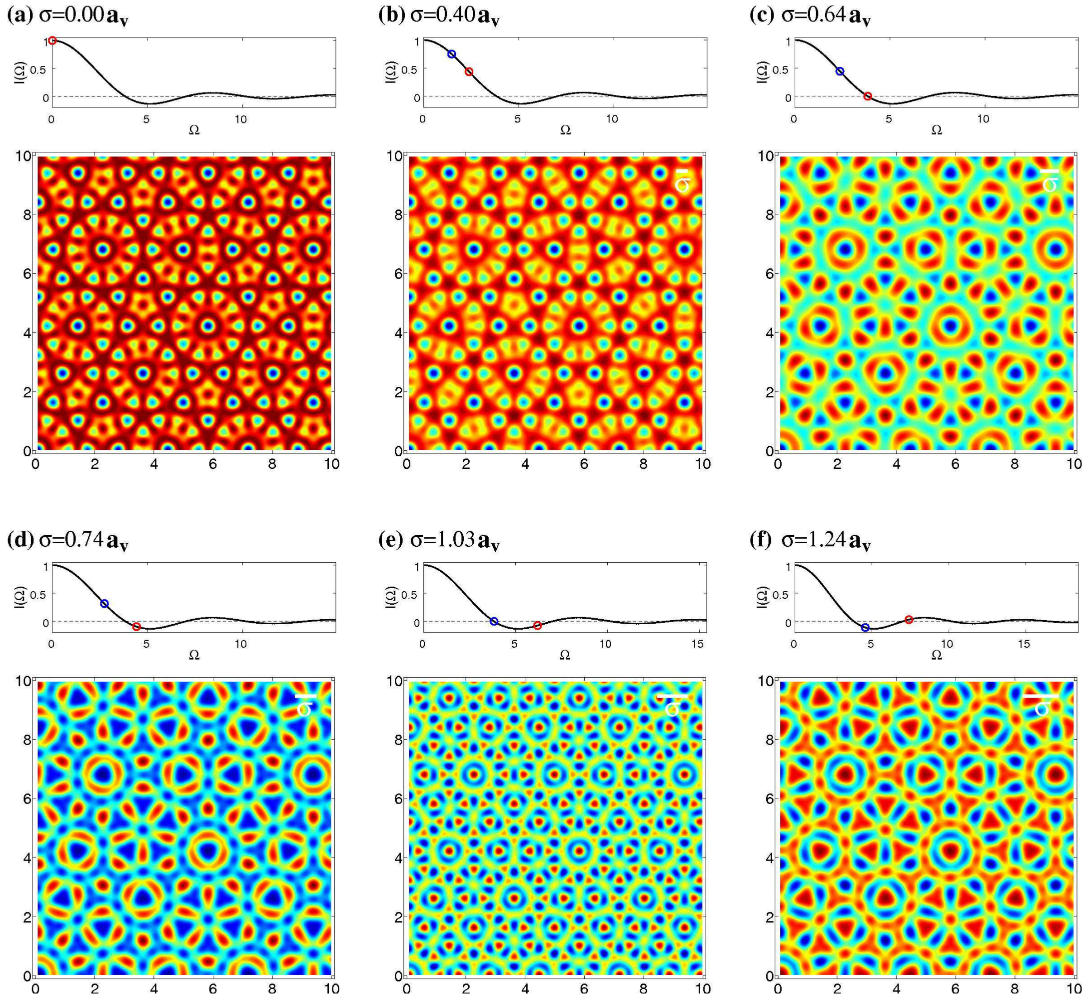

Figure 4.4.: The decagonal laser potential for spherical colloids with different diameter σ. The respective modulation value $I(\Omega)$ for each star is indicated in the top panel. The color of the dots corresponds to the color code in Figure 4.3. In the panel below, the potential $V_\sigma(\mathbf{r}_0)$ is displayed with units in a_V. For visibility the contrast has been corrected to counter balance the averaging of the integration. The bar in the top right corner represents the diameter of a colloid. As σ is increased the minima become at first more pronounced before changing sign. All patterns belong to different *local isomorphism* classes. In addition, they exhibit a certain self-similarity. Discounting the inversion of minima and maxima in the potential, the patterns in (c) and (e) as well as in (d) and (f) respectively seem to differ only in the length scale.

4.3. Trajectories of colloidal particles under phasonic drift

Phasons are additional hydrodynamic modes of quasicrystals [238]. Despite the fact that the discovery of quasicrystals already dates back thirty years, phasons remain an active and controversial topic of research [246, C]. Although today thermal excitations related to phason flips can experimentally be detected in atomic quasicrystalline systems [244], a colloidal system resembles a feasible approach to investigate the complexity of the phasonic modes.

In this section we analyze the behavior of colloids in quasicrystalline laser fields with octagonal, dodecagonal and tetradecagonal symmetry to which, in addition, a phasonic drift is applied. Thereby we expand a method originally developed by Kromer *et al.* on the basis of the decagonal laser field [138]. While the influence of a phasonic drift on the colloidal dynamics for the case $V_0 \approx k_B T$ has been investigated as well [139], we consider the limit of high potential strengths or low temperatures, e.g., $V_0 \gg k_B T$, such that all colloids are always located in local minima of the external potential. Under these conditions, the colloids serve as tracer particles to visualize phasonic excitations.

While in a periodic crystal many properties can be deduced from a single unit cell [14, 237], Kromer *et al.* showed for this quasicrystalline system that every colloid can be mapped into characteristic areas of reduced phononic and phasonic displacement [138]. Here, we generalize their method further. In section 4.3.1, we derive the colloidal trajectories for phasonic drifts in octagonal and dodecagonal symmetry. Therefore, we demonstrate the applicability of the approach to all symmetries of rank $D = 4$. In section 4.3.2, we show on the basis of the tetradecagonal laser field that the method can even be extended to quasicrystalline fields of rank $D = 6$.

The contents of this section have undergone external revision and are published in [A] for $D = 4$ and in [271, B] for $D = 6$.

4.3.1. Interference pattern of rank four

In this section we study the colloidal suspension exposed to a quasicrystalline laser interference pattern of rank $D = 4$ in the limit of high intensities while a phasonic drift is applied. The characteristic areas for octagonal and dodecagonal rotational symmetry are determined and the resulting colloidal trajectories derived. We observe similar types of trajectories as in the decagonal case [138].

Phasonic drifts

A phasonic drift can be incorporated into the potential of Eq. (4.2) for the interference patterns by tuning the phases φ_j of the laser beams. These phases can be parameterized in accordance with [232, 238] to

$$\varphi_j = \mathbf{G}_j \cdot \mathbf{u} + \mathbf{G}_{kj \bmod N} \cdot \mathbf{w} + \gamma/N \tag{4.15}$$

where we use $k = 3$ for $N = 8$ and $k = 5$ for $N = 12$. The vector $\mathbf{u} = (u_x, u_y)$ describes the phononic and $\mathbf{w} = (w_x, w_y)$ the phasonic displacement. In contrast to $\mathbf{u}$ and $\mathbf{w}$, the global phase γ is not a hydrodynamic variable and vanishes in the interference patterns. We denote a potential with a phasonic displacement $\mathbf{w}$ by $V_{\mathbf{w}}(\mathbf{r})$. We apply a phasonic drift to the potential, i.e., the phasonic displacement is changed at a constant rate in time. The effect of such a drift is illustrated in Fig. 4.5. Initially the colloid resides inside the minimum. Upon increasing $\mathbf{w}$ the depth of the minimum decreases. At some point, the minimum has completely vanished, while in the vicinity a new minimum is emerging. Finally, the colloid slides to the new site. Since the applied phasonic drift is globally applied, it induces rather complex trajectories comprised of such particle jumps throughout the sample.

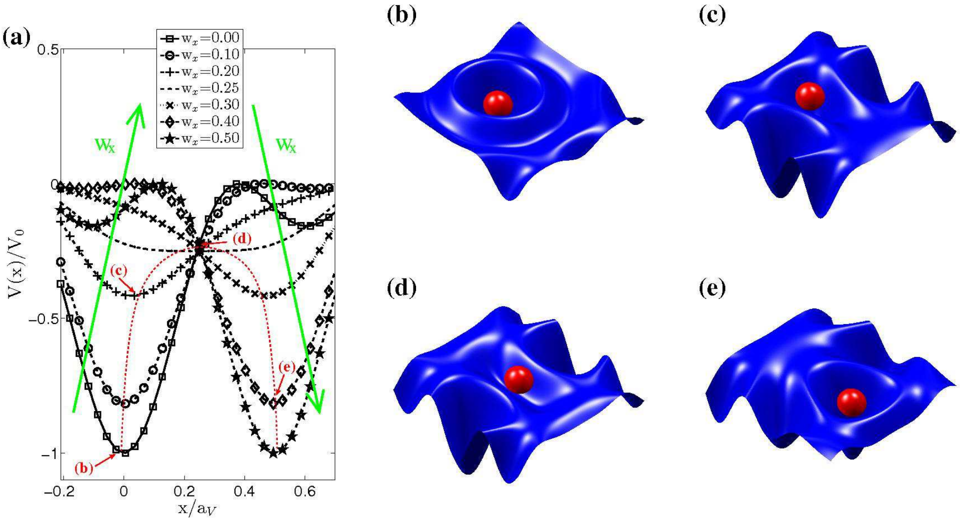

Figure 4.5.: (a) Cross section $y = 0$ of the octagonal laser potential for increasing values of the phasonic displacement w_x. The applied phasonic drift causes the local minimum to gradually disappear and a new one to appear in the vicinity. Due to this change in the potential landscape colloidal transitions occur as slides from one vanishing minimum to another growing one. (b)-(e) Illustrations of typical stages of such transitions corresponding to the red markings in (a).

Table 4.1.: The step lengths u_r and w_r of phononic and phasonic displacement vectors used in Eq. (4.16) such that there is no change to the laser field for all integer numbers n and m. In the last two columns the size of the characteristic areas is given.

Beams	u_r/a_V	w_r/a_V	$\delta u/2a_V$	$\delta w/2a_V$
5	$\frac{2}{5}n+\left(\frac{1}{5}+\frac{1}{\sqrt{5}}\right)m$	$\frac{2}{5}n+\left(\frac{1}{5}-\frac{1}{\sqrt{5}}\right)m$	$(1+\sqrt{5})/10$	$(1+\sqrt{5})/10$
10	$\frac{2}{\sqrt{5}}n+\left(1+\frac{1}{\sqrt{5}}\right)m$	$-\frac{2}{\sqrt{5}}n+\left(1-\frac{1}{\sqrt{5}}\right)m$	$\frac{1}{2}\left(1+\frac{1}{\sqrt{5}}\right)$	$\frac{1}{2}\left(1+\frac{1}{\sqrt{5}}\right)$
8	$\frac{1}{2}n+\frac{1}{\sqrt{2}}m$	$\frac{1}{2}n-\frac{1}{\sqrt{2}}m$	$\frac{1}{2\sqrt{2}}$	$\frac{1}{2}\left(\frac{1}{2}+\frac{1}{\sqrt{2}}\right)$
12	$n+\frac{1}{\sqrt{3}}m$	$n-\frac{1}{\sqrt{3}}m$	$\frac{1}{2}$	$\frac{1}{2}\left(1+\frac{1}{\sqrt{3}}\right)$

Characteristic areas

Although a quasicrystal does not possess a unit cell to derive global properties, all colloidal positions can be mapped onto particles inside characteristic areas of small phononic and phasonic displacements. The reason is that there are combinations of phononic and phasonic displacements $\mathbf{\Delta u}$ and $\mathbf{\Delta w}$ that do not change the potential, i.e., $V_{\mathbf{w}}(\mathbf{r}) = V_{\mathbf{w}+\mathbf{\Delta w}}(\mathbf{r}+\mathbf{\Delta u})$. For example, for $j = 0, 1, \ldots, M$ displacements with

$$\begin{aligned} \mathbf{\Delta u} &= \left(u_r \cos\left[2\pi j/M\right],\, u_r \sin\left[2\pi j/M\right]\right) \\ \text{and } \mathbf{\Delta w} &= \left(w_r \cos\left[2\pi k j/M\right],\, w_r \sin\left[2\pi k j/M\right]\right) \end{aligned} \tag{4.16}$$

change the differences between phases $\varphi_j - \varphi_k$ in Eq. (4.2) only by integer multiples of 2π if the step lengths u_r and w_r are chosen appropriately (see Table 4.1 for possible values). The number of symmetry axes is $M = 2N$ for an odd number of beams and $M = N$ for an even one.

By using suitable combinations obeying Eq. (4.16), we can map a colloid at position $\mathbf{r}$ in a potential $V_{\mathbf{w}}(\mathbf{r})$ onto a particle at reduced position $\mathbf{r}^{(\mathrm{red})} = \mathbf{r} - \mathbf{\Delta u}$ in a potential $V_{\mathbf{w}^{(\mathrm{red})}}(\mathbf{r}^{(\mathrm{red})})$ with reduced phasonic displacement $\mathbf{w}^{(\mathrm{red})} = \mathbf{w} + \mathbf{\Delta w}$ within characteristic areas whose size is determined as follows: We first consider the mapping along a phononic direction given by $\mathbf{e}_j = (\cos[2\pi j/M], \sin[2\pi j/M])$ and its phasonic counterpart. The sizes of the characteristic intervals δu and δw have to be chosen at least such that the two-dimensional subspace spanned by the considered phononic and phasonic directions can be completely covered with rectangles of dimensions δu and δw that are displaced by $\mathbf{\Delta u}$ in phononic and $\mathbf{\Delta w}$ in phasonic direction. We list the appropriate interval lengths δu and δw in Table 4.1. Considering all symmetry directions, we end up on reduced values $\mathbf{r}^{(\mathrm{red})}$ and $\mathbf{w}^{(\mathrm{red})}$ within areas of polygonal shape defined by

$$\left|\mathbf{r}^{(\mathrm{red})} \cdot \mathbf{e}_j\right| \leq \frac{\delta u}{2a_V} \text{ and } \left|\mathbf{w}^{(\mathrm{red})} \cdot \mathbf{e}_j\right| \leq \frac{\delta w}{2a_V} \tag{4.17}$$

for all $j = 1, \ldots, M$ (see also black polygons in Fig. 4.6).

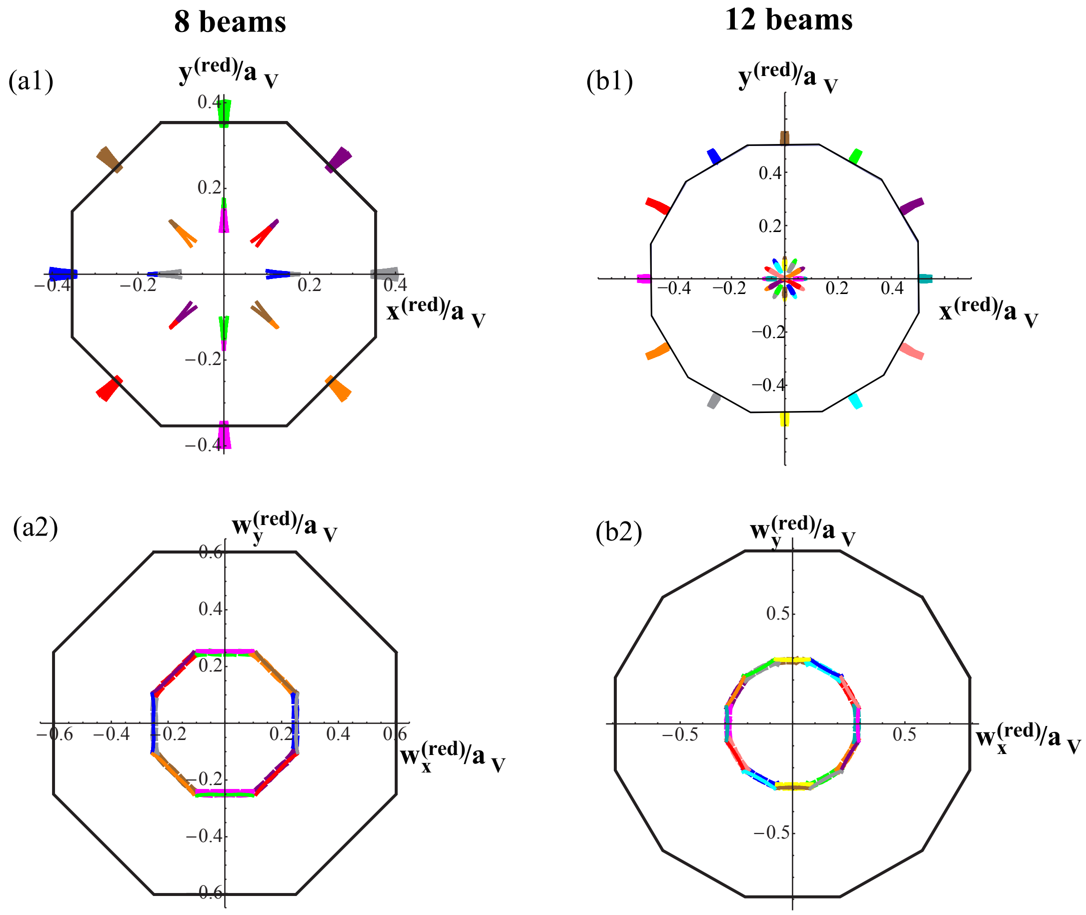

Figure 4.6.: Characteristic areas for octagonal and dodecagonal laser field (cf. [A]). The areas of reduced positions $\mathbf{r}^{(\mathrm{red})}$ (a1,b1) and phasonic displacements $\mathbf{w}^{(\mathrm{red})}$ (a2,b2) are depicted for different laser potentials. The characteristic areas are marked by black polygons. The threshold value of $\mathbf{w}^{(\mathrm{red})}$ where a minimum disappears is shown by solid colored lines drawn on top. If this threshold value is surpassed, the colloid slides into a new minimum whose position is marked by the outermost colored spots in the diagrams for $\mathbf{r}^{(\mathrm{red})}$. Note that the reduced positions are drawn with the same color as the associated reduced phasonic displacements. Afterwards $\mathbf{r}^{(\mathrm{red})}$ and $\mathbf{w}^{(\mathrm{red})}$ are mapped back into the characteristic areas as illustrated by the innermost colored dashed lines or spots that lie on the opposite site of the lines where the sliding started. The remapping ends exactly underneath the lines where a slide for opposite phasonic drift starts. Note that the mapping does not change the real position or the real phasonic displacement. Examples of colloidal paths within the diagrams are given in Fig. 4.7 and Fig. 4.8

To gain a complete understanding of the colloidal dynamics, it is sufficient to study the colloidal behavior within the characteristic areas. We follow the paths of colloids that are started at the origin for phasonic drifts in all directions. In Fig. 4.6, the important points of these trajectories are shown as described in more detail in the caption of the figure. Note the color is always the same for the reduced phononic displacement and its corresponding reduced position. Therefore, the color indicates in what direction a colloid is moving depending on the direction of the phasonic drift. A detailed description of the analysis for a laser field created by five beams is given in [138]. In the next section, we will show that the path of a colloid started at an arbitrary position can be predicted by using the diagrams shown in Fig. 4.6.

Colloidal trajectories

With the diagrams deduced in the previous section one can predict colloidal trajectories due to phasonic drifts. Similar to the decagonal case $N = 5$, we identify two types of trajectories: a straight path and a zig-zag path. Examples of trajectories caused by a phasonic drift in x-direction are given for $N = 8$ beams in Fig. 4.7 and for $N = 12$ in Fig. 4.8. Note that due to symmetry reasons a phasonic drift in y-direction leads to similar paths. The Figures are to be viewed columnwise as each column contains the description of a single trajectory. A trajectory depends on the starting value of $\mathbf{w}^{(\mathrm{red})}$. All initial conditions that lead to similar trajectories are marked by the crosshatched areas in Fig. 4.7. At the beginning, the colloidal position changes only gradually under increase of $\mathbf{w}$. The colloid remains firmly located in its local minimum. Yet at some point, $\mathbf{w}$ will reach a critical value such that the local minimum occupied by the colloid vanishes. Thus, the colloid slides to a new local minimum in the vicinity which appeared due to the phasonic drift. As a consequence of this transition, the position of the colloid $\mathbf{r}$ is now outside of the characteristic area. However, we can employ a suitable choice from Eq. (4.16) to map its reduced coordinate back inside the characteristic area by $\mathbf{r}^{(\mathrm{red})} = \mathbf{r}^{(\mathrm{red})} - \mathbf{\Delta u}$. Since a phononic displacement has to be accompanied by a phasonic one in order to leave the physical system invariant, $\mathbf{w}^{(\mathrm{red})}$ has to be updated by $\mathbf{w}^{(\mathrm{red})} = \mathbf{w}^{(\mathrm{red})} + \mathbf{\Delta w}$ as well. After this mapping, a new cycle of gradually vanishing minima, sliding colloids and again mapping to updated reduced quantities begins. We obtain a straight path if this procedure repeats after one slide and a zig-zag path in case it repeats after two slides.

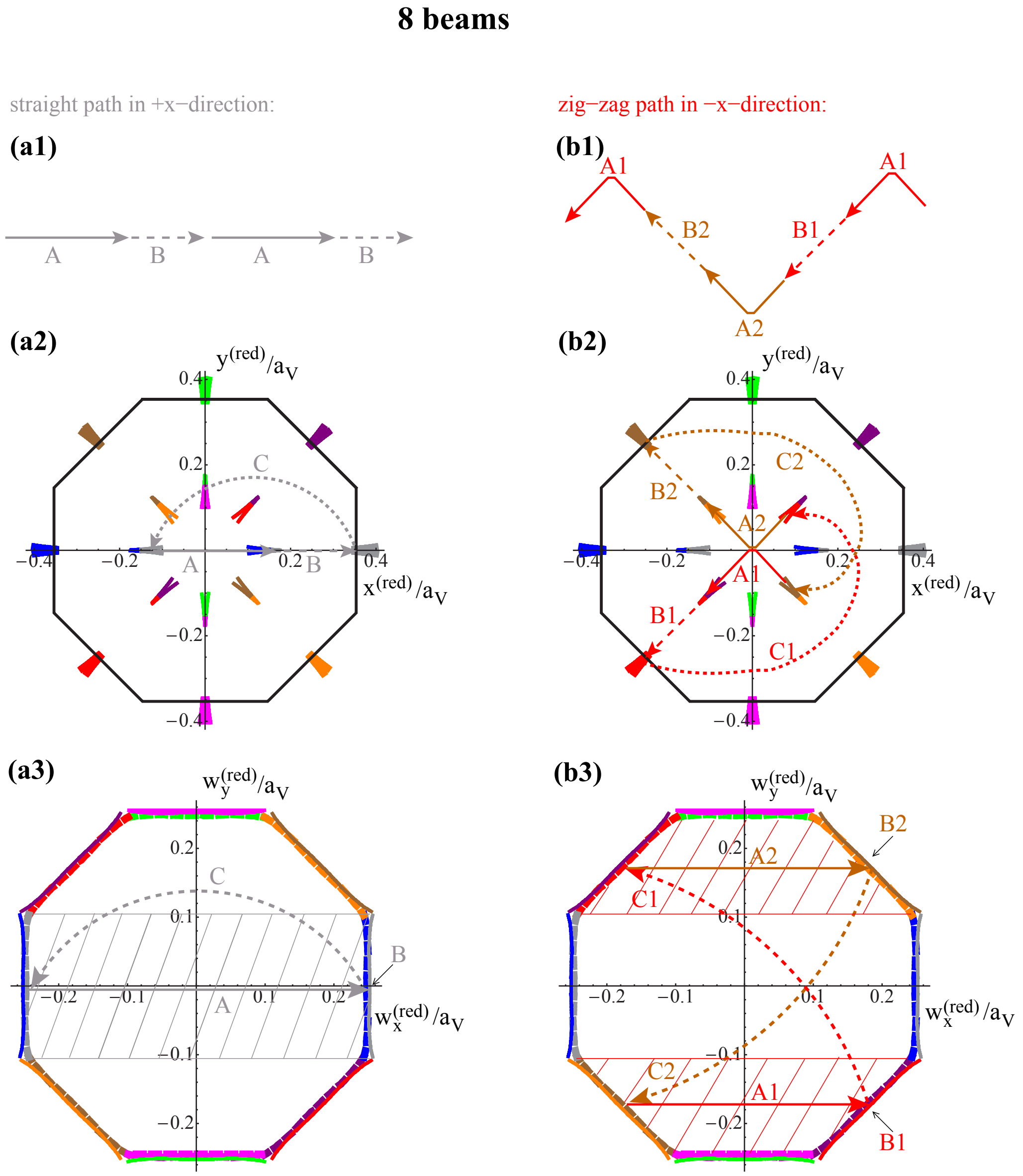

Figure 4.7.: A selection of colloidal trajectories in laser fields created by eight beams for a phasonic drift in x-direction (cf. [A]). For symmetry reasons, a phasonic drift in the y-direction causes analogue particle movements. In each column, a trajectory is shown that is typical for all colloids starting inside the crosshatched area. In the first row, the paths of the colloids are outlined, while in the second row, the corresponding reduced positions $\mathbf{r}^{(\mathrm{red})}$, and in the last row, the reduced phasonic displacements $\mathbf{w}^{(\mathrm{red})}$ are given. At the beginning, $\mathbf{r}^{(\mathrm{red})}$ changes only gradually in response to an increase of the phasonic displacement. When $\mathbf{w}^{(\mathrm{red})}$ reaches the colored solid border, the local minimum occupied by the colloid vanishes. As a result, the colloid slides into another local minimum depicted by the same color. After that $\mathbf{r}^{(\mathrm{red})}$ and $\mathbf{w}^{(\mathrm{red})}$ are mapped such that they are close to the origin and all steps are repeated for the new reduced quantities.

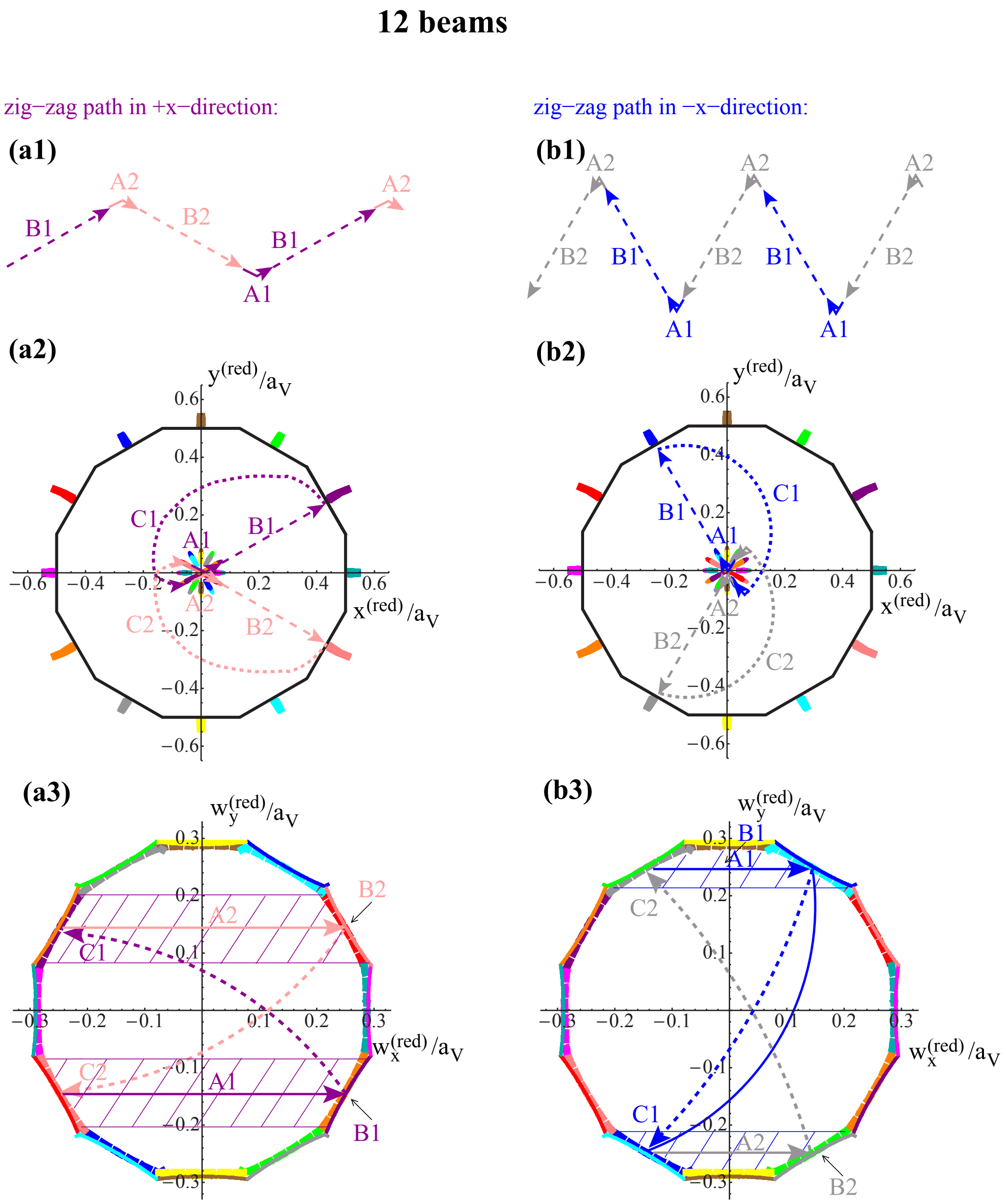

Figure 4.8.: A selection of colloidal trajectories in laser fields created by twelve beams for a phasonic drift in x-direction (cf. [A]). A phasonic drift in the y-direction causes analogue particle movements due to symmetry reasons. Each column represents a trajectory that is typical for all colloids starting inside the crosshatched area. The first row contains the paths of the colloids, the second row the corresponding reduced positions $\mathbf{r}^{(\mathrm{red})}$, and the last the reduced phasonic displacements $\mathbf{w}^{(\mathrm{red})}$. Similar to the case of eight beams, $\mathbf{r}^{(\mathrm{red})}$ changes only gradually at first in response to an increase of the phasonic displacement. When $\mathbf{w}^{(\mathrm{red})}$ reaches the colored solid border, the local minimum occupied by the colloid vanishes. Consequently, the colloid slides into another local minimum depicted by the same color. After that $\mathbf{r}^{(\mathrm{red})}$ and $\mathbf{w}^{(\mathrm{red})}$ are mapped such that they are close to the origin and all steps are repeated for the new reduced quantities.

4.3.2. Interference pattern of rank six

In the previous section, quasicrystalline interference patterns with octagonal and dodecagonal rotational symmetry were considered, which are all of rank $D = 4$. Here, we show on the basis of the tetradecagonal symmetry how the method of Kromer *et al.* can be further extended to laser fields with rank $D = 6$. Compared to the $D = 4$ case, the additional phasonic modes lead to a more complex behavior and we identify several new types of colloidal trajectories.

Characteristic areas

As a consequence of the tetradecagonal symmetry the parameterization from Eq. (4.15) has to be adjusted:

$$\varphi_j = \mathbf{G}_j \cdot \mathbf{u} + \mathbf{G}_{3j \bmod 7} \cdot \mathbf{v} + \mathbf{G}_{5j \bmod 7} \cdot \mathbf{w}\,, \tag{4.18}$$

where $\mathbf{u} = (u_x,\, u_y)$ denotes the phononic, $\mathbf{v} = (v_x,\, v_y)$ and $\mathbf{w} = (w_x,\, w_y)$ the phasonic displacements. Let us note that compared to a $D = 4$ quasicrystal an additional phasonic displacement vector is required.

As demonstrated in section 4.3.1 or in [138] we can map all particle positions in a quasicrystal onto particles inside characteristic areas of small phononic and phasonic displacements. In order to determine the characteristic areas, we calculate, analogue to the $D = 4$ case, phononic and phasonic displacements $\mathbf{\Delta u}$, $\mathbf{\Delta v}$ and $\mathbf{\Delta w}$ that change the differences between the phases $\varphi_j - \varphi_k$ in Eq. (4.2) only by integers of 2π. We solve $V_{\mathbf{v}+\mathbf{\Delta v},\mathbf{w}+\mathbf{\Delta w}}(\mathbf{r} + \mathbf{\Delta u}) = V_{\mathbf{v},\mathbf{w}}(\mathbf{r})$, where $V_{\mathbf{v},\mathbf{w}}(\mathbf{r})$ denotes a potential with the phasonic displacements $\mathbf{v}$ and $\mathbf{w}$. For $j = 0, \ldots, 13$, we obtain as suitable combinations

$$\begin{aligned}
\mathbf{\Delta u} &= (u_r\, \cos[j\pi/7],\, u_r\, \sin[j\pi/7]),\\
\mathbf{\Delta v} &= (v_r\, \cos[3j\pi/7],\, v_r\, \sin[3j\pi/7]),\ \text{and}\\
\mathbf{\Delta w} &= (w_r\, \cos[5j\pi/7],\, w_r\, \sin[5j\pi/7]).
\end{aligned} \tag{4.19}$$

These displacements do not modify the potential when

$$\begin{aligned}
u_r/a_V &= \frac{8}{49}\,(n_1\, a + n_2\, b + n_3\, c)\,,\\
v_r/a_V &= \frac{8}{49}\,(n_2\, a + n_3\, b + n_1\, c)\,,\\
w_r/a_V &= \frac{8}{49}\,(n_3\, a + n_1\, b + n_2\, c)\,,
\end{aligned} \tag{4.20}$$

where n_1, n_2, and $n_3 \in \mathbb{Z}$ and a, b, and c are the constant values

$$\begin{aligned} a &= (1-\cos[10\pi/7])^2 - (1-\cos[2\pi/7])(1-\cos[6\pi/7]), \\ b &= (1-\cos[6\pi/7])^2 - (1-\cos[2\pi/7])(1-\cos[10\pi/7]), \\ c &= (1-\cos[2\pi/7])^2 - (1-\cos[6\pi/7])(1-\cos[10\pi/7]). \end{aligned} \tag{4.21}$$

Thus, a colloid at position $\mathbf{r}$ in a tetradecagonal potential with phasonic displacements $\mathbf{v}$ and $\mathbf{w}$ can be mapped to a reduced position $\mathbf{r}^{(\text{red})} = \mathbf{r} - \mathbf{\Delta u}$ in a potential with reduced phasonic displacements $\mathbf{v}^{(\text{red})} = \mathbf{v} + \mathbf{\Delta v}$ and $\mathbf{w}^{(\text{red})} = \mathbf{w} + \mathbf{\Delta w}$ inside the particular characteristic area.

Analogue to the $D = 4$ cases, we consider the subspaces spanned by a chosen phononic direction $\mathbf{e}_j = (\cos[\pi j/7], \sin[\pi j/7])$ and its phasonic counterparts to determine the size of the characteristic areas. In contrast to the quasicrystals of rank $D = 4$ from section 4.3.1, we get for the tetradecagonal symmetry a three-dimensional subspace in every direction. Therefore, we have to find cuboids of the side lengths δu, δv, and δw that fill out the whole volume when shifted about Δu in phononic and Δv and Δw in phasonic directions. Then all reduced positions and reduced phasonic displacements are limited by

$$\begin{aligned} |\mathbf{r}^{(\text{red})}\,\mathbf{e}_j| &\le \delta u/2a_V, \\ |\mathbf{v}^{(\text{red})}\,\mathbf{e}_j| &\le \delta v/2a_V, \\ \text{and} \quad |\mathbf{w}^{(\text{red})}\,\mathbf{e}_j| &\le \delta w/2a_V \end{aligned} \tag{4.22}$$

for all symmetry directions $j = 0, \ldots, 13$. A possible choice is $\delta u/2a_V = \delta v/2a_V = \delta w/2a_V = 1/2(-a-b)$.

Analyzing colloidal trajectories

For a complete description of the colloidal dynamics in a quasicrystal with tetradecagonal symmetry a four-dimensional phasonic space spanned by v_x, v_y, w_x, and w_y has to be analyzed. Since it is too complex to sample the complete space, we restrict our analysis to drifts on selected planes in the phasonic space.

As a first attempt either $\mathbf{w}$ is varied while $\mathbf{v} = \mathbf{0}$ or $\mathbf{v}$ is changed while $\mathbf{w} = \mathbf{0}$. We trace the paths of colloids started at the origin for all drift directions within the respective phasonic plane. Then the important points of the trajectories for reduced phasonic displacements $\mathbf{w}^{(\text{red})}$ or $\mathbf{v}^{(\text{red})}$ and the corresponding reduced positions $\mathbf{r}^{(\text{red})}$ can be presented in the diagrams of Fig. 4.9. Note the similarity to the diagrams obtained for the $D = 4$ quasicrystals in Fig. 4.6.

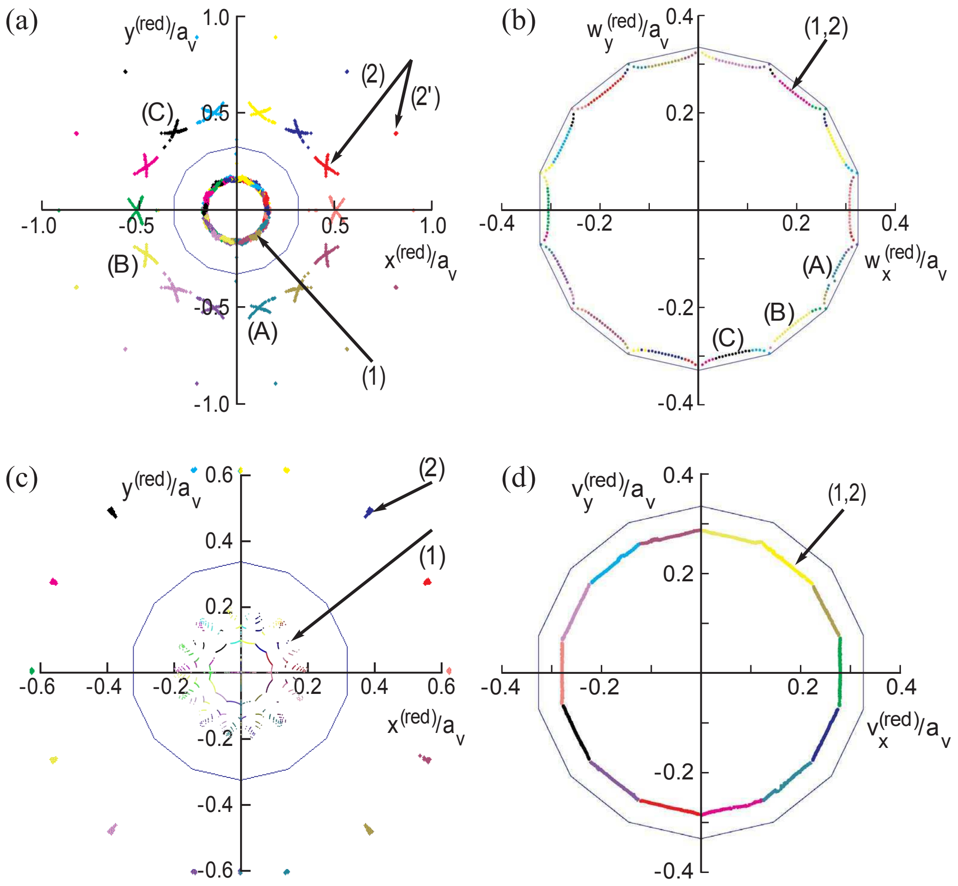

Figure 4.9.: Characteristic areas for the tetradecagonal laser field (cf. [B]). (a,b) Areas of reduced positions $\mathbf{r}^{(\mathrm{red})}$ and reduced phasonic displacements $\mathbf{w}^{(\mathrm{red})}$ for $\mathbf{v} = \mathbf{0}$. (c,d) Areas of reduced positions $\mathbf{r}^{(\mathrm{red})}$ and reduced phasonic displacements $\mathbf{v}^{(\mathrm{red})}$ for $\mathbf{w} = \mathbf{0}$. The characteristic areas are limited by blue polygons. The lines where particle start to slide or end up after sliding or remapping are marked by different colors. Selected lines are also labeled by letters (A), (B), or (C) in order to denote corresponding lines.

To derive now a trajectory for the case $\mathbf{v} = 0$ (see Fig. 4.9 (a,b)) we attempt the procedure explained in detail for the $D = 4$ case: When the phasonic displacement $\mathbf{w}^{(\mathrm{red})}$ reaches a point marked by (1,2) the colloid jumps from its old position (1) to a new one (2). Note that the positions (2') are only reached for a drift along a symmetry axis or slightly beside it. Since the colloidal position is now outside the characteristic area, one has to map it back inside by employing combinations of $\mathbf{\Delta u}$, $\mathbf{\Delta w}$ and also $\mathbf{\Delta v}$. Due to the latter, for the mapped quantity $\mathbf{v}^{(\mathrm{red})} \neq \mathbf{0}$. Thus, one has to consider a new diagram for the reduced phasonic displacements $\mathbf{w}^{(\mathrm{red})}$ and the reduced positions $\mathbf{r}^{(\mathrm{red})}$ after every jump. The same difficulty arises for drifts in the $\mathbf{w} = \mathbf{0}$ plane. Therefore, in contrast to quasicrystals with rank $D = 4$, the derivation of a colloidal trajectory for an arbitrary drift is for $D = 6$ in most cases quite complex, as many diagrams would be required for a complete prediction.

Selected colloidal trajectories

Despite the higher-dimensional complexity, there are drifts in the tetradecagonal potential for which it is possible to deduce the trajectories with a single diagram for the reduced phasonic displacements. For certain drifts in the plane with $v_y = w_y = 0$, the colloid moves in x direction. In addition, the phasonic counterparts $\mathbf{\Delta w}$ and $\mathbf{\Delta v}$ to the required $\mathbf{\Delta u}$ only affect the x components w_x and v_x. As a consequence, the phasonic plane with $v_y^{(\mathrm{red})} = w_y^{(\mathrm{red})} = 0$ is never left during the mapping process. In the following, we discuss the colloidal trajectories that can be completely derived from the diagram in Fig. 4.10 (a) for selected drifts.

For a phasonic drift in the direction $(v_x,\, v_y,\, w_x,\, w_y) = (\cos[3\pi/7],\, 0,\, \cos[5\pi/7],\, 0)$ we observe a zig-zag path illustrated in Fig. 4.10 (b). The trajectory resembles the zig-zag paths detected in quasicrystals with rank $D = 4$ from section 4.3.1.

On the other hand, a new type of trajectory is depicted in Fig. 4.10 (c). It is comprised of straight paths interrupted by jumps in the opposite direction and occurs when a drift in the direction $(v_x,\, v_y,\, w_x,\, w_y) = (\cos[9\pi/70],\, 0,\, \cos[3\pi/14],\, 0)$ is deployed. The particle slides on a straight line until the phasonic displacement reaches a point in the diagram in Fig. 4.10 (a) such that the particle jumps. The phasonic displacements and the positions can be mapped back into the characteristic areas to predict the further path of the colloids upon a further increase of the phasonic displacement.

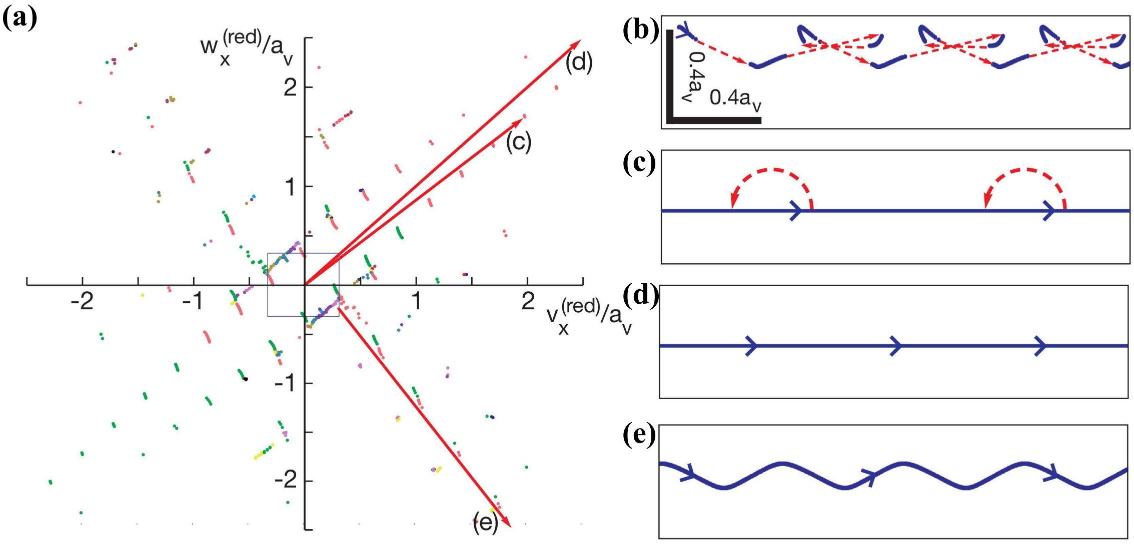

Figure 4.10.: (a) Section of the characteristic diagram for the reduced phasonic displacements $v_x^{(\mathrm{red})}$ and $w_x^{(\mathrm{red})}$ with $v_y = w_y = 0$. (b)-(e) Selected typical colloidal trajectories arising for $(v_x,\, w_x)$ drifts in certain directions. The directions of motion are indicated by arrows. The scale bar denotes the length scales in x- and y-direction. The figure has been adapted from [B].

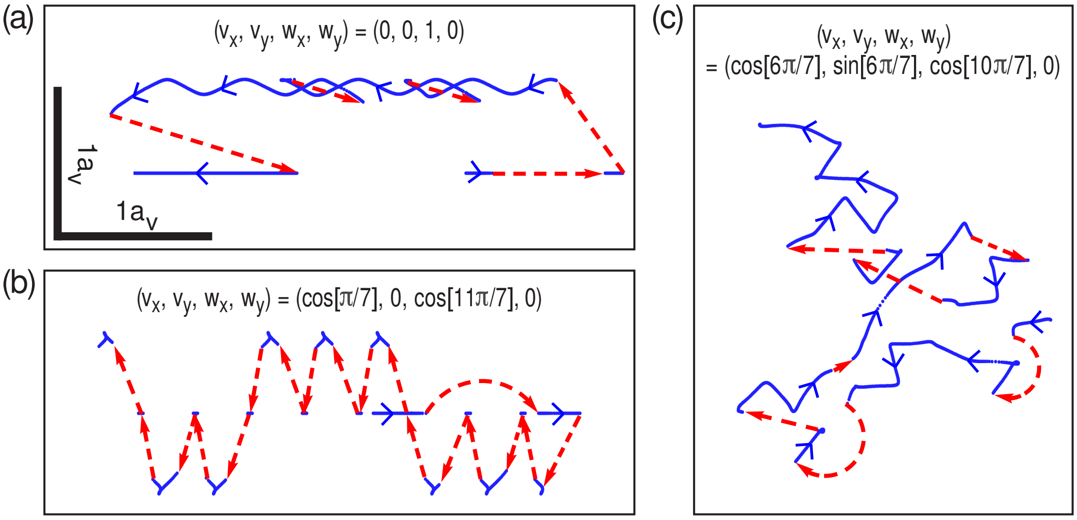

Figure 4.11.: Selection of typical colloidal trajectories comprising the majority of the observed colloidal paths (cf. [B]). Glide motion of the colloid is depicted by solid blue lines, while jumps are marked by dashed red lines. (a) The trajectory exhibits combinations of straight and winding lines separated by jumps. (b) The trajectory consists of several jumps following an irregular zig-zag path. (c) The chaotic trajectory is interrupted by jumps and exhibits otherwise irregular slides without preferred direction.

In Fig. 4.10 (d) an example of a straight path without any jumps is displayed. It arises for a phasonic drift in the direction $(v_x,\, v_y,\, w_x,\, w_y) = (1,\, 0,\, 1,\, 0)$. In this case, the phasonic displacement never reaches a point in the diagram of Fig. 4.10 (a) as the particle never leaves a minimum. Therefore, the phasonic displacement is simply mapped back when it crosses the border of its characteristic area. This drift proceeds along a symmetry plane in the phasonic space such that the form of the trajectory is a straight line.

Another new type of trajectory has the shape of a winding line as shown in Fig. 4.10 (e). It arises, e.g., when a drift in the direction $(v_x,\, v_y,\, w_x,\, w_y) = (\cos[3\pi/7],\, 0,\, \cos[5\pi/7],\, 0)$ is applied for a colloid position whose initial reduced phasonic displacement is not in the origin but at $v_x = 0.3a_V$ and $w_x = -0.2a_V$. Just as in the example before, the colloid never jumps. Compared to the previous case the drift does not move along a symmetry plane in the phasonic space which leads to the occurrence of curves in the path.

Note that aside from this selection of typical paths, most phasonic drifts give rise to much more complex trajectories. Further examples are shown in Fig. 4.11. All displayed paths of the colloids are composed of the typical trajectories such that every section can be explained separately.

4.4. Conclusion

We have investigated new aspects in laser induced colloidal quasicrystals by considering a finite particle diameter and phasonic drifts in octagonal, dodecagonal and tetradecagonal rotational symmetry as possible degrees of freedom. The insight gained from studying this basic model of a two-dimensional monolayer of colloidal particles is also relevant for other quasicrystalline systems. For instance regarding the colloidal diameter, the deposition of macromolecules on atomic quasicrystalline surfaces seems to result in similar degenerate adsorption patterns [270]. Our model contributes to the understanding of the origin of these patterns whose rotational symmetry is identical to the substrate.

A similar case can be made concerning the phasonic drifts in laser interference pattern. In principle, the method is also applicable to intrinsic quasicrystals, e.g. atomic systems characterized by a density distribution where atoms reside at the most pronounced maxima. By analyzing the properties of these maxima within the reduced phononic and phasonic areas it is possible to predict the correlated rearrangements of atoms due to phasonic fluctuations.

Besides, we have extended the method originally developed by Kromer *et al.* to octagonal, dodecagonal and tetradecagonal symmetry and demonstrated the universality of the approach. In particular, for the tetradecagonal case with rank $D = 6$ we showed how one can still predict colloidal trajectories that are caused by phasonic drifts in spite of the increased complexity in the phasonic space. In addition, we were able to identify new types of trajectories compared to the regular straight and zig-zag paths that are already known from quasicrystals with rank $D = 4$.

> When you stop growing you start dying.
>
> *(William Burroughs* 1914-1997*)*

CHAPTER 5

Colloidal Epitaxy on clean Quasicrystalline Substrates

In contrast to the previous chapter, in which we discussed the properties of a quasicrystalline monolayer of colloidal particles, we now make the step to three-dimensional colloidal quasicrystals. Pushed by experimental discoveries of mesoscopic quasicrystals in star polymers [108] or micelles [109] an active field of soft matter quasicrystals has emerged [105]. On the theoretical side, much effort has been invested to stabilize quasicrystals in bulk by tuning in particular the interaction potential in great detail [117, 119]. In this chapter, we want to harness the potential of a template-directed approach and the fact that most three-dimensional quasicrystals like the octagonal [179], decagonal [272] or dodecagonal [5] phase are periodic stackings of two-dimensional aperiodic tilings.

For colloids, the method of template-directed growth has been successfully applied to obtain periodic crystals and is controlled for various solvent conditions [143, 145]. Under gravity as an external field, colloidal particles sediment onto a patterned substrate. The specific design of the substrate influences the grown colloidal structure. Hence, crystal structures differing from the bulk behavior can be achieved. Here, we investigate the colloidal sedimentation on quasicrystalline substrates by Monte-Carlo simulations. In contrast to other approaches, no fine-tuning of the interaction potential between the colloids is required. So far, comparable studies only exist for the adsorption of rare gas elements on metallic quasicrystalline surfaces [73, 74].

The outline of the chapter is as follows: In the first part, we introduce the epitaxial model in general before explaining the simulation procedure or suitable interaction parameters in detail. Afterwards, we retrieve the results for simple periodically crystalline substrate symmetries. From this basis, we consider the deposition of colloids on quasicrystalline substrates and show that stackings with several quasicrystalline layers develop for various substrate symmetries. We continue to evaluate the formed layers in detail and discuss the limitations of this approach as dislocations start to emerge in higher layers. Briefly, we outline a possible experimental realization before finally concluding in section 5.3.

5.1. Sedimentation model

We introduce the model in two stages. First, we explain the colloidal suspension and the quasicrystalline substrate construction. Second, we discuss the simulation procedure in detail with suitable values for interaction parameters and retrieve the results for simple crystalline substrates.

5.1.1. Template and colloidal interaction

We consider a suspension of colloidal particles of diameter σ in a common solvent. Under the influence of a gravitational field $V_{\text{ext}} = V_0 \cdot z/\sigma$ the colloids sediment onto a patterned substrate. The design of the substrate is borrowed from the aperiodic tilings presented in section 1.3. It is comprised of cylindrical holes with a certain depth that are arranged according to the vertices of an aperiodic tiling on the otherwise plain surface (see Fig. 5.1). Therefore, these slots represent beneficial locations for the colloids in the gravitational field. In experiments a corresponding substrate might be realized by a lithography patterned template (cf. [143, 230, 273]). The interaction between the colloids is described by the screened Coulomb potential

$$V(r) = \begin{cases} \epsilon \frac{\sigma}{r} \exp\left[-\kappa(r-\sigma)\right] & , r > \sigma \\ \infty & , r < \sigma \end{cases} , \tag{5.1}$$

where r denotes the distance between the center positions of two colloids, κ is the inverse Debye screening length, and ϵ determines the strength of the Yukawa interaction. The interaction between the colloids and the substrate surface is hard-core like. For good growth conditions, the gravitational strength has to be strong enough to imprint the substrate on the colloidal ordering while it still leaves the colloids able to explore the surface landscape during sedimentation.

5.1.2. Simulation details and parameters

We choose the values for the parameters of the pair potential in Eq. (5.1) in accordance with [274] such that $\beta\epsilon = 20$ and $\kappa\sigma = 100$. Thus, the interaction between the colloids is dominated by excluding volume effects. The substrate contains cylindrical holes with depth 0.25σ and diameter 0.88σ arranged like an aperiodic tiling. In addition, the substrate pattern is controlled by the edge length a_0 of the basic tiles. For a sensible regime of a_0 the lower limiting value is forced such that all vertices can be occupied by non-overlapping holes and consequently colloids. The upper limiting value is chosen such that sedimenting colloids of the second layer are prevented from falling through to the surface. The gravitational force has to be tuned in order to compromise two features. On the one hand, the gravitation must not be too strong such that the colloids are restricted in exploring the surface landscape. On the other hand, gravitation must still imprint the substrate order on the grown colloidal

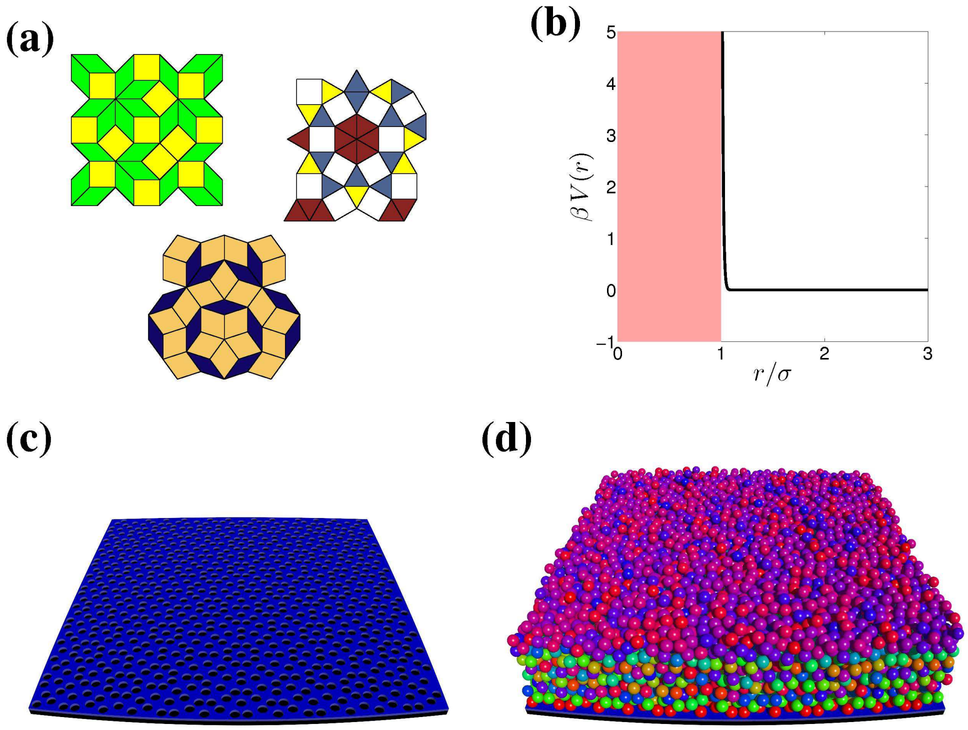

Figure 5.1.: Overview of the colloidal deposition model. The substrates are derived from periodic approximants of aperiodic tilings. (a) Schematic excerpts of the three tilings used in the scope of this chapter as quasicrystalline substrates: the octagonal Ammann-Beenker, the dodecagonal Square-Triangle, and the decagonal Penrose-Rhomb tiling. The substrate is constructed as a planar surface that exhibits circular slots. These slots are arranged according to the aperiodic tilings from (a). The interaction of the colloids and the substrate surface is determined by excluded volume such that the slots represent energetically favored positions due to the external gravitational field. (b) The interaction potential between the colloids is almost hard-core like. (c) A clean octagonal substrate whose size is typical for the simulated system. (d) Final adsorbed structure by colloidal sedimentation under a gravitational field. The coloring of the particles is generated by their z coordinates and indicates the formation of several layers. (c,d) are adapted from [D].

structure. Therefore, we scanned both V_0 and a_0 for each substrate tiling and obtained $V_0/\epsilon = 12$ as suitable value for the gravitational strength.

The simulation procedure is designed such that a layer by layer growth is supported: First, colloids that could occupy half of the holes contained in the substrate pattern are injected with random positions in the top xy-plane of the box and sedimented onto the grown structure. The system is relaxed for at least $2.5 \cdot 10^5$ Monte-Carlo steps before the next particles are injected. In the end, the final adsorbate structure consists of roughly 10^4 colloidal particles for substrates with 800 holes. On each substrate, the process is independently repeated 200 times, in order to improve the statistics of the analysis. Then, from the average number density distribution in vertical direction the layers are identified.

5.1.3. Growth on periodic substrates

Before we simulate the sedimentation on quasicrystalline substrates, we test the simulation for periodic ones. We apply the procedure described in the previous section on square and hexagonal lattice substrates. From the independently grown colloidal structures we determine the average vertical distribution $\langle N(z) \rangle$, i.e. a histogram of occurring z values in the structure. In case of a layerwise growth, $\langle N(z) \rangle$ exhibits distinct peaks (see, e.g. Fig. 5.2 (a)). Based on this information we divide the whole structure into individual layers. If the choice of higher layers is no longer distinct because of peak broadening, the grown structure is split into layers based on the width of the previous layers. Moreover, each layer is treated as a two-dimensional system with a structured colloidal density $\rho(r)$ such that its structure factor $S(q)$ reveals the order within the layer. By integrating over the peaks belonging to the first ring of $S(q)$, we calculate an average intensity that allows to compare the extend of order between higher layers. These results are displayed for the square lattice in Fig. 5.2 and for the hexagonal lattice substrate in Fig. 5.3.

In case of the square lattice, we observe a perfect layerwise structure as $\langle N(z) \rangle$ exhibits sharp and separated peaks. In addition, for each layer $S(q)$ indicates square ordering, while at the same time the average intensity of the structure factor remains at a constant high value throughout the grown structure. Therefore, a continued sedimentation of colloids leads to a bcc crystal, i.e. an unlimited stacking of square layers.
On the other hand, the sedimentation on the hexagonal substrate results into a structure that, as z increases, consists of broadening layers, even though these remain distinctly visible in $\langle N(z) \rangle$. Yet, the individual structure factors of the layers suggest a transition to a disordered state for higher layers accompanied by a decrease of the average intensity.

These two different outcomes of the deposition process originate directly from the different substrate symmetry. On the square lattice, the adsorption sites are uniquely defined, as all colloids reside on the center of a square from the layer below (see Fig. 5.4 (a)). Since this allows a rigid $abab\ldots$ stacking of square lattices, the tetragonal symmetry is conserved throughout the grown structure. In contrast, the excluded volume interaction of the colloids divides the adsorption sites of the hexagonal lattice into two groups, namely the center of

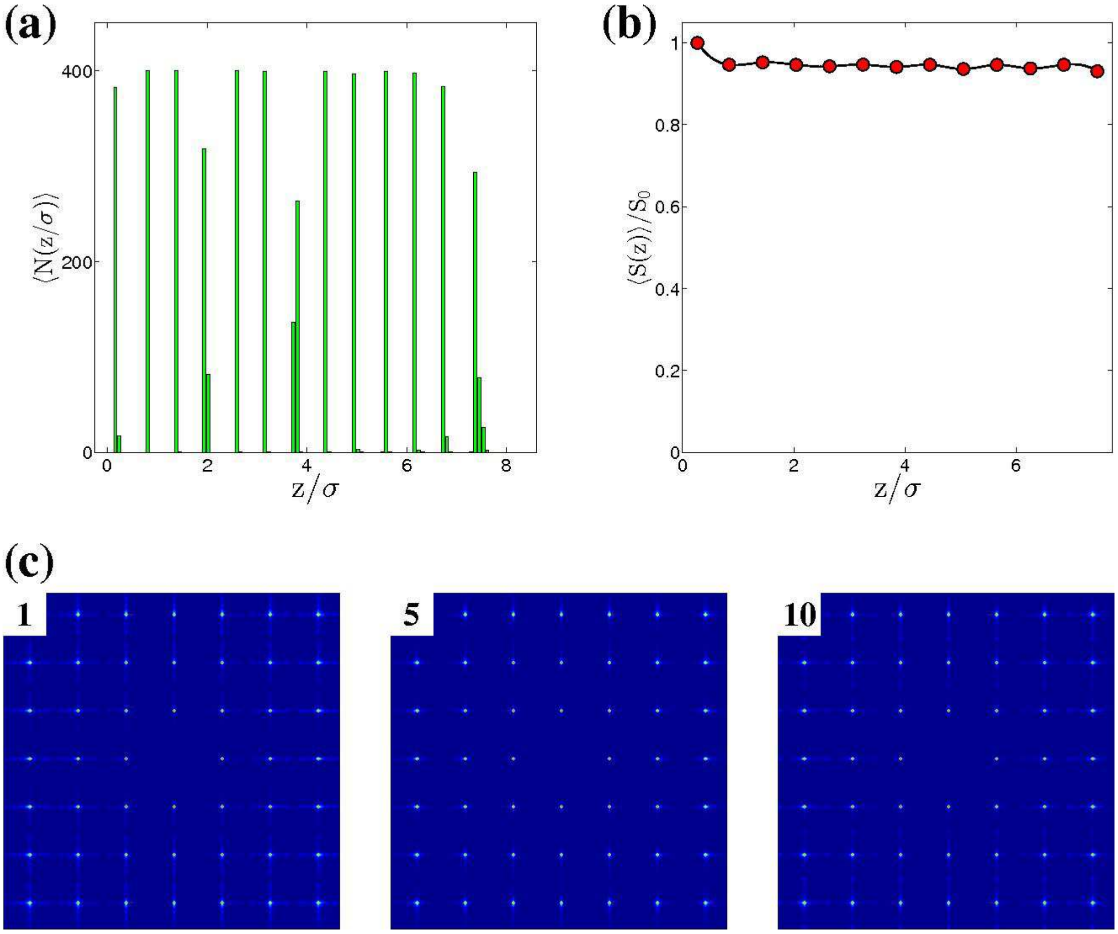

Figure 5.2.: Crystalline layers on the square lattice with lattice constant $a_0/\sigma = 1.13$. (a) From the vertical distribution of particles $\langle N(z) \rangle$, several periodically stacked layers are distinctly recognizable. The width of the peaks remains sharp throughout the sample. (b) The average intensity of the four inner peaks of the structure factor relative to the first layer remains constant. (c) The individual structure factors reveal that ordering is conserved and that the whole structure is comprised of stacked square lattices.

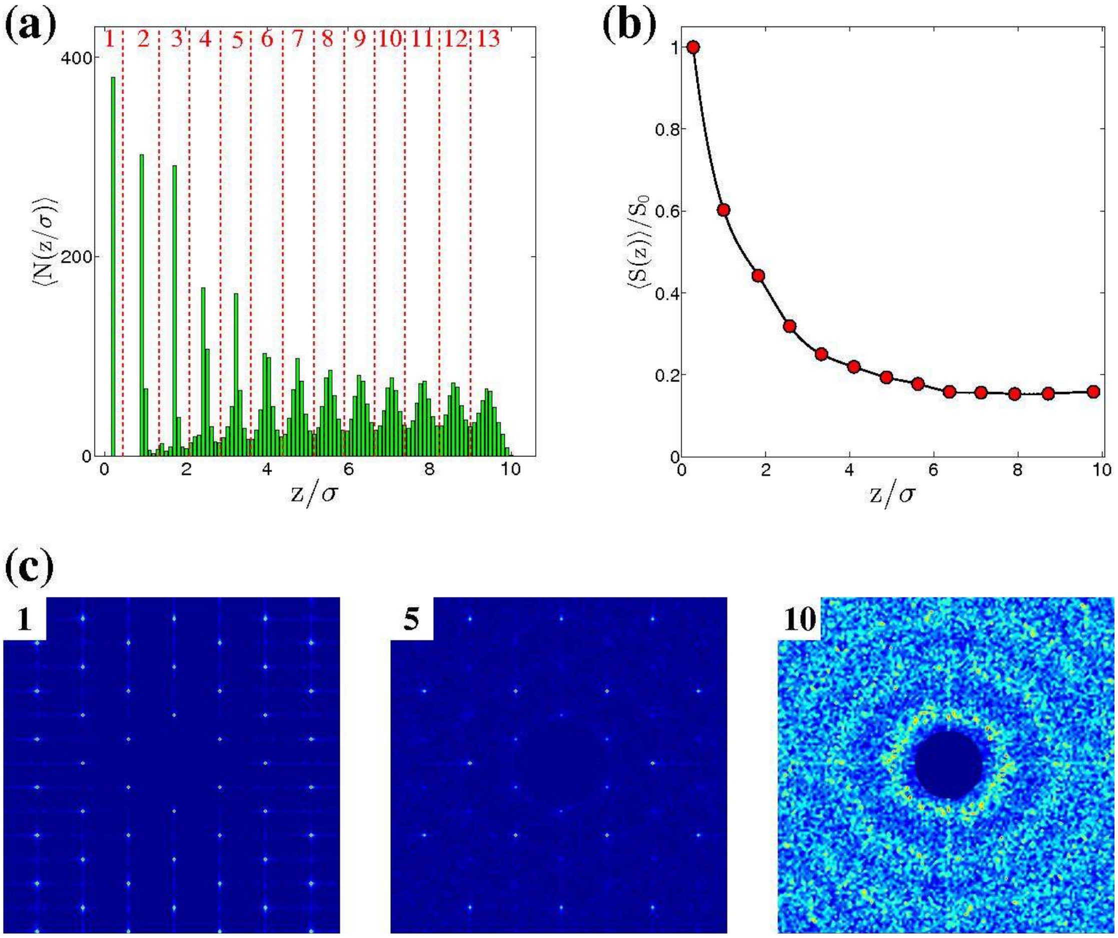

Figure 5.3.: Crystalline layers on the hexagonal lattice with lattice constant $a_0/\sigma = 1.13$. (a) From the vertical distribution $\langle N(z) \rangle$ several layers can be identified, while their width increases with height. (b) Consequently, the average intensity of the six inner peaks of the structure factor seems to decrease exponentially relative to the value of the first layer. (c) The individual structure factors of the layers show a transition by decaying higher modes into a disordered state.

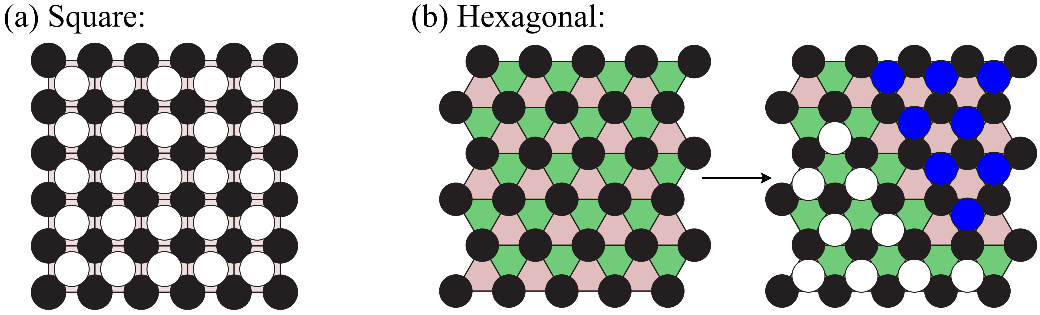

Figure 5.4.: Schematic stacking of hard sphere lattices for the square and hexagonal case. Black circles denote substrate particles while adsorbed particles on top are represented by white and blue circles respectively. (a) On a square substrate the subsequent square layer is uniquely defined and the stacking sequence is $abab\ldots$. Hence, the combined symmetry of substrate and layer remains four. (b) On a hexagonal lattice two configurations of the subsequent layer are possible. The particles may either reside on the center of a green (blue circles) or red triangle (white circles). These two domains are incompatible with each other and the boundary between them affects further layers. The stacking sequence may be random $abc\ldots$, $aba\ldots$, $acb\ldots$ as long as adjacent layers are different. In addition, the combined symmetry of substrate and each domain of adlayer is reduced to three.

upward and downward pointing triangles, as illustrated in Fig. 5.4 (b). Adjacent positions of different groups cannot be occupied simultaneously. As a consequence, multiple colloidal domains with incompatible orientations can form within a layer. The boundaries between these domains affect the subsequent growth during the sedimentation process by interrupting the stacking of an otherwise random sequence of a, b, and c with differing adjacent layers. This corresponds to a mixed hcp and fcc crystal. In the long run, the amount of domain borders increases until the layer becomes disordered.

5.2. Colloidal deposition on quasicrystalline substrates

After simulating the sedimentation of colloidal particles on periodic commensurate substrates in the previous section, we now consider quasicrystalline substrates that are by definition completely incommensurate. This can give rise to complex phenomena. For example, regarding the deposition of metals on quasicrystalline surfaces, many interesting phenomena have been reported in literature like polymorphic film growth [82, 90], or the evolution of uniaxially aperiodic copper [84]. In this section, we show that for our colloidal expitaxy approach quasicrystalline substrate symmetry in combination with sedimentation of colloids under gravity suffices to achieve several quasicrystalline layers in the grown structure. Besides, this can be exploited to realize rotational symmetries that are unlikely to form for our particle model under conditions of self-assembly like for instance octagonal symmetry [115]. In the first part, we compare the grown structures on the basis of the average vertical distribution as well as the properties of the structure factors. In the second part, we analyze changes in the individual layers in more detail by discussing the stacking potential and the limit of defect free growth. In the last part, we discuss a possible experimental realization.

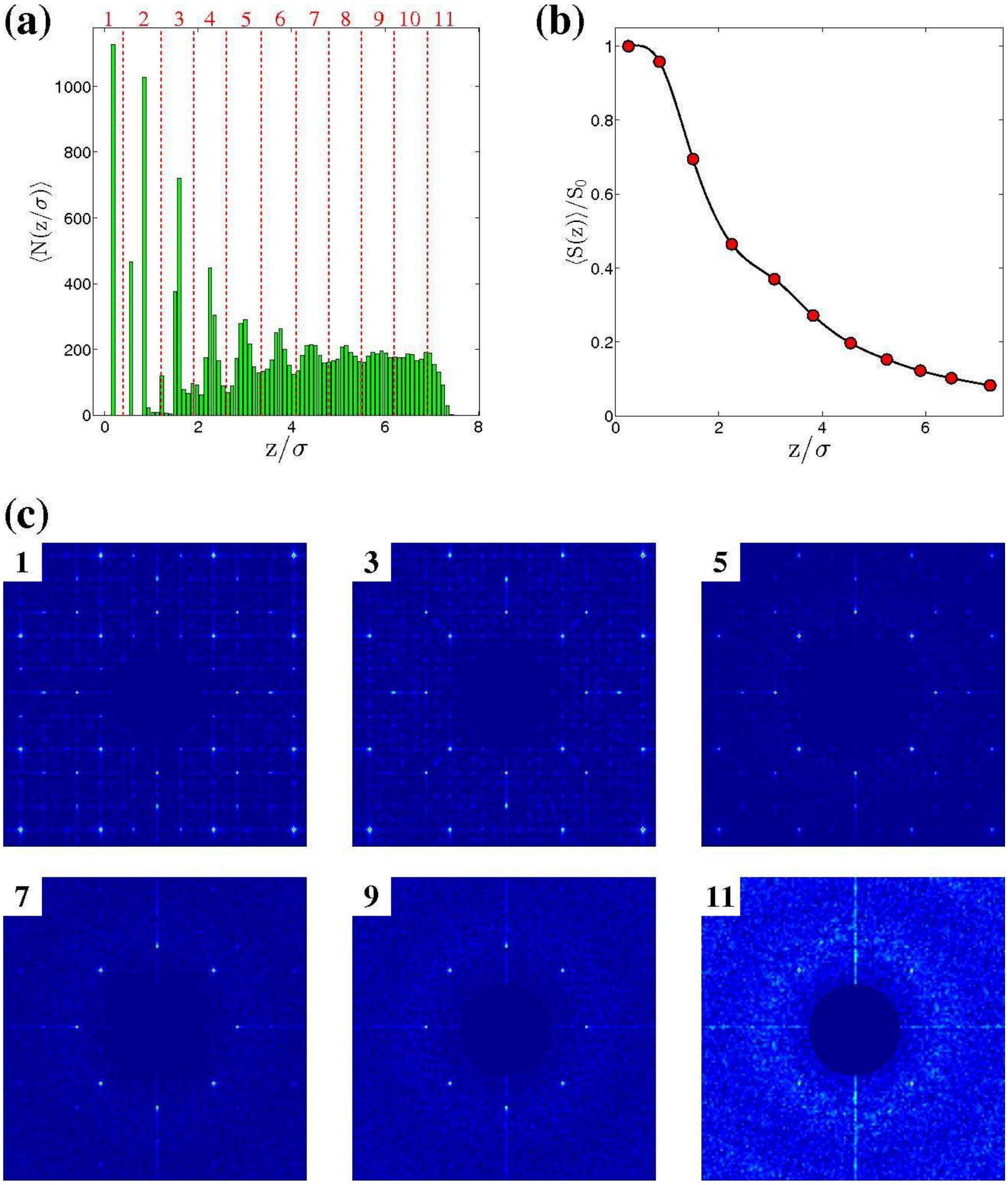

Figure 5.5.: Quasicrystalline layers on the octagonal Ammann-Beenker substrate with tile edge length $a_0/\sigma = 1.33$. (a) In the vertical distribution $\langle N(z) \rangle$ the first layers are distinctly visible, while the higher ones are chosen with similar layer width. (b) The average intensity of the peaks in the first ring of the structure factor seems to decay exponentially. (c) The individual structure factors reveal that octagonal order seems to persist for a considerable height, though higher modes decay fast.

5.2.1. Development of quasicrystalline layers

We apply the sedimentation procedure explained in section 5.1.2 on three different quasicrystalline substrates in order to obtain three-dimensional colloidal quasicrystals. The results comprised of the vertical distribution $\langle N(z)\rangle$, selected structure factors $S(q)$ of individual layers as well as their average intensity course are displayed in Fig. 5.5 for the Ammann-Beenker, in Fig. 5.6 for the Square-Triangle as well as in Fig. 5.7 for the Penrose-Rhomb tiling. In all cases, the first layer is completely induced by the substrate tiling as each hole in the patterned surface is occupied by a colloid. Since each tiling consists of two elementary tiles, the ground layer offers two types of adsorption sites with different height respectively. For example, the Ammann-Beenker tiling is constructed from squares and rhombs such that colloids belonging to the second layer are either located on the center of a square or on the center of triangles comprising the rhomb. Thus, $\langle N(z)\rangle$ exhibits in fact two peaks in the first layer as can be seen in Fig. 5.5 (a). In general, the presence of two length scales in the adsorption sites contributes to broadening layer widths for all tilings as z increases. In the end, higher layers are not directly visible anymore, but are defined by dividing the remaining structure in z direction in segments with width equaling the previous layers.

Despite the fact that the layers become less pronounced, they possess clearly quasicrystalline symmetry in $S(q)$, albeit with only weak higher modes. This might indicate an increasing disorder starting on a local level. Surprisingly, the colloidal structure grown on the Ammann-Beenker like patterned substrate exhibits even in the ninth layer distinct octagonal arranged peaks in the structure factor and thus seems to surpass the growth on the dodecagonal Square-Triangle tiling, even though dodecagonal symmetry is mostly reported for self-assembled soft quasicrystals [117, 119]. The average intensity of peaks on the first ring of the structure factor seems to decay for the structures on all templates exponentially. In order to reveal small differences, the courses from all samples are assembled in Fig. 5.8. For classification, the values from the periodic lattice substrates are contained as well. While the quality of the square substrate is unrivaled, the next best substrate, in this respect at least for the first seven layers, is represented by the Ammann-Beenker tiling. To measure the potential of the Ammann-Beenker substrate we analyze the individual layers in more detail in the following section.

5.2.2. Characterization of growth quality

In this section, we investigate the stacked layers of colloids on the Ammann-Beenker, Square-Triangle, and Penrose-Rhomb tiling in more detail. The independently grown structures on each substrate yield an average colloidal density with distinct maxima. These sites are occupied with a higher probability and reveal the presence of quasicrystalline order even in real space. As examples, the fourth layer grown on the Ammann-Beenker substrate and the fifth layer from the structure on the Square-Triangle tiling are depicted in Fig. 5.9.

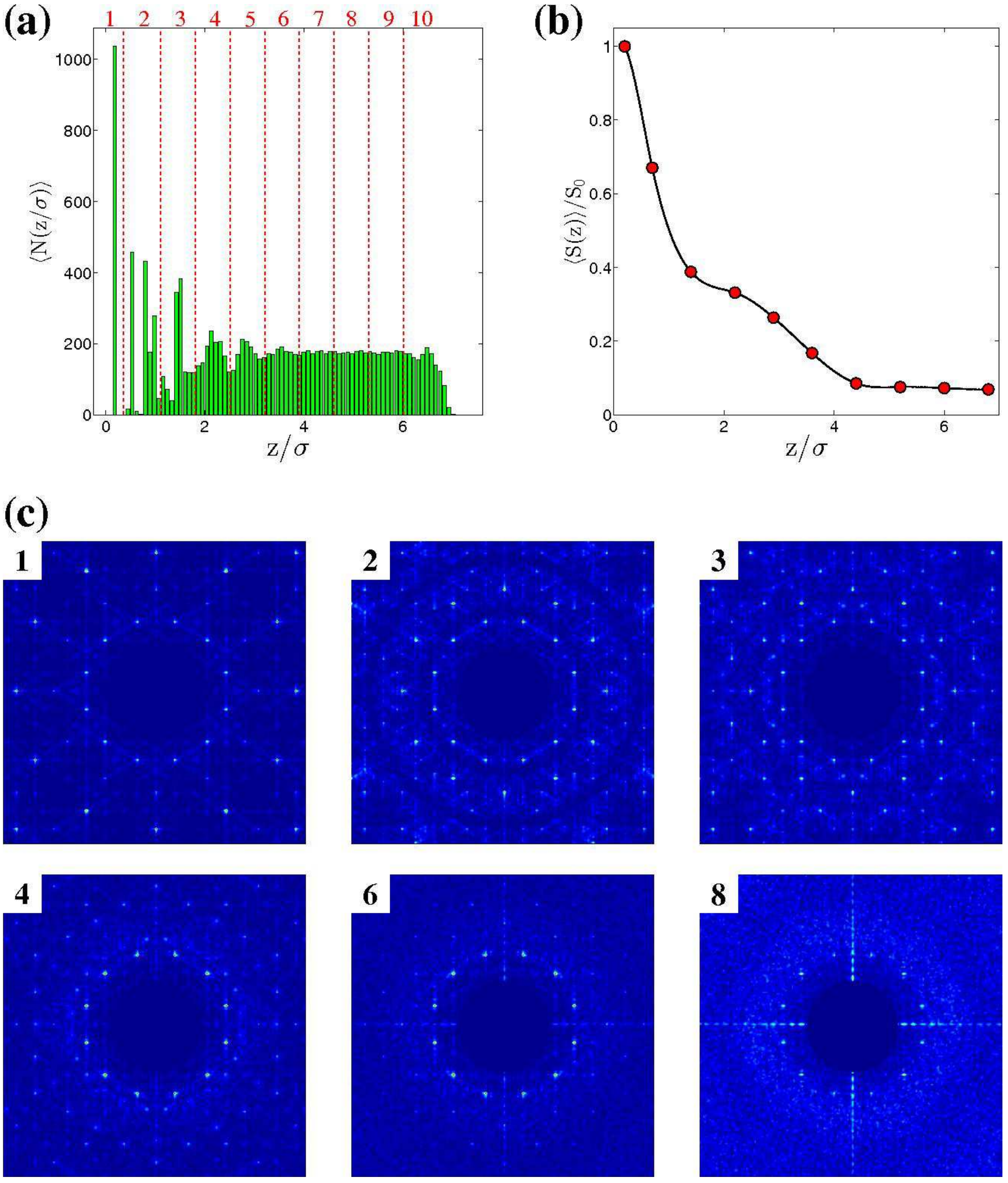

Figure 5.6.: Quasicrystalline layers on the dodecagonal Square-Triangle substrate with tile edge length $a_0/\sigma = 1.30$. (a) From the vertical distribution $\langle N(z) \rangle$ only the first four layers are visible. Since the layers broaden very fast, the borders are determined such that each layer exhibits the same width. (b) The average intensity of the peaks in the first ring of the structure factor seems to decay exponentially. (c) In the bottom lines, while higher modes vanish with layer height, the structure factors show that dodecagonal quasicrystalline order remains in the higher layers, albeit the fuzziness hints at the presence of defects.

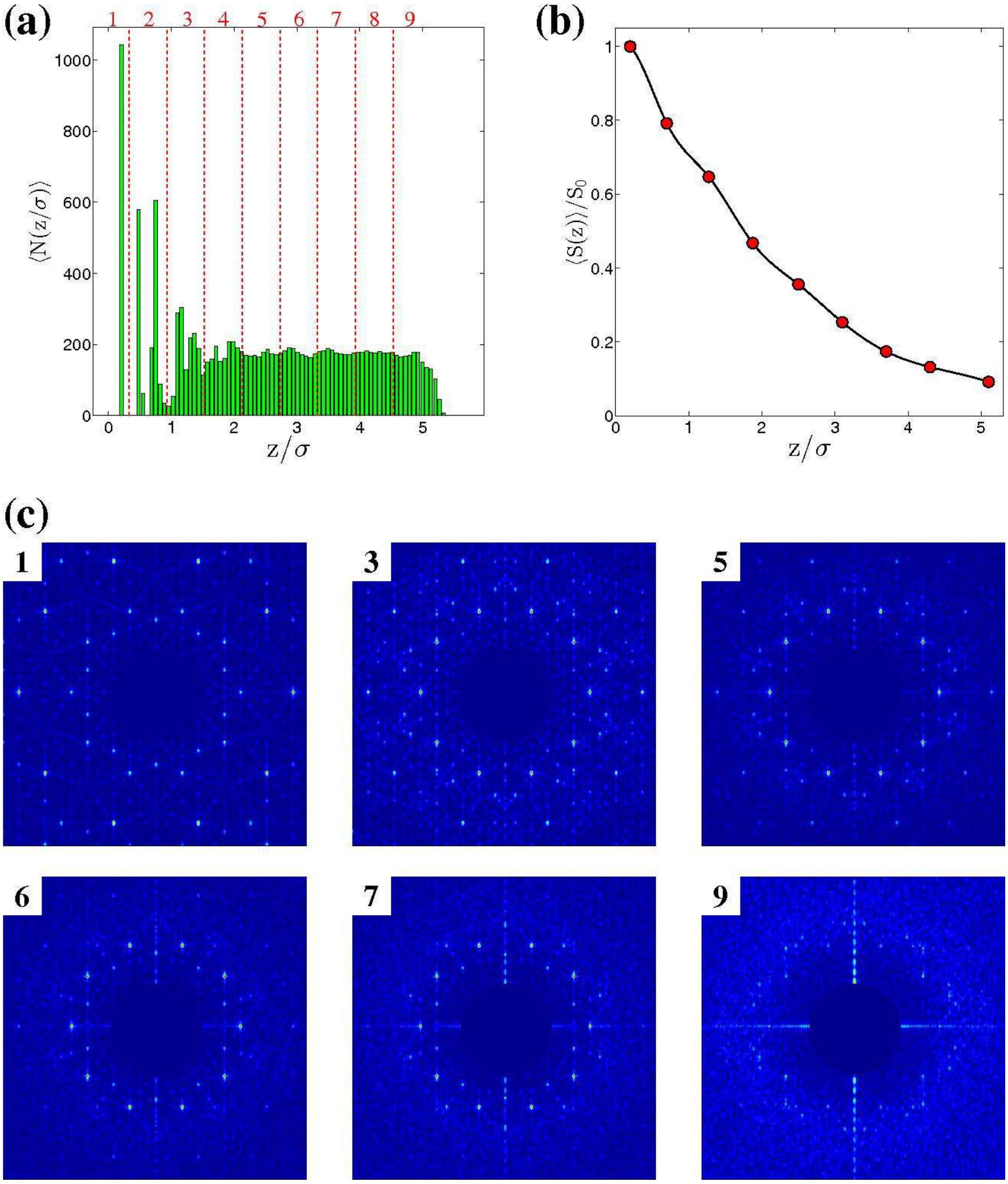

Figure 5.7.: Quasicrystalline layers on the decagonal Penrose-Rhomb substrate with tile edge length $a_0/\sigma = 1.62$. (a) Only the first three layers are visible in the vertical distribution $\langle N(z)\rangle$ and exhibit already broad peaks. Therefore, all higher ones are chosen by similar width. (b) The average intensity of the peaks in the first ring of the structure factor seems to decay exponentially. (c) The individual structure factors in the bottom line reveal a persistence of the first decagonal ring with vanishing higher modes for increasing layer height. Again, the fuzziness suggests the presence of defects.

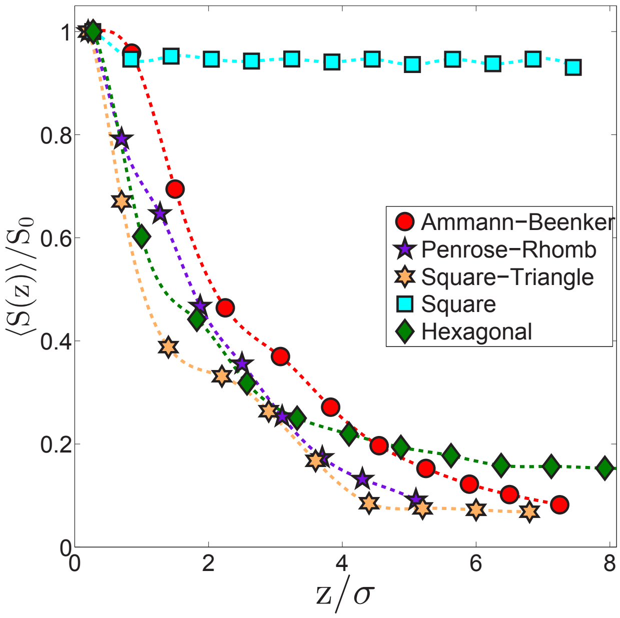

Figure 5.8.: Average intensity of the structure factor peaks in the first ring as a function of layer height for various substrate symmetries. The intensity values are scaled relative to the first layer. The dashed lines serve as guide to the eye while the symbols denote the results for the projected layers. Aside from the square lattice, the intensities seem to decrease exponentially.

In case of the Ammann-Beenker, the favored occupation sites reside around local symmetry centers and form octagons whose size ratio equals exactly the silver mean $\alpha = 1+\sqrt{2}$, the inflation factor of the tiling (see Fig. 5.9 (a)). For a Square-Triangle substrate, the higher hierarchical order of the tiling remains visible, even though the local order decreased as a consequence of local flips. Note that with increasing height the structured density $\rho(\mathbf{r})$ becomes fuzzier until further information regarding order has to be extracted from reciprocal space.

In the following, we determine the fixed adsorption sites within the grown structure. These are sites that are occupied at least in 70% of the grown structures. To account for local thermal fluctuations we integrate $\rho(\mathbf{r})$ in each layer locally around the maxima over an area with radius $\sigma/4.0$. If the resulting value exceeds 70%, this site is considered to be fixed. As illustrated in Fig. 5.10, every grown three-dimensional colloidal structure lacks those from the fourth layer onwards. For the sedimentation on the Penrose-Rhomb and Square-Triangle tiling, these numbers decay monotonically, as both tilings exhibit sites that exclude each other for hard-core interactions similar to the conditions on the hexagonal substrate in section 5.1.3. In case of the Penrose-Rhomb tiling, these sites are located on adjacent rhombs and in case of the Square-Triangle tiling one has to differentiate oppositely pointing neighboring triangles within the dodecagonal patches. On the other hand, the number of fixed sites in the second layer of the Ammann-Beenker tiling exceeds the number of substrate holes.

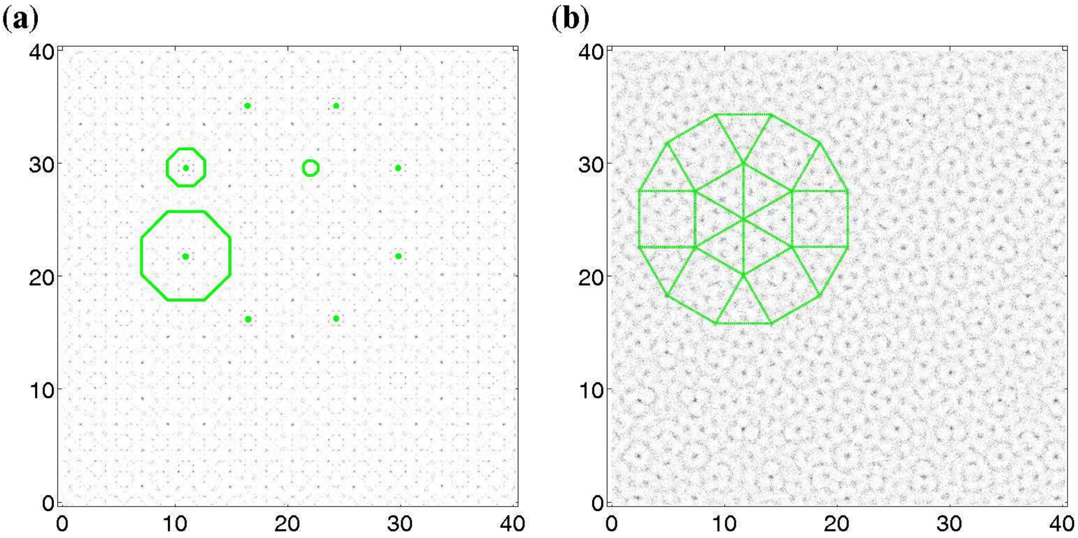

Figure 5.9.: Average real space position of the colloids in higher layers. Dark areas resemble a high probability of occupation whereas sites with minor probability are color coded from gray to white. The coordinates are given in units of the colloidal diameter σ. (a) In the fourth layer grown on an Ammann-Beenker substrate the sites predominantly occupied form octagons whose ratio is the silver mean $\alpha = 1 + \sqrt{2}$, the inflation factor of the tiling. (b) In the fifth colloidal layer grown on a Square-Triangle substrate the higher hierarchical order of symmetry centers is still visible as indicated by the green dodecagonal arrangement, the characteristic building block of the tiling.

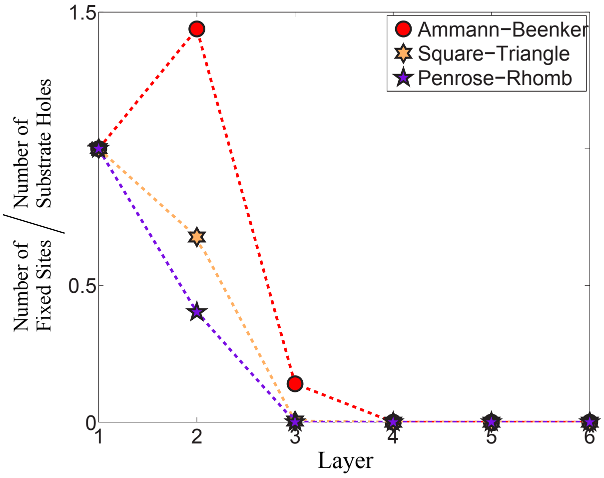

Figure 5.10.: Fixed adsorbtion sites in the epitaxial structures for various substrate tilings. While the number of fixed sites relative to the amount of substrate holes decreases for sedimentation on Square-Triangle and Penrose-Rhomb tiling, it increases in the case of the Ammann-Beenker tiling. In higher layers no fixed sites are present for neither substrate.

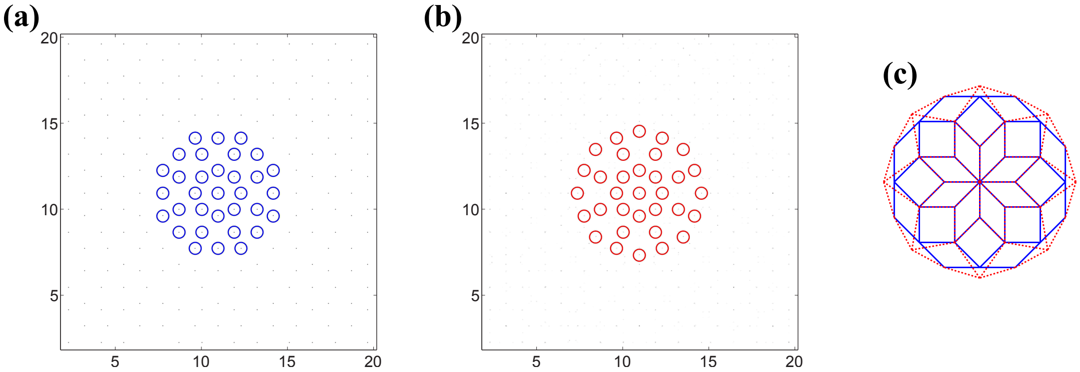

Figure 5.11.: Stacking sequence on the Ammann-Beenker substrate. Coordinates are given in units of σ and dark areas correspond to a high probability of occupation. (a) The colloidal positions in the first layer are directly given by the substrate slots. The average positions around a symmetry center are enclosed by blue circles. In (b), the average colloidal positions in the third layer above the area in (a) are displayed. The spots with highest probability are enclosed by red circles and form a similar octagon. (c) The symmetry centers of the first and second layer almost overlap completely.

This is due to the fact that within the second layer one colloid is definitely placed on top of a square in central position, while at least one is placed on either triangle belonging to a rhomb. Excluding sites are between adjacent rhombs. Therefore, compared to the other two tilings, more information is transferred to the third layer. This leads to an aba stacking on a local level around the symmetry centers as illustrated in Fig. 5.11. The first and third layer form an almost identical octagonal tiling patch above the local symmetry centers. However, this sequence is not maintained as z increases because of the two length scales in adsorbtion sites and possible local disorder due to flips.

In order to determine, when the global order begins to break down due to the subsequent emergence of defects to compensate for accumulated strain, we conduct a mode analysis for each layer as explained in section 3.3. Excerpts of this analysis are depicted in Fig. 5.12. For sedimentation on the Square-Triangle substrate, dislocations emerge already in the seventh layer, while the structure on the Penrose-Rhomb tiling exhibits defects from the ninth layer on. The tiling where global order seems to be conserved best is the Ammann-Beenker as the first dislocation is identified in the eleventh layer. Therefore, taking into account the resilience of global order as well as the local stacking properties, the octagonal Ammann-Beenker tiling seems to be a promising candidate for the template-directed growth to obtain three-dimensional colloidal quasicrystals.

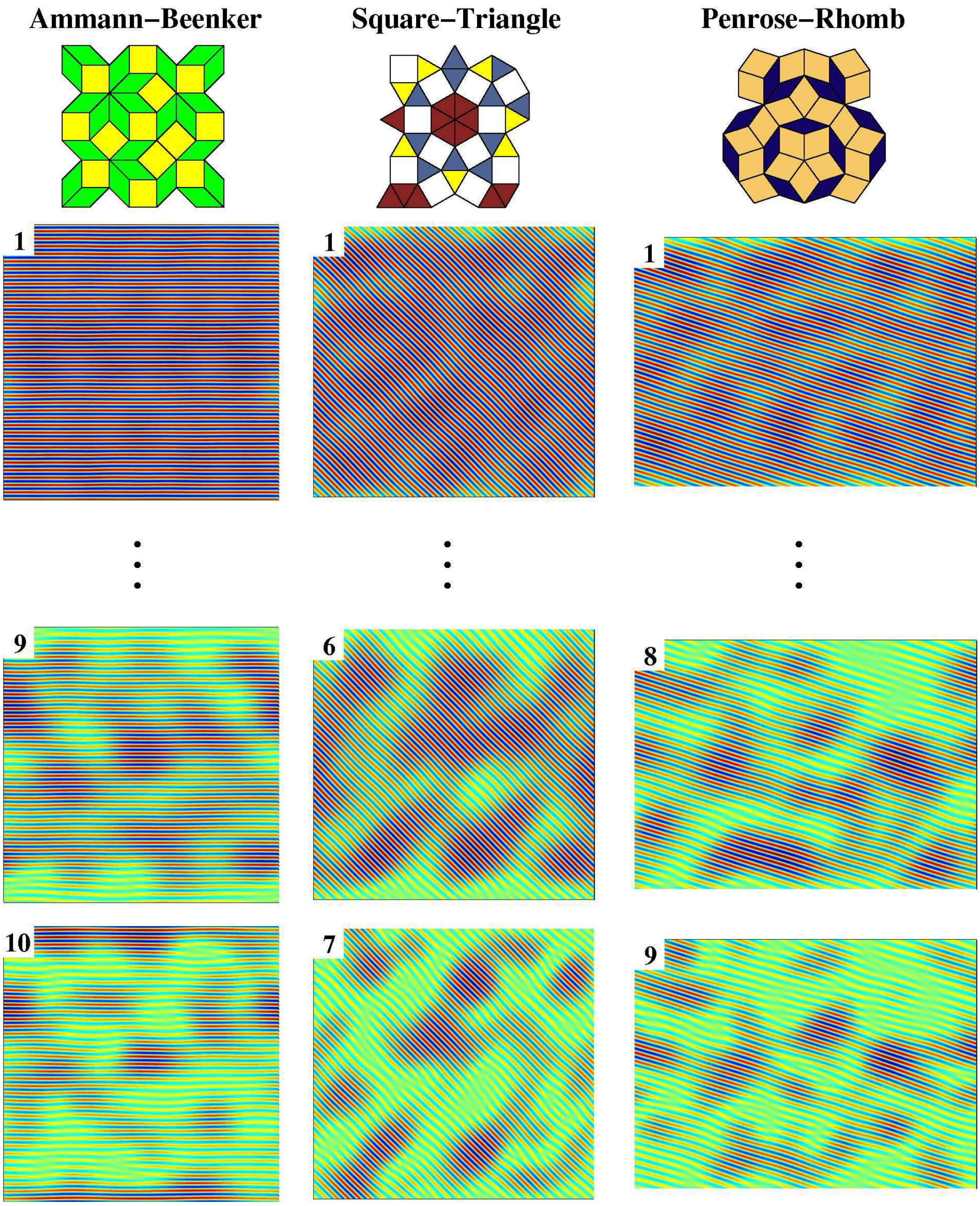

Figure 5.12.: Excerpts of the mode analysis for the quasicrystalline layers obtained by colloidal epitaxy. Each column corresponds to a different substrate. The aspect ratio of the modes resembles the aspect ratio of the rational approximant. In each column, one specific density mode of the average colloidal position is depicted for various layers. Note the different layer numbers. For the octagonal Ammann-Beenker substrate defects start to emerge from the tenth layer, while the colloidal structures grown by deposition on the dodecagonal Square-Triangle and decagonal Penrose-Rhomb tiling exhibit already defects in the seventh and ninth layer.

5.2.3. Potential for experimental realization

Based on the conducted simulation studies, the octagonal Ammann-Beenker tiling seems to be a promising candidate of quasicrystalline template-directed growth. From all tested substrates, it exhibits the highest number of defect free quasicrystalline layers. In addition, octagonal symmetry seems to be more beneficial for stacking. At the moment, similar experiments to [143, 145] but with quasicrystalline templates, are being realized by the group of C. Bechinger in Stuttgart. At present, order on periodic as well as aperiodic substrates forms with considerably more defects probably due to too small gravitational forces or too fast sedimentation velocities. Nevertheless, the colloids attach as desired on the quasicrystalline tiling and yield the exact tiling in the first layer. Therefore, we remain confident that our results will soon be confirmed experimentally.

5.3. Conclusion

We have shown that three-dimensional colloidal quasicrystals of various rotational symmetries can be obtained by a template-directed growth approach. No fine tuning of the interaction potential in the solvent is required, a sedimentation under gravity suffices to achieve several quasicrystalline layers. Moreover, we have identified the octagonal Ammann-Beenker tiling as the most promising candidate from the studied tilings. The mode analysis reveals a long lasting resilience in global order surpassing the structures on the dodecagonal Square-Triangle and the decagonal Penrose-Rhomb tiling. Our results demonstrate the potential of colloidal epitaxy as an alternative route to obtain three-dimensional colloidal quasicrystals, especially if different symmetries are desired. In principle, our results should be reproducible by sedimentation experiments like [143, 145] and preliminary results seem to indicate that. Experimental progress might be important for photonic applications [148]. As the next step, we study the influence of designed defects within the quasicrystalline template on the grown colloidal structure.

> Women love us for our defects. If we have enough of them, they will forgive us everything, even our gigantic intellects.
>
> (*Oscar Wilde* 1854-1900)

CHAPTER 6

Colloidal Epitaxy on Quasicrystalline Substrates with Defects

In the previous chapter, we demonstrated the potential of a template-directed approach to obtain three-dimensional colloidal quasicrystals with different rotational symmetries. Here, we elaborate this further by investigating the influence of substrate defects on the growth process. Apart from modified substrates, the model as well as all interaction parameters remain completely unchanged to section 5.1. First, local flips as caused by phasonic excitations are inserted into the substrate tiling without observing a significant effect on the sedimented structure regarding the global order. Second, we design the template patterns with well-defined dislocations. Upon sedimentation stable defect lines evolve within the grown colloidal structure. We elucidate how shape and direction of these defect lines can be influenced in a controlled manner. In particular, we present sets of basis Burgers vectors that lead to stable defect lines. The prospect of controlled defect lines in the colloidal quasicrystal might complement the potential for photonic applications [150].

Almost all material properties of a crystal are influenced by possible defects of the structure [236]. For example, in two dimensions melting is caused by the formation and subsequent separation of pairs of dislocations, which in a second step disassociate into isolated disclinations [236]. Dislocations occur along points where additional lattice lines start or end and are characterized by Burgers vectors. Around the dislocation, the crystal structure is usually strained. In quasicrystals, lattice lines cannot be inserted or removed in a straightforward way and therefore the characterization of defects in quasicrystals is more complicated as explained in section 2.3.

Quasicrystals possess additional degrees of freedom. Beside phonons, there exist additional hydrodynamic modes called phasons, which do not occur in periodic crystals. Such phasons correspond to correlated rearrangements that in the limit of long wavelengths do not cost any free energy [238] and influence many material properties of quasicrystals, ranging from crack propagation [48] to entropic stability [56]. Dislocations in quasicrystals require a positional as well as a phasonic strain around a dislocation line [232]. As a consequence, a Burgers vector that describes a dislocation in a quasicrystal possesses additional components because not only the positional fault is denoted but also the disturbance of the phasonic degree of freedom has to be considered.

Up to now, similar colloidal epitaxy systems have only been considered to study periodic colloidal crystals with dislocation lines [230, 231]. We observe some specific quasicrystalline properties. While in a periodic lattice the course of a dislocation line does not depend on the starting position, in quasicrystals the starting position matters and might influence the bending of a dislocation line. Besides, in periodic crystals, all Burgers vectors are sums of integer multiples of lattice basis vectors. As a consequence, the length of all Burgers vectors is larger than or equal to the length of the basis vectors. In quasicrystals, there is a larger variety of dislocations because there are more basis vectors. Furthermore, the phononic part of a Burgers vector might be arbitrary small. While in a periodic crystal the energy cost of dislocations with large Burgers vectors is usually larger than for those with small Burgers vectors, dislocations with small phononic Burgers vectors in quasicrystals might even decompose into multiple dislocations with larger phononic Burgers vectors during the growth process. This underlines the importance of the phasonic distortions associated with a dislocation in a quasicrystal, which is taken into account by the additional, phasonic part of the Burgers vector. We identify a set of basis Burgers vectors that lead to stable defect lines.

In section 6.1, the sedimentation of colloids on a template tiling containing phasonic excitations is investigated. In section 6.2, the construction of substrates containing well-defined dislocations is explained and a set of basis Burgers vectors that lead to stable defect lines in the growth process is presented. In section 6.3, we discuss the sedimentation of colloidal particles on substrates with dislocations for two quasicrystalline symmetries. In the first part, the octagonal system is studied which has proven to be most suited for the epitaxial approach from the previous chapter, while in the second part, defect lines for dodecagonal symmetry are explored, since this rotational symmetry is frequently reported in mesoscopic quasicrystalline systems [119, 161]. The contents of this chapter have undergone external revision and are already published in [D].

6.1. Growth on substrates with local phasonic excitations

In chapter 5, we demonstrated that the sedimentation of colloids on quasicrystalline substrates leads to three-dimensional colloidal structures comprised of stacked two-dimensional quasicrystalline layers. Analyzing the particular layers has revealed that the average colloidal density becomes less structured for higher layers due to flips during the growth process. Phasonic flips are expected to be easily excited by thermal fluctuations, since the increase of the free energy due to a phasonic flip is small [239]. Here, we estimate their effect regarding the global order of the structure by inserting phasonic excitations directly into the substrate tiling. As tiling, we chose the octagonal Ammann-Beenker and incorporate the excitations by randomly flipping some tiles, namely two rhombs and a square (see Figs. 6.1(a) and (c)). A feature to incorporate selected flips is implemented in the program *Tilingbuilder* in the appendix. We compare the structure that grows on a perfect tiling to structures obtained from deposition on substrates with different amounts of phasonic flips. The amount of displaced vertices, i.e. substrate holes, ranges from 1% to 7% of the total number of vertices. Such imperfections might also be caused in an experimental construction process.

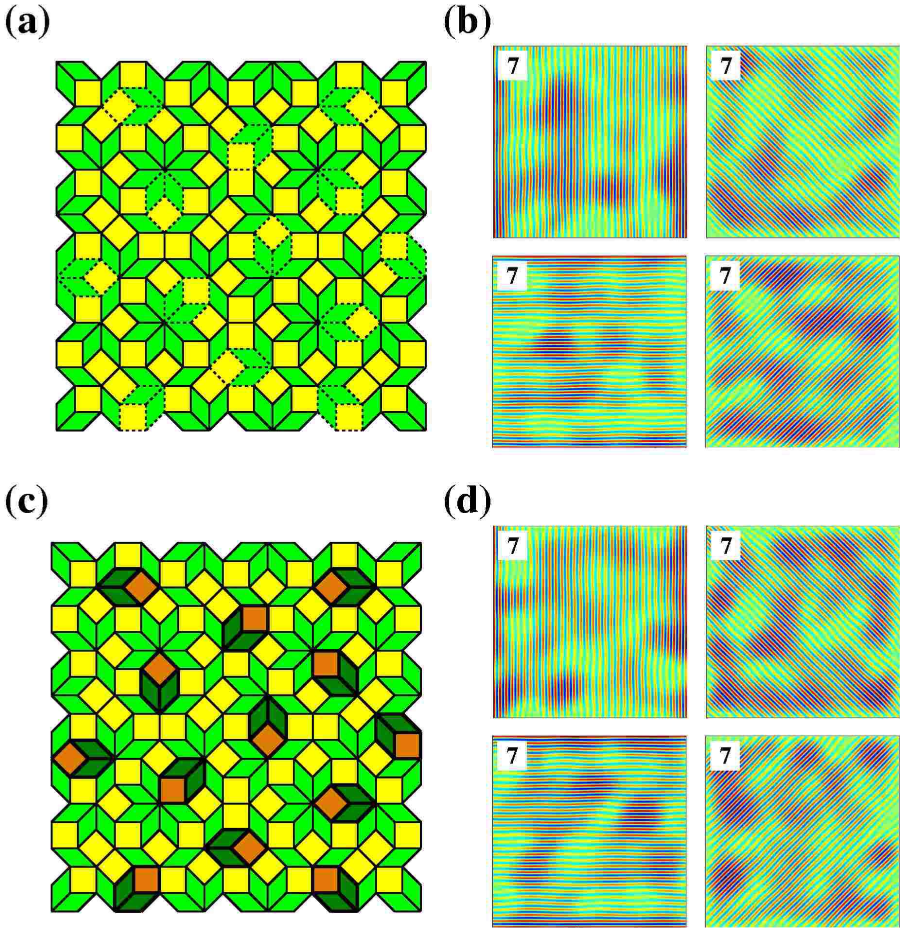

Figure 6.1.: The growth on a octagonal substrate is compared to a structure obtained from a substrate containing local phasonic excitations (cf. [D]). As a consequence, 5% of the vertex coordinates differ. The tilings that correspond to the substrates without and with flipped tiles are shown in (a) and (c), respectively. The flipped tiles in (c) are colored orange and dark green. The analysis of the density modes for the seventh layer of the colloidal structure grown on the defect-free substrate is shown in (b) and for the structure grown on a substrate where local phasonic flips were introduced in (d). In both cases, some strain has been accumulated during the sedimentation process as apparent by the green areas without resulting in the formation of dislocations. Regarding the global order that is analyzed here, there is no significant difference between the defect-free substrate and the substrate with local disorder.

We determine the long-range order by analyzing the basic density modes [55]. The modes of the seventh layer for the perfect and a structure containing a flip concentration of 5% are displayed in Fig. 6.1(b) and (d). Compared to the sedimentation on the perfect Ammann-Beenker tiling the global order of the substrate with flips is only slightly less pronounced for all tested concentrations. Therefore, there is no significant effect of isolated uncorrelated flips on the long-range order regardless whether these flips are induced by the substrate or occur during the growth process. Our epitaxially obtained quasicrystal is almost not affected.

6.2. Construction of substrates with built-in dislocations

In this section, the design of quasicrystalline substrates with well-defined dislocations is explained. Following the theoretical description for two-staged melting of two-dimensional quasicrystals originally derived in [234, 250, 251] and summarized in section 2.3, dislocations are incorporated into quasicrystalline intensity fields from interfering laser beams. The properties of these fields have been studied in [137] as well as in section 4.1. In particular, phononic and phasonic displacement vectors have been derived that leave these intensity fields invariant [138, A]. Here, we expand these studies to determine basic Burgers vectors for the octagonal and dodecagonal interference pattern. Furthermore, we illuminate conditions how the strain fields due to a dislocation can be accommodated into the rational approximant of the simulation box.

6.2.1. Burgers vector in interference pattern

Laser intensity fields with quasicrystalline symmetry are realized by interfering N symmetrically arranged laser beams [131]. In this continuous description, dislocations can be incorporated by spatially varying laser phases $\varphi(\mathbf{r})$ [238]. Thus, Eq. (4.2) is rewritten to

$$V(\mathbf{r}) = -\frac{V_0}{N^2}\sum_{i=0}^{N-1}\sum_{j=0}^{N-1}\cos[(\mathbf{G}_i-\mathbf{G}_j)\cdot\mathbf{r}+\varphi_i(\mathbf{r})-\varphi_j(\mathbf{r})]\,, \tag{6.1}$$

where $\mathbf{r}$ denotes a positional vector in the xy-plane of the template and $\mathbf{G}_j$ a projected wave vector. By placing holes at the positions of pronounced maxima of laser interference patterns we generate templates with tiling patterns similar to the ones from chapter 5 yet with dislocations. The phases in Eq. (6.1) are parameterized in the conventional manner according to [238] by

$$\varphi_i(\mathbf{r}) = \mathbf{G}_i\cdot\mathbf{u}(\mathbf{r}) + \mathbf{G}_{k\,\cdot\,i \bmod N}\cdot\mathbf{w}(\mathbf{r})\,, \tag{6.2}$$

where $\mathbf{u}(\mathbf{r})$ and $\mathbf{w}(\mathbf{r})$ are the phononic and phasonic displacement fields belonging to a dislocation. For both periodic and aperiodic crystals, the sum of displacements along a path around the core of a dislocation has to amount to the components $\mathbf{\Delta u}$ and $\mathbf{\Delta w}$ of the Burgers vector such that $\Delta\mathbf{u} = \oint d\mathbf{u}(\mathbf{r})$ and $\Delta\mathbf{w} = \oint d\mathbf{w}(\mathbf{r})$. Furthermore, for a well-defined dislocation, i.e. a dislocation whose strain field causes no discontinuous gap in the structure, the components $\mathbf{\Delta u}$ and $\mathbf{\Delta w}$ must represent combinations of phononic and phasonic displacements that leave the structure invariant in the static case, where

$$V_{\mathbf{w}=\mathbf{0}}(\mathbf{r}) = V_{\mathbf{w}+\mathbf{\Delta w}}(\mathbf{r}+\mathbf{\Delta u}) \tag{6.3}$$

is fulfilled. Therefore, the Burgers vector are related to the displacements applied for the mapping to characteristic areas of colloidal particles in quasicrystalline laser fields deployed in [138, A] as well as in section 4.3. In quasicrystals, all Burgers vectors must obey Eq. (6.3).

Regarding the rotational symmetries studied here, namely the octagonal $N = 8$ and dodecagonal $N = 12$ laser field, any Burgers vector can be expressed as integer linear combination of the basic Burgers vectors ($\mathbf{b}_j^{(u)}$, $\mathbf{b}_j^{(w)}$) with

$$\begin{aligned}\mathbf{b}_j^{(u)} &= (u_r \cos[\pi(2j-1)/N], u_r \sin[\pi(2j-1)/N]) \\ \text{and } \mathbf{b}_j^{(w)} &= (w_r \cos[k\pi(2j-1)/N], w_r \sin[k\pi(2j-1)/N])\end{aligned} \tag{6.4}$$

for $j = 1 \ldots N$. A set of D of these vectors, where D is the rank of the quasicrystal, is a suitable basis for all Burgers vectors. For octagonal symmetry, we find $k = 3$, $u_r = (1+\sqrt{2}/2)^{\frac{1}{2}} a_V/2$, and $w_r = -u_r/(1+\sqrt{2})$, while in case of dodecagonal symmetry, $k = 5$, $u_r = \sqrt{2}/(3-\sqrt{3})a_V$, and $w_r = (\sqrt{3}-2)u_r$. a_V denotes the shorter length scale of the quasicrystal. Since both quasicrystals are of rank $D = 4$, four Burgers vectors from Eq. (6.4) are sufficient to characterize the topological charge of any dislocation.

6.2.2. Strain field in interference pattern

In order to incorporate a dislocation with well-defined Burgers vector $\mathbf{B} = (\Delta\mathbf{u}, \Delta\mathbf{w})$ in the octagonal and dodecagonal quasicrystalline laser field, a four-dimensional displacement field $\mathbf{D}(\mathbf{r}) = (\mathbf{u}(\mathbf{r}), \mathbf{w}(\mathbf{r}))$ is required. Its phononic $\mathbf{u}(\mathbf{r})$ and phasonic $\mathbf{w}(\mathbf{r})$ components are tuned by the phases $\varphi_j(\mathbf{r})$ of the laser beams. The full expression is derived in [234] and is given by the form

$$2\pi\mathbf{D}_j(\mathbf{r}) = B_j \arctan\left(\frac{y}{x}\right) + \sum_{k=1}^{4}\sum_{l=1}^{2} \alpha_{jkl}(\lambda, \mu, K_1, K_2, K_3) f_{jkl}(\mathbf{r}) B_k. \tag{6.5}$$

Also compare to Eq. (2.13) in section 2.3. The arctan-term in Eq. (6.5) constitutes the topology of the dislocation, while the elasticity in the strain field is controlled by the second term containing the elastic constants λ, μ, K_1, K_2, and K_3. Minimizing the increase of the free energy due to the strain in phononic and phasonic displacement fields for a given Burgers vector yields the geometric $f_{jkl}(\mathbf{r})$ as well as the elastic functions

$\alpha_{jkl}(\lambda, \mu, K_1, K_2, K_3)$ [234]. The topological properties of the dislocation do not depend on $\alpha_{jkl}(\lambda, \mu, K_1, K_2, K_3)$ but are entirely characterized by the Burgers vector. For simplicity, in the following we will employ $\alpha_{jkl}(\lambda, \mu, K_1, K_2, K_3) = \alpha$ with either $\alpha = 0$ or $\alpha = 1$. While these two cases are the same regarding the topology of the dislocation, the strain distribution in the vicinity of the defect might differ. In order to keep eventual discontinuities experienced by colloids crossing the periodic boundaries small, the strain field $\mathbf{D}(\mathbf{r})$ has to decay towards the box edges. This can be achieved by demanding a total Burgers vector of zero for the whole template such that the substrate contains at least two dislocations with opposite charge. In addition, to decrease $\mathbf{D}$ completely to zero towards the boundaries of the simulation box, we also add a sigmoid function in Eq. (6.5). In Fig. 6.2, an example for an octagonal laser interference pattern with two dislocations as well as the resulting discretized Ammann-Beenker tiling for the substrate are displayed. The template holes are placed at the most pronounced maxima of the intensity, i.e. the vertices of the tiling.

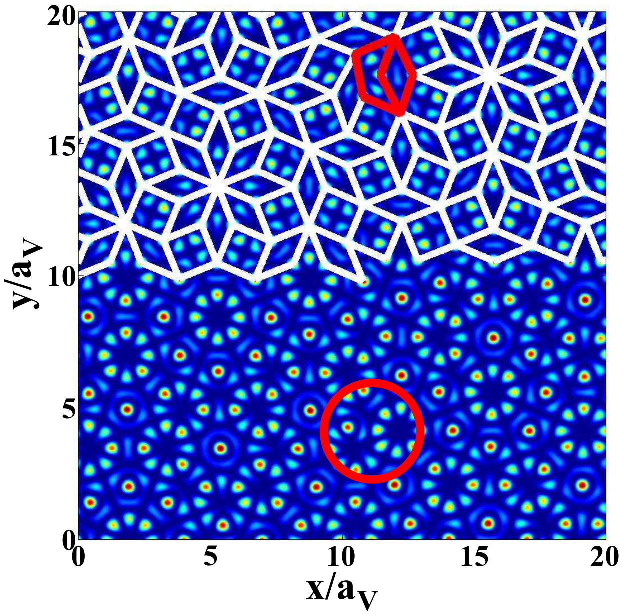

Figure 6.2.: Construction of the substrate tiling with dislocation seed from octagonal laser field by interfering eight symmetrically arranged laser beams. At local maxima of the intensity holes of the substrate are located, if the distance between them amounts at least to the colloidal diameter σ. Thus, an Ammann-Beenker-like tiling is formed (drawn in white, see also [163]). The cores of two dislocations are marked in red. The upper one is given by the Burgers vector $\mathbf{B} = (\mathbf{b}_1^{(u)}, \mathbf{b}_1^{(w)})$ where $\mathbf{b}_1^{(u)}$ and $\mathbf{b}_1^{(w)}$ are given by Eq. (6.5), the bottom one by the opposite Burgers vector. The figure is adopted from [D].

6.3. Growth on substrates with dislocations

In this section, results for the sedimentation of colloidal particles on designed quasicrystalline templates containing dislocation pairs with opposite Burgers vector are presented. We focus on octagonal and dodecagonal substrate symmetry. Analyzing individual density modes for each layer of the stacked colloidal structure reveals that the Burgers vectors are preserved in all layers. As a desired consequence, there exist well-defined lines connecting the positions of dislocations through the layers. Though in a quasicrystal there exist Burgers vectors with arbitrarily small phononic part, our simulation show that defect lines given by the basis Burgers vectors are stable and do not split up into multiple dislocations with smaller phononic part.

In the first part, we explore on the basis of the octagonal template how the local environment of a dislocation seed tunable by its location as well as the applied strain field in the vicinity affects the course of the dislocation line. In addition, we discuss topological properties like annihilation and forking of defect lines. In the second part, we present additional topological features arising in particular for the dodecagonal symmetry.

The major results are illustrated in Fig. 6.3 to Fig. 6.8 which share a common composition: Each one contains a schematic representation of the Burgers vector at hand, an excerpt of the relevant density modes, and a three-dimensional representation of the defect line within the structure for visual clarity. Since the presence of dislocations distorts the template tiling, the overall growth quality is reduced such that dislocations might already emerge for deeper layers than for perfect templates deployed in section 5.2.2. Therefore, in order to exclude unintended interactions between induced and emerging dislocations, we restrict our analysis to seven layers for the octagonal and six for the dodecagonal template.

6.3.1. Dislocation lines in quasicrystals with octagonal symmetry

We conducted the sedimentation on numerous substrate samples with different environments for the dislocation seed. This includes various locations for the individual dislocation as well as different relative orientations for the complete dislocation pair in the template plane and different displacement fields in the vicinity controlled by the parameter α.

In Fig. 6.3, the defect lines of a pair of dislocations are shown. The substrate is prepared with two dislocations as described in the previous subsection. The phononic part of the Burgers vector of one dislocation is given by the first basis Burgers vector $\mathbf{b}_1^{(u)}$, of the second dislocation by $-\mathbf{b}_1^{(u)}$. As a consequence, the phasonic components of the Burgers vectors must be $\mathbf{b}_1^{(w)}$ and $-\mathbf{b}_1^{(w)}$. Therefore, the first Burgers vector is $\mathbf{B} = (\mathbf{b}_1^{(u)}, \mathbf{b}_1^{(w)})$ and the second dislocation is given by the inverse Burgers vector $-\mathbf{B}$ such that the total Burgers vector for the whole simulation box is zero.

First, we explain how the local environment of a dislocation seed in the substrate tunable by the position or the strain field affects the course of the dislocation line through the grown structure. For instance, the dislocation lines in Fig. 6.3 are obtained for the sedimentation on a template with $\alpha = 0$ while in Fig. 6.4 dislocations with the same Burgers vectors were placed at identical positions but for $\alpha = 1$. While in Fig. 6.3 the dislocation lines are vertical, the corresponding lines in Fig. 6.4 bend away from each other. Finite size effects through the boundaries retire as origin of the observed bending of the lines towards the box edges, as we tested different modulations of the sigmoid function in Eq. (6.5), even a violation of the rational approximant, without observing any affects on the bending direction at all. However, if the orientation of the dislocation pair in Fig. 6.4 is slightly rotated in the substrate sample the course of the dislocation line becomes almost vertical again (yellow dislocation line), though now for $\alpha = 1$. In general, we observe that the bending of dislocation lines depends on the strain in the surrounding phononic and phasonic displacement fields, which changes if the value of α is varied. The position of the dislocation in the substrate is of similar influence on the bending of the dislocation line. Note that in a periodic crystal the only choice concerning the position of a dislocation is where it crosses the unit cell. However, in a quasicrystal, no unit cells exist and therefore there are infinite possibilities where to place dislocations. Our simulations reveal that different starting positions might lead to different bending of the dislocation lines.

Aside from different local environments, templates containing dislocations with other Burgers vector from the basis set in Eq. (6.4) were also considered. In Fig. 6.5 the substrate is prepared such that two dislocation lines with opposite Burgers vectors bend towards each other. They meet between the second and third layer and annihilate, i.e. in higher layers there is no more dislocation. The course of the dislocation lines can also be perceived as a single dislocation line that starts at one dislocation on the substrate bends around and ends up at the second dislocation on the substrate. This is in perfect agreement with the conservation of the sum of all Burgers vectors but has never been reported for quasicrystals before.

Finally, in Fig. 6.6 we prepare a substrate with dislocations that are given by Burgers vectors that are composed of two basis Burgers vectors. We observe that the dislocation lines split up into two dislocation lines given by basis Burgers vectors. At the forks the sum of Burgers vectors is preserved.

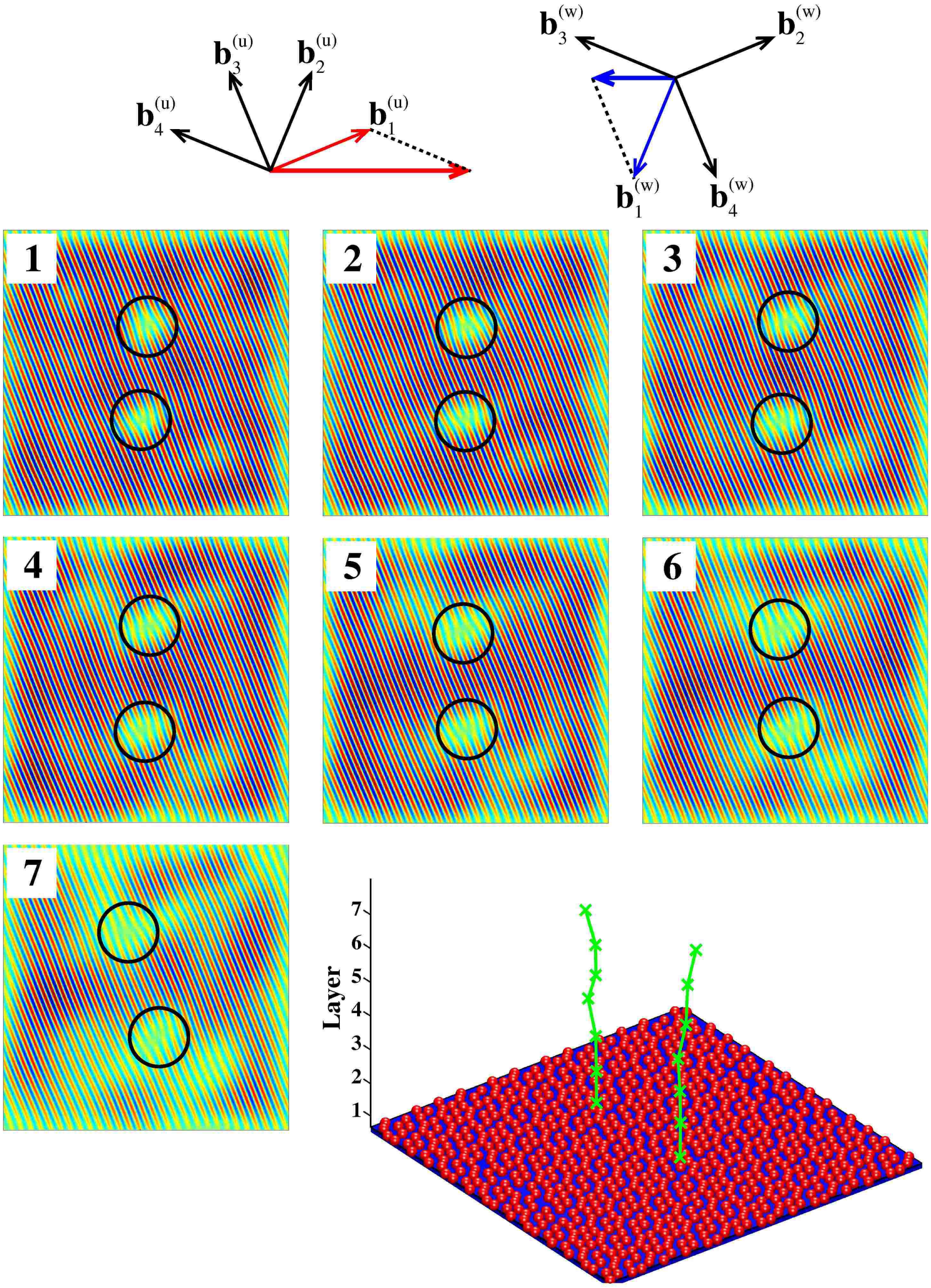

Figure 6.3.: Vertical defect lines with Burgers vector $\mathbf{B} = (\mathbf{b}_1^{(u)}, \mathbf{b}_1^{(w)})$ (upper defect) and $-\mathbf{B}$ (bottom defect) as well as $\alpha = 0$. In the top, a schematic representation of the Burgers vector of the upper dislocation with phononic (red) and phasonic contribution (blue) is given in context with the basis Burgers vectors. The middle line contains the mode analysis for the mode in direction of $\mathbf{b}_1^{(u)}$ for each layer such that the position and topology of the dislocations are revealed in each layer. Below, this analysis is summarized into a three-dimensional illustration for the course of defect lines through the grown colloidal quasicrystal. Figure is adopted from [D].

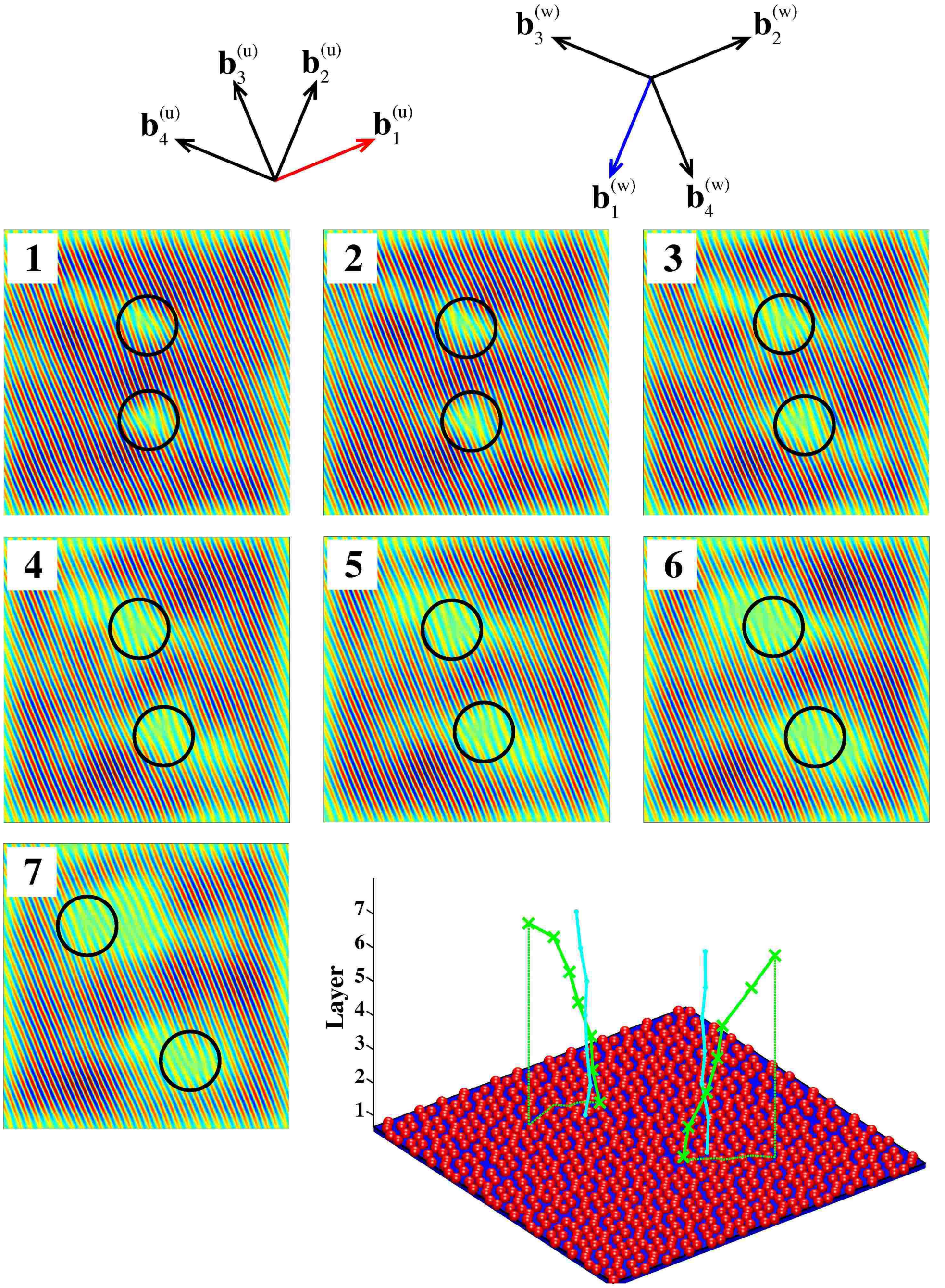

Figure 6.4.: Bending defect lines with Burgers vector $\mathbf{B} = (\mathbf{b}_1^{(u)}, \mathbf{b}_1^{(w)})$ (upper defect) and $-\mathbf{B}$ (bottom defect) are obtained with $\alpha = 1$. In the top, a schematic representation of the Burgers vector of the upper dislocation with phononic (red) and phasonic contribution (blue) is given in context of the basis Burgers vectors. In the middle row, the mode analysis is displayed for the mode in direction of $\mathbf{b}_1^{(u)}$. In the bottom, the course of these bending defect lines is illustrated in three dimensions (green lines). If the dislocation pair is rotated around the substrate center by an angle of approximately $\pi/8$, the induced course of the defect line is vertical (yellow lines). Figure is adopted from [D].

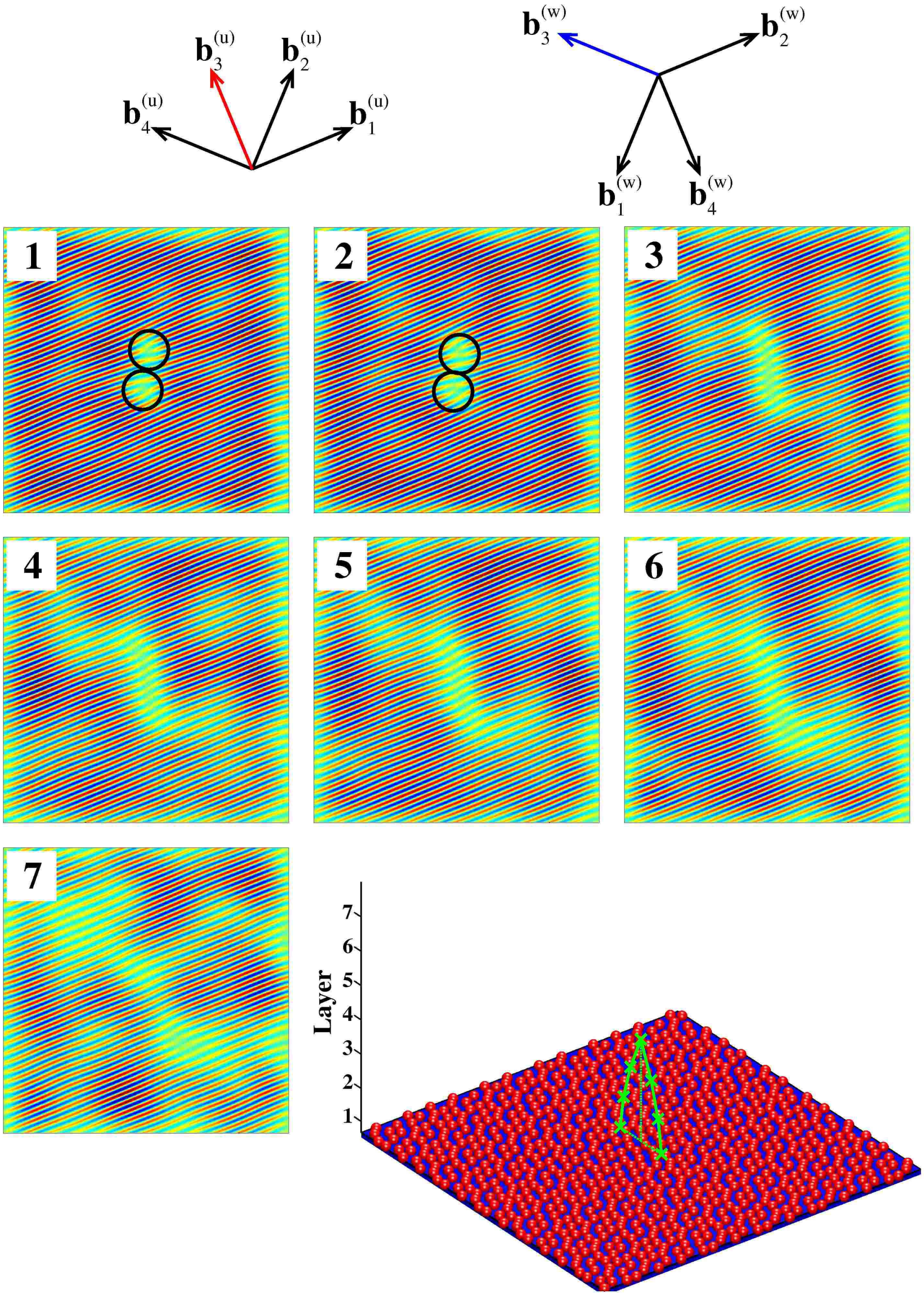

Figure 6.5.: Annihilation of defect lines (cf. [D]). The dislocations in the substrate are given by the Burgers vectors $\mathbf{B} = (\mathbf{b}_3^{(u)}, \mathbf{b}_3^{(w)})$ (upper dislocation) and its inverse counterpart (bottom dislocations). The top row contains a schematic representation of the Burgers vector. The center images display the mode analysis along a selected mode, and in the bottom row a three-dimensional picture of the course of the dislocation lines is shown. The dislocations bend towards each other and ultimately anneal.

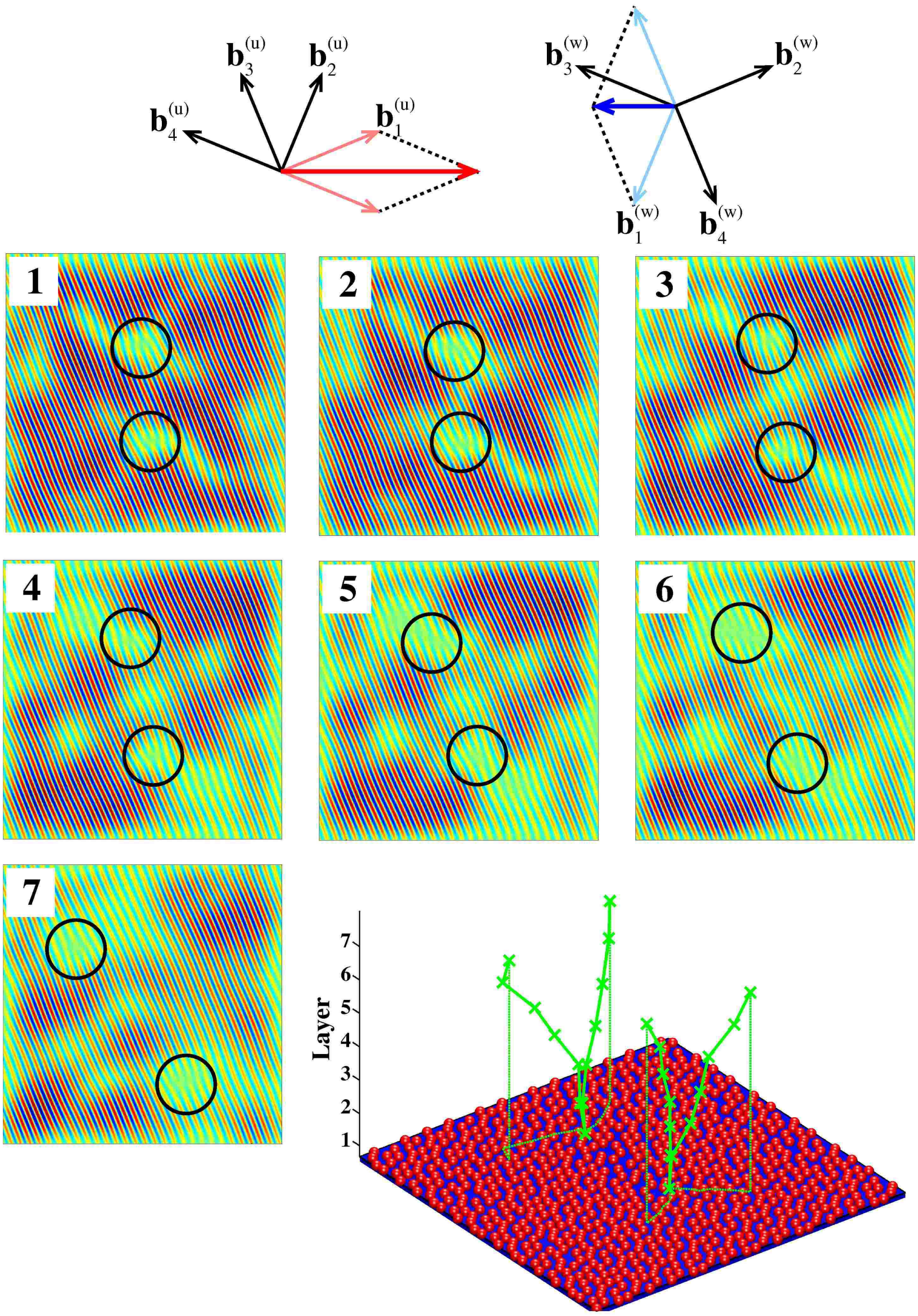

Figure 6.6.: Forking of defect lines (cf. [D]). The dislocations in the substrate are given by the Burgers vectors $\mathbf{B} = (\mathbf{b}_1^{(u)} - \mathbf{b}_4^{(u)}, \mathbf{b}_1^{(w)} - \mathbf{b}_4^{(w)})$ (upper dislocation) and their inverse counterparts (bottom dislocation). In the top row, a schematic representation of the Burgers vector is given, the center images display the mode analysis along a selected mode, and in the bottom row the three-dimensional course of the dislocation lines is depicted. The dislocation lines split up into dislocation lines given by basis Burgers vectors, i.e., $(\mathbf{b}_1^{(u)}, \mathbf{b}_1^{(w)})$ and $(-\mathbf{b}_4^{(u)}, -\mathbf{b}_4^{(w)})$ or the corresponding inverse vectors.

6.3.2. Dislocation lines in quasicrystals with dodecagonal symmetry

Extensions to templates with other quasicrystalline symmetries are straight forward. For instance, discretizing the interference pattern of Eq. (6.1) for $N = 12$ laser beams yields a pattern similar to the Square-Triangle tiling with dodecagonal rotational symmetry. Dislocations are completely described by sums of integer multiples of the four basis Burgers vectors given in Eq. (6.4). As an advantage, the dodecagonal symmetry might be more suited for applications, because for several pair potentials the intrinsic formation of two-dimensional quasicrystals with dodecagonal symmetry has been reported (e.g., [117, 119]). We complement this list of pair potentials by depletion forces for the colloid-polymer mixture in chapter 7. Note that the situations presented in the previous section on the basis of the octagonal substrate are also observed for the growth on the dodecagonal substrate. Therefore, we concentrate on two new topological features arising for the dodecagonal symmetry in the following.

In contrast to octagonal rotational symmetry, a dislocation in a dodecagonal substrate given by a basis Burgers vector from Eq. (6.4) is always visible in two density modes (see also [55]). In addition, for geometric reasons, every Burgers vector of the length of a basis Burgers vector can be decomposed into two other basis vectors, such that $(\mathbf{b}_i^{(u)}, \mathbf{b}_i^{(w)}) = (\mathbf{b}_{i-2}^{(u)}, \mathbf{b}_{i-2}^{(w)}) + (\mathbf{b}_{i+2}^{(u)}, \mathbf{b}_{i+2}^{(w)})$. For example, the green vector $\mathbf{b}_3^{(u)}$ in the top panel of Fig. 6.7 equals the sum of $\mathbf{b}_1^{(u)}$ and $\mathbf{b}_5^{(u)}$ (yellow and blue vectors in Fig. 6.7). The substrate employed in Fig. 6.7 contains two dislocation pairs. The upper pair consists of dislocations where the phononic part of the Burgers vectors are $\mathbf{b}_1^{(u)}$ (yellow vector and yellow dislocation line) and $\mathbf{b}_5^{(u)}$ (blue vector and blue dislocation line). While these dislocation lines start at slightly different positions in the substrate, they bend towards each other and when they meet a single dislocation line with $\mathbf{b}_3^{(u)} = \mathbf{b}_1^{(u)} + \mathbf{b}_5^{(u)}$ (green vector and green dislocation line) continues to grow. In the bottom dislocation pair all dislocations possess the negative Burgers vectors of the corresponding upper defects, but the same merger of dislocation lines can be observed. Note that, regarding a complete dislocation pair, the sum of Burgers vectors is preserved in both cases. However, the example shown in Fig. 6.7 demonstrates that in the case of dodecagonal substrate symmetry the characterization as single, double, or n-fold dislocation is ambiguous because in principle every dislocation can be split into two dislocations with Burgers vectors of the same length.

The fact that a basis Burgers vector in a dodecagonal template is always visible in two density modes complicates tracking the defect lines through the layers as two modes have to be analyzed in order to determine the course of a dislocation. Besides, we also observe the case, in which the defects that we identify in the two respective modes are separated by a significant distance (see Fig. 6.8). This implies that Eq. (6.3) is violated on a local level. In Fig. 6.8, first the dislocation lines grow almost vertically and the defects in both modes indicate almost the same position for the dislocation. In the fifth layer, the defects anneal partially in one mode, resulting in a defect plane.

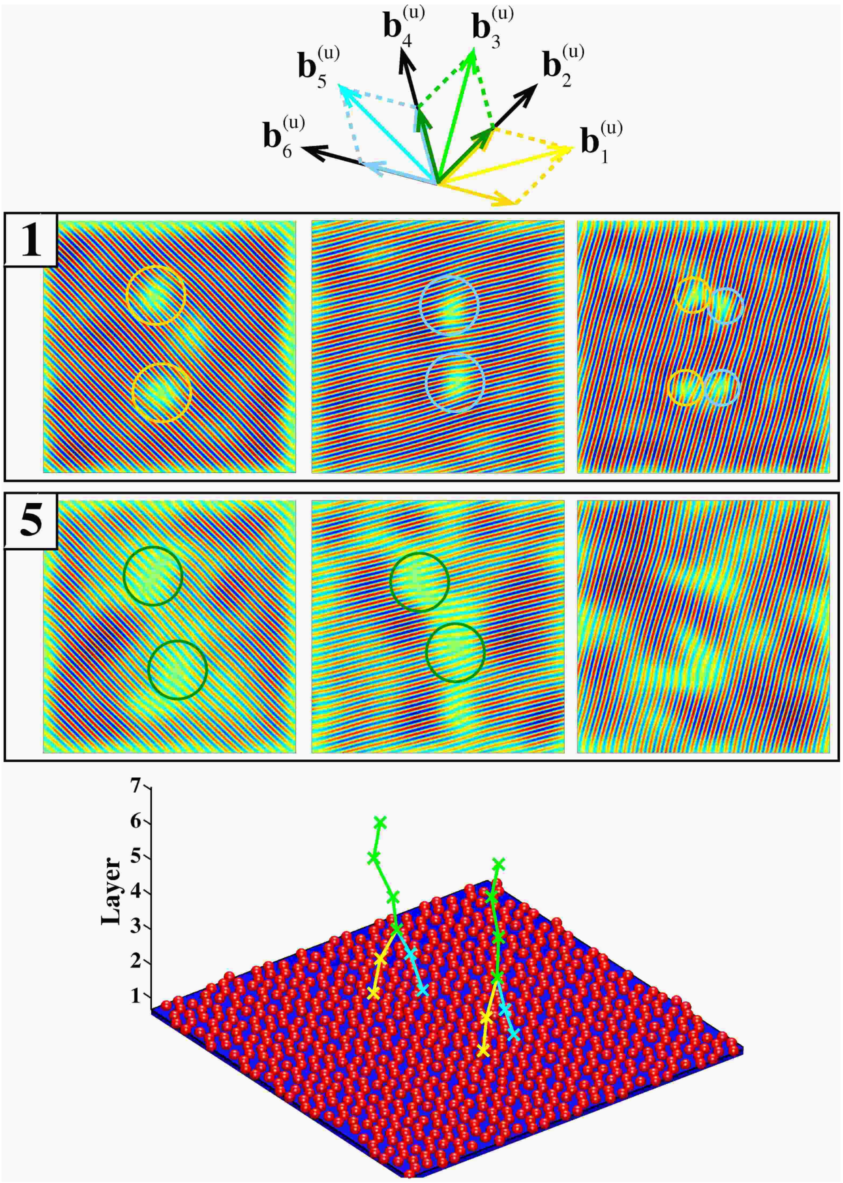

Figure 6.7.: Coalition of defect lines on a dodecagonal substrate (cf. [D]). The dislocation pairs in the substrate are given by the Burgers vectors $\mathbf{B}_1 = (\mathbf{b}_1^{(u)}, \mathbf{b}_1^{(w)})$ and $\mathbf{B}_2 = (\mathbf{b}_5^{(u)}, \mathbf{b}_5^{(w)})$ (upper pair) and their inverse counterparts (lower pair). The top row contains a schematic representation of the phononic contribution of the Burgers vectors, excerpts of the mode analysis are shown in the center, and in the bottom row the three-dimensional course of the dislocation lines is illustrated. Note that all dislocations are visible in two modes (denoted by the smaller vectors in the top panel). In all rows, the respective color coding for Burgers vector, associated density modes, and defect lines is the same. The dislocations $\mathbf{B}_1$ (yellow) and $\mathbf{B}_2$ (blue) bend towards each other. By partially annealing in one mode, they form a coalition in the third layer and yield a defect line with Burgers vector $(\mathbf{b}_3^{(u)}, \mathbf{b}_3^{(w)})$ (green). The sum of Burgers vectors is preserved throughout the coalition.

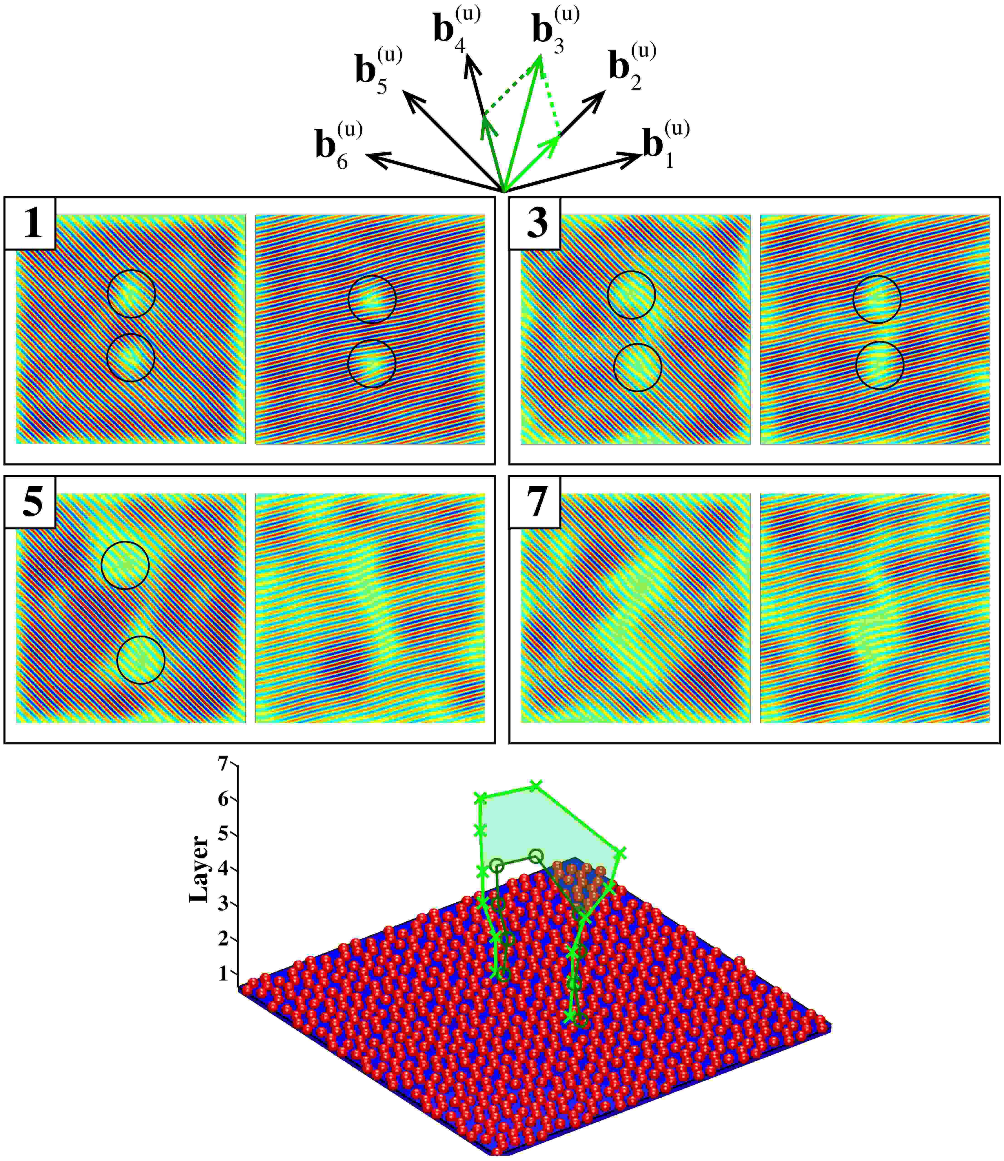

Figure 6.8.: Development of a defect plane on a dodecagonal substrate (cf. [D]). The dislocations are given by the Burgers vectors $\mathbf{B} = (\mathbf{b}_3^{(u)}, \mathbf{b}_3^{(w)})$ (upper dislocation) and their inverse counterparts (lower dislocation). In the top, a schematic representation of the phononic contribution of the Burgers vectors and the mode directions is depicted. The defect is visible in two modes (light green and dark green). The mode analysis in the center images contains the two modes associated with the dislocation. The bottom panel shows the three-dimensional course of the defects that are observed in the individual modes, i.e. the light green and the dark green line together correspond to a dislocation line. Until the fourth layer, the induced dislocations develop vertical in both modes preserving a well-defined and well-localized dislocation within the resolution of our analysis. In the fifth layer, the defects anneal in one mode (dark green), while they progress in the second one (light green). This leads to the formation of a defect plane which vanishes in the seventh layer.

The defect plane vanishes two layers later when the defects in the second mode anneal. Note that when crossing the area shaded in green Eq. (6.3) is violated, i.e. there have to be distortions corresponding to nonfitting tiles close to this plane.

Substrates with decagonal symmetry can be constructed by interfering $N = 5$ laser beams, while the basis Burgers vector correspond to the phononic and phasonic displacements employed for the mapping in [138]. Similar to the dodecagonal case, dislocations with basis Burgers vectors should be visible in two individual density modes.

6.4. Conclusion

We have augmented our three-dimensional colloidal quasicrystals obtained from sedimenting colloids with hard-core and screened Coulomb pairwise interaction on quasicrystalline substrates with the feature to exhibit designed dislocation lines. Therefore, well-defined dislocations are inserted into the substrate and continue as defect line through the stacked layers. While local excitations, i.e. phasonic flips, might occur during the growth process, we can exclude them to exert a significant effect on the global order and the dislocation lines.

Though, in principle, there exist dislocations with arbitrarily small phononic Burgers vectors, we observe that dislocation lines do not necessarily split up into dislocations with smaller phononic Burgers vector. For quasicrystals with octagonal and dodecagonal rotational symmetry we have identified basis Burgers vectors that are stable. While dislocation lines with Burgers vectors comprised of multiple basis Burgers vectors dissociate into multiple lines charged with the basis Burgers vector, defect lines already charged with basis Burgers vectors do not decompose further.

Moreover, we have found the annihilation of dislocations when two defect lines with inverse Burgers vectors meet each other. We have observed bending of defect lines that depends on the strain of the phononic and phasonic displacement field in the vicinity of the dislocation and, in contrast to the behavior in periodic crystals, might also depend on the position of the dislocation in the substrate. In all cases, e.g. for all defect lines we have studied and that can bend, fork or anneal, the sum of all Burgers vectors is always conserved along all defect lines and at all forks.

In principle, the defect induced colloidal structures that we consider in simulations can also be realized in experiments analogue to the structures obtained from perfect tiling templates. In fact, sedimentation experiments on tilings containing different concentration of local phasonic flips have been tried [private comm.]. The colloidal structures grown in such a way to exhibit induced defect lines might be of additional importance for applications in photonics [150]. Furthermore, our results can lead to a deeper understanding of how physical properties of quasicrystals are influenced by defects. For example, the quasicrystal to fluid transition might depend on dislocation lines intruding from a surface or on the direct formation and unbinding of dislocation pairs. After all, in two dimensions such defects are probably the main cause for melting [234, 250, 251].

> Have no fear of perfection - you'll never reach it.
>
> *(Salvador Dal?* 1904-1989*)*

CHAPTER 7

Colloid-Polymer Mixture

In the previous two chapters three-dimensional stackings of quasicrystalline layers were obtained by sedimenting colloids under gravity as an external potential on a designed substrate. The template-guided approach enabled one to avoid the preferred bulk ordering of the monodisperse colloidal particles in order to produce quasicrystals of various symmetries. In this chapter however, we modify the internal bulk behavior of a two-dimensional charged-stabilized colloidal suspension such that the particles self-assemble into a stable quasicrystalline state. For this purpose, many options to influence the preferred bulk structure are known in colloidal physics: For instance, designed particle shapes [123, 124], patchy particle surfaces [125] or tuned pair potentials [117, 119, 126] may give rise to quasicrystalline order. Here, we modify the pair interaction potential of the colloids by adding small polymer coils to the suspension. Therefore, the repulsive interaction is augmented by a short-range attraction leading to a stable quasicrystalline state.

For the past years, a lot of effort has been devoted to study quasicrystals in soft matter [105]. Several mesoscopic systems exhibiting quasicrystalline states have been reported in experimental as well as theoretical and computational studies respectively. Regarding the former, quasicrystals have been observed in a supermolecular dendritic liquid [107], polymeric networks [108, 275], and in an aqueous solution of micelles [109]. On the theoretical side, various forms of pair interactions have been considered that yield quasicrystalline states like square-shoulder [112, 113, 119], square-well [114] or Gaussian double well potential [126]. All these examples confirm the general assessment that an interacting system of two incommensurate length scales is a basic requirement for quasirystalline stability [115, 116].

Yet, up to now a technical gap between experiment and theory seems to remain. After all, an experimental setup in which the particle-particle interaction can be controlled to the required degree to assemble soft quasicrystals by design has not been reported. Regarding experimental feasibility, one possible drawback may be that the interaction potentials often discussed are too artificial. In a recent theoretical study on quasicrystalline cluster crystals specific instructions for the properties of the required synthesized particles were provided [128]. Here, we follow an alternative way to bridge this gap and enable quasicrystalline self-assembly by design. Therefore, we consider a two-dimensional colloidal suspension of hard electrically charged spheres containing small polymer coils. These augment the screened Coulomb repulsion by a short-range attraction due to the osmotic pressure of the polymers [276]. Numerous systems governed by this depletion potential have been experimentally investigated. Hence, the general feasibility of our system is warranted [120–122]. We conduct Monte-Carlo simulations to explore the phase space and obtain a dodecagonal quasicrystal. Besides, density functional theory has been applied to predict a stable quasicrystalline phase for this colloid-polymer mixture in three dimensions [111].

The goal of the following investigations is not to derive a complete and quantitative phase diagram. Instead, it is to support a laboratory realization by narrowing the parameter space down to a manageable range. Therefore, we concentrate on the qualitative topology of the simulation space. Typical configurations obtained from simulations provide a guideline for the experimental parameters. As the focus lies in assisting an experimental realization, this chapter complements our work on tailoring colloidal quasicrystals which may be utilized for photonic applications [148, 150].

In section 7.1, the model of the colloid and polymer mixture is introduced in detail, while the simulation procedure is also explained. In addition, the ground state phase diagram derived by E. C. Oğuz is presented which serves as a starting point for promising simulation parameters. In section 7.2, we address the quality of the self-assembled quasicrystals and investigate the topology and transitions of the simulation space depending on colloidal and polymer density as well as temperature. Finally, we conclude in section 7.3.

7.1. Model of the colloid and polymer mixture

The model is introduced in three stages. First, the isotropic interaction potential between the colloidal particles in the presence of small dispersed polymer coils is explained. Second, a ground state phase diagram derived by E. C. Oğuz is presented and allows to narrow the parameter space down. Third, details on the simulation procedure are given.

7.1.1. Depletion interaction

The two-dimensional system consists of spherical colloidal particles with hardcore diameter σ_c and small polymer coils of diameter σ_p dispersed in a common solvent. This binary mixture is illustrated in Fig. 7.1. In order to stabilize the suspension the colloids carry an electric charge. Therefore, one contribution to the interaction is given by Coulomb repulsion in addition to screening effects due to counter ions from the solvent. So far, this contribution of the pair potential is identical to the one considered in the epitaxial systems from chapters 5 and 6. For convenience it is rewritten here as

$$V_{\mathrm{Yk}}(r) = \left\{ \begin{array}{cl} \epsilon \frac{\sigma_c}{r} \exp\left[-\kappa(r-\sigma_c)\right] & , r > \sigma_c \\ \infty & , r < \sigma_c \end{array} \right. . \tag{7.1}$$

The second contribution arises from the presence of the polymers. Their influence on the colloidal interactions can be described by associating an osmotic pressure Ω_p that favors short-range attraction between colloids [276]. As two colloids come close to each other an overlap volume is liberated for the polymers to explore, resulting in an increase of entropy (cf. Fig. 7.1 (a)). This depletion potential is given by (see also [111, 274])

$$V_{\mathrm{AO}}(r) = \begin{cases} -\frac{\pi}{6}\sigma_c^3\Omega_p(1+q)^3\left[1-\frac{3r}{2(1+q)\sigma_c}+\frac{1}{2}\left(\frac{r}{(1+q)\sigma_c}\right)^3\right] & , r > \sigma_c \wedge r < \sigma_c+\sigma_p \\ 0 & , \text{otherwise} \end{cases}, \tag{7.2}$$

where $q = \sigma_p/\sigma_c$ is the size ratio between colloidal and polymer diameter. The complete behavior is governed by $V_{\mathrm{AO}}(r) + V_{\mathrm{Yk}}(r)$ and displayed for various size ratios q in Fig. 7.1 (b). Note that q affects the ratios of both the length scale and the energy scale. The thermal energy is given by $\beta = 1/k_{\mathrm{B}}T$.

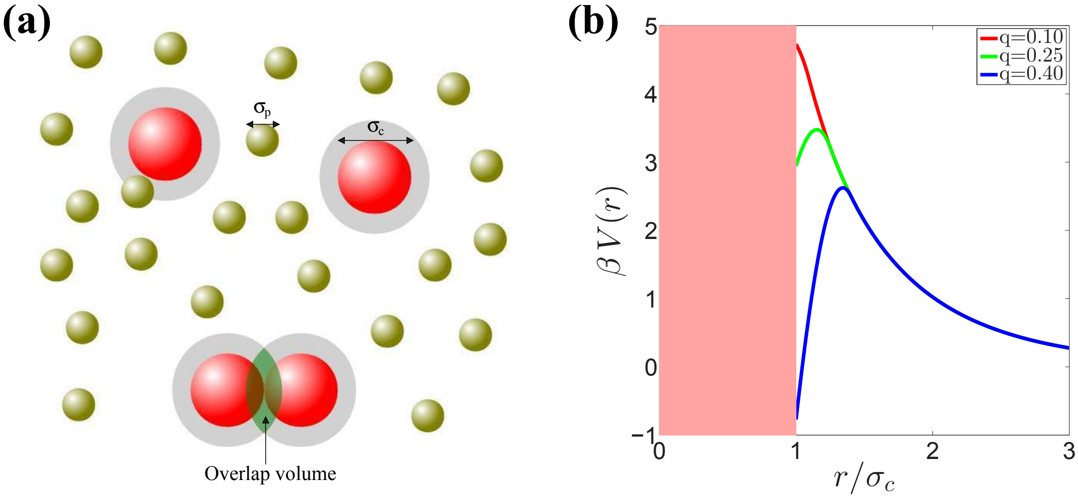

Figure 7.1.: System of the colloid-polymer mixture. (a) Schematic illustration of the colloidal suspension. Aside from charged spherical colloidal particles (red) of hardcore diameter σ_c, the suspension contains small polymer coils (green) of diameter σ_p. The gray shaded shell around a colloidal particle marks the area that cannot be occupied by the polymers due to excluded volume interaction. An increase in entropy is achieved, when the colloids come close to each other, since the resulting overlap volume of the shells is now free for the polymers to explore. Therefore, the screened Coulomb repulsive pair potential of the colloids is augmented by a short-range attraction. (b) Two length scale pair potential of the colloids from Eq. (7.2) and (7.1) for various size ratios q. The short-range attraction is due to the presence of the polymer coils, while the repulsive decay originates from the electrical charges of the colloids. The parameter q affects both the length scale of the attraction and its strength. With the inverse temperature β the ability of the colloids to overcome the barrier in the potential is controlled. A sufficient mobility is crucial for the self-assembly of quasicrystals.

Furthermore, we introduce dimensionless quantities for discussion:

$$\eta = \bar{\rho}(\sigma_c + \sigma_p)^2 \quad \text{and} \quad \Gamma = \frac{\pi \Omega_p \sigma_c^2}{6\epsilon\kappa}(1+q)\exp[-\kappa\sigma_c]\,. \tag{7.3}$$

In Eq. (7.3), η denotes a scaled density from the average number density $\bar{\rho}$, while Γ represents the ratio between attractive and repulsive contribution in the total interaction potential.

The challenge amounts to finding the precise tuning in the parameter space spanned by η, Γ, q, $\kappa\sigma_c$, and $\beta\epsilon$ that leads to stable quasicrystals. For this purpose, Barkan *et al.* presented a method based in reciprocal space to obtain the right ratios for isotropic pair potentials to stabilize quasicrystalline formation [117, 128]. Unfortunately, it is not applicable to our system because of the divergence in the electrostatic repulsion or the hardcore interactions. That is why we rely on ground state calculations to narrow the parameter space down in a first stage.

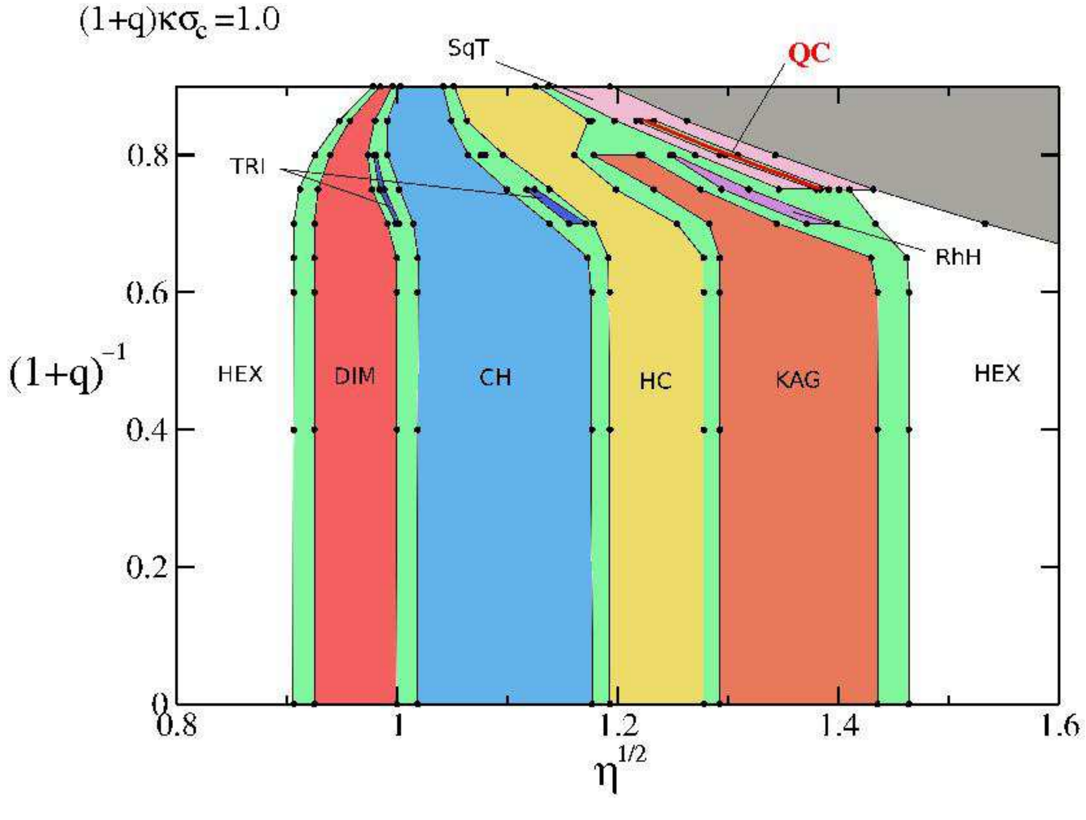

Figure 7.2.: Ground state phase diagram of the colloid-polymer mixture by courtesy of E. C. Oğuz. The obtained structures are categorized into hexagonal (HEX), dimer (DIM), trimer (TRI), chains (CH), honey comb (HC), kagome (KAG), a mixed phase of rhombs and hexagons (RhH) as well as a mixed phase of periodic arrangements of squares and triangles (SqT). Within the SqT-region, the red line marks the area, where the Square-Triangle tiling yields the lowest energy.

7.1.2. Phasediagram of the ground state $T = 0$

In this section, we present the work by E. C. Oğuz who conducted lattice sum calculations and free minimization of unit cells. Provided with periodic approximants for various tilings from section 3.2.2, he obtained a phase diagram for the case $T = 0$ that is depicted in Fig. 7.2. It supports us in choosing promising sets of interaction parameters for it exhibits a stable dodecagonal phase. In this phase, a structure where colloids are located on the vertices of a Square-Triangle tiling yields the minimal energy.

However for dynamic reasons, not all sets from Fig. 7.2 might be equally suitable for simulations or experiments. If the attractive contribution is too strong, the simulations often end up in clustered or gellike configurations. Therefore, we prefer monotonic repulsive interactions such that the overall particle pressure pushes some particles towards the short distance as the density increases. Purely repulsive interactions are in perfect agreement with previous studies [117, 119].

7.1.3. Simulation details and parameters

We employ static Monte-Carlo simulations as explained in section 3.1. In order to assure that significantly diverse configurations are visited in configurational space during the *Metropolis* algorithm, different initial configurations for the particle positions are considered, in particular the neighboring or rather competing phases in the ground state. Therefore, each point in parameter space in fact represents four independent simulation runs starting from a tetragonal, hexagonal, dodecagonal, and random initial configuration. The state obtained from these four routes, whose average energy per particle is minimal, is reckoned the global minimum.

The system contains 800 to 1000 particles depending on the actual periodic approximant. It is equilibrated for $8 \cdot 10^5$ Monte-Carlo steps before a two-dimensional density field $\rho(\mathbf{r})$ is determined by averaging over every 1000th for 200 configurations in total. The density field exhibits distinct maxima that can easily be translated to discrete tilings for further evaluations.

7.2. Self-assembled colloidal quasicrystal

In the following the simulation results are discussed. To begin, the general quality of the quasicrystalline configurations that can be expected under self-assembly conditions is addressed. Afterwards, the qualitative topology of the simulation space is presented. Finally, the transition regions are elucidated in more detail such that useful guidelines for an experimental search can be formulated.

7.2.1. Characterization of the self-assembled quasicrystalline structures

The isotropic interaction potential between two colloids gives rise to a short S and a large L separation distance. A one-dimensional analogy would be a chain of S and L segments similar to the silver mean chain from section 1.3.3 or a Fibonacci sequence [187]. Assuming a finite chain like for instance $LSLLS\ldots$ has already assembled, which type of segment, S or L, is the correct sequel of the chain? For a perfect aperiodic order information about the whole chain is required. Such can hardly be provided by isotropic interactions, though a quasicrystal may be favored for entropic reasons [56]. In our case, the resulting chain is most likely a random sequence of S and L segments, while the ratio of S and L would depend on the particle density and the temperature. Although this approach appears slightly simplistic to be directly transferred to higher-dimensional self-assembly of quasicrystals, where criss-crossing effects may play an additional role [187], it illustrates the basic feature.

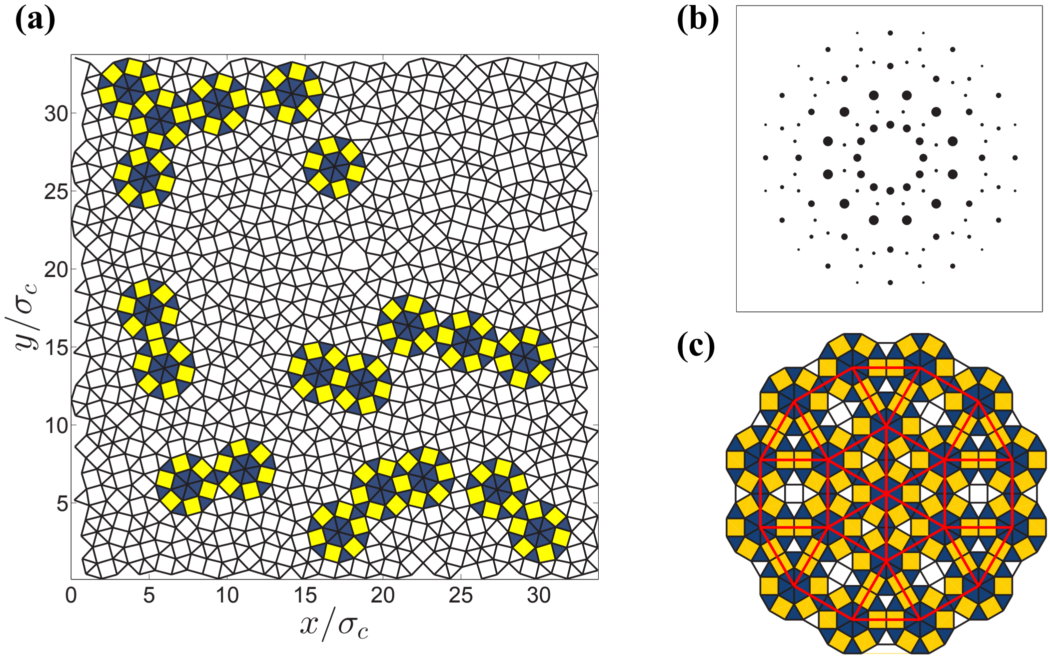

Figure 7.3.: Typical quasicrystal obtained from an initial random configuration in simulation or a possible self-assembly in an experimental setup. (a) The maxima of the structured colloidal density form a tiling comprised of squares and triangles but randomly arranged. (b) Nevertheless, the corresponding structure exhibits sharp peaks and reveals distinct dodecagonal rotational symmetry. (c) In a perfect dodecagonal quasicrystal, characterized by the Square-Triangle tiling, the squares and triangles form dodecagons arranged in a self-similar network. The configuration shown in (a) exhibits several of these basic units (blue and yellow shading).

In our self-assembly simulations in two dimensions, the random arrangement of basic building blocks due to local isotropic interactions is reflected. A typical example obtained from a random initial configuration is displayed in Fig. 7.3. The tiling from the structured density $\rho(\mathbf{r})$ is comprised of squares and triangles. To some extend, the tiling contains basic dodecagons which are highlighted by colored shading. These are randomly distributed, whereas in case of an ideal Square-Triangle tiling, these basic units yield a self-similar network. However, this higher hierarchy is unlikely to be accomplished by self-assembly processes alone. Nevertheless, the structure factor of the self-assembled random structure reveals distinct dodecagonal rotational symmetry comparable to an ideal Square-Triangle tiling.

Therefore, for a more quantitative assessment, we compare the amount of squares and triangles between the ideal tiling and the simulated configuration. In case of an ideal Square-Triangle tiling the area fraction of squares $f_\square$ equals the area fraction of triangles $f_\triangle$, i.e. $f_\square = f_\triangle = 1/2$ [181]. This is equivalent to a ratio of $\sqrt{3}/4$ for the number of squares divided by the number of triangles. For the configuration from Fig. 7.3 (a) we determine the corresponding values to $f_\square = 0.499$ and $f_\triangle = 0.501$. This is close to the ideal case. Hence, this configuration represents the typical quality of a dodecagonal quasicrystal that can be obtained in simulations from a random initial configuration or in a comparable experiment under laboratory conditions.

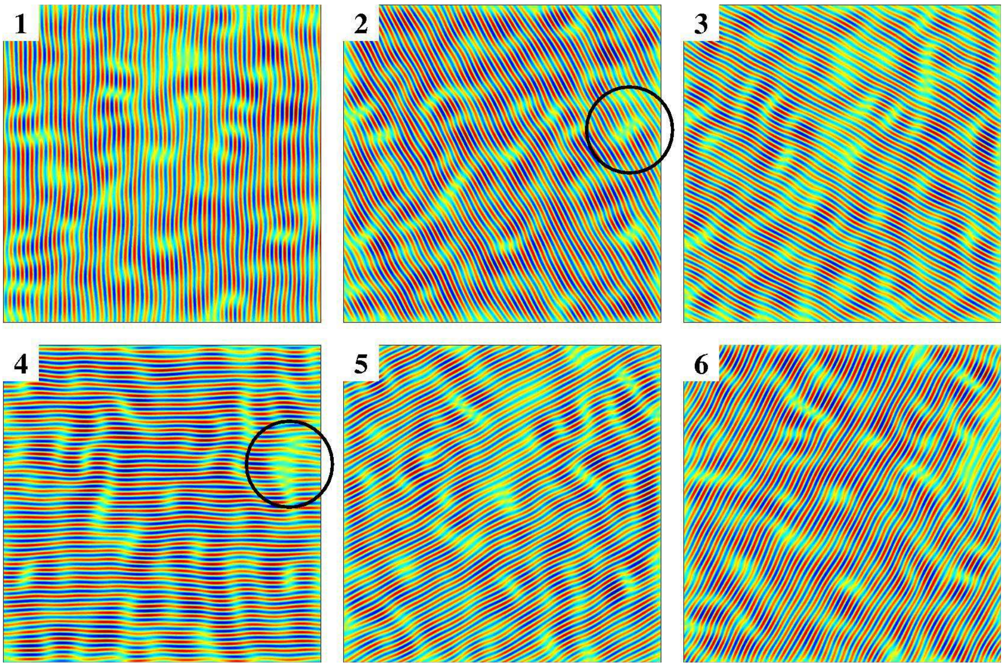

Figure 7.4.: Analysis of the density modes of the dodecagonal configuration from Fig. 7.3 (a). Defects are detected in two modes, marked by black circles. Thus a pair of dislocations is identified with oppositely charged basic Burgers vector. Apart from the random arrangement of squares and triangles, the number of performed simulation steps seems to be sufficient for the system to relax in a state with only a few global defects.

Moreover, in order to detect possible global defects, the mode analysis from section 3.3 is conducted. Usually, mesoscopic quasicrystals obtained by processes of self-assembly contain several defects [55, 161]. The basic density modes are displayed in Fig. 7.4. We identify a neutral pair of dislocations with basic Burgers vector. Therefore, the general quality of our simulated structures is only restricted by local randomness of tiles but not by global defects.

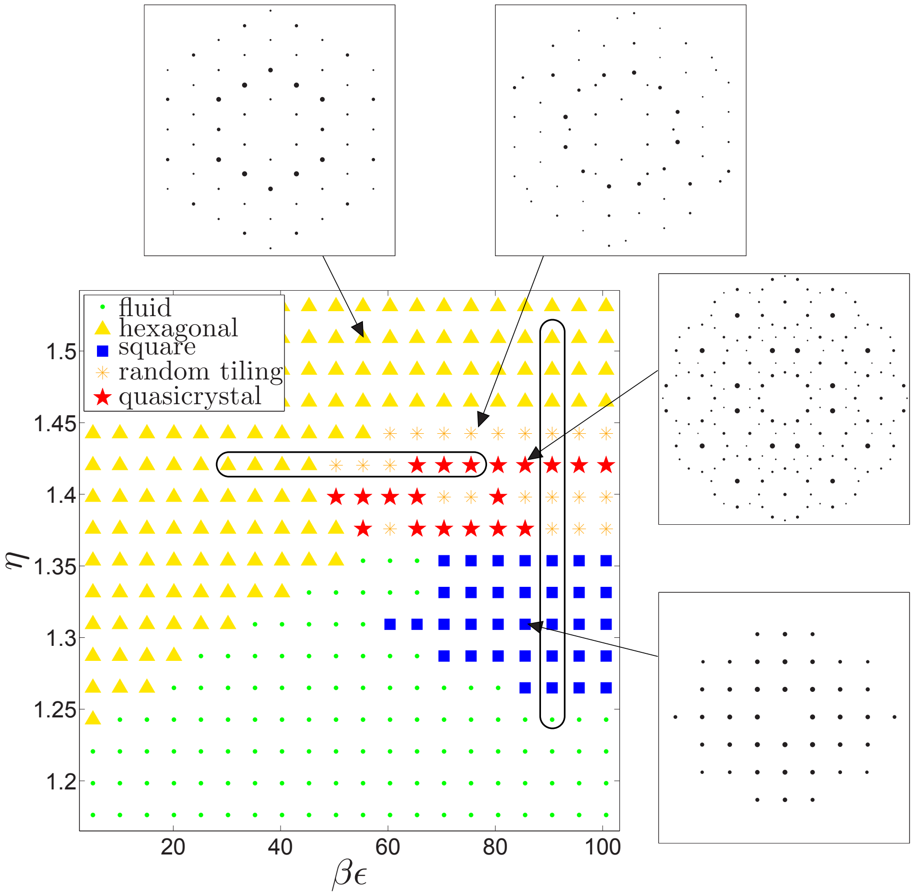

Figure 7.5.: Diagram of stable configurations obtained from Monte-Carlo simulations for various densities and temperatures. The parameters are set to $\Gamma = 1.610$, $q = 0.1704$, and $\kappa\sigma_c = 0.9$. The configurations are classified according to their structure factor. One can differentiate between four areas. For low densities, a fluid like phase is detected which is characterized by a nonstructured average colloidal density and an absence of sharp peaks in the structure factor. Upon increasing the density, hexagonal order is predominantly observed in regions of higher temperature and tetragonal order for lower temperatures. Between these two zones resides an area in which in general dodecagonal order as a mixture of square and hexagonal arrangement can be observed. However, not all configurations comprised of squares and triangles exhibit distinct dodecagonal rotational symmetry. In these cases, the ratio of squares and triangles deviates significantly from the ratio in the ideal Square-Triangle tiling. The encirclements represent paths that are discussed in section 7.2.3.

Usually, we consider different initial configurations for the colloids in simulation and compare the energy per particle of the evolving state. Note that an arrangement according to the perfect tiling might be stable, but is unlikely to form by self-assembly from any other initial state deviating from the ideal tiling (cf. Fig. 7.3). Therefore, we expect a state as in Fig. 7.3 to resemble the quality attainable in experiments. In the next section, the topology of the simulation space is explored. There, snapshots featuring the ideal Square-Triangle tiling represent the configuration with the lowest energy.

7.2.2. Topology of the simulation space

In the following, the qualitative topology of the simulation space spanned by the colloidal density as well as the thermal energy is discussed to provide support for an experimental search for a quasicrystalline state. The Monte-Carlo simulations are conducted as previously explained in section 7.1.3 and the generated structure is characterized by its structure factor. A selection of results for iterations over η and β is depicted in the diagram of Fig. 7.5. We differentiate between four different areas: Fluid or disordered configurations are characterized by a nonstructured density in real space or an absence of sharp peaks in the structure factor. Further enclosed by predominantly tetragonal and hexagonal orderings resides an area, where stable dodecagonal quasicrystals can be observed. Beside perfect dodecagonal symmetry, we also detect more randomly ordered tilings. While these arrangements are mostly composed of squares and triangles as well, the respective area fractions of squares and triangles may deviate considerably from the value of the ideal Square-Triangle tiling. Consequently, these configurations lack dodecagonal rotational symmetry.

If the ratio Γ between attraction an repulsion varies, for instance by changing the polymer concentration, the boundaries between the phases shift along the $\beta\epsilon$-axis. This behavior is illustrated in Fig. 7.6. In general, the higher the depletion strength, the higher is the maximal temperature under which a dodecagonal or tetragonal configuration remains stable. For a fixed density, the estimated course between a preferred hexagonal and a dodecagonal or rather random ordering is displayed in Fig. 7.6 (a). Note that for a value $\Gamma = 0.716$ or below a dodecagonal state is not detected within the applied search window. In this case, the course of the interaction potential is purely convex and a tilting of the potential course expressing an effective overall particle pressure cannot yield a minimum at short range. Based on our simulation data, a concave potential course seems to set the required attraction strength, i.e. polymer concentration, to yield a stable dodecagonal quasicrystal.

As an advice for an experimentally conducted search, we recommend to search for the fluid to square transition region. From there onwards, the density should be gradually increased such that the particles remain mobile to arrange themselves accordingly. At some point, a dodecagonal-like structure is expected to occur representing the compromise between packing efficiency and energy.

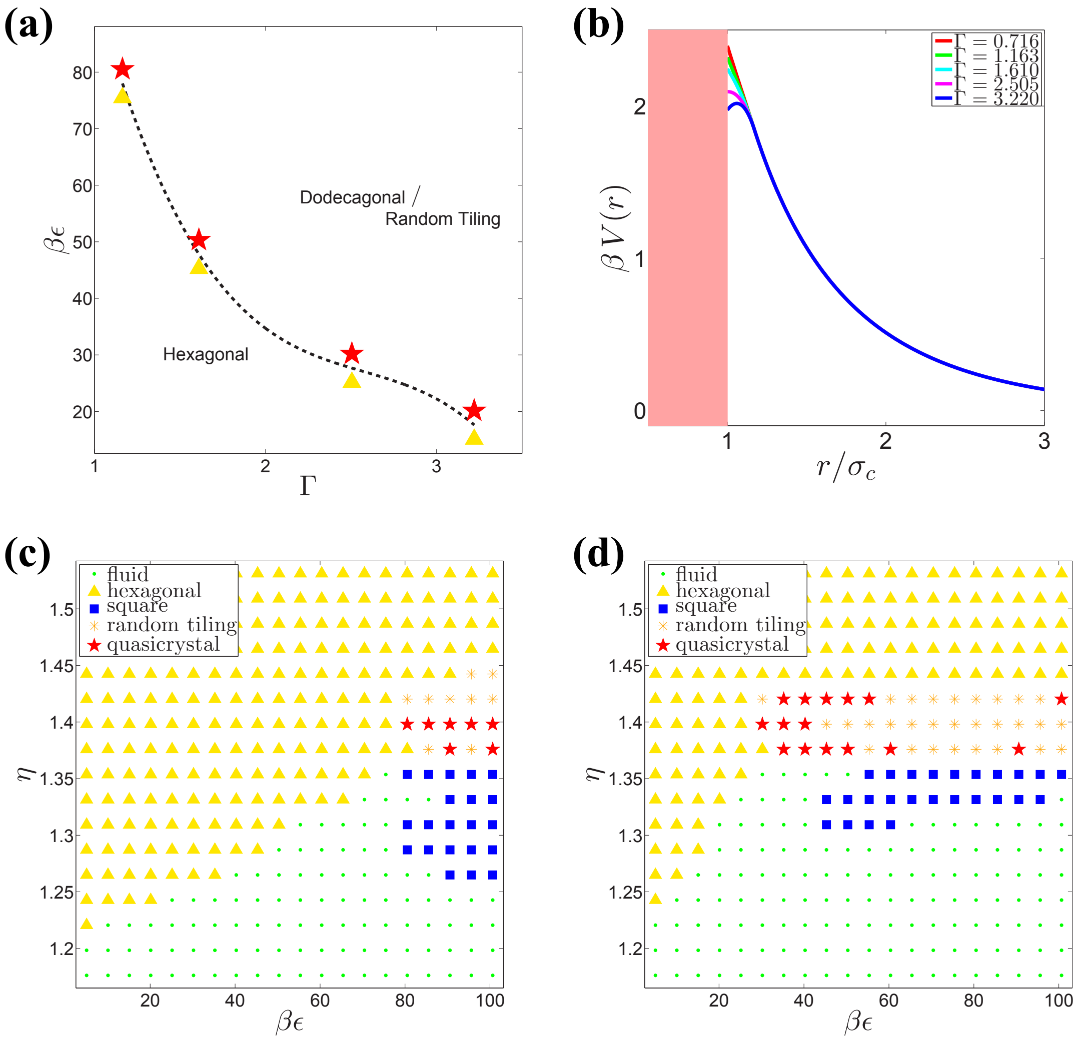

Figure 7.6.: Influence of the polymer concentration, i.e. the parameter Γ, on the obtained phases. (a) Stable quasicrystalline configuration for $\eta = 1.39$ under minimal value of $\beta\epsilon$ as a function of Γ. The symbols denote simulation values from the diagrams, while the dashed line is a guide to the eye representing the border. For higher Γ, i.e. stronger attraction, the maximal temperature under which the quasicrystalline configuration remains stable increases. (b) The corresponding pair potentials to the simulated values from (a). Compared to the Coulomb contribution the depletion interaction is weak such that nearly all courses are monotonic repulsive. The overall particle pressure may push some particles on the small length scale. (c) Diagram of the simulation space for $\Gamma = 1.163$. The quasicrystalline and square domains are restricted to low temperatures in the search window. (d) Diagram of the simulation space for $\Gamma = 2.505$. Compared to (c) the quasicrystalline and square domain extend to higher temperature values. Qualitatively, the topology is identical.

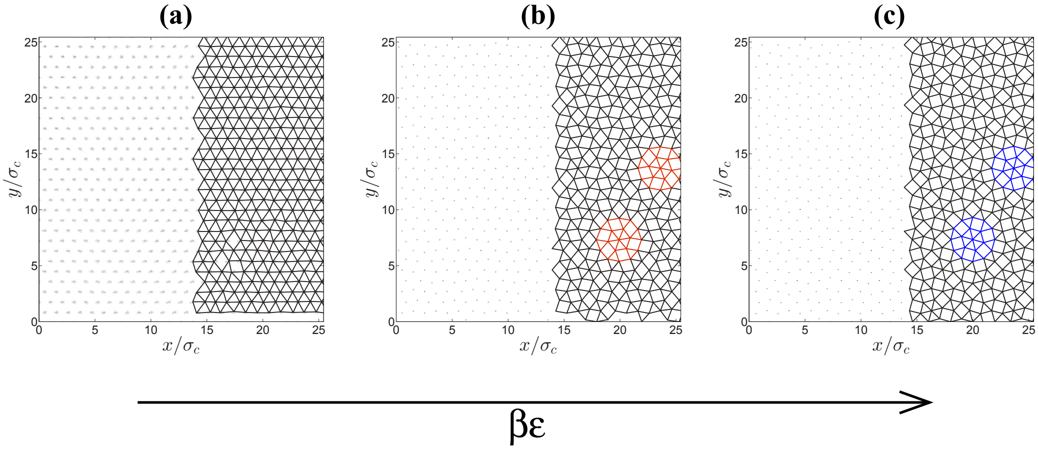

Figure 7.7.: Excerpts of configurations on a path in the simulation space of Fig. 7.5 with constant density $\eta = 1.42$ along $\beta\epsilon$. (a) Hexagonal phase for $\beta\epsilon = 30.19$. (b) Distorted Square-Triangle like tiling for $\beta\epsilon = 50.32$. (c) Perfect dodecagonal Square-Triangle tiling for $\beta\epsilon = 75.49$. An increase in temperature, i.e. a decrease in $\beta\epsilon$, excites thermal fluctuations in the dodecagonal tiling. These culminate in phasonic flips that twist the elementary dodecagons. Compare the orientation of the orange (b) and blue dodecagons (d). In addition, the overall structure is distorted such that squares become rhombic. Upon further increasing the temperature the rhombs seem to separate into equilateral triangles such that hexagonal order is established.

7.2.3. Investigation of the transitions

Based on the diagrams of the previous section the route to stimulate quasicrystal self-assembly is either by lowering the temperature or by increasing the density, whereas the latter seems to be more feasible in experiments. Here, we explore the transitions towards the dodecagonal ordering in more detail as, in particular, finite temperatures and accompanying fluctuations may lead to different states compared to the ground state. Therefore, we elaborate the particle configuration on certain paths in simulation space with either density η or thermal energy $\beta\epsilon$ fixed. Besides, such paths also resemble a systematically conducted search in experiments. The considered paths are located in the search window of Fig. 7.5, i.e. the parameters are $\Gamma = 1.610$, $q = 0.1704$, and $\kappa\sigma_c = 0.9$.

First, considering a path along a fixed density $\eta = 1.42$, three meaningful configurations are depicted in Fig. 7.7. These contain hexagonal and dodecagonal ordering. The state in-between would be classified as a random tiling according to its structure factor. Starting from a stable dodecagonal configuration with low temperature, phasonic flips can be detected as the temperature is increased. In addition, the intermediate configuration is partially distorted compared to the Square-Triangle tiling for the squares have become rhombic. This indicates a tendency towards preferred hexagonal ordering that is eventually accomplished when the temperature is increased further. Thermal fluctuations seem to shield away the shorter length scale in the interaction potential such that the effective

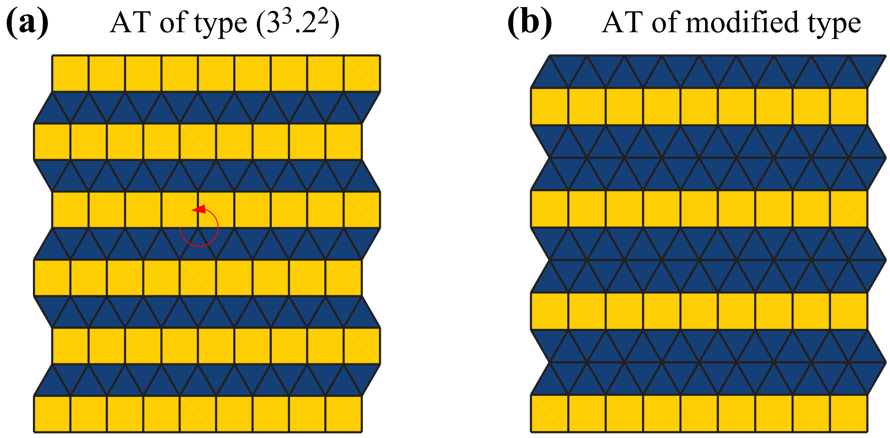

Figure 7.8.: (a) Archimedean tiling (AT) of type $(3^3.2^2)$. It consists of alternating rows of squares and triangles. Thus, we expect it also in the transition region between square and hexagonal phase. (b) A modified version of the AT in (a) as it contains double rows of triangles instead of single rows. In our simulations, the detected domains are not as big as shown here. In addition, we observe a mixture of these two cases (cf. [132]).

interaction is felt as completely repulsive.

More relevant to an experimental realization might be a path for fixed temperature and varied density. In principle, such a path could be achieved in a laboratory by means of optical tweezing. Along this path various mixtures of squares and triangles are to be expected. Aside from the dodecagonal Square-Triangle tiling, another famous group of tilings comprised of squares and triangles is the Archimedean tiling [132]. This tiling consists of alternating rows of squares and triangles. Yet, similar to the case already made for the dodecagonal tiling in section 7.2.1, we expect finite domains of random orientations in simulations. In case of an ideal Archimedean tiling of type $(3^3.2^2)$ as schematically depicted in Fig. 7.8, the area fractions of squares and tiles amount to $f_\square = 2/(2+\sqrt{3}) \approx 0.536$ and $f_\triangle = \sqrt{3}/(2+\sqrt{3}) \approx 0.464$ respectively.

While thermal energy is kept at $\beta\epsilon = 90.58$, mixed configurations with different values of square and triangle area fraction are generated by gradually increasing η. The course of the area fractions is displayed in Fig. 7.9. The three plateaus correspond to the tetragonal for $f_\square \approx 1.0$, the dodecagonal for $f_\square \approx f_\triangle \approx 0.5$ as well as the hexagonal phase for $f_\triangle \approx 1.0$. In-between the tetragonal and dodecagonal plateau, a configuration whose area fractions equal the values for the ideal Archimedean tiling can be identified. In the corresponding tiling, we observe extended Archimedean tilinglike domains. A further increase of the density from the dodecagonal phase onwards leads to the formation of larger hexagonal domains separated by squares as a higher packing efficiency is demanded. Eventually, hexagonal order prevails completely.

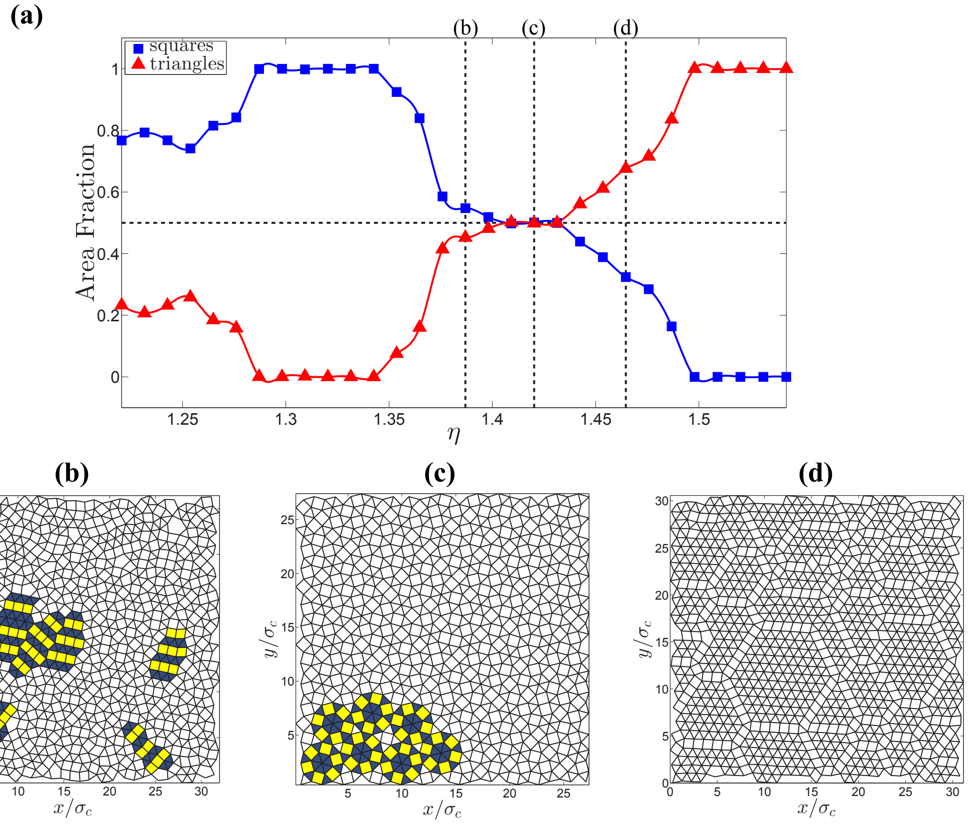

Figure 7.9.: Area fractions of squares and triangles for configurations on a path in the simulation space of Fig. 7.5 with constant temperature $\beta\epsilon = 90.58$ along η. (a) Area fraction of square and triangles as a function of the colloidal density η. The dashed horizontal line marks the value of a perfect dodecagonal Square-Triangle tiling, while the dashed vertical lines mark the configurations displayed in (b-d). The plateaus in the course of the area fraction correspond to the tetragonal, dodecagonal and hexagonal domains in the simulation space. In-between we find mixed phases of squares and triangles. (b) This configuration resembles an Archimedean tilinglike phase. Some domains of alternating rows of squares and triangles are highlighted. The value of the area fraction is close to the ideal value for an Archimedean tiling. (c) Perfect dodecagonal tiling. A patch of basic dodecagons is shaded for visual clarity. (d) As the density increases further, squares are gradually replaced by triangles for better packing efficiency.

7.3. Conclusion

We have qualitatively explored the rich phase behavior in two dimensions of a binary mixture of charged colloids and smaller polymer coils. We detected hexagonal, tetragonal, and dodecagonal configurations as well as intermediate orderings. Furthermore, we provided a suitable range of parameters that should in principle be accessible in experiments to obtain colloidal quasicrystalline structures by processes of self-assembly. Additional feasibility is ensured as the potential can be monotonic repulsive. A small concentration of polymers that leads to a concave course in the isotropic interaction potential is probably sufficient to stabilize dodecagonal order. With respect to the template-guided approach employed in the two previous chapters, the prospect of self-assembly by an isotropic interaction potential offers an alternative route to mesoscopic quasicrystalline structures that might be important in photonics [148]. After all, complete band gaps were engineered by devices of a similar Square-Triangle tiling like arrangement [152]. Aside from concrete technical applications, a possible realization in a laboratory could also be a prosperous model system to investigate thermally excited phasonic fluctuations directly in real space by means of video microscopy.

> Experience is the name so many people give to their mistakes.
>
> (*F. Scott Fitzgerald* 1896-1940)

CHAPTER 8

Summary & Outlook

On the mesoscopic level, the behavior of a colloidal suspension can be influenced by various external and internal mechanisms. In this work, we applied three different methods in order to obtain tailored colloidal quasicrystals. First, we considered a two-dimensional suspension consisting of a colloidal monolayer, where the quasicrystalline order of the particles was induced externally by optical laser fields. Second, adding a small polymer concentration modified the internal isotropic pairwise interactions between the charged particles in a way that self-assembly occurred into a stable quasicrystalline state. Third, we employed a template-guided approach together with colloidal epitaxy to grow three-dimensional colloidal quasicrystals from aperiodic substrates. Under gravitation, the colloidal particles sedimented onto specifically designed substrates with quasicrystalline rotational symmetry to yield structures comprised of stacked quasicrystalline layers. Compared to corresponding atomic systems, colloidal suspensions offer the advantage of a more feasible analysis in real space. They grant an access to the unique properties of quasicrystals that is often denied for most metal compound systems. Therefore, we were able to trace and to predict the complex trajectories of particles under a phasonic drift or to follow the courses of dislocation lines in three-dimensional quasicrystals. As method, we employed Monte-Carlo simulations to obtain quasicrystalline structures in two and three dimensions.

Quasicrystalline laser fields have been deployed before to induce two-dimensional colloidal quasicrystals [131–133]. The rich phase behavior has been analyzed in both experiment and theory. On the basis of a decagonal laser interference pattern, Kromer *et al.* developed a method to predict colloidal trajectories originating from an applied phasonic drift [138]. Although a quasicrystal exhibits per definition no repeating unit cell, Kromer *et al.* showed that all colloidal particles can be mapped into characteristic areas. From these characteristic areas, the trajectory of every colloidal particle could be derived. Here, we extended their method to octagonal, dodecagonal, and tetradecagonal rotational symmetry. In particular, the tetradecagonal case establishes the universality of the method for it requires the mapping in six dimensions in contrast to four dimensions for the other cases. In principle, the method can be utilized to describe phasonic fluctuations in intrinsic quasicrystalline systems.

Moreover, we considered a finite diameter for the colloidal particles in the light induced suspension to describe the acting optical forces on the particles more accurately. The ratio between this particle length scale and the length scale of the potential can give rise to degenerate orderings. While the rotational symmetry remains predetermined by the laser field, the local isomorphism class depends on the length scale ratio. This behavior is reminiscent to the degenerate patterns observed for molecular deposition on atomic quasicrystalline surfaces [270].

Aside from enforcements by external fields, colloids may self-assemble into a stable quasicrystalline ordering for a specifically tuned isotropic pair potential [117]. We demonstrated that a small concentration of polymers added to the charged stabilized suspension is sufficient to promote dodecagonal order in simulations. By exploring the phase behavior of this colloid-polymer mixture we determined the range in density and temperature, where the quasicrystal remained stable. Since this depletion potential has been frequently implemented in experimental setups [120–122], we are confident that our work provides concrete support for a future realization in a laboratory. The warranted feasibility may pave the way for generated soft matter quasicrystals by design, which might be important for photonic applications.

However, for such purposes, three-dimensional quasicrystalline structures might be more desirable. Therefore, we applied the method of template-guided colloidal epitaxy to simulate the growth of three-dimensional colloidal quasicrystals from substrates whose design is borrowed from aperiodic tilings. So far, this method has only been attempted on periodic substrates [143, 145]. We showed that, in contrast to self-assembly approaches, no fine tuning of the pairwise interaction is required. The quasicrystalline template is sufficient to avoid the bulk behavior such that several layers of quasicrystalline rotational symmetry form as the colloids sediment under gravity. We considered different substrate symmetries, namely the octagonal Ammann-Beenker, the decagonal Penrose-Rhomb, and the dodecagonal Square-Triangle tiling. Out of these, the octagonal Ammann-Beenker tiling emerged as the most promising candidate because it showed the best stacking properties. Besides, the conducted mode analysis revealed that the structure grown from such a substrate exhibits the highest amount of layers without global defects.

While the quality of the quasicrystalline layers decreased in general as the layer height increased, the overall quality still allowed for a systematic analysis about the effect of substrate defects on the epitaxial structures. Two kinds of defects were added to the substrate. While local tile flips that might occur as a possible result of thermal phasonic fluctuations had hardly any detectable effect, global defects in the substrate, e.g. dislocations with well-defined Burgers vectors, lead to stable defect lines in the three-dimensional grown colloidal structure. We illustrated how the respective strain field surrounding the dislocation seed and the Burgers vector can influence the shape and course of the resulting defect line. In contrast to periodic crystals, the course also depends sensitively on the position of the seed. In addition, the topological behavior of the defect lines was explored and we observed the annihilation, forking and coalition of defect lines. Furthermore, we determined the basic set of Burgers vectors that yield stable defect lines during the growth process, i.e. lines that do not decompose further. Eventually, such three-dimensional colloidal quasicrystals augmented by controlled defect lines might offer a diverse potential for future applications.

In principle, all colloidal quasicrystalline structures that we tailored in simulations can be achieved in experiments. After all, the discussed colloid-polymer mixture as well as the template-guided approach have already been successfully implemented in order to obtain periodic structures. However, especially intriguing seems to be a combination of both approaches. On the one hand, the self-assembled dodecagonal structures in the two-dimensional colloid-polymer mixture are comprised to a certain extend of random tiling arrangements and lack the consistent hierarchical order of a perfect tiling. On the other hand, in the template-guided three-dimensional growth this higher hierarchical network of the symmetry centers is imprinted by the substrate tiling to higher two-dimensional layers, where the order on a local level has already decreased significantly due to local flips. Therefore, translating the tuned isotropic interactions from the two-dimensional colloid-polymer mixture to the epitaxial growth in three dimensions seems to be a prosperous prospect for future research.

List of Publications

- [A] M. Sandbrink and M. Schmiedeberg, *Trajectories of colloidal particles in laser fields with eight-, ten-, or twelve-fold symmetry and phasonic drift*, in Aperiodic Crystals, edited by S. Schmid, R.L. Withers, and R. Lifshitz (Springer, Berlin, 2013).
- [B] M. Martinsons, M. Sandbrink, and M. Schmiedeberg, *Colloidal trajectories in two-dimensional light-induced quasicrystals with 14-fold symmetry due to phasonic drifts*, Acta Phys. Pol. A **126**, 568 (2014).
- [C] M. Sandbrink, J. Roth, and M. Schmiedeberg, *Comment on "Quantum quasicrystals of spin-orbit-coupled dipolar bosons"*, Phys. Rev. Lett. **113**, 079601 (2014).
- [D] M. Sandbrink and M. Schmiedeberg, *Course of dislocation lines in templated three dimensional colloidal quasicrystals*, Phys. Rev. B **90**, 064108 (2014).

- [E] F. Rühle, M. Sandbrink, H. Stark, and M. Schmiedeberg, *Effective substrate potentials with quasicrystalline symmetry depend on the size of the adsorbed particles*, submitted (2015).
- [F] C. V. Achim, M. Sandbrink, M. Schmiedeberg, and H. Löwen, *Phason-assisted grain merging in quasicrystal*, in preparation (2014).

The content of the published articles from the list above constitutes a significant part of the thesis. In the following, the author contributions are explicitly listed:

- Ref. [A] represents the foundation of section 4.3.1 about colloidal trajectories arising in quasicrystalline laser fields of rank $D = 4$ under a phasonic drift. M. Sandbrink did the calculations and performed the numerical analysis to obtain the diagrams of reduced phononic and phasonic position. M. Schmiedeberg supervised the project. M. Sandbrink and M. Schmiedeberg wrote the manuscript.
- Ref. [B] represent the base of section 4.3.2 about colloidal trajectories arising in quasicrystalline laser fields of tetradecagonal symmetry of rank $D = 6$ under a phasonic drift. In the scope of her master-thesis, M. Martinsons performed the calculations and the numerical analysis to obtain the diagrams. The project was supervised by M. Schmiedeberg and M. Sandbrink. All authors wrote the manuscript together.

- In Ref. [C], we refute the claim that quantum quasicrystals exhibit more phason modes than their classical counterparts. In joint discussions, the authors outlined their argumentation. Under supervision by M. Schmiedeberg, M. Sandbrink performed the calculations and the numerical illustrations. All authors wrote the manuscript together.
- Ref. [D] represents the foundation of chapter 6 about colloidal epitaxy on quasicrystalline substrates containing defects. M. Sandbrink did the calculations to obtain the Burgers lattice and implemented the simulations. He analyzed the data to obtain the three-dimensional courses of the defect lines. M. Schmiedeberg supervised the project. M. Sandbrink and M. Schmiedeberg wrote the manuscript.
- Ref. [E] will contain the content of section 4.2 about the influence of a finite diameter for the colloids in a quasicrystalline interference pattern as a model for molecular deposition on atomic quasicrystalline surfaces. M. Sandbrink did the calculations as shown in section 4.2, while F. Rühle performed simulations. The projects are under supervision by M. Schmiedeberg and H. Stark.
- Ref. [F] does not feature in this thesis.

So far, the results for the colloidal sedimentation on aperiodic tilings with different symmetries from chapter 5 and for the two-dimensional colloid-polymer mixture are unpublished.

Bibliography

[1] A. Bravais, *Memoirs sur les systemes formes par des point distribues regulierement sur un plan ou dans l'espace*, J. Ec. Polytech. **33**, 1 (1850).

[2] D. Shechtman, I. Blech, D. Gratias, and J. W. Cahn, *Metallic phase with long-range orientational order and no translational symmetry*, Phys. Rev. Lett. **53**, 1951 (1984).

[3] D. Shechtman and I. Blech, *The microstructure of rapidly solidified* Al_6Mn, Metall. Trans. A **16**, 1005 (1985).

[4] N. Wang, H. Chen, and K. H. Kuo, *Two-dimensional quasicrystal with eightfold rotational symmetry*, Phys. Rev. Lett. **59**, 1010 (1987).

[5] T. Ishimasa, H.-U. Nissen, and Y. Fukano, *New ordered state between crystalline and amorphous in Ni–Cr particles*, Phys. Rev. Lett. **55**, 511 (1985).

[6] L. Pauling, *Apparent icosahedral symmetry is due to directed multiple twinning of cubic crystals*, Nature (London) **317**, 512 (1985).

[7] P. A. Heiney, *Quasicrystals - respectable icosahedral symmetry*, Nature (London) **315**, 176 (1985).

[8] J. W. Cahn, D. Gratias, and D. Shechtman, *Pauling's model not universally accepted*, Nature (London) **319**, 102 (1986).

[9] L. Pauling, *So-called icosahedral and decagonal quasicrystals are twins of an 820-atom cubic crystal*, Phys. Rev. Lett. **58**, 365 (1987).

[10] L. Pauling, *Icosahedral and decagonal quasicrystals of intermetallic compounds are multiple twins of cubic or orthorhombic crystals composed of very large atomic complexes with icosahedral point-group symmetry in cubic close packing or body-centered packing: Structure of decagonal* Al_6Pd, Proc. Natl. Acad. Sci. USA **86**, 9637 (1989).

[11] D. Levine and P. J. Steinhardt, *Quasicrystals: A new class of ordered structures*, Phys. Rev. Lett. **53**, 2477 (1984).

[12] D. Levine and P. J. Steinhardt, *Quasicrystals. I. Definition and structure*, Phys. Rev. B **34**, 596 (1986).

[13] International Union of Crystallography, *Report of the executive committee for 1991*, Acta Cryst. A **48**, 922 (1992).

[14] R. Lifshitz, *What is a crystal?*, Z. Kristallogr. **222**, 313 (2007).

[15] B. Dubost, J. Lang, M. Tanaka, P. Sainfort, and M. Audier, *Large AlCuLi single quasicrystals with triacontahedral solidification morphology*, Nature (London) **324**, 48 (1986).

[16] W. Ohashi and F. Spaepen, *Stable Ga–Mg–Zn quasi-periodic crystals with pentagonal dodecahedral solidification morphology*, Nature (London) **330**, 555 (1987).

[17] A.-P. Tsai, A. Inoue, and T. Masumoto, *A stable quasicrystal in Al–Cu–Fe system*, Jpn. J. Appl. Phys. **26**, L1505 (1987).

[18] A.-P. Tsai, A. Inoue, and T. Masumoto, *New stable icosahedral Al–Cu–Ru and Al–Cu–Os alloys*, Jpn. J. Appl. Phys. **27**, L1587 (1988).

[19] L. X. He, Y. K. Wu, X. M. Meng, and K. H. Kuo, *Stable Al–Cu–Co decagonal quasicrystals with decaprismatic solidification morphology*, Philos. Mag. Lett. **61**, 15 (1990).

[20] E. Abe, *Electron microscopy of quasicrystals – Where are the atoms?*, Chem. Soc. Rev. **41**, 6787 (2012).

[21] S. J. Poon, *Electronic properties of quasicrystals – An experimental review*, Adv. Phys. **41**, 303 (1992).

[22] J. L. Wagner, K. M. Wong, and S. J. Poon, *Electronic properties of stable icosahedral alloys*, Phys. Rev. B **39**, 8091 (1989).

[23] D. Mayou, C. Berger, F. Cyrot-Lackmann, T. Klein, and P. Lanco, *Evidence for unconventional electronic transport in quasicrystals*, Phys. Rev. Lett. **70**, 3915 (1993).

[24] F. S. Pierce, S. J. Poon, and B. D. Biggs, *Band-structure gap and electron transport in metallic quasicrystals and crystals*, Phys. Rev. Lett. **70**, 3919 (1993).

[25] B. D. Biggs, S. J. Poon, and N. R. Munirathnam, *Stable Al–Cu–Ru icosahedral crystals: A new class of electronic alloys*, Phys. Rev. Lett. **65**, 2700 (1990).

[26] F. S. Pierce, Q. Guo, and S. J. Poon, *Enhanced insulatorlike electron transport behavior of thermally tuned quasicrystalline states of Al–Pd–Re alloys*, Phys. Rev. Lett. **73**, 2220 (1994).

[27] F. S. Pierce, S. J. Poon, and Q. Guo, *Electron localization in metallic quasicrystals*, Science **261**, 737 (1993).

[28] X. Wu, S. W. Kycia, C. G. Olson, P. J. Benning, A. I. Goldman, and D. W. Lynch, *Electronic band dispersion and pseudogap in quasicrystals: Angular-resolved photoemission studies on icosahedral* $Al_{70}Pd_{21.5}Mn_{8.5}$, Phys. Rev. Lett. **75**, 4540 (1995).

[29] P. A. Thiel and J. M. Dubois, *Quasicrystals: Electrons in a strange sea*, Nature (London) **406**, 570 (2000).

[30] E. Rotenberg, W. Theis, K. Horn, and P. Gille, *Quasicrystalline valence bands in decagonal AlNiCo*, Nature (London) **406**, 602 (2000).

[31] S. Martin, A. F. Hebard, A. R. Kortan, and F. A. Thiel, *Transport properties of* $Al_{65}Cu_{15}Co_{20}$ *and* $Al_{70}Ni_{15}Co_{15}$ *decagonal quasicrystals*, Phys. Rev. Lett. **67**, 719 (1991).

[32] S. Yamamoto and T. Fujiwara, *Electronic transport of quasicrystals with random phason strain: The two-dimensional penrose lattice*, Phys. Rev. B **51**, 8841 (1995).

[33] B. Passaro, C. Sire, and V. G. Benza, *Anomalous diffusion and conductivity in octagonal tiling models*, Phys. Rev. B **46**, 13751 (1992).

[34] T. Fujiwara, S. Yamamoto, and G. Trambly de Laissardière, *Band structure effects of transport properties in icosahedral quasicrystals*, Phys. Rev. Lett. **71**, 4166 (1993).

[35] T. Odagaki and D. Nguyen, *Electronic and vibrational spectra of two-dimensional quasicrystals*, Phys. Rev. B **33**, 2184 (1986).

[36] M. Kohmoto and B. Sutherland, *Electronic states on a penrose lattice*, Phys. Rev. Lett. **56**, 2740 (1986).

[37] Z. M. Stadnik, G. Stroink, H. Ma, and G. Williams, *Magnetic properties of icosahedral alloys: The case of* $Al_{65}Cu_{20}Fe_{15}$, Phys. Rev. B **39**, 9797 (1989).

[38] M. E. McHenry, V. Srinivas, D. Bahadur, R. C. O'Handley, D. J. Lloyd, and R. A. Dunlap, *Structural, thermal, and magnetic properties of icosahedral Al–Cr–Mn–Si alloys*, Phys. Rev. B **39**, 3611 (1989).

[39] V. Srinivas, M. E. McHenry, and R. A. Dunlap, *Magnetic properties of icosahedral Al–Mo–Fe and Al–Ta–Fe alloys*, Phys. Rev. B **40**, 9590 (1989).

[40] R. A. Dunlap, M. E. McHenry, V. Srinivas, D. Bahadur, and R. C. O'Handley, *Ferromagnetism in icosahedral Al–Mn–Si alloys*, Phys. Rev. B **39**, 4808 (1989).

[41] R. C. O'Handley, R. A. Dunlap, and M. E. McHenry, *Icosahedral quasicrystals and magnetism*, Philos. Mag. B **61**, 677 (1990).

[42] T. J. Sato, H. Takakura, A. P. Tsai, K. Shibata, K. Ohoyama, and K. H. Andersen, *Antiferromagnetic spin correlations in the Zn–Mg–Ho icosahedral quasicrystal*, Phys. Rev. B **61**, 476 (2000).

[43] R. Lifshitz, *Symmetry of magnetically ordered quasicrystals*, Phys. Rev. Lett. **80**, 2717 (1998).

[44] S. Wessel, A. Jagannathan, and S. Haas, *Quantum antiferromagnetism in quasicrystals*, Phys. Rev. Lett. **90**, 177205 (2003).

[45] E. Y. Vedmedenko, U. Grimm, and R. Wiesendanger, *Noncollinear magnetic order in quasicrystals*, Phys. Rev. Lett. **93**, 076407 (2004).

[46] J. M. Kang, S S Dubois, *Pressure-induced phase transitions in quasi-crystals and related compounds*, Europhys. Lett. **18**, 45 (1992).

[47] S. S. Kang and J. M. Dubois, *Compression testing of quasicrystalline materials*, Philos. Mag. A **66**, 151 (1992).

[48] R. Mikulla, J. Stadler, F. Krul, H.-R. Trebin, and P. Gumbsch, *Crack propagation in quasicrystals*, Phys. Rev. Lett. **81**, 3163 (1998).

[49] S. Takeuchi, H. Iwanaga, and T. Shibuya, *Hardness of quasicrystals*, Jpn. J. Appl. Phys. **30**, 561 (1991).

[50] S. Takeuchi and T. Hashimoto, *Plastic deformation of Al–Pd–Mn icosahedral quasicrystal*, Jpn. J. Appl. Phys. **32**, 2063 (1993).

[51] M. Wollgarten, D. Gratias, Z. Zhang, and K. Urban, *On the determination of the Burgers vector of quasicrystal dislocations by transmission electron microscopy*, Philos. Mag. A **64**, 819 (1991).

[52] R. Wang and M. X. Dai, *Burgers vector of dislocations in an icosahedral* $Al_{62}Cu_{25.5}Fe_{12.5}$ *quasicrystal determined by means of convergent-beam electron diffraction*, Phys. Rev. B **47**, 15326 (1993).

[53] W. Yang, R. Wang, M. Feuerbacher, P. Schall, and K. Urban, *Determination of the Burgers vector of dislocations in icosahedral quasicrystals by a high-resolution lattice-fringe technique*, Philos. Mag. Lett. **80**, 281 (2000).

[54] M. Feuerbacher, *Dislocations in icosahedral quasicrystals*, Chem. Soc. Rev. **41**, 6745 (2012).

[55] L. Korkidi, K. Barkan, and R. Lifshitz, *Analysis of dislocations in quasicrystals composed of self-assembled nanoparticles*, in *Aperiodic Crystals*, edited by S. Schmid, R. L. Withers, and R. Lifshitz, 117–124, Springer Netherlands (2013).

[56] A. Kiselev, M. Engel, and H.-R. Trebin, *Confirmation of the random tiling hypothesis for a decagonal quasicrystal*, Phys. Rev. Lett. **109**, 225502 (2012).

[57] R. D. Diehl, J. Ledieu, N. Ferralis, A. W. Szmodis, and R. McGrath, *Low-energy electron diffraction from quasicrystal surfaces*, J. Phys.: Condens. Matter **15**, R63 (2003).

[58] N. Ferralis, K. Pussi, E. J. Cox, M. Gierer, J. Ledieu, I. R. Fisher, C. J. Jenks, M. Lindroos, R. McGrath, and R. D. Diehl, *Structure of the tenfold Al–Ni–Co quasicrystal surface*, Phys. Rev. B **69**, 153404 (2004).

[59] K. Pussi, N. Ferralis, M. Mihalkovic, M. Widom, S. Curtarolo, M. Gierer, C. J. Jenks, P. Canfield, I. R. Fisher, and R. D. Diehl, *Use of periodic approximants in a dynamical LEED study of the quasicrystalline tenfold surface of decagonal Al–Ni–Co*, Phys. Rev. B **73**, 184203 (2006).

[60] P. A. Thiel, *Quasicrystal surfaces**, Annu. Rev. of Phys. Chem. **59**, 129 (2008).

[61] J. Dubois, S. Kang, and J. V. Stebut, *Quasicrystalline low-friction coatings*, J. Mater. Sci. Lett. **10**, 537 (1991).

[62] R. Matthews, C. Lang, and D. Shechtman, *Sliding wear of quasicrystalline coatings*, Tribol. Lett. **7**, 179 (1999).

[63] J. Y. Park, D. F. Ogletree, M. Salmeron, R. A. Ribeiro, P. C. Canfield, C. J. Jenks, and P. A. Thiel, *High frictional anisotropy of periodic and aperiodic directions on a quasicrystal surface*, Science **309**, 1354 (2005).

[64] J. Y. Park, D. F. Ogletree, M. Salmeron, R. A. Ribeiro, P. C. Canfield, C. J. Jenks, and P. A. Thiel, *Tribological properties of quasicrystals: Effect of aperiodic versus periodic surface order*, Phys. Rev. B **74**, 024203 (2006).

[65] A. E. Filippov, A. Vanossi, and M. Urbakh, *Origin of friction anisotropy on a quasicrystal surface*, Phys. Rev. Lett. **104**, 074302 (2010).

[66] T. Bohlein, J. Mikhael, and C. Bechinger, *Observation of kinks and antikinks in colloidal monolayers driven across ordered surfaces*, Nat. Mater. **11**, 126 (2012).

[67] T. Bohlein and C. Bechinger, *Experimental observation of directional locking and dynamical ordering of colloidal monolayers driven across quasiperiodic substrates*, Phys. Rev. Lett. **109**, 058301 (2012).

[68] A. Vanossi, N. Manini, and E. Tosatti, *Static and dynamic friction in sliding colloidal monolayers*, Proc. Natl. Acad. Sci. USA **109**, 16429 (2012).

[69] J.-M. Dubois, *Useful quasicrystals*, Singapore: World Scientific (2005).

[70] J. Y. Park, D. F. Ogletree, M. Salmeron, R. A. Ribeiro, P. C. Canfield, C. J. Jenks, and P. A. Thiel, *Elastic and inelastic deformations of ethylene-passivated tenfold decagonal Al–Ni–Co quasicrystal surfaces*, Phys. Rev. B **71**, 144203 (2005).

[71] J. T. Hoeft, J. Ledieu, S. Haq, T. A. Lograsso, A. R. Ross, and R. McGrath, *Adsorption of benzene on the five-fold surface of the i–$Al_{70}Pd_{21}Mn_9$ quasicrystal*, Philos. Mag. **86**, 869 (2006).

[72] K. M. Young, J. A. Smerdon, H. R. Sharma, M. Lahti, K. Pussi, and R. McGrath, *Acene adsorption on a Fibonacci-modulated Cu film*, Phys. Rev. B **87**, 085407 (2013).

[73] N. Ferralis, R. D. Diehl, K. Pussi, M. Lindroos, I. Fisher, and C. J. Jenks, *Low-energy electron diffraction study of Xe adsorption on the ten-fold decagonal Al–Ni–Co quasicrystal surface*, Phys. Rev. B **69**, 075410 (2004).

[74] W. Setyawan, N. Ferralis, R. D. Diehl, M. W. Cole, and S. Curtarolo, *Xe films on a decagonal Al–Ni–Co quasicrystalline surface*, Phys. Rev. B **74**, 125425 (2006).

[75] R. D. Diehl, N. Ferralis, K. Pussi, M. W. Cole, W. Setyawan, and S. Curtarolo, *The ordering of a Xe monolayer on quasicrystalline Al–Ni–Co*, Philos. Mag. **86**, 863 (2006).

[76] W. Setyawan, R. Diehl, N. Ferralis, M. Cole, and S. Curtarolo, *Noble gas films on a decagonal AlNiCo quasicrystal*, J. Phys.: Condens. Matter **19**, 016007 (2007).

[77] R. D. Diehl, W. Setyawan, N. Ferralis, R. A. Trasca, M. W. Cole, and S. Curtarolo, *Ordering of rare gas films on a decagonal Al–Ni–Co quasicrystal*, Philos. Mag. **87**, 2973 (2007).

[78] R. D. Diehl, W. Setyawan, and S. Curtarolo, *Gas adsorption on quasicrystalline surfaces*, J. Phys.: Condens. Matter **20**, 314007 (2008).

[79] M. Shimoda, T. J. Sato, A. P. Tsai, and J. Q. Guo, *Epitaxial crystalline film with psuedo-tenfold symmetry formed by Au-deposition on a decagonal $Al_{72}Ni_{12}Co_{16}$ quasicrystal*, Phys. Rev. B **62**, 11288 (2000).

[80] V. Fournée, T. C. Cai, A. R. Ross, T. A. Lograsso, J. W. Evans, and P. A. Thiel, *Nucleation and growth of Ag films on a quasicrystalline AlPdMn surface*, Phys. Rev. B **67**, 033406 (2003).

[81] Y. Weisskopf, R. Lüscher, and M. Erbudak, *Structural modifications upon deposition of Fe on the icosahedral quasicrystal Al–Pd–Mn*, Surf. Sci. **578**, 35 (2005).

[82] J. Ledieu, J. T. Hoeft, D. E. Reid, J. A. Smerdon, R. D. Diehl, T. A. Lograsso, A. R. Ross, and R. McGrath, *Pseudomorphic growth of a single element quasiperiodic ultrathin film on a quasicrystal substrate*, Phys. Rev. Lett. **92**, 135507 (2004).

[83] J. Ledieu, J. T. Hoeft, D. E. Reid, J. A. Smerdon, R. D. Diehl, N. Ferralis, T. A. Lograsso, A. R. Ross, and R. McGrath, *Copper adsorption on the fivefold $Al_{70}Pd_{21}Mn_9$ quasicrystal surface*, Phys. Rev. B **72**, 035420 (2005).

[84] K. Pussi, M. Gierer, and R. D. Diehl, *The uniaxially aperiodic structure of a thin Cu film on fivefold i-Al–Pd–Mn*, J. Phys.: Condens. Matter **21**, 474213 (2009).

[85] H. R. Sharma, M. Shimoda, A. R. Ross, T. A. Lograsso, and A. P. Tsai, *Real-space observation of quasicrystalline Sn monolayer formed on the fivefold surface of icosahedral AlCuFe quasicrystal*, Phys. Rev. B **72**, 045428 (2005).

[86] J. Ledieu, P. Unsworth, T. A. Lograsso, A. R. Ross, and R. McGrath, *Ordering of Si atoms on the fivefold Al–Pd–Mn quasicrystal surface*, Phys. Rev. B **73**, 012204 (2006).

[87] V. Fournée and P. A. Thiel, *New phenomena in epitaxial growth: Solid films on quasicrystalline substrates*, J. Phys. D: Appl. Phys. **38**, R83 (2005).

[88] J. A. Smerdon, *The various modes of growth of metals on quasicrystals*, J. Phys.: Condens. Matter **22**, 433002 (2010).

[89] R. McGrath, J. Ledieu, E. J. Cox, and R. D. Diehl, *Quasicrystal surfaces: Structure and potential as templates*, J. Phys.: Condens. Matter **14**, R119 (2002).

[90] J. A. Smerdon, H. R. Sharma, J. Ledieu, and R. McGrath, *Nucleation and growth of pseudomorphic monolayers on quasicrystal surfaces*, J. Phys.: Condens. Matter **20**, 314005 (2008).

[91] V. Fournée, H. R. Sharma, M. Shimoda, A. P. Tsai, B. Unal, A. R. Ross, T. A. Lograsso, and P. A. Thiel, *Quantum size effects in metal thin films grown on quasicrystalline substrates*, Phys. Rev. Lett. **95**, 155504 (2005).

[92] P. Moras, Y. Weisskopf, J.-N. Longchamp, M. Erbudak, P. H. Zhou, L. Ferrari, and C. Carbone, *Quantum size effects arising from incompatible point-group symmetries: Angle-resolved photoemission study*, Phys. Rev. B **74**, 121405 (2006).

[93] K. J. Franke, P. Gille, K.-H. Rieder, and W. Theis, *Achieving epitaxy between incommensurate materials by quasicrystalline interlayers*, Phys. Rev. Lett. **99**, 036103 (2007).

[94] K. J. Franke, H. R. Sharma, W. Theis, P. Gille, P. Ebert, and K. H. Rieder, *Quasicrystalline epitaxial single element monolayers on icosahedral Al–Pd–Mn and decagonal Al–Ni–Co quasicrystal surfaces*, Phys. Rev. Lett. **89**, 156104 (2002).

[95] H. Sharma, K. Nozawa, J. Smerdon, P. Nugent, I. McLeod, V. Dhanak, M. Shimoda, Y. Ishii, A. Tsai, and R. McGrath, *Templated three-dimensional growth of quasicrystalline lead*, Nat. Commun. **4**, 2715 (2013).

[96] R. A. Trasca, N. Ferralis, R. D. Diehl, and M. W. Cole, *The adsorption of Xe and Ar on quasicrystalline Al–Ni–Co*, J. Phys.: Condens. Matter **16**, S2911 (2004).

[97] S. Curtarolo, W. Setyawan, N. Ferralis, R. D. Diehl, and M. W. Cole, *Evolution of topological order in Xe films on a quasicrystal surface*, Phys. Rev. Lett. **95**, 136104 (2005).

[98] B. Bilki, M. Erbudak, M. Mungan, and Y. Weisskopf, *Structure formation of a layer of adatoms on a quasicrystalline substrate: Molecular dynamics study*, Phys. Rev. B **75**, 045437 (2007).

[99] M. Mungan, Y. Weisskopf, and M. Erbudak, *Deposition of atoms on a quasicrystalline substrate: Molecular dynamics study in three dimensions*, Phys. Rev. B **76**, 195443 (2007).

[100] S. Burkardt, S. Deloudi, M. Erbudak, A. R. Kortan, M. Mungan, and W. Steurer, *Bulk and surface structure of the clean and adsorbate-covered decagonal Al–Co–Ni quasicrystal*, J. Phys.: Condens. Matter **20**, 314006 (2008).

[101] M. Erbudak, M. Mungan, and S. Burkardt, *Nanoepitaxy on quasicrystal surfaces*, Appl. Surf. Sci. **256**, 1284 (2009).

[102] L. Bindi, P. J. Steinhardt, N. Yao, and P. J. Lu, *Natural quasicrystals*, Science **324**, 1306 (2009).

[103] L. Bindi, P. J. Steinhardt, N. Yao, and P. J. Lu, *Icosahedrite, $Al_{63}Cu_{24}Fe_{13}$, the first natural quasicrystal*, Am. Mineral. **96**, 928 (2011).

[104] L. Bindi, J. M. Eiler, Y. Guan, L. S. Hollister, G. MacPherson, P. J. Steinhardt, and N. Yao, *Evidence for the extraterrestrial origin of a natural quasicrystal*, Proc. Natl. Acad. Sci. USA **109**, 1396 (2012).

[105] T. Dotera, *Quasicrystals in soft matter*, Isr. J. Chem. **51**, 1197 (2011).

[106] T. Dotera, *Toward the discovery of new soft quasicrystals: From a numerical study viewpoint*, J. Polym. Sci. B Polym. Phys. **50**, 155 (2012).

[107] X. Zeng, G. Ungar, Y. Liu, V. Percec, A. E. Dulcey, and J. K. Hobbs, *Supramolecular dendritic liquid quasicrystals*, Nature (London) **428**, 157 (2004).

[108] K. Hayashida, T. Dotera, A. Takano, and Y. Matsushita, *Polymeric quasicrystal: Mesoscopic quasicrystalline tiling in ABC star polymers*, Phys. Rev. Lett. **98**, 195502 (2007).

[109] S. Fischer, A. Exner, K. Zielske, J. Perlich, S. Deloudi, W. Steurer, P. Lindner, and S. Förster, *Colloidal quasicrystals with 12-fold and 18-fold diffraction symmetry*, Proc. Natl. Acad. Sci. USA **108**, 1810 (2011).

[110] S. C. Glotzer and M. Engel, *Complex order in soft matter*, Nature (London) **471**, 309 (2011).

[111] A. R. Denton and H. Löwen, *Stability of colloidal quasicrystals*, Phys. Rev. Lett. **81**, 469 (1998).

[112] E. A. Jagla, *Phase behavior of a system of particles with core collapse*, Phys. Rev. E **58**, 1478 (1998).

[113] E. A. Jagla, *Minimum energy configurations of repelling particles in two dimensions*, J. Chem. Phys. **110**, 451 (1999).

[114] A. Skibinsky, S. V. Buldyrev, A. Scala, S. Havlin, and H. E. Stanley, *Quasicrystals in a monodisperse system*, Phys. Rev. E **60**, 2664 (1999).

[115] R. Lifshitz and D. M. Petrich, *Theoretical model for Faraday waves with multiple-frequency forcing*, Phys. Rev. Lett. **79**, 1261 (1997).

[116] R. Lifshitz and H. Diamant, *Soft quasicrystals – Why are they stable?*, Philos. Mag. **87**, 3021 (2007).

[117] K. Barkan, H. Diamant, and R. Lifshitz, *Stability of quasicrystals composed of soft isotropic particles*, Phys. Rev. B **83**, 172201 (2011).

[118] A. J. Archer, A. M. Rucklidge, and E. Knobloch, *Quasicrystalline order and a crystal-liquid state in a soft-core fluid*, Phys. Rev. Lett. **111**, 165501 (2013).

[119] T. Dotera, T. Oshiro, and P. Ziherl, *Mosaic two-lengthscale quasicrystals*, Nature (London) **506**, 208 (2014).

[120] D. Rudhardt, C. Bechinger, and P. Leiderer, *Direct measurement of depletion potentials in mixtures of colloids and nonionic polymers*, Phys. Rev. Lett. **81**, 1330 (1998).

[121] C. Bechinger, D. Rudhardt, P. Leiderer, R. Roth, and S. Dietrich, *Understanding depletion forces beyond entropy*, Phys. Rev. Lett. **83**, 3960 (1999).

[122] R. Tuinier, G. A. Vliegenthart, and H. N. W. Lekkerkerker, *Depletion interaction between spheres immersed in a solution of ideal polymer chains*, J. Chem. Phys. **113**, 10768 (2000).

[123] A. Haji-Akbari, M. Engel, A. S. Keys, X. Zheng, R. G. Petschek, P. Palffy-Muhoray, and S. C. Glotzer, *Disordered, quasicrystalline and crystalline phases of densely packed tetrahedra*, Nature (London) **462**, 773 (2009).

[124] C. R. Iacovella, A. S. Keys, and S. C. Glotzer, *Self-assembly of soft-matter quasicrystals and their approximants*, Proc. Natl. Acad. Sci. USA **108**, 20935 (2011).

[125] A. Reinhardt, F. Romano, and J. P. K. Doye, *Computing phase diagrams for a quasicrystal-forming patchy-particle system*, Phys. Rev. Lett. **110**, 255503 (2013).

[126] M. Engel and H.-R. Trebin, *Self-assembly of monatomic complex crystals and quasicrystals with a double-well interaction potential*, Phys. Rev. Lett. **98**, 225505 (2007).

[127] F. Scheffler, P. Maass, J. Roth, and H. Stark, *Quasicrystalline order in binary dipolar systems*, Eur. Phys. J. B **42**, 85 (2004).

[128] K. Barkan, M. Engel, and R. Lifshitz, *Controlled self-assembly of periodic and aperiodic cluster crystals*, Phys. Rev. Lett. **113**, 098304 (2014).

[129] C. V. Achim, M. Schmiedeberg, and H. Löwen, *Growth modes of quasicrystals*, Phys. Rev. Lett. **112**, 255501 (2014).

[130] C. Das and H. R. Krishnamurthy, *Laser-induced quasicrystalline order in charge-stabilized colloidal systems*, Phys. Rev. B **58**, R5889 (1998).

[131] S. P. Gorkhali, J. Qi, and G. P. Crawford, *Switchable quasi-crystal structures with five-, seven-, and ninefold symmetries*, J. Opt. Soc. Am. B **23**, 149 (2006).

[132] J. Mikhael, J. Roth, L. Helden, and C. Bechinger, *Archimedean-like tiling on decagonal quasicrystalline surfaces*, Nature (London) **454**, 501 (2008).

[133] M. Schmiedeberg and H. Stark, *Colloidal ordering on a 2d quasicrystalline substrate*, Phys. Rev. Lett. **101**, 218302 (2008).

[134] J. Mikhael, G. Gera, T. Bohlein, and C. Bechinger, *Phase behavior of colloidal monolayers in quasiperiodic light fields*, Soft Matter **7**, 1352 (2011).

[135] J. Mikhael, M. Schmiedeberg, S. Rausch, J. Roth, H. Stark, and C. Bechinger, *Proliferation of anomalous symmetries in colloidal monolayers subjected to quasiperiodic light fields*, Proc. Natl. Acad. Sci. USA **107**, 7214 (2010).

[136] M. Schmiedeberg, J. Mikhael, S. Rausch, J. Roth, L. Helden, C. Bechinger, and H. Stark, *Archimedean-like colloidal tilings on substrates with decagonal and tetradecagonal symmetry*, Eur. Phys. J. E **32**, 25 (2010).

[137] M. Schmiedeberg and H. Stark, *Comparing light-induced colloidal quasicrystals with different rotational symmetries*, J. Phys.: Condens. Matter **24**, 284101 (2012).

[138] J. A. Kromer, M. Schmiedeberg, J. Roth, and H. Stark, *What phasons look like: Particle trajectories in a quasicrystalline potential*, Phys. Rev. Lett. **108**, 218301 (2012).

[139] J. A. Kromer, M. Schmiedeberg, J. Roth, and H. Stark, *Phason-induced dynamics of colloidal particles on quasicrystalline substrates*, Eur. Phys. J. E **36**, 1 (2013).

[140] C. Reichhardt and C. J. Olson Reichhardt, *Dynamical ordering and directional locking for particles moving over quasicrystalline substrates*, Phys. Rev. Lett. **106**, 060603 (2011).

[141] P. Kählitz and H. Stark, *Phase ordering of hard needles on a quasicrystalline substrate*, J. Chem. Phys. **136**, 174705 (2012).

[142] P. Kählitz, M. Schoen, and H. Stark, *Clustering and mobility of hard rods in a quasicrystalline substrate potential*, J. Chem. Phys. **137**, 224705 (2012).

[143] A. Van Blaaderen, R. Ruel, and P. Wiltzius, *Template-directed colloidal crystallization*, Nature (London) **385**, 321 (1997).

[144] A. van Blaaderen and P. Wiltzius, *Growing large, well-oriented colloidal crystals*, Adv. Mater. **9**, 833 (1997).

[145] J. P. Hoogenboom, A. Yethiraj, A. K. van Langen-Suurling, J. Romijn, and A. van Blaaderen, *Epitaxial crystal growth of charged colloids*, Phys. Rev. Lett. **89**, 256104 (2002).

[146] J. P. Hoogenboom, P. Vergeer, and A. van Blaaderen, *A real-space analysis of colloidal crystallization in a gravitational field at a flat bottom wall*, J. Chem. Phys. **119**, 3371 (2003).

[147] J. P. Hoogenboom, A. K. van Langen-Suurling, J. Romijn, and A. van Blaaderen, *Epitaxial growth of a colloidal hard-sphere hcp crystal and the effects of epitaxial mismatch on crystal structure*, Phys. Rev. E **69**, 051602 (2004).

[148] R. Lifshitz, *Nanotechnology and quasicrystals: From self-assembly to photonic applications*, in *Silicon Versus Carbon*, edited by Y. Magarshak, S. Kozyrev, and A. Vaseashta, NATO Science for Peace and Security Series B: Physics and Biophysics, 119–136, Springer Netherlands (2009).

[149] Z. V. Vardeny, A. Nahata, and A. Agrawal, *Optics of photonic quasicrystals*, Nat. Photon. **7**, 177 (2013).

[150] Y. S. Chan, C. T. Chan, and Z. Y. Liu, *Photonic band gaps in two dimensional photonic quasicrystals*, Phys. Rev. Lett. **80**, 956 (1998).

[151] A. Della Villa, S. Enoch, G. Tayeb, V. Pierro, V. Galdi, and F. Capolino, *Band gap formation and multiple scattering in photonic quasicrystals with a penrose-type lattice*, Phys. Rev. Lett. **94**, 183903 (2005).

[152] M. E. Zoorob, M. D. B. Charlton, G. J. Parker, J. J. Baumberg, and M. C. Netti, *Complete photonic bandgaps in 12-fold symmetric quasicrystals*, Nature (London) **404**, 740 (2000).

[153] X. Zhang, Z.-Q. Zhang, and C. T. Chan, *Absolute photonic band gaps in 12-fold symmetric photonic quasicrystals*, Phys. Rev. B **63**, 081105 (2001).

[154] W. Man, M. Megens, P. J. Steinhardt, and P. M. Chaikin, *Experimental measurement of the photonic properties of icosahedral quasicrystals*, Nature (London) **436**, 993 (2005).

[155] M. C. Rechtsman, H.-C. Jeong, P. M. Chaikin, S. Torquato, and P. J. Steinhardt, *Optimized structures for photonic quasicrystals*, Phys. Rev. Lett. **101**, 073902 (2008).

[156] S. S. M. Cheng, L.-M. Li, C. T. Chan, and Z. Q. Zhang, *Defect and transmission properties of two-dimensional quasiperiodic photonic band-gap systems*, Phys. Rev. B **59**, 4091 (1999).

[157] R. Lifshitz, A. Arie, and A. Bahabad, *Photonic quasicrystals for nonlinear optical frequency conversion*, Phys. Rev. Lett. **95**, 133901 (2005).

[158] S. M. Thon, W. T. M. Irvine, D. Kleckner, and D. Bouwmeester, *Polychromatic photonic quasicrystal cavities*, Phys. Rev. Lett. **104**, 243901 (2010).

[159] N. A. Wasio, R. C. Quardokus, R. P. Forrest, C. S. Lent, S. A. Corcelli, J. A. Christie, K. W. Henderson, and S. A. Kandel, *Self-assembly of hydrogen-bonded two-dimensional quasicrystals*, Nature (London) **507**, 86 (2014).

[160] S. Förster, K. Meinel, R. Hammer, M. Trautmann, and W. Widdra, *Quasicrystalline structure formation in a classical crystalline thin-film system*, Nature (London) **502**, 215 (2013).

[161] D. V. Talapin, E. V. Shevchenko, M. I. Bodnarchuk, X. Ye, J. Chen, and C. B. Murray, *Quasicrystalline order in self-assembled binary nanoparticle superlattices*, Nature (London) **461**, 964 (2009).

[162] A. van Blaaderen, *Materials science: Quasicrystals from nanocrystals*, Nature (London) **461**, 892 (2009).

[163] A. Jagannathan and M. Duneau, *An eightfold optical quasicrystal with cold atoms*, Europhys. Lett. **104**, 66003 (2013).

[164] S. Gopalakrishnan, I. Martin, and E. A. Demler, *Quantum quasicrystals of spin-orbit-coupled dipolar bosons*, Phys. Rev. Lett. **111**, 185304 (2013).

[165] R. Berger, *The undecidability of the domino problem*, American Mathematical Soc. (1966).

[166] R. M. Robinson, *Undecidability and nonperiodicity for tilings of the plane*, Invent. Math. **12**, 177 (1971).

[167] P. J. Lu and P. J. Steinhardt, *Decagonal and quasi-crystalline tilings in medieval islamic architecture*, Science **315**, 1106 (2007).

[168] E. Makovicky, *Comment on "decagonal and quasi-crystalline tilings in medieval islamic architecture"*, Science **318**, 1383 (2007).

[169] P. J. Lu and P. J. Steinhardt, *Response to comment on "decagonal and quasi-crystalline tilings in medieval islamic architecture"*, Science **318**, 1383 (2007).

[170] C. A. Reiter, *Atlas of quasicrystalline tilings*, Chaos, Solitons & Fractals **14**, 937 (2002).

[171] E. Harriss and D. Frettlöh, *Tilings encyclopedia,* `http://tilings.math.uni-bielefeld.de/`.

[172] R. Penrose, *The role of aesthetics in pure and applied mathematical research*, In: Bull. J. Inst. Math. Appl. **10**, 266 (1974).

[173] M. Baake and U. Grimm, *Mathematical diffraction of aperiodic structures*, Chem. Soc. Rev. **41**, 6821 (2012).

[174] M. Gardner, *Extraordinary nonperiodic tiling that enriches the theory of tiles*, Sci. Amer.(USA) **236**, 110 (1977).

[175] R. Penrose, *Pentaplexity a class of non-periodic tilings of the plane*, Math. Intelligencer **2**, 32 (1979).

[176] B. Grünbaum and G. C. Shephard, *Tilings and patterns*, WH Freeman & Co., New York (1986).

[177] P. Hemenway, *Divine proportion: Phi in art, nature, and science*, Sterling Publishing Company, Inc. (2005).

[178] R. Ammann, B. Grünbaum, and G. Shephard, *Aperiodic tiles*, Discrete Comput. Geom. **8**, 1 (1992).

[179] S. I. Ben-Abraham and F. Gähler, *Covering cluster description of octagonal MnSiAl quasicrystals*, Phys. Rev. B **60**, 860 (1999).

[180] M. Oxborrow and C. L. Henley, *Random square-triangle tilings: A model for twelvefold-symmetric quasicrystals*, Phys. Rev. B **48**, 6966 (1993).

[181] M. Widom, *Bethe ansatz solution of the square-triangle random tiling model*, Phys. Rev. Lett. **70**, 2094 (1993).

[182] J. de Gier and B. Nienhuis, *Integrability of the square-triangle random tiling model*, Phys. Rev. E **55**, 3926 (1997).

[183] E. O. Harriss, *Non-periodic rhomb substitution tilings that admit order n rotational symmetry*, Discrete Comput. Geom. **34**, 523 (2005).

[184] F. P. M. Beenker, *Algebraic theory of non-periodic tilings of the plane by two simple building blocks: A square and a rhombus*, Department of Mathematics and Computing Science, Eindhoven University of Technology (1982).

[185] N. De Bruijn, *Algebraic theory of penrose's non-periodic tilings of the plane I*, in *Indag. Math. (Proceedings)*, volume 84, 39–52, North-Holland (1981).

[186] N. G. De Bruijn, *Algebraic theory of penrose's non-periodic tilings of the plane II*, in *Indag. Math. (Proceedings)*, volume 84, 53–66, North-Holland (1981).

[187] C. Janot, *Quasicrystals: A Primer*, Oxford University Press (2012).

[188] M. Baake, R. Klitzing, and M. Schlottmann, *Fractally shaped acceptance domains of quasiperiodic square-triangle tilings with dodecagonal symmetry*, Phys. A **191**, 554 (1992).

[189] M. Baake and U. Grimm, *Aperiodic Order*, Cambridge University Press (2013).

[190] M. Duneau and A. Katz, *Quasiperiodic patterns*, Phys. Rev. Lett. **54**, 2688 (1985).

[191] J. E. S. Socolar, P. J. Steinhardt, and D. Levine, *Quasicrystals with arbitrary orientational symmetry*, Phys. Rev. B **32**, 5547 (1985).

[192] V. Elser, *The diffraction pattern of projected structures*, Acta Cryst. A **42**, 36 (1986).

[193] J. H. Conway and K. M. Knowles, *Quasiperiodic tiling in two and three dimensions*, J. Phys. A: Math. Gen. **19**, 3645 (1986).

[194] E. J. W. Verwey and J. T. G. Overbeek, *Theory of the stability of lyophobic colloids*, Courier Dover Publications (1999).

[195] B. V. Derjaguin and L. Landau, *The theory of stability of highly charged lyophobic sols and coalescence of highly charged particles in electrolyte solutions*, Acta Physicochim. URSS **14**, 633 (1941).

[196] H. Löwen, *Colloidal soft matter under external control*, J. Phys.: Condens. Matter **13**, R415 (2001).

[197] D. J. W. Aastuen, N. A. Clark, L. K. Cotter, and B. J. Ackerson, *Nucleation and growth of colloidal crystals*, Phys. Rev. Lett. **57**, 1733 (1986).

[198] S. Auer and D. Frenkel, *Prediction of absolute crystal-nucleation rate in hard-sphere colloids*, Nature (London) **409**, 1020 (2001).

[199] U. Gasser, E. R. Weeks, A. Schofield, P. N. Pusey, and D. A. Weitz, *Real-space imaging of nucleation and growth in colloidal crystallization*, Science **292**, 258 (2001).

[200] S. van Teeffelen, C. N. Likos, and H. Löwen, *Colloidal crystal growth at externally imposed nucleation clusters*, Phys. Rev. Lett. **100**, 108302 (2008).

[201] N. Hoffmann, F. Ebert, C. N. Likos, H. Löwen, and G. Maret, *Partial clustering in binary two-dimensional colloidal suspensions*, Phys. Rev. Lett. **97**, 078301 (2006).

[202] J. Baumgartl, R. P. A. Dullens, M. Dijkstra, R. Roth, and C. Bechinger, *Experimental observation of structural crossover in binary mixtures of colloidal hard spheres*, Phys. Rev. Lett. **98**, 198303 (2007).

[203] P. Pusey and W. Van Megen, *Phase behaviour of concentrated suspensions of nearly hard colloidal spheres*, Nature (London) **320**, 340 (1986).

[204] P. N. Pusey and W. van Megen, *Observation of a glass transition in suspensions of spherical colloidal particles*, Phys. Rev. Lett. **59**, 2083 (1987).

[205] J. Dzubiella, G. P. Hoffmann, and H. Löwen, *Lane formation in colloidal mixtures driven by an external field*, Phys. Rev. E **65**, 021402 (2002).

[206] J. Chakrabarti, J. Dzubiella, and H. Löwen, *Reentrance effect in the lane formation of driven colloids*, Phys. Rev. E **70**, 012401 (2004).

[207] M. Rex and H. Löwen, *Lane formation in oppositely charged colloids driven by an electric field: Chaining and two-dimensional crystallization*, Phys. Rev. E **75**, 051402 (2007).

[208] T. Glanz and H. Löwen, *The nature of the laning transition in two dimensions*, J. Phys.: Condens. Matter **24**, 464114 (2012).

[209] D. J. Pine, J. P. Gollub, J. F. Brady, and A. M. Leshansky, *Chaos and threshold for irreversibility in sheared suspensions*, Nature (London) **438**, 997 (2005).

[210] R. Besseling, E. R. Weeks, A. B. Schofield, and W. C. K. Poon, *Three-dimensional imaging of colloidal glasses under steady shear*, Phys. Rev. Lett. **99**, 028301 (2007).

[211] L. Corte, P. Chaikin, J. P. Gollub, and D. Pine, *Random organization in periodically driven systems*, Nature Physics **4**, 420 (2008).

[212] I. S. Aranson, *Active colloids*, Phys.-Usp. **56**, 79 (2013).

[213] R. Dreyfus, J. Baudry, M. L. Roper, M. Fermigier, H. A. Stone, and J. Bibette, *Microscopic artificial swimmers*, Nature (London) **437**, 862 (2005).

[214] J. Bialké, T. Speck, and H. Löwen, *Crystallization in a dense suspension of self-propelled particles*, Phys. Rev. Lett. **108**, 168301 (2012).

[215] A. Zöttl and H. Stark, *Nonlinear dynamics of a microswimmer in Poiseuille flow*, Phys. Rev. Lett. **108**, 218104 (2012).

[216] A. Kaiser, H. H. Wensink, and H. Löwen, *How to capture active particles*, Phys. Rev. Lett. **108**, 268307 (2012).

[217] A. M. Menzel and H. Löwen, *Traveling and resting crystals in active systems*, Phys. Rev. Lett. **110**, 055702 (2013).

[218] F. Kümmel, B. ten Hagen, R. Wittkowski, I. Buttinoni, R. Eichhorn, G. Volpe, H. Löwen, and C. Bechinger, *Circular motion of asymmetric self-propelling particles*, Phys. Rev. Lett. **110**, 198302 (2013).

[219] I. Buttinoni, J. Bialké, F. Kümmel, H. Löwen, C. Bechinger, and T. Speck, *Dynamical clustering and phase separation in suspensions of self-propelled colloidal particles*, Phys. Rev. Lett. **110**, 238301 (2013).

[220] A. Zöttl and H. Stark, *Hydrodynamics determines collective motion and phase behavior of active colloids in quasi-two-dimensional confinement*, Phys. Rev. Lett. **112**, 118101 (2014).

[221] T. Speck, J. Bialké, A. M. Menzel, and H. Löwen, *Effective Cahn-Hilliard equation for the phase separation of active brownian particles*, Phys. Rev. Lett. **112**, 218304 (2014).

[222] B. ten Hagen, F. Kümmel, R. Wittkowski, D. Takagi, H. Löwen, and C. Bechinger, *Gravitaxis of asymmetric self-propelled colloidal particles*, Nat. Commun. **5**, 4829 (2014).

[223] A. Ashkin, *Acceleration and trapping of particles by radiation pressure*, Phys. Rev. Lett. **24**, 156 (1970).

[224] A. Ashkin, *Applications of laser radiation pressure*, Science **210**, 1081 (1980).

[225] M. M. Burns, J.-M. Fournier, and J. A. Golovchenko, *Optical matter: Crystallization and binding in intense optical fields*, Science **249**, 749 (1990).

[226] I. Williams, E. C. Oğuz, P. Bartlett, H. Löwen, and C. P. Royall, *Direct measurement of osmotic pressure via adaptive confinement of quasi hard disc colloids*, Nat. Commun. **4**, 2555 (2013).

[227] A. Chowdhury, B. J. Ackerson, and N. A. Clark, *Laser-induced freezing*, Phys. Rev. Lett. **55**, 833 (1985).

[228] C. Bechinger and E. Frey, *Phase behaviour of colloids in confining geometry*, J. Phys.: Condens. Matter **13**, R321 (2001).

[229] C. Bechinger, M. Brunner, and P. Leiderer, *Phase behavior of two-dimensional colloidal systems in the presence of periodic light fields*, Phys. Rev. Lett. **86**, 930 (2001).

[230] P. Schall, I. Cohen, D. A. Weitz, and F. Spaepen, *Visualization of dislocation dynamics in colloidal crystals*, Science **305**, 1944 (2004).

[231] P. Schall, I. Cohen, D. A. Weitz, and F. Spaepen, *Visualizing dislocation nucleation by indenting colloidal crystals*, Nature (London) **440**, 319 (2006).

[232] J. E. S. Socolar, T. C. Lubensky, and P. J. Steinhardt, *Phonons, phasons, and dislocations in quasicrystals*, Phys. Rev. B **34**, 3345 (1986).

[233] J. E. S. Socolar and P. J. Steinhardt, *Quasicrystals. II. Unit-cell configurations*, Phys. Rev. B **34**, 617 (1986).

[234] P. De and R. A. Pelcovits, *Linear elasticity theory of pentagonal quasicrystals*, Phys. Rev. B **35**, 8609 (1987).

[235] C. Kittel and P. McEuen, *Introduction to solid state physics*, Wiley New York (1986).

[236] D. R. Nelson, *Defects and geometry in condensed matter physics*, Cambridge University Press (2002).

[237] R. Lifshitz, *Symmetry breaking and order in the age of quasicrystals*, Isr. J. Chem. **51**, 1156 (2011).

[238] D. Levine, T. C. Lubensky, S. Ostlund, S. Ramaswamy, P. J. Steinhardt, and J. Toner, *Elasticity and dislocations in pentagonal and icosahedral quasicrystals*, Phys. Rev. Lett. **54**, 1520 (1985).

[239] M. Engel, M. Umezaki, H.-R. Trebin, and T. Odagaki, *Dynamics of particle flips in two-dimensional quasicrystals*, Phys. Rev. B **82**, 134206 (2010).

[240] K. J. Strandburg, *Random-tiling quasicrystal*, Phys. Rev. B **40**, 6071 (1989).

[241] K. J. Strandburg, *Entropy of a three-dimensional random-tiling quasicrystal*, Phys. Rev. B **44**, 4644 (1991).

[242] M. De Boissieu, *Phason modes in quasicrystals*, Philos. Mag. **88**, 2295 (2008).

[243] M. de Boissieu, *Phonons, phasons and atomic dynamics in quasicrystals*, Chem. Soc. Rev. **41**, 6778 (2012).

[244] K. Edagawa, K. Suzuki, and S. Takeuchi, *High resolution transmission electron microscopy observation of thermally fluctuating phasons in decagonal Al-Cu-Co*, Phys. Rev. Lett. **85**, 1674 (2000).

[245] B. Freedman, R. Lifshitz, J. W. Fleischer, and M. Segev, *Phason dynamics in nonlinear photonic quasicrystals*, Nat. Mater. **6**, 776 (2007).

[246] C. Henley, M. De Boissieu, and W. Steurer, *Discussion on clusters, phasons and quasicrystal stabilisation*, Philos. Mag. **86**, 1131 (2006).

[247] S. Gopalakrishnan, I. Martin, and E. A. Demler, *Gopalakrishnan, Martin, and Demler reply:*, Phys. Rev. Lett. **113**, 079603 (2014).

[248] R. Lifshitz, *Comment on "Quantum quasicrystals of spin-orbit-coupled dipolar bosons"*, Phys. Rev. Lett. **113**, 079602 (2014).

[249] P. De and R. A. Pelcovits, *Disclinations in pentagonal quasicrystals*, Phys. Rev. B **36**, 9304 (1987).

[250] P. De and R. A. Pelcovits, *Interaction energy of disclinations in pentagonal quasicrystals*, Phys. Rev. B **38**, 5042 (1988).

[251] P. De and R. A. Pelcovits, *Defect-mediated melting of pentagonal quasicrystals*, J. Phys. A: Math. Gen. **22**, 1167 (1989).

[252] J. M. Kosterlitz and D. J. Thouless, *Ordering, metastability and phase transitions in two-dimensional systems*, J. Phys. C **6**, 1181 (1973).

[253] B. I. Halperin and D. R. Nelson, *Theory of two-dimensional melting*, Phys. Rev. Lett. **41**, 121 (1978).

[254] D. R. Nelson, *Study of melting in two dimensions*, Phys. Rev. B **18**, 2318 (1978).

[255] D. R. Nelson and B. I. Halperin, *Dislocation-mediated melting in two dimensions*, Phys. Rev. B **19**, 2457 (1979).

[256] A. Young, *On the theory of the phase transition in the two-dimensional planar spin model*, J. Phys. C **11**, L453 (1978).

[257] A. P. Young, *Melting and the vector coulomb gas in two dimensions*, Phys. Rev. B **19**, 1855 (1979).

[258] N. Metropolis, A. W. Rosenbluth, M. N. Rosenbluth, A. H. Teller, and E. Teller, *Equation of state calculations by fast computing machines*, J. Chem. Phys. **21**, 1087 (1953).

[259] N. Metropolis and S. Ulam, *The Monte Carlo method*, J. Amer. Statist. Assoc. **44**, 335 (1949).

[260] M. E. J. Newman and G. T. Barkema, *Monte Carlo methods in statistical physics*, Clarendon Press Oxford (1999).

[261] K. Binder and D. W. Heermann, *Monte Carlo simulation in statistical physics: an introduction*, Springer (2010).

[262] M. Matsumoto and T. Nishimura, *Mersenne Twister: A 623-dimensionally equidistributed uniform pseudo-random number generator*, ACM Trans. Model. Comput. Simul. **8**, 3 (1998).

[263] O. Entin-Wohlman, M. Kléman, and A. Pavlovitch, *Penrose tiling approximants*, J. Phys. (France) **49**, 587 (1988).

[264] E. A. Lord, K. Ramakrishnan, and S. Ranganathan, *An algorithm for generating quasiperiodic patterns and their approximants*, Bull. Mater. Sci. **23**, 119 (2000).

[265] A. Subramaniam and K. Ramakrishnan, *Rational approximants to 5, 8 and 7-fold two-dimensional tilings*, Z. Kristallogr. **218**, 590 (2003).

[266] P. Stampfli, *A dodecagonal quasi-periodic lattice in 2 dimensions*, Helv. Phys. Acta **59**, 1260 (1986).

[267] X. Zeng and G. Ungar, *Inflation rules of square-triangle tilings: From approximants to dodecagonal liquid quasicrystals*, Philos. Mag. **86**, 1093 (2006).

[268] M. I. Bodnarchuk, E. V. Shevchenko, and D. V. Talapin, *Structural defects in periodic and quasicrystalline binary nanocrystal superlattices*, J. Am. Chem. Soc. **133**, 20837 (2011).

[269] B. Freedman, G. Bartal, M. Segev, R. Lifshitz, D. N. Christodoulides, and J. W. Fleischer, *Wave and defect dynamics in nonlinear photonic quasicrystals*, Nature (London) **440**, 1166 (2006).

[270] J. A. Smerdon, K. M. Young, M. Lowe, S. Hars, T. P. Yadav, D. Hesp, V. Dhanak, A.-P. Tsai, H. R. Sharma, and R. Mcgrath, *Templated quasicrystalline molecular ordering*, Nano Lett. **14**, 1184 (2014).

[271] M. Martinsons, *Phasonische Drift und Fluktuationen in Quasikristallen*, Master-Arbeit, Heinrich-Heine-Universität Düsseldorf (2013).

[272] L. X. He, Y. K. Wu, and K. H. Kuo, *Decagonal quasicrystals with different periodicities along the tenfold axis in rapidly solidified* $Al_{65}Cu_{20}M_{15}$ *(M=Mn, Fe, Co or Ni)*, J. Mater. Sci. Lett. **7**, 1284 (1988).

[273] R. Ganapathy, M. R. Buckley, S. J. Gerbode, and I. Cohen, *Direct measurements of island growth and step-edge barriers in colloidal epitaxy*, Science **327**, 445 (2010).

[274] D. Deb and H. H. von Grünberg, *Colloidal model system for island formation*, J. Phys.: Condens. Matter **21**, 245102 (2009).

[275] J. Zhang and F. S. Bates, *Dodecagonal quasicrystalline morphology in a poly(styrene-b-isoprene-b-styrene-b-ethylene oxide) tetrablock terpolymer*, J. Am. Chem. Soc. **134**, 7636 (2012).

[276] S. Asakura and F. Oosawa, *On interaction between two bodies immersed in a solution of macromolecules*, J. Chem. Phys. **22**, 1255 (1954).

List of Figures

APPENDIX A

Tilingbuilder

In this appendix we present our program that we implemented in order to construct the aperiodic tilings used in the preceding computational studies. The program is written in *C*++ and exhibits a graphical user interface (GUI). In the following, the features of the program are explained as in a short user guide. In the first part, the general functionality of the program is introduced. In the second part, the individual controls in the GUI are elucidated in more detail. In the third part, the feature to incorporate user defined tile flips is presented, while, as an example, a rational approximant for a tiling with tetradecagonal rotational symmetry is constructed.

A.1. Program overview

The implemented aperiodic tilings are obtained by the inflation method from section 1.3.1. An initial configuration of basic tiles is scaled by an irrational inflation factor. Afterwards, each scaled tile is substituted by conglomerations of the basic tiles according to its inflation rule. By conducting this procedure several times a large patch of the aperiodic tiling is generated. Then a rectangular segment from this patch is cut out. All vertex coordinates are exported to a file and thus made available for further computational studies. In section A.3, we explain how the cut out segments can be modified by the user to comply with periodic boundary conditions.

The program is implemented in *C*++ and possesses the advantages of an object orientated architecture. The general composition follows the model-view-controller principle (MVC). Therefore, an extension to other inflation based tilings is straight forward. Since the classes of the basic tiles are all derived from an abstract base class, a concrete implementation of the member function performing the inflation step is all that is required. A current list of realized aperiodic tilings comprises the octagonal Ammann-Beenker and Watanabe-Ito-Soma, the dodecagonal Square-Triangle, the decagonal Penrose-Rhomb, the tetradecagonal Danzer-Original and the octadecagonal Harris tiling. These and further tilings can be found here [a1].

A typical window of the program is illustrated in Fig. A.1. It is divided into two parts, a control panel and a display panel with the tiling. The red rectangle defines the cut out

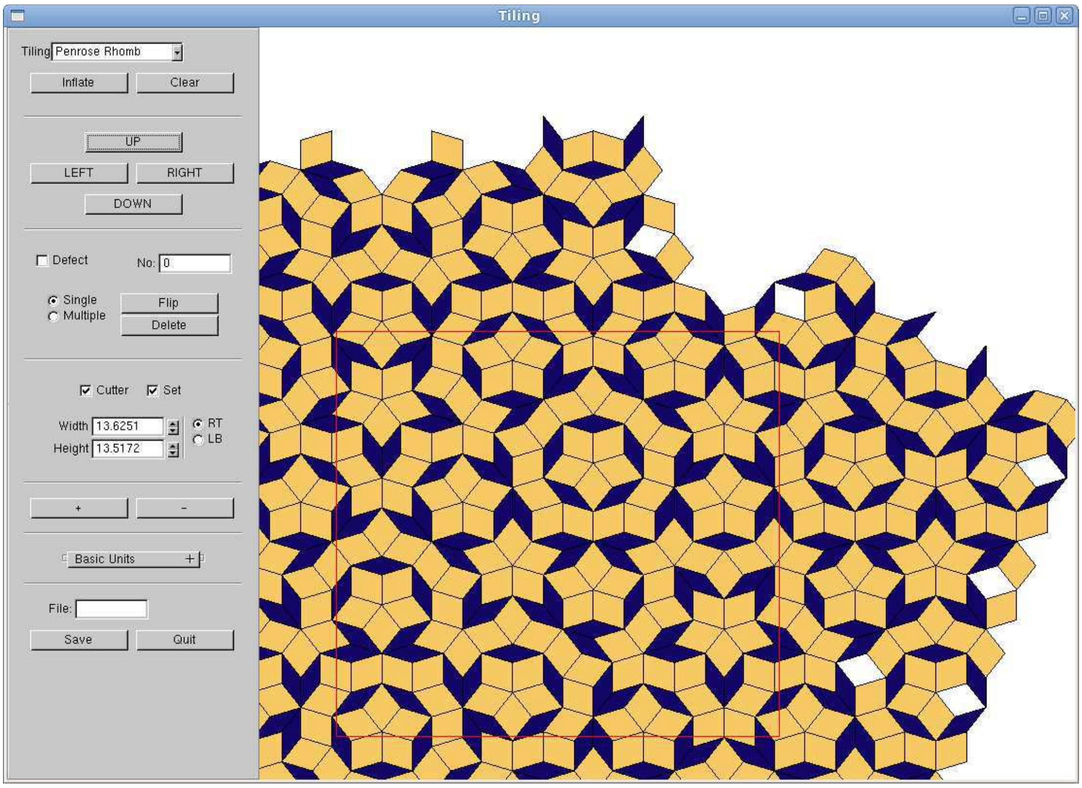

Tiling: Penrose Rhomb

☐ Defect No: 0

● Single
○ Multiple

☑ Cutter ☑ Set

Width 13.6251
Height 13.5172

● RT
○ LB

File:

Figure A.1.: Screenshot illustrating the typical usage of the program. The graphical user interface is divided into two parts, a control panel on the left and a display panel with the tiling on the right side. The red rectangle denotes a simulation box, namely the segment of the tiling whose vertices are exported to an external file. The current view on the displayed tiling can be modified by zooming or displacing the focus point. In addition, the control panel offers options to manipulate the tiling by performing the next inflation step or by inserting flips of different tiles as defects. The location of these defects is set directly by mouse clicks and should be chosen in such a way that opposite edges of the exported segment form periodic boundaries.

segment whose vertex coordinates are exported. Aside from the *C++* standard libraries, several external libraries are embedded into the program. Nevertheless, the program is portable to various systems. For the graphical implementation we rely on OpenGL which is he premier application programming interface (API) for developing portable, interactive 2D and 3D graphics applications [a2]. While the OpenGL utility toolkit (GLUT) is sufficient in our case to carry out the window handling, it also offers a window-system independent, portable API [a3]. In addition, GLUI, a GLUT based C++ user interface library, provides basic controls such as buttons, check boxes, radio buttons, and spinners to our OpenGL application [a4]. The mathematical operations of the inflation procedure are managed in Eigen, a template library for linear algebra [a5].

A.2. User interface

The control components from the GLUI library allow the user to construct his tiling patch individually. A detailed explanation of the control interface is presented in Fig. A.2. The user selects a tiling from a list and executes the inflation procedure as far as desired. He can move the camera to view different regions of the aperiodic tiling. In addition, he can set the size of the cut out segment and place it to any desired region. For more sophisticated needs, defects can be incorporated as certain groups of tiles depending on the respective tiling may be flipped. In this way, the user can obtain his own devised tiling patch.

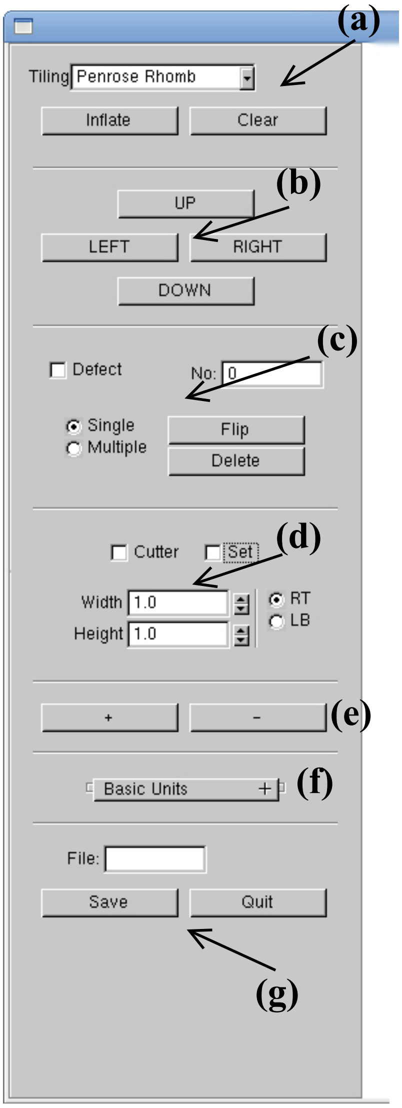

Tiling: Penrose Rhomb

☐ Defect No: 0

● Single
○ Multiple

☐ Cutter ☐ Set

Width 1.0
Height 1.0

● RT
○ LB

File:

Figure A.2.: Detailed explanation of the control interface. (a) After the desired tiling has been selected from the list box the starting configuration of that tiling is displayed. Every time the button *Inflate* is pushed the next generation of the tiling is produced, while a click on *Clear* resets the whole process. (b) The steering cross allows to shift either the focus point of the camera view or the exported segment region of the tiling that is defined by a red rectangle. (c) If the option for defects is turned on, mouse clicks within the tiling may lead to tile flips. Defects that affect only the position of one vertex are characterized as *Single* and are incorporated by a mouse click close to the vertex. The neighboring tiles forming this vertex rearrange in a different manner such that the position of the vertex is slightly displaced. On the other hand, defects that affect several vertex positions are characterized as *Multiple*. Tiles are marked by mouse clicks and the rearrangement is executed by pushing *Flip*. (d) Displays the current values for width and height of the exported segment. The size of the rectangle can be modified by the spinners or by selecting vertices within the tiling as corners of the rectangle. Therefore, the box size of the rational approximant can be adjusted precisely. (e) The two buttons allow to zoom in and out. (f) If necessary the edge length of the tiles or the depth and diameter of the substrate holes can be set, otherwise the default settings remain hidden. (g) If *Save* is pushed, the vertices located inside the red bordered region are written to the named file. Via *Quit* the program terminates.

A.3. Tools to construct approximants

The most important feature of the program is the ability to design rational approximants for the aperiodic tilings. These are a necessity for most computational studies involving quasicrystals. The method to select suitable box sizes from section 3.2.1 is sufficient for octagonal, decagonal or dodecagonal continuous quasicrystalline fields, i.e. rotational symmetries with rank $D = 4$. It is less applicable for rotational symmetries with rank $D = 6$, like for instance tetradecagonal or octadecagonal symmetry, as it requires the rational approximation not for two but for three incommensurate length scales. Therefore, a subtle choice for the cut out segment from the aperiodic tiling is not sufficient to produce an approximant.

Tilingbuilder offers tools to the user exploiting the phasonic degrees of quasicrystals to produce phasonic approximants. By flipping certain tiles close to the edges of the cut out segment, opposite edges may match under periodic conditions. For each tiling an individual solution has been implemented. An example for the tetradecagonal Danzer tiling is shown in Fig. A.3. If the original rhombic patch satisfying the matching rules is translated as a basic periodic cell, the boundaries of the original and translated cells do not match each other. However, the flipping of tiles in the area of mismatch leads to edges of the rhombic cell that fulfill periodic conditions.

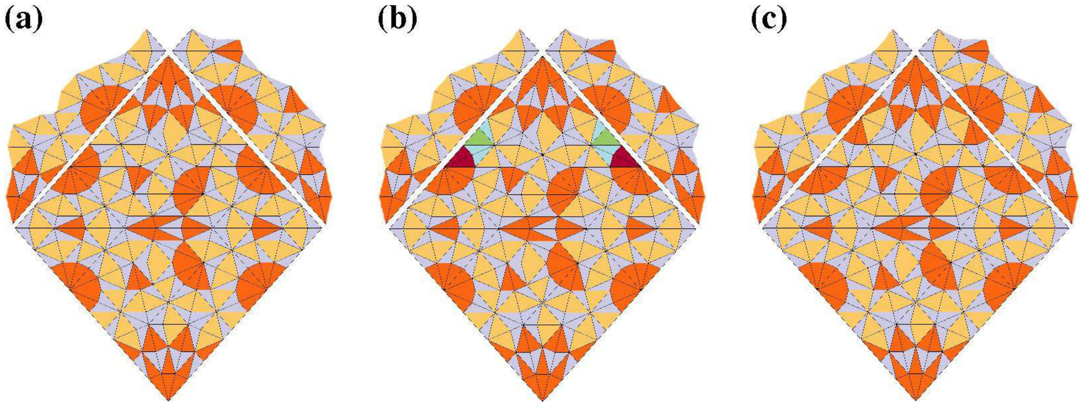

Figure A.3.: Construction of a rational approximant for the tetradecagonal Danzer tiling. (a) A rhombic patch of Danzer's Original tiling is displayed. The premorse patches correspond to translations of the original patch as in a simulation box with periodic boundary conditions. Yet, at the moment the adjacent patches do not fulfill periodic conditions. (b) Tiles in the region of the unmatched boundaries are marked for rearrangement. Note the different color shading. (c) After the flip routine has been executed the selected tiles have been rearranged in such a way that periodic boundary conditions are now fulfilled for the rhombic tiling patch. The patch can now be exported for computational studies.

A.4. Conclusion

Whether the construction of quasicrystalline substrates for colloidal epitaxy or the competing configurations of colloids in the colloid-polymer mixture, Tilingbuilder represents the first step in investigating these systems. Since its object orientated architecture follows the model-view-controller principle, adjustments to the program can be easily implemented as the possible need arises during research. In principle, any tiling for which inflation rules exist can be incorporated. In the end, the portability ensures the usage for colleagues and coworkers.

References

[a1] E. Harriss, and D. Frettlöh, *Tilings Encyclopedia*, `http://tilings.math.uni-bielefeld.de/substitution_rules`

[a2] *OpenGL*, `https://www.opengl.org/`

[a3] *GLUT*, `https://www.opengl.org/resources/libraries/glut/`

[a4] P. Rademacher, *GLUI*, `https://www.cs.unc.edu/~rademach/glui/`

[a5] *Eigen*, `http://www.eigen.tuxfamily.org`

Danksagung

Zum Schluss möchte ich mich bei allen aus dem Institut für Theoretische Physik 2 bedanken, denn die vergangenen Jahre, die tolle Arbeitsatmosphäre und das Klima im Büro werde ich immer in guter Erinnerung behalten. Letztlich gebührt der Dank dafür jedem, von den Professoren bis zu den Sekretärinnen und Administratoren sowie den Assistenten, Doktoranden und Studenten. Allen, die sich für das Themengebiet interessieren, kann ich das Institut und die Forschungsgruppen nur empfehlen.

Dann gilt besonderer Dank meinem Betreuer Dr. Schmiedeberg, der mir das faszinierende Thema anvertraut hat. Er hatte, im wahrsten Sinne des Wortes, immer eine offene Tür und ein offenes Ohr für Belange meiner Arbeit. Ich erinnere mich an viele unterhaltsame und motivierende Diskussionen quer durch das Feld der Quasikristalle. Unter seinem Einfluss wurde das Forschungsfeld frühzeitig neben der Epitaxie auf quasikristalline Substrate um die optischen und selbst-anordnenden Systeme erweitert und so auf eine breitere Basis gestellt. Dies hat sich gerade rückblickend als segensreich erwiesen. Bei ihm und auch bei Prof. Dr. Löwen möchte ich mich zudem dafür bedanken, dass mir der Besuch zahlreicher Konferenzen ermöglicht wurde. Erstaunlicherweise zählen die Wochen davor zu den produktivsten und die danach zu den besonders motivierenden.

Darüber hinaus waren viele interessante Gespräche und Diskussionen wertvoll für mich. Dank geht an Cristian Achim, der mir durch intensive bis erschöpfende Diskussionen dabei geholfen hat, mein eigenes Verständnis zu vertiefen; ebenso an Aleksandar Mijailović und Erdal Oğuz. Danke an Kobi Barkan für die Gespräche zu Dislokationen in Quasikristallen und an Johannes Roth für seine Anmerkungen zu aperiodischen Parkettierungen.

Wie sehr man heute auf einen Computer angewiesen ist, merkt man erst, wenn nichts mehr geht. Glücklicherweise bin ich während meiner Arbeit von katastrophalen Pannen verschont geblieben. Deswegen geht für das Verwalten der Computer und Rechencluster ein Danke Schön an Joachim Wenk, der immer hilfsbereit war, wenn sich Probleme oder Änderungen im Laufe meiner Arbeit ergaben.

Die Arbeit im Dasein eines Doktoranden besteht nicht immer aus interessanter Forschung. Von Zeit zu Zeit sieht man sich mit organisatorischen Verwaltungsaufgaben konfrontiert. Vielen Dank an Frau Wildhagen und Brigitte Schumann, die mich bei der Bewältigung von Anträgen aller Art, Reisekostenabrechnungen und allem, was sonst noch so anfiel, unterstützt haben.

Trotz aller oben genannter Unterstützung, am Ende kann nur ein gesunder Mensch Leistung bringen. Aus diesem Grund gebührt mein Dank auch dem gewissenhaft arbeitenden betriebsärztlichen Dienst der Universität. Nun sind Mediziner nicht gerade für ihre Kalligraphie

berühmt, sodass auf dem Klemmbrett ganz schnell Physik zu Physiologie werden kann. Einem Beschäftigten aus letzterem Arbeitsfeld wird selbstverständlich eine sorgfältigere Behandlung zu Teil. Bis man als ahnungsloser Patient dieses Missverständnis korrigiert hat, ist schon ein halber Arbeitstag erfolglos vergangen.

Um Erfolg zu haben, sollte man Arbeit und Privates nicht voneinander trennen, sondern miteinander verbinden. Das gelingt nicht immer. In meinem Fall wurde die Verbindung von der Deutschen Bahn AG bereit gestellt, wofür ich mich an dieser Stelle bedanken möchte. In den Zügen auf der Strecke Düsseldorf-Hannover bzw. Düsseldorf-Berlin ist so mancher Artikel gelesen worden. Außerdem sind dort auch wesentliche Teile der verwendeten Programmcodes entstanden. Negative Auswirkungen auf die Laufzeit oder die Performance könnte man vermuten, haben sich aber nicht bestätigt.

Andere Dinge hingegen haben sich sehr wohl bestätigt: Ich bin kein Rheinländer. Mit Bierersatz und Sauerbraten kann ich mich noch anfreunden. Tatsächlich mag ich beides sogar, genau wie die Stadt Düsseldorf. Aber meine Integrationsbereitschaft kennt auch irgendwo Grenzen, die an ganz bestimmten Tagen getestet werden. An Tagen wie diesen wünscht man sich nicht Unendlichkeit, sondern eine Zuflucht, wie sie mir gewährt wurde. Deswegen bedanke ich mich bei Kathrin für kulturelles Asyl und bei Corinna, Tobias, Franzi, Martin, Frank, Juliane, Christoph, Lena, Benno, Markus, Johannes, Karsten und Johanna für zahlreiche freudige Wochenenden in hochdeutschen Landen. Düsseldorfer mögen mir dies bitte verzeihen, aber schon ein gewisser Heinrich Heine soll seiner Zeit der Gegend dort etwas abgewonnen haben.

Wenn man einmal nicht vorankommt, kann es ratsam sein, einen Schritt zurück zu gehen. Manchmal reicht dazu schon etwas Ablenkung. Dafür, dass ich davon nie zu wenig hatte, sorgte schon meine Freundin: Kathrin, trotz, aber auch wegen dir ist das hier die letzte Seite!

Aber auch nur eine von vielen Seiten. Die meisten hat Karsten dankenswerter Weise Korrektur gelesen, während Andreas Kommentare zum Manuskript ebenfalls sehr hilfreich gewesen sind. Alle übrigen sprachlichen Fehler, die in dieser Schrift noch enthalten sind, mögen bitte unerkannt bleiben.

Zu guter Letzt möchte ich noch ein Wort des Dankes aber auch der Entschuldigung an meine Referenten, Dr. Schmiedeberg und Prof. Dr. Löwen, richten, die diese Seiten am Ende lesen mussten. Ihnen zu Liebe mache ich hier endgültig einen Punkt.

Eidesstattliche Versicherung

Ich versichere an Eides Statt, dass die Dissertation von mir selbständig und ohne unzulässige fremde Hilfe unter Beachtung der „Grundsätze zur Sicherung guter wissenschaftlicher Praxis an der Heinrich-Heine-Universität Düsseldorf“ erstellt worden ist.

Düsseldorf,